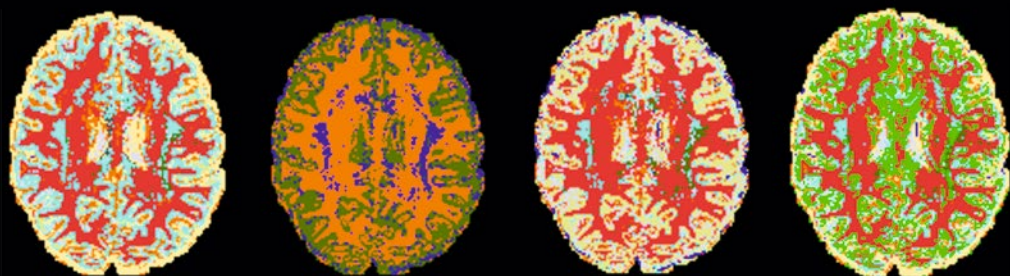


Mathematics and Visualization



Andrea Fuster · Aurobrata Ghosh  
Enrico Kaden · Yogesh Rathi  
Marco Reisert *Editors*

# Computational Diffusion MRI

MICCAI Workshop, Munich, Germany,  
October 9th, 2015



# Mathematics and Visualization

## Series Editors

Gerald Farin

Hans-Christian Hege

David Hoffman

Christopher R. Johnson

Konrad Polthier

Martin Rumpf

More information about this series at <http://www.springer.com/series/4562>

Andrea Fuster • Aurobrata Ghosh • Enrico Kaden •  
Yogesh Rathi • Marco Reisert  
Editors

# Computational Diffusion MRI

MICCAI Workshop, Munich, Germany,  
October 9th, 2015

With 73 Figures, 68 in color

 Springer

*Editors*

Andrea Fuster  
Dept. of Mathematics and Computer  
Science  
Eindhoven University of Technology  
Eindhoven, The Netherlands

Aurobrata Ghosh  
Centre for Medical Image Computing  
University College London  
London, United Kingdom

Enrico Kaden  
Centre for Medical Image Computing  
University College London  
London, United Kingdom

Yogesh Rathi  
Brigham and Women's Hospital  
Harvard Medical School  
Boston, MA, USA

Marco Reisert  
Department of Radiology  
University Medical Center  
Freiburg, Germany

ISSN 1612-3786

Mathematics and Visualization

ISBN 978-3-319-28586-3

DOI 10.1007/978-3-319-28588-7

ISSN 2197-666X (electronic)

ISBN 978-3-319-28588-7 (eBook)

Library of Congress Control Number: 2016937327

Mathematics Subject Classification (2010): 92Bxx, 62P10, 65Z99, 00A66, 65Cxx, 65Dxx

© Springer International Publishing Switzerland 2016

This work is subject to copyright. All rights are reserved by the Publisher, whether the whole or part of the material is concerned, specifically the rights of translation, reprinting, reuse of illustrations, recitation, broadcasting, reproduction on microfilms or in any other physical way, and transmission or information storage and retrieval, electronic adaptation, computer software, or by similar or dissimilar methodology now known or hereafter developed.

The use of general descriptive names, registered names, trademarks, service marks, etc. in this publication does not imply, even in the absence of a specific statement, that such names are exempt from the relevant protective laws and regulations and therefore free for general use.

The publisher, the authors and the editors are safe to assume that the advice and information in this book are believed to be true and accurate at the date of publication. Neither the publisher nor the authors or the editors give a warranty, express or implied, with respect to the material contained herein or for any errors or omissions that may have been made.

Cover illustration: Cover illustration by Aurobrata Ghosh

Printed on acid-free paper

This Springer imprint is published by Springer Nature  
The registered company is Springer International Publishing AG Switzerland

# Preface

These proceedings of the 2015 MICCAI Workshop “Computational Diffusion MRI” offer a snapshot of the current state of the art on a broad range of topics within the highly active and growing field of diffusion MRI. The topics vary from fundamental theoretical work on mathematical modeling to the development and evaluation of robust algorithms, new computational methods applied to diffusion magnetic resonance imaging data, and applications in neuroscientific studies and clinical practice. Over the last decade interest in diffusion MRI has exploded. The technique provides unique insights into the microstructure of living tissue and enables in vivo connectivity mapping of the brain. Computational techniques are key to the continued success and development of diffusion MRI and to its widespread transfer into clinical practice. New processing methods are essential for addressing issues at each stage of the diffusion MRI pipeline: acquisition, reconstruction, modeling and model fitting, image processing, fiber tracking, connectivity mapping, visualization, group studies, and inference. This volume, which includes both careful mathematical derivations and a wealth of rich, full-color visualizations and biologically or clinically relevant results, offers a valuable starting point for anyone interested in learning about computational diffusion MRI and mathematical methods for mapping brain connectivity, as well as new perspectives and insights on current research challenges for those currently working in the field. It will be of interest to researchers and practitioners in the fields of computer science, MR physics, and applied mathematics.

Eindhoven, The Netherlands  
London, United Kingdom  
London, United Kingdom  
Boston, MA, USA  
Freiburg, Germany

Andrea Fuster  
Aurobrata Ghosh  
Enrico Kaden  
Yogesh Rathi  
Marco Reisert



# Contents

## Part I Orals

<b>An Efficient Finite Element Solution of the Generalised Bloch-Torrey Equation for Arbitrary Domains</b> .....	3
Leandro Beltrachini, Zeike A. Taylor, and Alejandro F. Frangi	
<b>Super-Resolution Reconstruction of Diffusion-Weighted Images Using 4D Low-Rank and Total Variation</b> .....	15
Feng Shi, Jian Cheng, Li Wang, Pew-Thian Yap, and Dinggang Shen	
<b>Holistic Image Reconstruction for Diffusion MRI</b> .....	27
Vladimir Golkov, Jorg M. Portegies, Antonij Golkov, Remco Duits, and Daniel Cremers	
<b>Alzheimer’s Disease Classification with Novel Microstructural Metrics from Diffusion-Weighted MRI</b> .....	41
Talia M. Nir, Julio E. Villalon-Reina, Boris A. Gutman, Daniel Moyer, Neda Jahanshad, Morteza Dehghani, Clifford R. Jack Jr., Michael W. Weiner, and Paul M. Thompson, for the Alzheimer’s Disease Neuroimaging Initiative (ADNI)	
<b>Brain Tissue Micro-Structure Imaging from Diffusion MRI Using Least Squares Variable Separation</b> .....	55
Hamza Farooq, Junqian Xu, Essa Yacoub, Tryphon Georgiou, and Christophe Lenglet	
<b>Multi-Tensor MAPMRI: How to Estimate Microstructural Information from Crossing Fibers</b> .....	65
Mauro Zucchelli, Lorenza Brusini, C. Andrés Méndez, and Gloria Menegaz	



<b>On the Use of Antipodal Optimal Dimensionality Sampling Scheme on the Sphere for Recovering Intra-Voxel Fibre Structure in Diffusion MRI</b> .....	75
Alice P. Bates, Zubair Khalid, and Rodney A. Kennedy	
<b>Estimation of Fiber Orientations Using Neighborhood Information</b> .....	87
Chuyang Ye, Jiachen Zhuo, Rao P. Gullapalli, and Jerry L. Prince	
<b>Part II Posters</b>	
<b>A Framework for Creating Population Specific Multimodal Brain Atlas Using Clinical T1 and Diffusion Tensor Images</b> .....	99
Vikash Gupta, Grégoire Malandain, Nicholas Ayache, and Xavier Pennec	
<b>Alignment of Tractograms as Linear Assignment Problem</b> .....	109
Nusrat Sharmin, Emanuele Olivetti, and Paolo Avesani	
<b>Accelerating Global Tractography Using Parallel Markov Chain Monte Carlo</b> .....	121
Haiyong Wu, Geng Chen, Zhongxue Yang, Dinggang Shen, and Pew-Thian Yap	
<b>Adaptive Enhancement in Diffusion MRI Through Propagator Sharpening</b> .....	131
Tom Dela Haije, Neda Sepasian, Andrea Fuster, and Luc Florack	
<b>Angular Resolution Enhancement of Diffusion MRI Data Using Inter-Subject Information Transfer</b> .....	145
Geng Chen, Pei Zhang, Ke Li, Chong-Yaw Wee, Yafeng Wu, Dinggang Shen, and Pew-Thian Yap	
<b>Crossing Versus Fanning: Model Comparison Using HCP Data</b> .....	159
Aurobrata Ghosh, Daniel Alexander, and Hui Zhang	
<b>White Matter Fiber Set Simplification by Redundancy Reduction with Minimum Anatomical Information Loss</b> .....	171
Gali Zimmerman Moreno, Guy Alexandroni, and Hayit Greenspan	
<b>A Temperature Phantom to Probe the Ensemble Average Propagator Asymmetry: An In-Silico Study</b> .....	183
Marco Pizzolato, Demian Wassermann, Tanguy Duval, Jennifer S.W. Campbell, Timothé Boutelier, Julien Cohen-Adad, and Rachid Deriche	
<b>Registration Strategies for Whole-Body Diffusion-Weighted MRI Stitching</b> .....	195
Jakub Ceranka, Mathias Polfiet, Frederic Lecouvet, Nicolas Michoux, Johan de Mey, and Jef Vandemeulebroucke	

**Using Automatic HARDI Feature Selection, Registration, and Atlas Building to Characterize the Neuroanatomy of A $\beta$  Pathology** ..... 207  
Evan Schwab, Michael A. Yassa, Michael Weiner, and René Vidal

**Reliability of Structural Connectivity Examined with Four Different Diffusion Reconstruction Methods at Two Different Spatial and Angular Resolutions** ..... 219  
J.E. Villalon-Reina, T.M. Nir, L. Zhan, K.L. McMahon, G.I. de Zubicaray, M.J. Wright, N. Jahanshad, and P.M. Thompson

**Index** ..... 233

# **Part I**

## **Orals**

# An Efficient Finite Element Solution of the Generalised Bloch-Torrey Equation for Arbitrary Domains

Leandro Beltrachini, Zeike A. Taylor, and Alejandro F. Frangi

**Abstract** Nuclear magnetic resonance (NMR) is an invaluable tool for investigating porous media. Its use allows to study pore size distributions, fiber tortuosity, and permeability as a function of the relaxation time, diffusivity, and flow. This information was shown to be important in many applications, such as medical diagnosis and materials science. A complete NMR analysis involves the solution of the Bloch-Torrey (BT) equation. However, solving this equation analytically becomes intractable for all but the simplest geometries.

We present an efficient numerical framework for solving the generalised BT equation. This method allows to obtain computational simulations of the NMR experiment in arbitrarily complex domains. In addition to the standard BT equation, the generalised BT formulation takes into account the flow and relaxation terms, allowing a better representation of the phenomena under scope. This framework is flexible enough to deal parametrically with any order of convergence in the spatial domain. Moreover, we developed a second-order implicit scheme for the temporal discretisation with similar computational demands as the existing explicit methods. This represents a huge step forward for obtaining reliable results with few iterations. Comparisons with analytical solutions and real data show the flexibility and accuracy of the proposed method.

## 1 Introduction

Nuclear magnetic resonance (NMR) is a powerful and non-invasive technique that allows to study the translational motion of molecules in solution, either by diffusion or fluid flow, by using magnetic field gradient methods. The study of this motion reflects properties of the media and its surrounding environment, making NMR an

---

L. Beltrachini (✉) • Z.A. Taylor • A.F. Frangi

Department of Electronic and Electrical Engineering, Centre for Computational Imaging and Simulation Technologies in Biomedicine, CISTIB, University of Sheffield, Pam Liversidge Building, Mappin Street, Sheffield S1 3JD, UK

e-mail: [l.beltrachini@sheffield.ac.uk](mailto:l.beltrachini@sheffield.ac.uk); [z.a.taylor@sheffield.ac.uk](mailto:z.a.taylor@sheffield.ac.uk); [a.frangi@sheffield.ac.uk](mailto:a.frangi@sheffield.ac.uk)

extremely valuable methodology for probing the complex microstructure of natural and artificial materials [1]. A complete analysis of this phenomena involves the solution of the generalised Bloch-Torrey (BT) equation [2]. This equation describes the evolution of the transverse magnetisation due to diffusion and flow in the media, spin-spin relaxation, and the gradient field encoding scheme. The problem of solving this equation in arbitrary domains is of primary interest when relating variations in the acquired signals to the underlying structures.

There has been many attempts to solve the BT equation, which can be grouped into analytical and numerical approaches. The first group comprises solutions given by mathematical formulae relating the output signal with parameters of interest. These solutions are obtained by proper manipulation of the mathematical expressions describing the physical phenomena. Then, different forms of the solution can be found depending on the mathematical framework used and the approximations made [1, 3, 4]. These solutions have been shown to be very important to study the physical basis of experimental results (e.g. [3]), as well as to perform other mathematical analysis due to their parametric nature [1]. However, since the difficulty of such manipulation increases with the complexity of the domain, there exist solutions only for simple geometries, as multi-layered slabs (1D), cylinders (2D), and spheres (3D). This limits the application of these solutions to arbitrary domains, restricting their usefulness to idealised models. These disadvantages are addressed by numerical methods. This group is composed by the entire family of approximations of the true signals obtained by the application of a numerical algorithm. Such algorithms have the advantage of being unrestricted to simple geometries. However, they have many disadvantages when compared to the analytical solutions, such as their non-parametric nature and the intrinsic approximations and errors associated with them. Although the latter can be reduced in principle, it comes at the expense of computational effort, which can be prohibitive.

There exist many numerical methods that have been used to solve the BT equation explicitly, albeit none of them considers the flow term. This comprises solutions obtained by the finite difference method [5], the finite volume method [6], and the finite element (FE) method [7]. The latter is generally preferred owing to its flexibility for spatially discretising the domain. However, many proposed solutions based on the FE method rely on strong assumptions (e.g. narrow pulse limit approximation) that limit their general applicability. Recently, a flexible FE formulation of the standard BT equation (i.e. without flow and transverse relaxation terms) has been proposed [8]. There, the authors present a FE approach using first-order basis functions in space and an explicit second-order approximation in time, which does not make such constraining approximations. To the best of our knowledge, this latter paper by Nguyen et al. [8] is the first to do so.

In this paper, we present a numerical FE framework for the solution of the generalised BT equation. We extend the formulation given in [8] by considering the flow and relaxation terms, allowing a better representation of the phenomena under scope. We derive closed-form formulas for all the matrices involved in the numerical algorithm, which are specially useful to speed-up the computations. Finally, we

present a second order implicit method for the temporal discretisation. Unlike explicit schemes, implicit methods are unconditionally stable no matter the time-step selected [9]. This is crucial for achieving reliable solutions with a minimum number of iterations. We introduce an implicit scheme to solve the BT equation with similar computational load as the explicit method used in [8], which makes it highly competitive in the field.

*Notation:* In the following, we denote vectors with boldface lower case letters and matrices with boldface capital letters. We use  $\text{vec}(\cdot)$  to refer to the operator that, given a matrix, returns a vector with the matrix elements stacked columnwise, taking the columns in order from first to last. We express the Kronecker matrix product by  $\otimes$ , and the  $n$ th Kronecker product of  $\mathbf{A}$  with itself by  $\mathbf{A}^{\otimes n}$ . Finally, we denote the  $n \times n$  identity matrix as  $\mathbf{I}_n$ , and the  $m \times n$  matrix full of ones as  $\mathbf{1}_{m,n}$ .

## 2 Methods

### 2.1 Differential Formulation

Let  $\Omega$  be the domain under analysis, which can be split into  $L$  subdomains, such that  $\Omega = \bigcup_{l=1}^L \Omega_l$ . Also, let  $\Gamma_l^e$  be the external boundary of  $\Omega_l$ , and  $\Gamma_{ln}$  the boundary between  $\Omega_l$  and  $\Omega_n$ . Then, under generally valid assumptions (such as considering normal or Fickian diffusion, intermediate layers infinitely thin, incompressible flow, and absence of susceptibility effects and hardware imperfections; see [2, 4] for a detailed discussion), the evolution of the complex transverse magnetisation  $m_l(\mathbf{r}, t)$  in the rotating frame is described by [2, 10]

$$\begin{aligned} \frac{\partial m_l(\mathbf{r}, t)}{\partial t} = & \nabla \cdot (\mathbf{D}_l(\mathbf{r}) \nabla m_l(\mathbf{r}, t)) - i\gamma B(\mathbf{r}, t) m_l(\mathbf{r}, t) - \frac{1}{T_l} m_l(\mathbf{r}, t) \\ & - \mathbf{v}(\mathbf{r}, t) \cdot \nabla m_l(\mathbf{r}, t) \quad (\mathbf{r} \in \Omega_l), \end{aligned} \quad (1)$$

subject to the boundary conditions (BCs)

$$\mathbf{D}_l(\mathbf{r}) \nabla m_l(\mathbf{r}, t) \cdot \mathbf{n}_l(\mathbf{r}) = \kappa_{ln} (m_n(\mathbf{r}, t) - m_l(\mathbf{r}, t)) \quad (\mathbf{r} \in \Gamma_{ln}, \forall n), \quad (2a)$$

$$\mathbf{D}_l(\mathbf{r}) \nabla m_l(\mathbf{r}, t) \cdot \mathbf{n}_l(\mathbf{r}) = -\kappa_l^e m_l(\mathbf{r}, t) \quad (\mathbf{r} \in \Gamma_l^e), \quad (2b)$$

and the initial condition (IC)

$$m_l(\mathbf{r}, 0) = \rho_l(\mathbf{r}), \quad (\mathbf{r} \in \Omega_l), \quad (3)$$

where  $t \in [0, T_E]$  with  $T_E$  echo time,  $\gamma$  is the gyromagnetic ratio of protons ( $2.675 \times 10^8 \text{ rad T}^{-1} \text{ s}^{-1}$  for  $^1\text{H}$ ),  $\mathbf{D}_l(\mathbf{r})$  is the diffusion (rank-2) tensor,  $T_l$  is the spin-spin relaxation time,  $\mathbf{v}(\mathbf{r}, t)$  is the velocity field of the spins due to flow of the medium,  $\mathbf{n}_l(\mathbf{r})$  is the unitary outward pointing normal to  $\Omega_l$ ,  $\kappa_{ln}$  ( $\kappa_l^e$ ) is the

permeability constant in  $\Gamma_{ln}$  ( $\Gamma_l^e$ ), and  $B(\mathbf{r}, t)$  is the effective magnetic field. In the following analysis we considered  $T_l$  constant in each subdomain  $\Omega_l$  and the same permeability in both directions of the same membrane, i.e.  $\kappa_{ln} = \kappa_{nl}$ .

Equation (1) states that the transverse magnetisation evolves due to diffusion (first term), encoded through the applied magnetic field (second term), bulk relaxation (third term), and flow (last term). The BC (2a) accounts for the creation of the diffusive flux by the drop in magnetisation between layers. Noting that  $\Gamma_{ln} = \Gamma_{nl}$ , it is easily seen that it also accounts for the conservation of the magnetisation flux between adjacent layers. The flux conservation at the external boundary is considered by Eq. (2b). Finally, Eq. (3) represents the solution of (1) for the initial state ( $t = 0$  s).

Once the complex magnetisation is computed, the output signal is given by

$$S = \int_{\Omega} m(\mathbf{r}, TE) \tilde{\rho}(\mathbf{r}) d\mathbf{r}, \quad (4)$$

where  $\tilde{\rho}(\mathbf{r})$  is some pick-up function of the measuring coil or antenna [1].

## 2.2 Variational Formulation and Spatial Discretisation

The transverse magnetisation is obtained by solving (1)–(3). This problem requires a solution twice differentiable, thus restricting the solutions space. To relax this condition, a solution in the weighted residual sense is obtained [11]. This solution satisfies

$$\begin{aligned} \frac{\partial}{\partial t} \int_{\Omega_l} v(\mathbf{r}) m_l(\mathbf{r}, t) d\mathbf{r} &= \int_{\Omega_l} v(\mathbf{r}) \nabla \cdot (\mathbf{D}(\mathbf{r}) \nabla m_l(\mathbf{r}, t)) d\mathbf{r} - \frac{1}{T_l} \int_{\Omega_l} v(\mathbf{r}) m_l(\mathbf{r}, t) d\mathbf{r} \\ &\quad - i\gamma \int_{\Omega_l} v(\mathbf{r}) m_l(\mathbf{r}, t) B(\mathbf{r}, t) d\mathbf{r} - \int_{\Omega_l} v(\mathbf{r}) \mathbf{v}(\mathbf{r}, t) \cdot \nabla m_l(\mathbf{r}, t) d\mathbf{r}, \end{aligned} \quad (5)$$

valid for  $\mathbf{r} \in \Omega_l$  ( $l = 1, \dots, L$ ), and for all functions  $v(\mathbf{r})$  in a proper functional space. The Hilbert-Sovolev space  $\mathcal{H}^1(\Omega_l)$  of square-integrable functions with square-integrable derivatives [11] is generally chosen. After using the divergence theorem in the diffusion term and the BCs, we get

$$\begin{aligned} \frac{\partial}{\partial t} \int_{\Omega_l} v(\mathbf{r}) m_l(\mathbf{r}, t) d\mathbf{r} &= - \int_{\Omega_l} \nabla v(\mathbf{r}) \cdot (\mathbf{D}_l(\mathbf{r}) \nabla m_l(\mathbf{r}, t)) d\mathbf{r} - \frac{1}{T_l} \int_{\Omega_l} v(\mathbf{r}) m_l(\mathbf{r}, t) d\mathbf{r} \\ &\quad - i\gamma \int_{\Omega_l} v(\mathbf{r}) m_l(\mathbf{r}, t) B(\mathbf{r}, t) d\mathbf{r} - \int_{\Omega_l} v(\mathbf{r}) \mathbf{v}(\mathbf{r}, t) \cdot \nabla m_l(\mathbf{r}, t) d\mathbf{r} \\ &\quad - \kappa_l^e \int_{\Gamma_l^e} v(\mathbf{r}) m_l(\mathbf{r}, t) d\mathbf{r} + \sum_n \kappa_{ln} \int_{\Gamma_{ln}} v(\mathbf{r}) (m_n(\mathbf{r}, t) - m_l(\mathbf{r}, t)) d\mathbf{r}, \end{aligned} \quad (6)$$

also known as the *variational formulation* [11]. The solution under scope needs to be *only* one-time differentiable.

In order to obtain a discretisation of (6), it is necessary to find a solution belonging to  $\mathcal{V}_h$ , a finite-dimensional subspace of  $\mathcal{H}^1(\Omega_l)$ . Let  $\{\varphi_1^l(\mathbf{r}), \dots, \varphi_N^l(\mathbf{r})\}$  be a basis of  $\mathcal{V}_h$  such that for all  $g(t) \in \mathcal{V}_h$ ,  $g(t) = \sum_{i=1}^N \varphi_i^l(\mathbf{r}) \eta_i(t)$ , with  $\eta_i(t) \in \mathbb{C}$ . Then, the approximation of the transverse magnetisation  $m_l^*(\mathbf{r}, t) \in \mathcal{V}_h$  satisfying (6) is defined as

$$m_l^*(\mathbf{r}, t) = \sum_{i=1}^N \varphi_i^l(\mathbf{r}) \eta_i^l(t). \quad (7)$$

In the case of choosing the test functions as the basis functions, i.e.  $v(\mathbf{r}) = \varphi_j^l(\mathbf{r})$  ( $j = 1, \dots, N$ ), it is possible to obtain (after some algebra)

$$\mathbf{M}_l \frac{\partial \eta_l}{\partial t} = - \left( \mathbf{S}_l + i \mathbf{Q}_l(t) + \frac{1}{T_l} \mathbf{M}_l + \mathbf{J}_l(t) + \mathbf{F}_l \right) \eta_l - \sum_n \mathbf{H}_{ln} \eta_n, \quad (8)$$

where

$$\{\mathbf{M}_l\}_{ij} \triangleq M_{ij} = \int_{\Omega_l} \varphi_i^l(\mathbf{r}) \varphi_j^l(\mathbf{r}) d\mathbf{r}, \quad (9a)$$

$$\{\mathbf{S}_l\}_{ij} \triangleq S_{ij} = \int_{\Omega_l} \nabla \varphi_j^l(\mathbf{r})^T \mathbf{D}_l(\mathbf{r}) \nabla \varphi_i^l(\mathbf{r}) d\mathbf{r}, \quad (9b)$$

$$\{\mathbf{Q}_l(t)\}_{ij} \triangleq Q_{ij}(t) = \gamma \int_{\Omega_l} \varphi_i^l(\mathbf{r}) \varphi_j^l(\mathbf{r}) B(\mathbf{r}, t) d\mathbf{r}, \quad (9c)$$

$$\{\mathbf{J}_l(t)\}_{ij} \triangleq J_{ij}(t) = \int_{\Omega_l} \varphi_j^l(\mathbf{r}) \mathbf{v}(\mathbf{r}, t) \cdot \nabla \varphi_i^l(\mathbf{r}) d\mathbf{r}, \quad (9d)$$

$$\{\mathbf{F}_l\}_{ij} \triangleq F_{ij} = \kappa_l^e \int_{\Gamma_l^e} \varphi_j^l(\mathbf{r}) \varphi_i^l(\mathbf{r}) d\mathbf{r}, \quad (9e)$$

$$\{\mathbf{H}_{ln}\}_{ij} \triangleq H_{ij} = \kappa_{ln} \int_{\Gamma_{ln}} \varphi_j^l(\mathbf{r}) (\varphi_i^l(\mathbf{r}) - \varphi_i^n(\mathbf{r})) d\mathbf{r}. \quad (9f)$$

Therefore, the problem turned out to find  $\boldsymbol{\eta}(T_E)$  satisfying (8), for which (9) needs to be solved.



### 2.3 Formulation of Element Matrices for Polynomial Basis Functions

To proceed with the spatial discretisation, the volume and area coordinate systems were used. Basically, they are coordinate systems in which the location of a point of an element (triangle or tetrahedron) is specified as the center of mass. These coordinate systems allow to compute analytically (9) considering polynomial basis functions over a tetrahedral discretisation of the domain. We refer to [11] for further details related to them.

It is now possible to obtain numerical representations of (9a)–(9f) using the volume and area coordinate systems. To this end, linear basis functions were considered, achieving first order FE formulation. Since these basis functions are defined for each tetrahedron (or triangle), expressions of (9a)–(9f) valid for each element were derived, usually called *elemental matrices*, and denoted by the sub/superscript ‘ $e$ ’. The final matrices were then obtained by assembling the elemental matrices [11].

Once the basis functions are chosen, the computation of  $M^e$  is straightforward. To discretise (9b), it is useful to note that the gradient of any function  $f(\mathbf{r})$  can be expressed in the volumetric coordinate system as  $\nabla f(\mathbf{r}) = \frac{1}{6V} \mathbf{A} \nabla_{\xi} f(\xi)$ , where  $\xi$  is the volume coordinates vector, and  $\mathbf{A}$  is a  $3 \times 4$  constant matrix defined by the nodes of the corresponding tetrahedron [11]. Then, the elementary stiffness matrix is found to be

$$\mathbf{S}^e = \frac{1}{6V_e} \int_{\omega_n} \nabla_{\xi} \boldsymbol{\varphi}(\xi)^T \mathbf{A}^T \mathbf{D} \mathbf{A} \nabla_{\xi} \boldsymbol{\varphi}(\xi) d\omega_n, \quad (10)$$

where  $\nabla_{\xi} \boldsymbol{\varphi}(\xi) = [\nabla_{\xi} \varphi_1(\xi), \dots, \nabla_{\xi} \varphi_N(\xi)]$ . If the diffusion tensor is assumed constant within the element, it is possible to extract it (as well as  $\mathbf{A}$ ) outside the integral. This allows to separate the elementary matrix as the product of a coefficient (i.e. constant) matrix and a parametric matrix dependent on the diffusion tensor elements. To this end, the  $\text{vec}(\cdot)$  operator is utilised. Employing the identity  $\text{vec}(\mathbf{ABC}) = (\mathbf{C}^T \otimes \mathbf{A}) \text{vec}(\mathbf{B})$  [12] on (10) leads to

$$\text{vec}(\mathbf{S}^e) = \frac{1}{6V_e} \bar{\mathbf{S}}^T (\mathbf{A}^{\otimes 2})^T \text{vec}(\mathbf{D}), \quad (11)$$

where

$$\bar{\mathbf{S}} = \int_{\omega_n} (\nabla_{\xi} \boldsymbol{\varphi}(\xi))^{\otimes 2} d\omega_n, \quad (12)$$

is a constant matrix once the basis functions are selected. In the particular case of choosing first order basis functions,  $\nabla_{\xi} \boldsymbol{\varphi}(\xi) = \mathbf{I}_4$ , resulting in  $\bar{\mathbf{S}} = \mathbf{I}_{16}/6$ .

To obtain the representation of  $\mathbf{Q}^e(t)$ , it is first needed to select the spatial profile of the magnetic field  $B(\mathbf{r}, t)$ . For simplicity, we considered the linear gradient field, in which case  $B(\mathbf{r}, t) = \mathbf{g}(t) \cdot \mathbf{r}$ , with  $\mathbf{g}(t)$  being the effective

applied gradient field, which can vary over time. Examples of linear gradients are the single- and double-pulse gradient spin-echo sequences (sPGSE and dPGSE, respectively) [3, 4]. In this case, after some algebraic manipulations, we obtained  $\mathcal{Q}_{ij}^e(t) = \mathbf{g}(t) \cdot (\mathcal{Q}_{ij}^{(1)}, \mathcal{Q}_{ij}^{(2)}, \mathcal{Q}_{ij}^{(3)})$ , where  $\mathbf{g}(t) = [g_x(t), g_y(t), g_z(t)]^T$ . In matrix notation,  $\mathcal{Q}^e(t) = g_x(t)\mathcal{Q}_e^{(1)} + g_y(t)\mathcal{Q}_e^{(2)} + g_z(t)\mathcal{Q}_e^{(3)}$ , where  $\mathcal{Q}_e^{(k)}$  ( $k = 1, 2, 3$ ) are matrices defined by

$$\left[ \text{vec}(\mathcal{Q}_e^{(1)}), \text{vec}(\mathcal{Q}_e^{(2)}), \text{vec}(\mathcal{Q}_e^{(3)}) \right]^T = 6\gamma V_e (\mathbf{A}\mathbf{A}^T)^{-1} \mathbf{A} (6V_e \bar{\mathcal{Q}}_{lin} - \mathbf{a} \text{vec}(\mathbf{M}^e)^T), \quad (13)$$

where  $\bar{\mathcal{Q}}_{lin} = \int_{\omega_n} \boldsymbol{\xi} (\boldsymbol{\varphi}(\boldsymbol{\xi})^T)^{\otimes 2} d\omega_n$ , and  $\boldsymbol{\varphi}(\boldsymbol{\xi}) = [\varphi_1(\boldsymbol{\xi}), \dots, \varphi_N(\boldsymbol{\xi})]^T$ .

Computing (9d) requires adopting a model for the velocity field. Assuming  $\mathbf{v}(\mathbf{r}, t) = \mathbf{v}(\mathbf{r})h(t)$ , it is found

$$\mathbf{J}^e = h(t) \int_{\omega} \nabla \boldsymbol{\varphi}(\mathbf{r})^T \mathbf{v}(\mathbf{r}) \boldsymbol{\varphi}(\mathbf{r})^T d\omega, \quad (14)$$

which can be further simplified in the particular case of considering constant velocity in each element.

The computation of  $\mathbf{F}_l^e$  was straightforward when using the area coordinate system. Finally, to compute (9f), a discontinuous FE approach was considered. Under this method, the solution is allowed to be discontinuous at the compartment interfaces but not inside each region [8]. The discretisation was then obtained by doubling the nodes at the interfaces, each of them belonging to each region. Corresponding triangles share the basis functions (but not the nodes), hence  $\mathbf{H}^e$  was easily found integrating, as done for  $\mathbf{F}_l^e$ .

## 2.4 Temporal Discretisation

Once the spatial discretisation is obtained, Eq. (8) needs to be solved for all  $\Omega_l$  ( $l = 1, \dots, L$ ). For simplicity, the  $L$  systems of differential equations are merged into a single one. The global matrices involved in (8) are then defined as the assemble of the corresponding matrices in any region. Then, Eq. (8) could be expressed as

$$\mathbf{M} \frac{\partial \boldsymbol{\eta}(t)}{\partial t} = -(\boldsymbol{\Upsilon}(t) + i\mathcal{Q}(t))\boldsymbol{\eta}(t), \quad (15)$$

where  $\boldsymbol{\Upsilon}$  is the real part of the right term of the assemble, comprising the matrices  $\mathbf{S}$ ,  $\mathbf{M}$ ,  $\mathbf{J}$ ,  $\mathbf{F}$ , and  $\mathbf{H}$ , and the lack of subindex refers to the global matrix. Most of the matrices were block diagonal, as seen from their definitions in (9). This was extremely useful when computing inverse matrices efficiently.

Next, we present an approach to obtain  $\boldsymbol{\eta}(T_E)$  from (15), highlighting its pros and cons. Once  $\boldsymbol{\eta}(T_E)$  is obtained, the corresponding signal is found through (4) and (7), i.e.

$$\begin{aligned} S &= \int_{\Omega} \tilde{\rho}(\mathbf{r})m(\mathbf{r}, T_E)d\mathbf{r} \\ &\approx \sum_e \left( \int_{\omega_e} \tilde{\rho}(\mathbf{r})\boldsymbol{\varphi}_e(\mathbf{r})d\mathbf{r} \right)^T \boldsymbol{\eta}_e(T_E) = \sum_e \mathbf{y}_e^T \boldsymbol{\eta}_e(T_E) = \mathbf{y}^T \boldsymbol{\eta}(T_E), \end{aligned} \quad (16)$$

where  $\mathbf{y}_e = \int_{\omega_e} \tilde{\rho}(\mathbf{r})\boldsymbol{\varphi}_e(\mathbf{r})d\mathbf{r}$ .

As in [8], the solution vector in (15) is split into its real and imaginary parts, resulting in the following the coupled system of equations

$$\begin{cases} \mathbf{M} \frac{\partial \boldsymbol{\eta}_R(t)}{\partial t} = -\boldsymbol{\Upsilon}(t)\boldsymbol{\eta}_R(t) + \mathbf{Q}(t)\boldsymbol{\eta}_I(t) \\ \mathbf{M} \frac{\partial \boldsymbol{\eta}_I(t)}{\partial t} = -\boldsymbol{\Upsilon}(t)\boldsymbol{\eta}_I(t) - \mathbf{Q}(t)\boldsymbol{\eta}_R(t) \end{cases}, \quad (17)$$

where  $\boldsymbol{\eta}(t) = \boldsymbol{\eta}_R(t) + i\boldsymbol{\eta}_I(t)$ . To solve this system, the implicit trapezoidal method [9] was chosen. This is a second-order scheme characterised for being the only A-stable multistep method. Since this is an implicit method, it will generally demand a larger computational cost. However, in the sequel, we show that this problem can be solved. Under this scheme, Eq. (17) takes the form

$$\begin{cases} \boldsymbol{\eta}_R^{n+1} = \boldsymbol{\eta}_R^n + \frac{\Delta t}{2} \left( -\tilde{\boldsymbol{\Upsilon}}_{n+1}\boldsymbol{\eta}_R^{n+1} + \tilde{\mathbf{Q}}_{n+1}\boldsymbol{\eta}_I^{n+1} - \tilde{\boldsymbol{\Upsilon}}_n\boldsymbol{\eta}_R^n + \tilde{\mathbf{Q}}_n\boldsymbol{\eta}_I^n \right) \\ \boldsymbol{\eta}_I^{n+1} = \boldsymbol{\eta}_I^n + \frac{\Delta t}{2} \left( -\tilde{\boldsymbol{\Upsilon}}_{n+1}\boldsymbol{\eta}_I^{n+1} - \tilde{\mathbf{Q}}_{n+1}\boldsymbol{\eta}_R^{n+1} - \tilde{\boldsymbol{\Upsilon}}_n\boldsymbol{\eta}_I^n - \tilde{\mathbf{Q}}_n\boldsymbol{\eta}_R^n \right), \end{cases} \quad (18)$$

where  $\Delta t$  is the time-step length and the tilde indicates premultiplication of the corresponding matrix by  $\mathbf{M}^{-1}$ . Some tedious manipulations yield

$$\begin{cases} \boldsymbol{\eta}_R^{n+1} = (\mathbf{I}_N + h^2\mathbf{R}_n^2)^{-1} \left( h(\mathbf{L}_n + \mathbf{R}_n\mathbf{P}_n)\boldsymbol{\eta}_I^n + (\mathbf{P}_n - h^2\mathbf{R}_n^2)\boldsymbol{\eta}_R^n \right) \\ \boldsymbol{\eta}_I^{n+1} = -h\mathbf{R}_n\boldsymbol{\eta}_R^{n+1} - h\mathbf{L}_n\boldsymbol{\eta}_R^n + \mathbf{P}_n\boldsymbol{\eta}_I^n \end{cases}, \quad (19)$$

where  $h = \Delta t/2$ ,  $\mathbf{L}_n = (\mathbf{M} + h\boldsymbol{\Upsilon}_{n+1})^{-1}\mathbf{Q}_n$ ,  $\mathbf{R}_n = (\mathbf{M} + h\boldsymbol{\Upsilon}_{n+1})^{-1}\mathbf{Q}_{n+1}$ , and  $\mathbf{P}_n = (\mathbf{M} + h\boldsymbol{\Upsilon}_{n+1})^{-1}(\mathbf{M} - h\boldsymbol{\Upsilon}_n)$ . From (19), two inverse matrices need to be computed, instead of one as required by any other explicit method. However, since the absolute values of the eigenvalues of  $h^2\mathbf{R}_n^2$  are less than unity, it is possible to write [12]

$$(\mathbf{I}_N + h^2\mathbf{R}_n^2)^{-1} = \sum_{k=0}^{\infty} (-1)^k (h\mathbf{R}_n)^{2k} \approx \mathbf{I}_N - (h\mathbf{R}_n)^2 + (h\mathbf{R}_n)^4, \quad (20)$$

which reduces the needed inversion to one.

The proposed numerical scheme presents some advantages when compared to the Runge-Kutta-Chebyshev algorithm [8]. First, the selected method is A-stable, and therefore stable irrespectively of the selected temporal discretisation step. Second, it only needs one matrix inversion, which in case of considering constant flow, it only needs to be computed once.

### 3 Numerical Results

In this section we present two examples in which the capabilities of the numerical method were tested. The first was intended to show how the developed method performed in situations where the analytical solution was available [4], whereas the second presented a real application based on experimental data [3].

#### 3.1 Example 1: Bi-Layered Sphere

We simulated a sPGSE sequence ( $\delta = \Delta = 10$  ms) in a bi-layered spherical domain with radii  $r_{1,2} = [2.5, 5] \mu\text{m}$ , isotropic diffusivities  $D_{1,2} = [2, 2] \times 10^{-9} \text{ m}^2/\text{s}$ , innermost (outermost) permeability  $\kappa_{12} = 10^{-5}$  ( $\kappa_2^e = 10^{-9}$ ), and bulk relaxivities  $T_{1,2} = [0.1, 0.1] \text{ s}$ . This situation represents a typical scenario when analysing biological samples, as cells or axons [4].

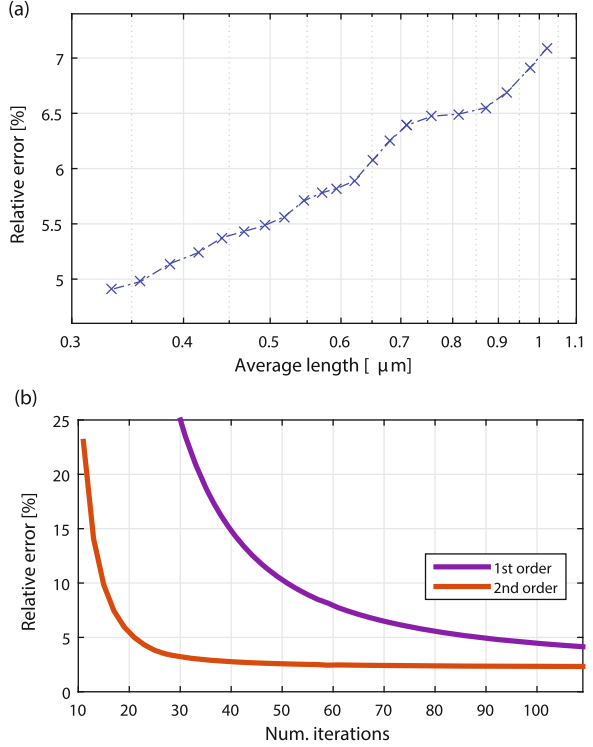
To account for the errors, we computed the relative error, defined as

$$Error = \max_g \left\{ \frac{\|S_a(g) - S_n(g)\|}{\|S_a(g)\|} \right\}, \quad (21)$$

where  $S_a$  and  $S_n$  are the analytical and numerical solutions, respectively, and  $|g| \in [0, 1] \text{ T/m}$ . In Fig. 1a we show the relative error for different model discretisations (obtained using the ISO2Mesh 2013 toolbox [13]) as a function of the mesh size. We considered the second order temporal scheme with 100 time steps. It is seen that the numerical approach gives accurate results even using a coarse discretisation.

One of the main advantages of the presented framework is the possibility to use coarser temporal discretisations without turning the scheme unstable. To illustrate this, we considered a spatial discretisation consisting in 11,464 elements (2198 nodes) and solved the aforementioned problem for varying time-steps. The purpose of this experiment was to test the convergence rate of the developed second order algorithm, and compare it with a similarly obtained first order implicit scheme. The small number of nodes allowed us to use the graphical processing unit (GPU) to speed-up the simulations. Although general-purpose GPUs' memory is limited to 1–2 Gb, the acceleration they provide turns them into a preferable device where to perform demanding computational simulations.

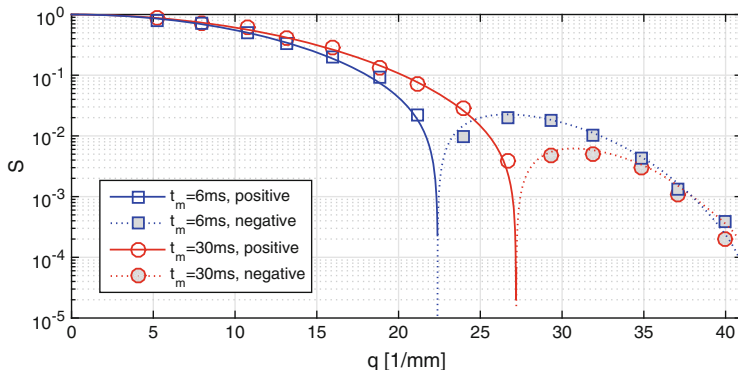
**Fig. 1** Performance of the finite element approximation for the bi-layered spherical domain. **(a)** Relative error as a function of the average element side length. The non-linearity appreciated in the curve is due to the automatic generation of tetrahedral meshes using ISO2Mesh [13]. **(b)** Relative error as a function of the number of time-steps. Results are shown for both first and second order implicit schemes. The difference in the convergence rate is clearly exposed



In Fig. 1b we show the relative error as a function of the temporal discretisation for both backward Euler (first order) and trapezoidal (second order) implicit schemes. The advantages of the implicit nature of both algorithms is clearly appreciated, as well as the advantage of the second order method over the backward Euler approach.

### 3.2 Example 2: Cylinder with dPGSE Sequence

To show the versatility of the numerical framework, we simulated the first experiment reported in [3]. It consists in the application of a dPGSE sequence ( $\delta_1 = \delta_2 = 2$  ms,  $\Delta_1 = \Delta_2 = 150$  ms,  $t_m = 6$  and 30 ms, both gradients applied in the  $x$  direction) perpendicular to impermeable cylindrical microcapillaries of inner diameter  $29 \pm 1$   $\mu\text{m}$ , oriented in the  $z$  direction, and centred in the origin. This experiment was carried out to study the echo attenuation for different mixing times as a function of the  $q$  value, defined as  $q = (2\pi)^{-1}\gamma\delta g$ . We refer to [3] for more details.



**Fig. 2** Signal intensity as a function of the  $q$  value. Different curves correspond to different mixing times. The experimental data points (extracted from [3]) are shown with *symbols*, whereas the curves obtained by numerical simulations are shown with *lines*. Positive values are depicted with *continuous lines* and *empty markers*, and negative values are shown with *dotted lines* and *filled markers*

We considered the first order FEM with 1050 nodes. We refined the temporal discretisation until no more improvement was obtained, resulting in 10,000 time-steps for this particular problem. In Fig. 2 we show both experimental (markers) and numerical (lines) results. There we plotted the acquired signal as a function of the  $q$  value for both mixing times. It can be seen that the signal can take negative values, in accordance with previous findings [3]. There is a very close agreement between the experimental results and the numerical simulations, even using a coarse mesh, confirming their validity for real-scenario experiments.

## 4 Discussion and Conclusions

We presented a FE formulation for solving the generalised BT equation in general domains. This method allows to simulate MR signals in realistic scenarios, including arbitrary geometries, physical properties of the material (diffusivities, permeabilities, relaxivities, and flow), and MR settings (sequences, field, and voxel volume). We obtained expressions for second order discretisations in the temporal domain. These expressions were flexible enough to work with arbitrary discretisations, not being restricted to symmetric meshes nor to specific step lengths to guarantee numerical stability. We showed its feasibility and flexibility to solve real problems achieving small relative errors even using coarse discretisations.

Unlike existing approaches, we obtained ad hoc formulae for computing the matrices involved in the numerical algorithm. This was shown to be helpful for avoiding errors due to numerical integration, as well as to increase the speed-up. As in [4] (and differently from [8]) we considered mixed BCs imposed on the

boundaries of the simulated structures. Whether these conditions are more suitable than the periodic BCs considered in [8] needs to be further explored.

One of the major results was a second order implicit numerical algorithm for solving the temporal discretisation of the BT equation. Implicit methods have the advantage (over explicit methods) of presenting stability properties that allow to choose coarser discretisations without compromising the validity of the result. However, implicit methods are generally discarded for solving large problems due to their computational load. In this paper, we adapted an implicit method for solving the temporal discretisation with similar requirements than explicit methods, hence drastically reducing the simulation time. This was highly efficient when compared to explicit methods, which require really small step-sizes to achieve stable results [8].

**Acknowledgements** The work has been supported by the European Commission FP7 project VPH-DARE@IT (FP7-ICT-2011-9-601055) and the project OCEAN (EP/M006328/1) funded by the EPSRC.

## References

1. Grebenkov, D.: NMR survey of reflected Brownian motion. *Rev. Mod. Phys.* **79**, 1077–1137 (2007)
2. Jeener, J.: Macroscopic molecular diffusion in liquid NMR. *Concepts Magn. Reson.* **14**, 79–88 (2002, revisited)
3. Ozarlan, E., Shemesh, N., Basser, P.J.: A general framework to quantify the effect of restricted diffusion on the NMR signal with applications to double pulsed field gradient NMR experiments. *J. Chem. Phys.* **130**, 104702 (2009)
4. Grebenkov, D.: Pulsed-gradient spin-echo monitoring of restricted diffusion in multilayered structures. *J. Magn. Reson.* **205**, 181–195 (2010)
5. Xu, J., Does, M., Gore, J.: Numerical study of water diffusion in biological tissues using an improved finite difference method. *Phys. Med. Biol.* **52**, 111–126 (2007)
6. Li, J., Le Bihan, D., Nguyen, T., Grebenkov, D., Poupon, C., Haddar, H.: Analytical and numerical study of the apparent diffusion coefficient in diffusion MRI at long diffusion times and low b-values. *Int. Rep.*, INRIA HAL Id: 00763885 (2012)
7. Moroney, B.F., Stait-Gardner, T., Ghadirian, B., Yadav, N.N., Price, W.S.: Numerical analysis of NMR diffusion measurements in the short gradient pulse limit. *J. Magn. Reson.* **234**, 165–75 (2013)
8. Nguyen, D.V., Li, J.-R., Grebenkov, D., Le Bihan, D.: A finite elements method to solve the Bloch-Torrey equation applied to diffusion magnetic resonance imaging. *J. Comput. Phys.* **236**, 283–302 (2014)
9. Burden, R., Faires, J.: *Numerical Analysis*, 9th edn. Brooks/Cole, Belmont (2011)
10. Callaghan, P.: *Translational Dynamics and Magnetic Resonance: Principles of Pulsed Gradient Spin Echo NMR*. Oxford University Press, New York (2011)
11. Silvester, P.P., Ferrari, R.L.: *Finite Elements for Electrical Engineers*. Cambridge University Press, Cambridge (1994)
12. Meyer, C.D.: *Matrix Analysis and Applied Linear Algebra*. SIAM, Philadelphia (2000)
13. Fang, Q., Boas, D.: Tetrahedral mesh generation from volumetric binary and gray-scale images. In: *Proceedings of IEEE International Symposium on Biomedical Imaging*, pp. 1142–1145 (2009)

# Super-Resolution Reconstruction of Diffusion-Weighted Images Using 4D Low-Rank and Total Variation

Feng Shi, Jian Cheng, Li Wang, Pew-Thian Yap, and Dinggang Shen

**Abstract** Diffusion-weighted imaging (DWI) provides invaluable information in white matter microstructure and is widely applied in neurological applications. However, DWI is largely limited by its relatively low spatial resolution. In this paper, we propose an image post-processing method, referred to as super-resolution reconstruction, to estimate a high spatial resolution DWI from the input low-resolution DWI, e.g., at a factor of 2. Instead of requiring specially designed DWI acquisition of multiple shifted or orthogonal scans, our method needs only a single DWI scan. To do that, we propose to model both the blurring and downsampling effects in the image degradation process where the low-resolution image is observed from the latent high-resolution image, and recover the latent high-resolution image with the help of two regularizations. The first regularization is four-dimensional (4D) low-rank, proposed to gather self-similarity information from both the spatial domain and the diffusion domain of 4D DWI. The second regularization is total variation, proposed to depress noise and preserve local structures such as edges in the image recovery process. Extensive experiments were performed on 20 subjects, and results show that the proposed method is able to recover the fine details of white matter structures, and outperform other approaches such as interpolation methods, non-local means based upsampling, and total variation based upsampling.

## 1 Introduction

Diffusion-weighted magnetic resonance imaging (DWI) is a key imaging modality for non-invasive and in vivo characterization of brain white matter microstructure. DWI has been used in early detection of stroke and characterization of neurological

---

F. Shi • L. Wang • P.-T. Yap • D. Shen (✉)

Department of Radiology and BRIC, University of North Carolina at Chapel Hill, Chapel Hill, NC, USA

e-mail: [dgshen@med.unc.edu](mailto:dgshen@med.unc.edu)

J. Cheng

Department of Radiology and BRIC, University of North Carolina at Chapel Hill, Chapel Hill, NC, USA

Section on Tissue Biophysics and Biomimetics, PPITS, National Institute of Child Health and Human Development, NIH, Bethesda, MD, USA



disorders, such as multiple sclerosis and epilepsy, where abnormal diffusion changes on specific white matter regions could be useful clues for disease diagnosis [1–5]. However, DWI is largely limited by its relatively low spatial resolution. For example, the resolution of current typical DWI data is  $2 \times 2 \times 2 \text{ mm}^3$ , which means its voxel is eight times larger than that in the standard T1-weighted structural data ( $1 \times 1 \times 1 \text{ mm}^3$ ). It has been reported that the scan needs to be repeated 64 times for averaging in order to increase the DWI resolution from  $2 \times 2 \times 2 \text{ mm}^3$  to  $1 \times 1 \times 1 \text{ mm}^3$  while keeping the similar signal-to-noise ratio [6].

Besides improving MRI scanner hardware to higher magnetic fields or using stronger gradients, image post-processing methods are considered as a promising alternative for resolution enhancement. Interpolation methods (e.g., with nearest neighbor or spline) are widely used to increase the resolution, but their results often show blurry edges and blocking artifacts. Recently, super-resolution reconstruction (SRR) methods attract increasing research attention, aiming to estimate a high-resolution image from one or more low-resolution inputs [7]. The term super-resolution refers to the consideration of image degradation process where the underlying high-resolution image is translated, blurred, and downsampled to be observed as the low-resolution image. For example, Yuan et al. [8] proposed to minimize total variation (TV) to regularize the recovery of natural images. Manjón et al. [9] used non-local means (NLM) to recover the high-frequency information in SRR of structural MR images on a patch-by-patch basis. Basically, NLM recovers a voxel using a weighted mean of all other similar voxels, with the weights calculated according to the similarity of patches around voxels.

There are only a handful of studies on SRR methods for DWI. In these methods, multiple shifted or orthogonal DWI scans were acquired and then fused into a high-resolution output [10, 11]. However, their methods are hampered for general applications due to two reasons. First, a specially designed image acquisition scheme is needed in these methods to acquire multiple image scans, with longer scanning time. Second, subject motion and eddy current effects in different scans could largely affect the final result. Some other methods attempted to learn the mapping from low resolution to high resolution through training sets using random forests [12] or sparse representation [13]. Here, we focus on the SRR problem for single input image with no training sets. Currently, existing single image SRR methods are generally proposed for 3D structural MR images, while not developed and evaluated in DWI [8, 9, 14, 15]. Note that diffusion-weighted images are in four-dimensional (4D) space, and more sensitive to noise, especially for the images with large diffusion factor b-value. Directly applying them to DWI may fail or compromise the performance.

In this paper, we proposed a novel SRR algorithm for DWI from single scan. We aim to increase the resolution of input low-resolution DWI to a high-resolution DWI, e.g., at the factor of 2. Our contributions are threefold: (1) we model both the blurring and downsampling effects in the image degradation process to recover the latent high-resolution image; (2) we propose a novel 4D low-rank regularization to gather self-similarity information from both the spatial domain and the diffusion domain of 4D DWI; (3) we employ total variation to further preserve local structures

such as edges from noise. Extensive experiments were performed on 20 real subjects, by comparing the proposed method with the interpolation methods, NLM-based up-sampling, and also TV-based up-sampling method.

## 2 Method

We introduce below the proposed method for super-resolution reconstruction of diffusion-weighted images. First, an observation model is provided to formulate the reconstruction as a minimization problem for the input low-resolution image and to-be-recovered high-resolution image. Second, we propose a novel low-rank approximation in 4D space on DWI, for helping retrieve the remote self-similarity information. Third, total variation is adopted to further preserve local structures. Finally, we summarize the total cost function and also provide an efficient optimization scheme.

### 2.1 Observation Model

DWI requires the acquisition of a number of diffusion-sensitized images to probe the diffusion of water molecules in various directions and scales. Denote the latent 4D high-resolution DWI as  $X$ , which is composed of  $N$  3D diffusion volumes  $\{X_n | n = 1, 2, \dots, N\}$ . Similarly, we denote the observed low-resolution 4D image  $T$  containing 3D diffusion volumes  $\{T_n\}$ . Note that  $T$  is acquired from a single scan. In image acquisition, a degradation process is involved in to obtain a degraded low-resolution image from the latent high-resolution image:

$$T_n = DSX_n + z \quad (1)$$

where  $D$  is a 3D downsampling operator,  $S$  is a 3D blurring operator, and  $z$  represents the observation noise. In the spirit of super-resolution reconstruction, we estimate the latent high-resolution 4D image  $X$  by minimizing the following cost function:

$$\min_X \sum_{n=1}^N \|DSX_n - T_n\|^2 + \lambda \mathfrak{R}(X) \quad (2)$$

where the first term is a data fidelity term used for penalizing the difference between the degraded high-resolution image  $X$  and the observed low-resolution image  $T$ . The second term is a regularization term introducing prior information to help solve the ill-posed problem. Weight  $\lambda$  balances the contributions of the fidelity term and regularization term. Next we introduce two regularization terms, 4D low-rank and total variation, respectively.

## 2.2 4D Low-Rank Regularization

Rank is a measure of matrix complexity, corresponding to the number of linearly independent rows or columns of the matrix, or the number of nonzero singular values [16]. In natural and medical images, self-similarity is widely observed, where many rows or columns in the matrix could be linearly represented by other rows or columns, showing redundant information. This gives us the idea that diffusion weighted images could also be closely approximated by their low-rank components.

Here we use low rank as a regularization term to help retrieve useful information from all image regions. To compute the rank for a 4D image  $X$ , we first unfold it into a 2D matrix along each dimension [16]. Specifically, suppose the size of  $X$  is  $V_1 \times V_2 \times V_3 \times N$ , we unfold it into four 2D matrices  $\{X_{(i)}, i = 1, 2, 3, 4\}$  with size of  $V_1 \times (V_2 \times V_3 \times N)$ ,  $V_2 \times (V_1 \times V_3 \times N)$ ,  $V_3 \times (V_1 \times V_2 \times N)$ , and  $N \times (V_1 \times V_2 \times V_3)$ , where  $X_{(i)}$  means unfold  $X$  along dimension  $i$ . Then we compute the sum of the singular values in each matrix for their trace norms  $\|X_{(i)}\|_{tr}$ . Finally, the rank of  $X$  is approximated as the combination of trace norms of all unfolded matrices:

$$\mathfrak{R}_{rank}(X) = \sum_{i=1}^4 \alpha_i \|X_{(i)}\|_{tr} \quad (3)$$

where  $\{\alpha_i\}$  are parameters satisfying  $\alpha_i \geq 0$  and  $\sum_{i=1}^4 \alpha_i = 1$ . By minimizing this term, we could obtain a low-rank approximation of  $X$ . Note that the low rank is applied in 4D image, which means we could retrieve useful information for the reconstruction task from both spatial domain and diffusion domain.

## 2.3 Total Variation Regularization

Total variation is defined as integrals of absolute gradient of the signal [14]. For a 4D diffusion-weighted image  $X$ :

$$\mathfrak{R}_{tv}(X) = \sum_{n=1}^N \int |\nabla X_n| dx dy dz \quad (4)$$

where the gradient operator is performed in 3D spatial space. Here we use TV in 3D space instead of 4D space based on the notion that there is no explicit neighborhood consistency across different diffusion volumes and thus TV in diffusion domain may not be effective. In images, the latent signals without excessive and possibly spurious details generally have low total variation. Accordingly, minimizing the total variation of the signal could generate a close match to the original signal, and removes unwanted noise whilst preserving important details such as edges. In this work, minimizing total variation will reinforce local spatial consistency and preserve edges in the recovered high-resolution image.

## 2.4 Cost Function and Optimization

The proposed super-resolution reconstruction is thus formulated as below:

$$\min_X \sum_{n=1}^N \|DSX_n - T_n\|^2 + \lambda_{rank} \mathfrak{R}_{rank}(X) + \lambda_{tv} \sum_{n=1}^N \mathfrak{R}_{tv}(X_k) \quad (5)$$

We employ the alternating direction method of multipliers (ADMM) algorithm to minimize the cost function in Eq. (5). ADMM has been proven efficient for solving optimization problems with multiple non-smooth terms [17]. Briefly, we first introduce redundant variables  $\{M_i\}_{i=1}^4$  with equality constraints  $X_{(i)} = M_{(i)}$ , and then use Lagrangian dual variables  $\{U_i\}_{i=1}^4$  to integrate the equality constraints into the cost function:

$$\begin{aligned} \min_{X, \{M_i\}_{i=1}^4, \{U_i\}_{i=1}^4} & \sum_{n=1}^N \|DSX_n - T_n\|^2 + \lambda_{rank} \sum_{i=1}^4 \alpha_i \|M_{(i)}\|_{tr} \\ & + \sum_{i=1}^4 \frac{\rho}{2} \left( \|X - M_i + U_i\|^2 - \|U_i\|^2 \right) + \lambda_{tv} \sum_{n=1}^N \int |\nabla X_n| dx dy dz \end{aligned} \quad (6)$$

We break the cost function into subproblems for  $X$ ,  $M$ , and  $U$ , and iteratively update them. The optimization scheme is summarized in Algorithm 1 as below:

---

### Algorithm 1 Super-Resolution Reconstruction of Diffusion Weighted Images

---

**Input:** Low-resolution 4D diffusion-weighted image  $T$ ;

**Initialize** the desired high-resolution image  $X^{(0)}$  by upsampling  $T$  with nearest neighbor interpolation. Set redundant variables  $M_i^{(0)} = 0$ ,  $U_i^{(0)} = 0$ ,  $i = 1, 2, 3, 4$ ;

**For each iteration  $k$ ,**

Update  $X^k$  by using gradient descent:

$$\begin{aligned} \arg \min_X & \sum_{n=1}^N \|DSX_n^{(k-1)} - T_n\|^2 + \sum_{i=1}^4 \frac{\rho}{2} \|X^{(k-1)} - M_i^{(k-1)} + U_i^{(k-1)}\|^2 \\ & + \lambda_{tv} \sum_{n=1}^N \int |\nabla X_n^{(k-1)}| dx dy dz \end{aligned} \quad (7)$$

Update  $M_i^{(k)}$  by using Singular Value Thresholding (SVT) [18]:

$$M_i^{(k)} = \text{fold}_i \left[ \text{SVT}_{\lambda_{rank} \alpha_i / \rho} \left( X_{(i)}^{(k)} + U_{(i)}^{(k-1)} \right) \right] \quad (8)$$

with  $\text{fold}_i(M_{(i)}) = M_i$

$$\text{Update } U_i^{(k)} \text{ by : } U_i^{(k)} = U_i^{(k-1)} + \left( X^{(k)} - M_i^{(k)} \right) \quad (9)$$

Until difference between iterations  $\|X^k - X^{k-1}\| / \|T\| \leq \varepsilon$ ;

**End**

**Output:** Reconstructed high-resolution 4D diffusion-weighted image  $X$ .

---

## 3 Experiments

### 3.1 Data

The resolution of routine DWI images is of 2–3 mm. The goal of experiments is to evaluate the resolution enhancement performance of the proposed method on this resolution level. To make the evaluation in a controlled manner, as a general approach in super-resolution studies [2–4, 6], we simulate a group of data with such resolution. In this way, the ground truth data could be used to compare with the recovered results for quantitative performance evaluation.

We used a public dataset from WU-Minn Human Connectome Project (HCP) consortium [19, 20], where high-resolution images were acquired by using novel gradient hardware on a 3T Siemens Connectome scanner. We randomly selected 20 subjects (nine males and 11 females) with the age ranges from 22 to 30 years. Diffusion-weighted image were obtained for 145 axial slices with resolution of  $1.25 \times 1.25 \times 1.25 \text{ mm}^3$ . A total of 288 diffusion volumes were acquired, in which 18 without diffusion gradient ( $b = 0$ ), 90 at  $b = 1000 \text{ s/mm}^2$ , 90 at  $b = 2000 \text{ s/mm}^2$ , and 90 at  $b = 3000 \text{ s/mm}^2$ .

To evaluate the resolution recovery performance, we use HCP data to simulate a group of routine-resolution DWI. To do that, we apply blurring and downsampling operators to the original high-resolution images. Specifically, a Gaussian kernel with standard deviation of one voxel was performed to simulate blurring effect. Downsampling was carried out by averaging every eight voxels in an image to reduce the resolution at a factor of 2. Finally, we obtain DWI with resolution of  $2.5 \times 2.5 \times 2.5 \text{ mm}^3$ , which is at the similar level with current typical DWI resolution.

### 3.2 Experimental Setting

Parameters were defined experimentally. We set  $\alpha_1 = \alpha_2 = \alpha_3 = \alpha_4 = 1/4$ ,  $\lambda_{rank} = 0.01$ ,  $\lambda_{TV} = 0.01$ . The program stopped when the difference in iterations was less than  $\varepsilon = 1e - 5$ .

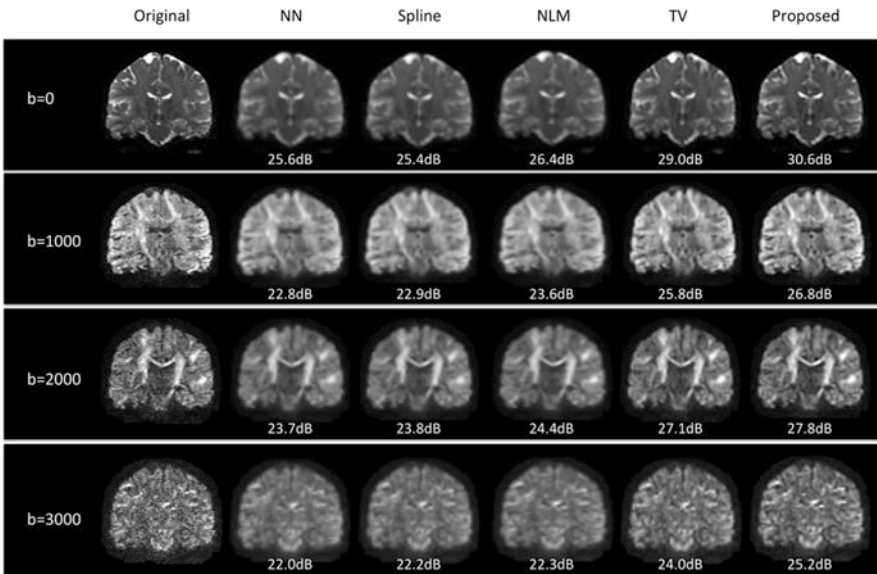
To evaluate the image recovery performance, we employ two metrics to compare the recovered high-resolution image to the original image, namely the peak signal-to-noise ratio (PSNR) and the structural similarity (SSIM) [21]. PSNR is measured in decibels (dB), and ranges from 0 to infinity. Higher PSNR generally means better reconstruction performance. SSIM ranges from 0 to 1, and 1 means perfect recovery.

### 3.3 Results

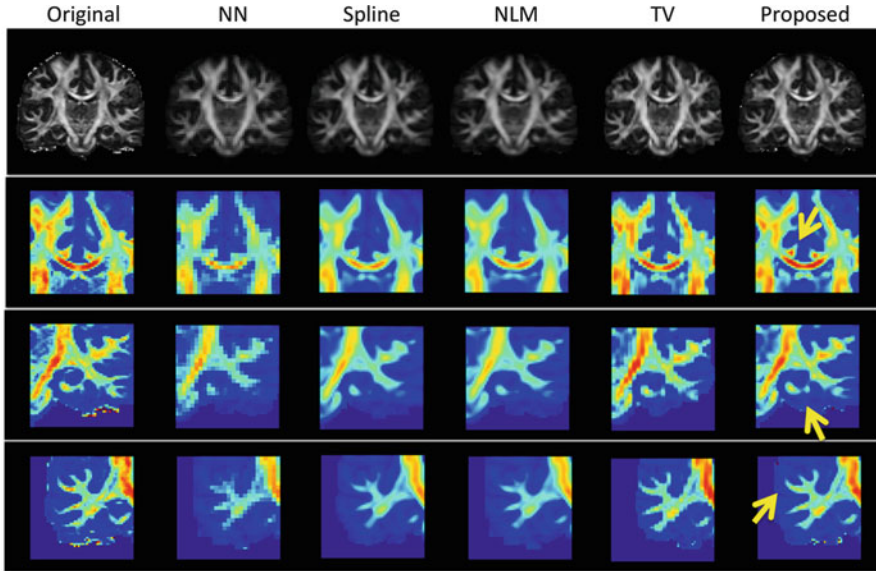
Experiments were performed on all 20 HCP subjects. We quantitatively measured the performance of the proposed method by comparing the reconstruction results with the original high-resolution images. The performance was further compared with other four methods, including nearest neighbor interpolation (NN), spline interpolation (Spline), non-local means upsampling (NLM), and total variation based upsampling (TV). Due to the availability of NLM implementation on 3D images [9], we run it on each diffusion volume to form the 4D output. TV was implemented through the proposed method by setting  $\lambda_{rank} = 0$ .

Figure 1 demonstrates representative reconstruction results of a subject, where coronal views of DWI with different gradients are shown for  $b = 0, 1000, 2000,$  and  $3000$ , respectively. It can be observed that the results of NN, Spline, and NLM show severe blurring artifacts. TV shows deblurred results while the results of the proposed method show best signal contrast and preserve most fine structural details.

We then estimated diffusion parameters using diffusion tensor model from the reconstructed multi-shell data (i.e., multiple  $b$ -values). Fractional anisotropy (FA) maps are shown in the top row of Fig. 2. Close-up views of three selected regions are also color-coded and presented for better visualization. As pointed by yellow arrows, the top row shows bilateral cingulum appearing as the symmetric red dots on the top of genu of the corpus callosum. The middle row shows



**Fig. 1** Reconstructed DWI of a typical subject using five different methods. PSNR values were provided, where higher PSNR indicating better reconstruction results

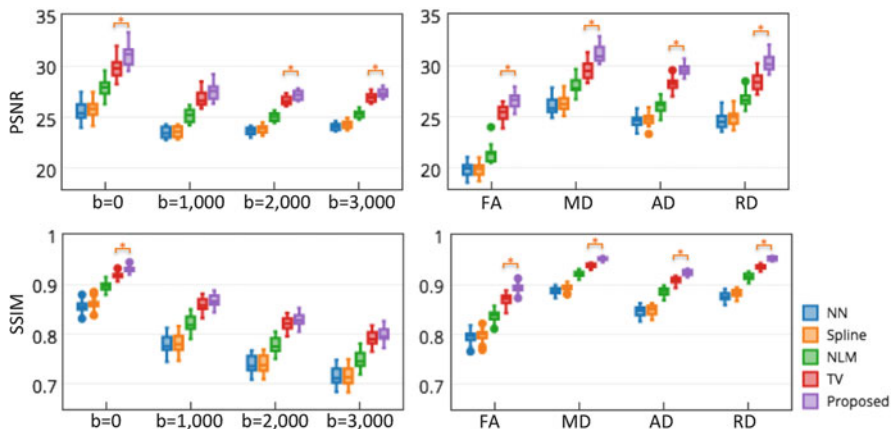


**Fig. 2** Illustration of FA maps of a typical subject, as well as close-up views of color-coded FA maps in three brain regions. *Red* indicates high FA value, and *blue* indicates low FA value

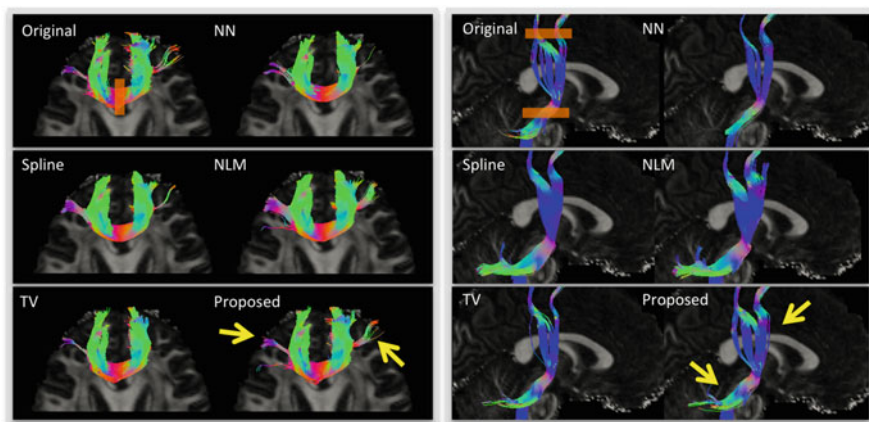
the fine folding of hippocampus layers, and the bottom row shows small white matter structures. The proposed method outperforms other comparison methods with best reconstruction results in preserving both FA magnitude and white matter shapes.

Quantitative results of DWI reconstructions and parameter maps on 20 HCP subjects are shown in Fig. 3. Both PSNR and SSIM values are provided for showing reconstruction performances on DWI with different gradients (left panel) and diffusion measures (right panel) such as FA, mean diffusivity (MD), axial diffusivity (AD) and radial diffusivity (RD). Similar to the observations from Figs. 1 and 2, the proposed method achieved significant higher PSNR than the comparison methods in most of measures.

We further performed a streamline fiber tractography on the estimated diffusion tensor parameters of these five reconstruction results using inhouse software, with minimal seed-point FA of 0.3, minimal allowed FA of 0.25, maximal turning angle of  $45^\circ$ , minimal fiber length of 20 mm, and maximal fiber length of 300 mm. Here one fiber orientation was estimated for each voxel. Genu and corticospinal tract (CST) were used as regions of interest (ROIs), respectively. Results in Fig. 4 show that the proposed method best preserves the fiber tracts that are the closest to those from the original image. Less or excessive fiber tracts could be observed on results from other methods.



**Fig. 3** Grouped boxplots of PSNR (*top*) and SSIM (*bottom*) results in recovering 20 HCP subjects using five different methods. Asterisk indicates the proposed method significantly outperforms the comparison methods ( $p < 0.01$  in two-sample  $t$ -tests)



**Fig. 4** Illustration of fiber tracking results from original image and five reconstruction methods. Gene (*left panel*) and CST (*right panel*) were used as ROIs, shown as orange rectangles in the results of original images. Only the fibers pass through ROIs are shown. Yellow arrows indicate the fiber tracts best preserved by the proposed method

## 4 Conclusion

We have presented a novel SRR method for 4D DWI from single scan. We sufficiently utilized the self-similarity of DWI in both spatial and diffusion domains, in terms of 4D low-rank and total variation regularizations in the model based resolution recovery. Comprehensive experiments were performed on 20 HCP subjects. NN, Spline, and NLM show inferior performance, which may be because



the image degradation is not explicitly modeled in these methods. The proposed method has better performance in recovering both white matter properties and fiber tracts than that of TV, which confirms the usefulness of the inclusion of 4D low-rank in image reconstruction. In future work, we intend to acquire paired low- and high-resolution images from same subjects to further evaluate the proposed method, and further improve the performance by considering more factors such as the influence of diffusion gradient orientations.

## References

1. Sundgren, P., Dong, Q., Gomez-Hassan, D., Mukherji, S., Maly, P., Welsh, R.: Diffusion tensor imaging of the brain: review of clinical applications. *Neuroradiology* **46**, 339–350 (2004)
2. Chilla, G.S., Tan, C.H., Xu, C., Poh, C.L.: Diffusion weighted magnetic resonance imaging and its recent trend—a survey. *Quant. Imaging Med. Surg.* **5**, 407 (2015)
3. Wee, C.-Y., Yap, P.-T., Li, W., Denny, K., Browndyke, J.N., Potter, G.G., Welsh-Bohmer, K.A., Wang, L., Shen, D.: Enriched white matter connectivity networks for accurate identification of MCI patients. *Neuroimage* **54**, 1812–1822 (2011)
4. Wee, C.-Y., Yap, P.-T., Zhang, D., Denny, K., Browndyke, J.N., Potter, G.G., Welsh-Bohmer, K.A., Wang, L., Shen, D.: Identification of MCI individuals using structural and functional connectivity networks. *Neuroimage* **59**, 2045–2056 (2012)
5. Shi, F., Yap, P.-T., Gao, W., Lin, W., Gilmore, J.H., Shen, D.: Altered structural connectivity in neonates at genetic risk for schizophrenia: a combined study using morphological and white matter networks. *Neuroimage* **62**, 1622–1633 (2012)
6. Brown, R.W., Cheng, Y.-C.N., Haacke, E.M., Thompson, M.R., Venkatesan, R.: *Magnetic Resonance Imaging: Physical Principles and Sequence Design*. Wiley, New York (2014)
7. Van Reeth, E., Tham, I.W., Tan, C.H., Poh, C.L.: Super-resolution in magnetic resonance imaging: a review. *Concepts Magn. Reson. Part A* **40**, 306–325 (2012)
8. Yuan, Q., Zhang, L., Shen, H.: Regional spatially adaptive total variation super-resolution with spatial information filtering and clustering. *IEEE Trans. Image Process.* **22**, 2327–2342 (2013)
9. Manjón, J.V., Coupé, P., Buades, A., Fonov, V., Louis Collins, D., Robles, M.: Non-local MRI upsampling. *Med. Image Anal.* **14**, 784–792 (2010)
10. Scherrer, B., Gholipour, A., Warfield, S.K.: Super-resolution reconstruction to increase the spatial resolution of diffusion weighted images from orthogonal anisotropic acquisitions. *Med. Image Anal.* **16**, 1465–1476 (2012)
11. Ning, L., Setsompop, K., Michailovich, O., Makris, N., Westin, C.-F., Rathi, Y.: A compressed-sensing approach for super-resolution reconstruction of diffusion MRI. In: *Information Processing in Medical Imaging*, pp. 57–68. Springer
12. Alexander, D.C., Zikic, D., Zhang, J., Zhang, H., Criminisi, A.: Image quality transfer via random forest regression: applications in diffusion MRI. In: *Medical Image Computing and Computer-Assisted Intervention—MICCAI 2014*, pp. 225–232. Springer (2014)
13. Tarquino, J., Rueda, A., Romero, E.: Shearlet-based sparse representation for super-resolution in diffusion weighted imaging (DWI). In: *2014 IEEE International Conference on Image Processing (ICIP)*, pp. 3897–3900. IEEE (2014)
14. Rudin, L.I., Osher, S., Fatemi, E.: Nonlinear total variation based noise removal algorithms. *Physica D. Nonlinear Phenomena* **60**, 259–268 (1992)
15. Shi, F., Cheng, J., Wang, L., Yap, P.-T., Shen, D.: LRTV: MR image super-resolution with low-rank and total variation regularizations. *IEEE Trans. Med. Imaging* **34**(12), 2459–2466 (2015). doi:[10.1109/TMI.2015.2437894](https://doi.org/10.1109/TMI.2015.2437894)

16. Liu, J., Musialski, P., Wonka, P., Ye, J.: Tensor completion for estimating missing values in visual data. *IEEE Trans. Pattern Anal. Mach. Intell.* **35**, 208–220 (2013)
17. Boyd, S., Parikh, N., Chu, E., Peleato, B., Eckstein, J.: Distributed optimization and statistical learning via the alternating direction method of multipliers. *Foundations Trends Mach. Learn.* **3**, 1–122 (2011)
18. Cai, J.-F., Candès, E.J., Shen, Z.: A singular value thresholding algorithm for matrix completion. *SIAM J. Optim.* **20**, 1956–1982 (2010)
19. Van Essen, D.C., Smith, S.M., Barch, D.M., Behrens, T.E., Yacoub, E., Ugurbil, K., Consortium, W.-M.H.: The WU-Minn human connectome project: an overview. *Neuroimage* **80**, 62–79 (2013)
20. Sotiropoulos, S.N., Jbabdi, S., Xu, J., Andersson, J.L., Moeller, S., Auerbach, E.J., Glasser, M.F., Hernandez, M., Sapiro, G., Jenkinson, M.: Advances in diffusion MRI acquisition and processing in the Human Connectome Project. *Neuroimage* **80**, 125–143 (2013)
21. Wang, Z., Bovik, A.C., Sheikh, H.R., Simoncelli, E.P.: Image quality assessment: from error visibility to structural similarity. *IEEE Trans. Image Process.* **13**, 600–612 (2004)

# Holistic Image Reconstruction for Diffusion MRI

Vladimir Golkov, Jorg M. Portegies, Antonij Golkov, Remco Duits,  
and Daniel Cremers

**Abstract** Diffusion MRI provides unique information on the microarchitecture of biological tissues. One of the major challenges is finding a balance between image resolution, acquisition duration, noise level and image artifacts. Recent methods tackle this challenge by performing super-resolution reconstruction in image space or in diffusion space, regularization of the image data or of postprocessed data (such as the orientation distribution function, ODF) along different dimensions, and/or impose data-consistency in the original acquisition space. Each of these techniques has its own advantages; however, it is rare that even a few of them are combined. Here we present a holistic framework for diffusion MRI reconstruction that allows combining the advantages of all these techniques in a single reconstruction step. In proof-of-concept experiments, we demonstrate super-resolution on HARDI shells and in image space, regularization of the ODF and of the images in spatial and angular dimensions, and data consistency in the original acquisition space. Reconstruction quality is superior to standard reconstruction, demonstrating the feasibility of combining advanced techniques into one step.

---

V. Golkov (✉) • D. Cremers

Department of Informatics, Technische Universität München, Garching, Germany  
e-mail: [golkov@cs.tum.edu](mailto:golkov@cs.tum.edu); [cremers@tum.de](mailto:cremers@tum.de)

J.M. Portegies

Department of Mathematics and Computer Science, Eindhoven University of Technology,  
Eindhoven, The Netherlands  
e-mail: [j.m.portegies@tue.nl](mailto:j.m.portegies@tue.nl)

A. Golkov

Department of Mathematics, Augsburg University, Augsburg, Germany  
e-mail: [antonij.golkov@student.uni-augsburg.de](mailto:antonij.golkov@student.uni-augsburg.de)

R. Duits

Department of Mathematics and Computer Science, and Department of Biomedical Engineering,  
Eindhoven University of Technology, Eindhoven, The Netherlands  
e-mail: [r.duits@tue.nl](mailto:r.duits@tue.nl)

## 1 Introduction

Among the main problems in diffusion MRI are scan duration limits (thus a limited amount of data), image resolution limits, noise, and image artifacts. In recent years, a host of methods [1–9] have been developed to tackle these issues. These methods use (simplified) assumptions about the data, such as specific types of smoothness / transform-domain sparsity / low-rankedness, specific types of data similarity between different coordinates in the 3-D space of diffusion directions and weightings ( $q$ -space), accurate or simplified image acquisition models, in some cases combined with a tailored acquisition strategy.

Super-resolution in diffusion MRI allows increasing the resolution beyond the hardware limits. In the original super-resolution techniques for diffusion MRI [10, 11], there is no coupling of different  $q$ -space coordinates, i.e. each  $q$ -space coordinate is treated independently without taking advantage of common structure. It is performed from image space to image space, independently of the image reconstruction step. Recent methods [12–14] couple  $q$ -space coordinates and use the original data-acquisition space but regularize only in the reconstruction space—not in additional spaces.

The proposed method allows leveraging complementary information by coupling in  $q$ -space, while imposing data consistency in the original space and balancing regularization in several arbitrary representations simultaneously.

The rest of the paper is organized as follows. In Sect. 2.1, we describe the data formation model. In Sect. 2.2, we introduce holistic reconstruction (raw data consistency, several regularization spaces, super-resolution reconstruction in image and diffusion space) and give details on sampling in acquisition and reconstruction spaces, the regularizers, the optimization procedure and its implementation. We show results of holistic super-resolution reconstruction after artificial subsampling of Human Connectome Project data in Sect. 3 and conclude with a discussion in Sect. 4.

## 2 Methods

### 2.1 Image Acquisition Model

The image is modeled on a domain  $\Omega \times \mathbb{R}^3$ , where  $\Omega \subset \mathbb{R}^3$  represents the domain in image space, and dimensions four to six of  $\Omega \times \mathbb{R}^3$  represent the space consisting of three-dimensional diffusion directions and diffusion weightings ( $q$ -space) for which discrete samples are acquired. A complex-valued diffusion MRI image  $\rho$  is a mapping

$$\rho : \Omega \times \mathbb{R}^3 \rightarrow \mathbb{C} \text{ given by} \tag{1}$$

$$(y, q) \mapsto \rho(y, q) = r(y, q) \exp(i\varphi(r, q)), \tag{2}$$

where  $r$  is the image magnitude and  $\varphi$  is the image phase at spatial coordinate  $y \in \Omega$  and  $q$ -space coordinate  $q \in \mathbb{R}^3$ . Magnitude  $r$  and phase  $\varphi$  are mappings

$$r: \Omega \times \mathbb{R}^3 \rightarrow \mathbb{R}, \quad (3)$$

$$\varphi: \Omega \times \mathbb{R}^3 \rightarrow S^1. \quad (4)$$

These images are not acquired directly. Acquisition is performed in  $k$ -space (more precisely: in the joint six-dimensional  $(k, q)$ -space), after Fourier transform  $\mathcal{F}_{1,2}$  along the spatial dimensions 1 and 2 of  $\Omega$ . When sampled at  $N$  data points, the resulting data  $d \in \mathbb{C}^N$  forms from  $r$  and  $\varphi$  according to

$$d = T(r, \varphi) + \varepsilon, \quad (5)$$

where  $\varepsilon$  is complex-valued i.i.d. Gaussian noise (thermal noise) and  $T$  is the encoding operator. The operator  $T$  composes  $r$  and  $\varphi$  pointwise into a complex-valued image via  $C(r, \varphi) = r \odot \exp(i\varphi)$  where “ $\odot$ ” is the pointwise product, followed by a Fourier transform into  $(k, q)$ -space and discrete sampling  $S$ :

$$T(r, \varphi) = S\mathcal{F}_{1,2}C(r, \varphi), \quad \text{with} \quad (6)$$

$$S: \mathbb{R}^3 \times \mathbb{R}^3 \rightarrow \mathbb{C}^N \quad \text{given by} \quad (7)$$

$$(S\hat{\rho})_n = \int_{[-0.5, 0.5]^3} \hat{\rho}(k_n + v, q_n) \, dv, \quad (8)$$

where the  $((k_n, q_n))_{n \in \{1, \dots, N\}}$  are the sampling points in  $(k, q)$ -space. Details can be found in [15, 16].

## 2.2 Holistic Reconstruction

Our goal is to reconstruct the image magnitude  $r$  and phase  $\varphi$  from the acquired data  $d$ . In order to improve image quality, such a reconstruction should include state-of-the-art image processing methods, such as denoising, super-resolution reconstruction and orientation distribution function<sup>1</sup> (ODF) enhancement. Rather than performing this in a classical manner, where each step is performed separately, we couple all transformations and regularizers into a single optimization problem. This allows performing the entire reconstruction in a single step, while having full control over the balance between all regularizers simultaneously. Furthermore, this avoids data-consistency formulations in intermediate spaces, where the noise

---

<sup>1</sup>The ODF is a formalism that characterizes the strength of diffusion in different directions. It is defined formally below in Eq. (10).

distribution is difficult to model correctly (e.g. Rician signal distribution and other cases)—our least squares data term penalizes deviation from  $k$ -space measurements, where noise is Gaussian, while still reconstructing and regularizing in arbitrary spaces. Finally, a holistic formulation allows regularizing in additional spaces other than the acquisition and the reconstruction space. This allows for example using information from the ODF (otherwise calculated independently at a later step) to inform the super-resolution reconstruction in image space.

In our proof-of-concept holistic reconstruction experiments, we treat the entire six-dimensional data jointly (rather than treating each  $q$ -space coordinate independently during image space reconstruction, followed by treating each image coordinate  $y$  independently during  $q$ -space-based processing) and combine the following concepts into a single optimization problem:

- Data consistency in the original  $(k, q)$ -space,
- Reconstruction into  $(y, q)$ -space with super-resolution in both the spatial and diffusional dimensions,
- Spatial regularization of  $(y, q)$ -space data,
- Angular regularization of  $(y, q)$ -space data by treating each  $q$ -space shell independently as functions on the (uncoupled) space  $\mathbb{R}^3 \times S^2$  of positions and orientations,
- Spatial and angular regularization of the ODFs which implicitly correspond to the reconstructed  $(y, q)$ -space data by treating them as functions on the (uncoupled) space  $\mathbb{R}^3 \times S^2$  of positions and orientations.

The general form of holistic reconstruction into  $(y, q)$ -space is

$$\arg \min_{r, \varphi} \frac{1}{2} \|T(r, \varphi) - d\|^2 + R(r), \quad (9)$$

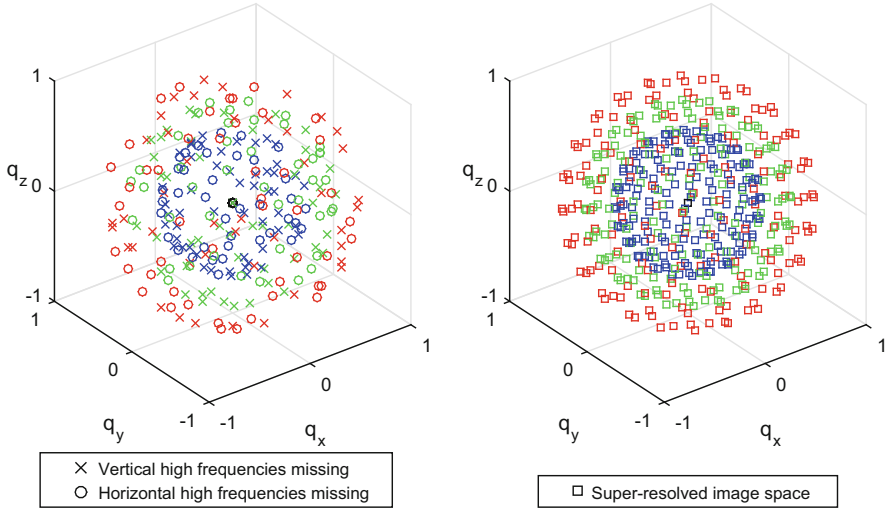
where  $R(r)$  is a sum of regularization terms which may or may not transform the image magnitude  $r$  into another space, such as ODFs, prior to penalizing non-regularity.<sup>2</sup>

The “codomain” of our pipeline, i.e. the reconstruction space, can be extended into diffusion models, as in [17, 18]. These model-based methods can be complemented by our regularizers in additional spaces to yield a holistic framework.

**Sampling Scheme in  $(k, q)$ -Space** In order to verify the super-resolution reconstruction capability of our holistic reconstruction, we use data of uniquely high resolution from the Human Connectome Project [19–26], assuming it to be the ground truth underlying image data, and simulate a low-resolution  $k$ -space sampling of these ground truth images. In order to leverage complementarity of data in  $q$ -space, we employ a low-resolution  $(k, q)$ -space sampling scheme [13] in which high resolution components are left out alternatingly in vertical or horizontal

---

<sup>2</sup>The precise formula that we use for  $R(r)$  will follow later in Eq. (12).



**Fig. 1** Sampling scheme in  $q$ -space during acquisition (*left*) and reconstruction (*right*). The acquired data have alternating artificial subsampling in vertical/horizontal high frequencies in  $k$ -space. All high frequencies for all images are reconstructed. Colors encode the  $b$ -value:  $\mathcal{B} = \{0, 1000, 2000, 3000\}$  s/mm<sup>2</sup>

image directions for different  $q$ -space coordinates. The  $q$ -space coordinates and the respective alternating vertical/horizontal  $k$ -space subsampling are shown in Fig. 1, left. Both acquisition and reconstruction (see next paragraph) use the set of  $b$ -values  $\mathcal{B} = \{0, 1000, 2000, 3000\}$  s/mm<sup>2</sup>.

**Super-Resolution Sampling Scheme in Reconstruction Space** While data are artificially subsampled in  $k$ -space for the experiments, the reconstruction space is discretized such that the original high image resolution is reconstructed. While 270  $q$ -space coordinates are sampled (Fig. 1, left), 486 are reconstructed (Fig. 1, right). This scheme achieves a super-resolution reconstruction in image and diffusion space.

**Regularization** We will regularize several images of the type  $U \in \mathbb{H}^2(\mathbb{R}^3 \times \mathbb{S}^2)$ , namely the ODF and the spherical shells in  $q$ -space (where  $\mathbb{H}^k$  denotes the respective Sobolev space).

The ODF [27] for image  $r$  at image location  $y \in \Omega$  and direction  $n \in \mathbb{S}^2$  can be calculated as

$$\text{ODF}(r)(y, n) = \frac{1}{Z_\kappa} \int_0^\infty (\mathcal{F}_{4,5,6}r)(y, pn) p^\kappa dp \quad (10)$$

with the usual choice  $\kappa = 2$ , where  $Z_\kappa$  is a normalization constant and  $\mathcal{F}_{4,5,6}$  is the Fourier transform along the diffusion dimensions four to six that calculates the diffusion propagator from  $q$ -space data in an idealized setting [28].

Let  $G_b$  be the linear operator that extracts a spherical  $q$ -space shell at a given  $b$ -value (diffusion weighting) from  $r$ :

$$(G_b(r))(y, n) = r(y, \sqrt{bn}). \quad (11)$$

In a proof-of-concept holistic reconstruction, the shells and the ODFs are regularized in the uncoupled space  $\mathbb{R}^3 \times S^2$  of positions and orientations as follows:

$$\begin{aligned} R(r) = & \sum_{b \in \mathcal{B}} \int_{\mathbb{R}^3 \times S^2} \alpha_1 \|\nabla_y G_b(r)(y, n)\|^2 \\ & - \alpha_2 \langle G_b(r)(y, n), \Delta_{S^2} G_b(r)(y, n) \rangle + \alpha_3 |\Delta_{S^2} G_b(r)(y, n)|^2 dy d\sigma(n) \\ & + \int_{\mathbb{R}^3 \times S^2} \alpha_4 \|\nabla_y \text{ODF}(r)(y, n)\|^2 \\ & - \alpha_5 \langle \text{ODF}(r)(y, n), \Delta_{S^2} \text{ODF}(r)(y, n) \rangle + \alpha_6 |\Delta_{S^2} \text{ODF}(r)(y, n)|^2 dy d\sigma(n), \end{aligned} \quad (12)$$

where  $\mathcal{B}$  is the set of reconstructed  $b$ -values, the  $\alpha_i$  are regularization parameters,  $\sigma$  is the usual surface measure on  $S^2$ ,  $\Delta_{S^2}$  is the Laplace–Beltrami operator on the sphere and the negative inner products correspond to first-order regularization according to  $\int -\langle U, \Delta U \rangle = \int \|\nabla U\|^2$  (i.e. Green’s identity with vanishing boundary conditions as we assume our functions  $U$  to vanish at the boundary).

Defining appropriate inner products on the space  $\mathbb{H}^2(\mathbb{R}^3 \times S^2) \ni U, V$  and on  $\mathbb{H}^1(\mathbb{R}^3 \times S^2, \mathbb{R}^3) \ni \nabla_y U, \nabla_y V$  as

$$\langle U, V \rangle = \int_{\mathbb{R}^3 \times S^2} U(y, n) V(y, n) dy d\sigma(n), \quad (13)$$

$$\langle \nabla_y U, \nabla_y V \rangle = \sum_{i \in \{1,2,3\}} \int_{\mathbb{R}^3 \times S^2} (\nabla_y U(y, n))_i (\nabla_y V(y, n))_i dy d\sigma(n), \quad (14)$$

and using the induced norms, we can rewrite the problem (9,12) as follows:

$$\begin{aligned} & \min_{r, \varphi} \frac{1}{2} \|T(r, \varphi) - d\|^2 \\ & + \sum_{b \in \mathcal{B}} \alpha_1 \|\nabla_y G_b(r)\|^2 - \alpha_2 \langle G_b(r), \Delta_{S^2} G_b(r) \rangle + \alpha_3 \|\Delta_{S^2} G_b(r)\|^2 \\ & + \alpha_4 \|\nabla_y \text{ODF}(r)\|^2 - \alpha_5 \langle \text{ODF}(r), \Delta_{S^2} \text{ODF}(r) \rangle + \alpha_6 \|\Delta_{S^2} \text{ODF}(r)\|^2. \end{aligned} \quad (15)$$

**Reformulations** To obtain a convenient min-max form with simpler expressions within the norms, we shall use the identity:

$$\|\hat{x}\|^2 = \sup_{\hat{y}} \langle \hat{x}, \hat{y} \rangle - \frac{1}{4} \|\hat{y}\|^2, \quad (16)$$

obtained by taking the convex biconjugate and completing the square. This reformulation introduces dual variables  $\hat{y}$ .



**Optimization Procedure** Our optimization problem (15) can be rewritten as a min-max problem of the form

$$\min_x \max_y G(x) + \langle K(x), y \rangle - F^*(y) \quad (17)$$

with convex  $G$ ,  $F^*$  and a nonlinear  $K$ , which can be solved with the modified primal-dual hybrid gradient method for nonlinear  $K$  [15, 29, 30]:

$$x^{i+1} := (I + \tau \partial G)^{-1}(x^i - \tau [\nabla K(x^i)]^* y^i), \quad (18a)$$

$$x_\omega^{i+1} := x^{i+1} + \omega(x^{i+1} - x^i), \quad (18b)$$

$$y^{i+1} := (I + \sigma \partial F^*)^{-1}(y^i + \sigma K(x_\omega^{i+1})), \quad (18c)$$

where  $\partial f$  represents the subdifferential of a function  $f$ , defined as

$$\partial f(x_0) = \{v \mid f(x) - f(x_0) \geq \langle v, x - x_0 \rangle \forall x \in \text{dom} f\}, \quad (19)$$

and  $(I + \lambda \partial f)^{-1}$  is the resolvent of the subdifferential, corresponding to the proximal operator [31]:

$$(I + \lambda \partial f)^{-1}x = \text{prox}_{\lambda f}(x) = \arg \min_z f(z) + \frac{1}{2\lambda} \|x - z\|^2. \quad (20)$$

The algorithm (18) has been applied [15] with the operator  $T(r, \varphi)$  to non-diffusion MRI, and with another operator to diffusion MRI. The author announces combining  $T(r, \varphi)$  with direct reconstruction of the diffusion tensor in a future study, while we present an application of  $T(r, \varphi)$  to reconstruction in image  $\times$  diffusion space.

By rewriting all five norms in our problem (15) using the identity (16), we obtain the min-max form

$$\begin{aligned} \min_{r, \varphi} \max_{\lambda, (\zeta_b)_{b \in \mathcal{B}}, (\eta_b)_{b \in \mathcal{B}}, \xi, v} & \langle T(r, \varphi), \lambda \rangle - \langle d, \lambda \rangle - \frac{1}{2} \|\lambda\|^2 \\ & + \sum_{b \in \mathcal{B}} \alpha_1 \left( \langle \nabla_y G_b(r), \zeta_b \rangle - \frac{1}{4} \|\zeta_b\|^2 \right) \\ & - \alpha_2 \langle G_b(r), \Delta_{S^2} G_b(r) \rangle + \alpha_3 \left( \langle \Delta_{S^2} G_b(r), \eta_b \rangle - \frac{1}{4} \|\eta_b\|^2 \right) \\ & + \alpha_4 \left( \langle \nabla_y \text{ODF}(r), \xi \rangle - \frac{1}{4} \|\xi\|^2 \right) \\ & - \alpha_5 \langle \text{ODF}(r), \Delta_{S^2} \text{ODF}(r) \rangle + \alpha_6 \left( \langle \Delta_{S^2} \text{ODF}(r), v \rangle - \frac{1}{4} \|v\|^2 \right). \end{aligned} \quad (21)$$

The primal variables are  $x = (r, \varphi)$  and the dual ones are  $y = (\lambda, (\zeta_b)_{b \in \mathcal{B}}, (\eta_b)_{b \in \mathcal{B}}, \xi, \nu)$ , where for example  $\eta_b$  denotes the dual variable associated to  $\|\Delta_{S^2} G_b(r)\|^2$ . This can be regrouped into the standard form (17) as follows:

$$\begin{aligned}
G(x) &= \sum_{b \in \mathcal{B}} -\alpha_2 \langle G_b(r), \Delta_{S^2} G_b(r) \rangle - \alpha_5 \langle \text{ODF}(r), \Delta_{S^2} \text{ODF}(r) \rangle, \\
\langle K(x), y \rangle &= \langle T(r, \varphi), \lambda \rangle + \sum_{b \in \mathcal{B}} \alpha_1 \langle \nabla_y G_b(r), \zeta_b \rangle + \alpha_3 \langle \Delta_{S^2} G_b(r), \eta_b \rangle \\
&\quad + \alpha_4 \langle \nabla_y \text{ODF}(r), \xi \rangle + \alpha_6 \langle \Delta_{S^2} \text{ODF}(r), \nu \rangle, \\
\pm F^*(y) &= \pm \langle d, \lambda \rangle \pm \frac{1}{2} \|\lambda\|^2 \\
&\quad \pm \frac{1}{4} \left( \sum_{b \in \mathcal{B}} \alpha_1 \|\zeta_b\|^2 + \alpha_3 \|\eta_b\|^2 + \alpha_4 \|\xi\|^2 + \alpha_6 \|\nu\|^2 \right).
\end{aligned} \tag{22}$$

For the implementation of algorithm (18), we calculate the proximal operators [31]:

$$(I + \tau \partial G)^{-1} x = (I + \tau(Q + Q^*))^{-1} x, \tag{23}$$

$$Q = \sum_{b \in \mathcal{B}} G_b^* \Delta_{S^2} G_b + \text{ODF}^* \Delta_{S^2} \text{ODF}, \tag{24}$$

$$(I + \sigma \partial F^*)^{-1} y = \begin{pmatrix} (\lambda - \sigma d)/(\sigma + 1) \\ (\zeta_b/(1 + \alpha_1 \sigma/2))_{b \in \mathcal{B}} \\ (\eta_b/(1 + \alpha_3 \sigma/2))_{b \in \mathcal{B}} \\ \xi/(1 + \alpha_4 \sigma/2) \\ \nu/(1 + \alpha_6 \sigma/2) \end{pmatrix}. \tag{25}$$

Calculating  $[\nabla K(x^i)]^*$  (18) for the nonlinear part  $T(r, \varphi)$  (22) yields

$$[\nabla T(r, \varphi)]^* = (S\mathcal{F}_{1,2}[\nabla C(r, \varphi)])^* = [\nabla C(r, \varphi)]^* \mathcal{F}_{1,2}^* S^*, \tag{26}$$

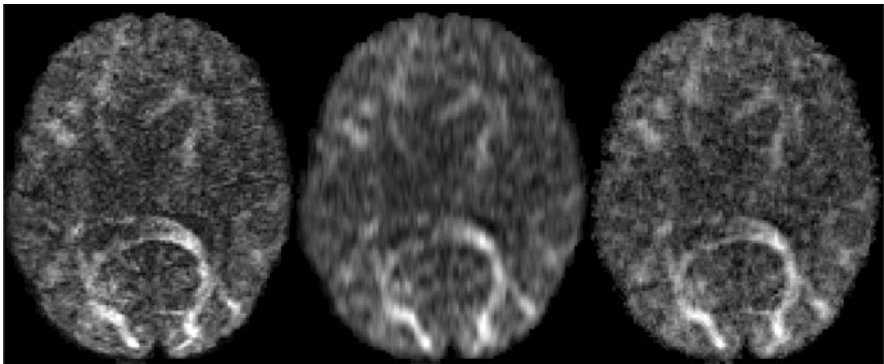
$$[\nabla C(r, \varphi)]^* \hat{\lambda} = \begin{pmatrix} \Re(\hat{\lambda}) \cos(\varphi) + \Im(\hat{\lambda}) \sin(\varphi) \\ r(\Im(\hat{\lambda}) \cos(\varphi) - \Re(\hat{\lambda}) \sin(\varphi)) \end{pmatrix}. \tag{27}$$

**Unbounded ODF Operator** When writing out the Fourier transform  $\mathcal{F}_{4,5,6}$  over  $Q \in \mathbb{R}^3$ , the ODF (10) contains the diverging term  $\exp(-i\langle pn, Q \rangle)p^2$ . Thus, the ODF operator is unbounded. Since an adjoint is required for the algorithm (18), the operator can be made bounded in the infinite-dimensional setting by including a Gaussian damping factor  $\exp(-p^2/\zeta^2)$  as a mollifier. The operator bound of the discrete operator depends on the discretization, and in our discretization scheme no mollifier was needed in practice.

**Implementation Details** The operators  $\mathcal{F}_{1,2}$ ,  $S$  (6), ODF (10),  $G_b$  (11),  $\nabla_y$  and  $\Delta_{S^2}$  are linear. In the implementation, the spaces in which acquisition, regularization and reconstruction take place are discretized and thus the operators can be written as matrices. We obtain these matrices explicitly. Where not evident, an operator matrix is computed by applying the operator to all standard basis vectors of the discretized space, yielding the columns of the matrix. For pointwise operators, we compute and store repeating coefficients only once. When computing  $[\nabla K(\cdot)]^*$  and  $K(\cdot)$  in the algorithm (18), having the operator matrices explicitly has the advantages of rapid computation by matrix multiplication and easy computation of the adjoint operators. Besides, in the discretized setting, the ODF operator is not unbounded anymore and thus has an adjoint, as required by the algorithm. The norm  $\|[\nabla K(\cdot)]^*\|$  of the operator  $[\nabla K(\cdot)]^*$  explodes as the discretization becomes finer, but in our discretization settings there was no need to include a Gaussian mollifier in (10). The practical implementation of the ODF operator is given by generalized  $q$ -sampling imaging [32].

### 3 Results

Figure 2 shows the high-resolution “ground truth” image data from the Human Connectome Project (Fig. 2, left) alongside the results of two reconstruction methods applied to the same data that has been artificially subsampled according to the sampling scheme in  $(k, q)$ -space described in section “Sampling Scheme in  $(k, q)$ -Space” and illustrated in Fig. 1, left. This artificial subsampling procedure emulates a clinical setting where resolution is considerably lower than in the Human Connectome Project, and enables a comparison to this exceptionally high-resolution ground truth data. The two compared reconstruction methods are standard reconstruction ( $\mathcal{F}_{1,2}$ -transformed subsampled data; Fig. 2, middle) and holistic



**Fig. 2** High-resolution ground truth (*left*), standard reconstruction (*middle*), holistic super-resolution reconstruction (*right*)

image reconstruction (as described above, with super-resolution sampling as in Fig. 1, right; results in Fig. 2, right).

The employed parameters were  $\alpha_1 = 0.3$ ,  $\alpha_2 = 0.1$ ,  $\alpha_3 = 0.1$ ,  $\alpha_4 = 0.01$ ,  $\alpha_5 = 0.3$ ,  $\alpha_6 = 0.01$ .

Holistic image reconstruction demonstrates considerably more detail than standard reconstruction. While standard reconstruction results have a visibly lower resolution, holistic reconstruction retrieves details that are present in the ground truth data due to its super-resolution scheme and regularization in image and diffusion space.

## 4 Discussion

The results of holistic reconstruction demonstrate considerably more detail than the standard reconstruction.

Among the numerous advanced diffusion MRI reconstruction methods existing in literature, many methods perform denoising, missing data reconstruction ( $q$ -space compressed sensing), enhancement, etc. as an intermediate post-processing step *after* image-space reconstruction. However, standard-reconstructed images can contain artifacts, intensity bias (e.g. Rician or more complicated), and irretrievably discard some parts of information present in the raw  $k$ -space data. Imposing data consistency in reconstructed image space can lead to these errors being propagated on into subsequent data processing steps, and/or introduce less tractable bias-correction terms. There is strong evidence that one-step pipelines are better than multi-step pipelines due to information loss in intermediate steps [33]. Particularly, imposing data consistency on the original raw data in  $k$ -space yields improved results compared to multi-step processing [13]. The holistic reconstruction framework presented herein allows imposing data consistency in the original data acquisition space, while also including regularization in several spaces (such as  $(y, q)$ -space and “ $(y, \text{ODF})$ -space”), and reconstructing into an arbitrary space, including super-resolution reconstruction sampling.

Super-resolution methods are beneficial for diffusion MRI due to their capability to exceed hardware limitations on resolution. In the presented holistic reconstruction framework, super-resolution is performed in image space *and* diffusion space simultaneously, cf. Fig. 1. At the same time, data consistency in the original space and regularizations in additional spaces are incorporated in a straightforward manner.

Many competing regularizers in different spaces exist in recent literature. Each of them incorporates certain assumptions and improves data quality at certain intermediate regularization strengths. Regularizations in different spaces can be combined into one procedure (including true data consistency and super-resolution) using holistic image reconstruction.

Reconstruction can be performed jointly with motion and distortion correction [5] in the future.

Finally, our choice of priors in (15) was based on isotropic Laplacians over the spatial and angular part, and as such defined on  $\mathbb{R}^3 \times S^2$ . Including anisotropies and alignment modeling in a crossing-preserving way via the *coupled* space  $\mathbb{R}^3 \rtimes S^2 = SE(3)/(\{\mathbf{0} \times SO(2)\})$ , see [1] Theorem 2, and [34], is expected to give better results in future work.

**Acknowledgements** V.G. is supported by the Deutsche Telekom Foundation. The research leading to the results of this article has received funding from the European Research Council under the ECs 7th Framework Programme (FP7/2007-2014)/ERC grant agr. no. 335555. Data were provided by the Human Connectome Project, WU-Minn Consortium (Principal Investigators: David Van Essen and Kamil Ugurbil; 1U54MH091657) funded by the 16 NIH Institutes and Centers that support the NIH Blueprint for Neuroscience Research; and by the McDonnell Center for Systems Neuroscience at Washington University.

## References

1. Duits, R., Franken, E.: Left-invariant diffusions on the space of positions and orientations and their application to crossing-preserving smoothing of HARDI images. *Int. J. Comput. Vis.* **92**(3), 231–264 (2010)
2. Lustig, M., Donoho, D., Pauly, J.M.: Sparse MRI: the application of compressed sensing for rapid MR imaging. *Magn. Reson. Med.* **58**(6), 1182–1195 (2007)
3. Khare, K., Hardy, C.J., King, K.F., Turski, P.A., Marinelli, L.: Accelerated MR imaging using compressive sensing with no free parameters. *Magn. Reson. Med.* **68**(5), 1450–1457 (2012)
4. Paquette, M., Merlet, S., Gilbert, G., Deriche, R., Descoteaux, M.: Comparison of sampling strategies and sparsifying transforms to improve compressed sensing diffusion spectrum imaging. *Magn. Reson. Med.* **73**, 401–416 (2015)
5. Tao, S., Trzasko, J.D., Shu, Y., Huston, J., Bernstein, M.A.: Integrated image reconstruction and gradient nonlinearity correction. *Magn. Reson. Med.* **74**(4), 1019–1031 (2015)
6. Feng, L., Grimm, R., Block, K.T., Chandarana, H., Kim, S., Xu, J., Axel, L., Sodickson, D.K., Otazo, R.: Golden-angle radial sparse parallel MRI: combination of compressed sensing, parallel imaging, and golden-angle radial sampling for fast and flexible dynamic volumetric MRI. *Magn. Reson. Med.* **72**, 707–717 (2014)
7. Cauley, S.F., Xi, Y., Bilgic, B., Xia, J., Adalsteinsson, E., Balakrishnan, V., Wald, L.L., Setsompop, K.: Fast reconstruction for multichannel compressed sensing using a hierarchically semiseparable solver. *Magn. Reson. Med.* **73**, 1034–1040 (2015)
8. Mani, M., Jacob, M., Guidon, A., Magnotta, V., Zhong, J.: Acceleration of high angular and spatial resolution diffusion imaging using compressed sensing with multichannel spiral data. *Magn. Reson. Med.* **73**, 126–138 (2015)
9. Rathi, Y., Michailovich, O., Laun, F., Setsompop, K., Grant, P.E., Westin, C.F.: Multi-shell diffusion signal recovery from sparse measurements. *Med. Image Anal.* **18**(7), 1143–1156 (2014)
10. Scherrer, B., Gholipour, A., Warfield, S.K.: Super-resolution reconstruction to increase the spatial resolution of diffusion weighted images from orthogonal anisotropic acquisitions. *Med. Image Anal.* **16**(7), 1465–1476 (2012)
11. Poot, D.H.J., Jeurissen, B., Bastiaensen, Y., Veraart, J., Van Hecke, W., Parizel, P.M., Sijbers, J.: Super-resolution for multislice diffusion tensor imaging. *Magn. Reson. Med.* **69**(1), 103–113 (2013)

12. Tobisch, A., Neher, P.F., Rowe, M.C., Maier-Hein, K.H., Zhang, H.: Model-based super-resolution of diffusion MRI. In: Schultz, T., Nedjati-Gilani, G., Venkataraman, A., O'Donnell, L., Panagiotaki, E. (eds.) *Computational Diffusion MRI and Brain Connectivity, MICCAI Workshops 2013. Mathematics and Visualization*, pp. 25–34. Springer International Publishing Switzerland (2014)
13. Golkov, V., Sperl, J.I., Menzel, M.I., Sprenger, T., Tan, E.T., Marinelli, L., Hardy, C.J., Haase, A., Cremers, D.: Joint super-resolution using only one anisotropic low-resolution image per q-space coordinate. In: O'Donnell, L., Nedjati-Gilani, G., Rathi, Y., Reisert, M., Schneider, T. (eds.) *Computational Diffusion MRI, MICCAI Workshop 2014*, pp. 181–191. Springer International Publishing Switzerland (2015)
14. Van Steenkiste, G., Jeurissen, B., Veraart, J., den Dekker, A.J., Parizel, P.M., Poot, D.H.J., Sijbers, J.: Super-resolution reconstruction of diffusion parameters from diffusion-weighted images with different slice orientations. *Magn. Reson. Med.* **75**(1), 181–195 (2016)
15. Valkonen, T.: A primal-dual hybrid gradient method for non-linear operators with applications to MRI. *Inverse Prob.* **30**(5), 055012 (2014)
16. Brown, R.W., Cheng, Y.C.N., Haacke, E.M., Thompson, M.R., Venkatesan, R.: *Magnetic Resonance Imaging: Physical Principles and Sequence Design*, 2nd edn. Wiley, Hoboken (published simultaneously in Canada) (2014)
17. Welsh, C.L., Dibella, E.V.R., Adluru, G., Hsu, E.W.: Model-based reconstruction of under-sampled diffusion tensor k-space data. *Magn. Reson. Med.* **70**(2), 429–440 (2013)
18. Valkonen, T., Bredies, K., Knoll, F.: TGV for diffusion tensors: a comparison of fidelity functions. *J. Inverse Ill-Posed Prob.* **21**(3), 355–377 (2013)
19. Van Essen, D.C., Smith, S.M., Barch, D.M., Behrens, T.E.J., Yacoub, E., Ugurbil, K.: The WU-Minn Human Connectome Project: an overview. *NeuroImage* **80**, 62–79 (2013)
20. Feinberg, D.A., Moeller, S., Smith, S.M., Auerbach, E., Ramanna, S., Glasser, M.F., Miller, K.L., Ugurbil, K., Yacoub, E.: Multiplexed echo planar imaging for sub-second whole brain fMRI and fast diffusion imaging. *PLoS ONE* **5**(12), e15710 (2010)
21. Setsompop, K., Cohen-Adad, J., Gagoski, B.A., Raj, T., Yendiki, A., Keil, B., Wedeen, V.J., Wald, L.L.: Improving diffusion MRI using simultaneous multi-slice echo planar imaging. *NeuroImage* **63**(1), 569–580 (2012)
22. Xu, J., Li, K., Smith, R.A., Waterton, J.C., Zhao, P., Chen, H., Does, M.D., Manning, H.C., Gore, J.C.: Characterizing tumor response to chemotherapy at various length scales using temporal diffusion spectroscopy. *PLoS ONE* **7**(7), e41714 (2012)
23. Sotiropoulos, S.N., Jbabdi, S., Xu, J., Andersson, J.L., Moeller, S., Auerbach, E.J., Glasser, M.F., Hernandez, M., Sapiro, G., Jenkinson, M., Feinberg, D.A., Yacoub, E., Lenglet, C., Van Essen, D.C., Ugurbil, K., Behrens, T.E.J.: Advances in diffusion MRI acquisition and processing in the Human Connectome Project. *NeuroImage* **80**, 125–143 (2013)
24. Glasser, M.F., Sotiropoulos, S.N., Wilson, J.A., Coalson, T.S., Fischl, B., Andersson, J.L., Xu, J., Jbabdi, S., Webster, M., Polimeni, J.R., Van Essen, D.C., Jenkinson, M.: The minimal preprocessing pipelines for the Human Connectome Project. *NeuroImage* **80**, 105–124 (2013)
25. Jenkinson, M., Beckmann, C.F., Behrens, T.E.J., Woolrich, M.W., Smith, S.M.: FSL. *NeuroImage* **62**(2), 782–790 (2012)
26. Fischl, B.: FreeSurfer. *NeuroImage* **62**(2), 774–781 (2012)
27. Lin, C.P., Wedeen, V.J., Chen, J.H., Yao, C., Tseng, W.Y.I.: Validation of diffusion spectrum magnetic resonance imaging with manganese-enhanced rat optic tracts and ex vivo phantoms. *NeuroImage* **19**, 482–495 (2003)
28. Stejskal, E.O.: Use of spin echoes in a pulsed magnetic-field gradient to study anisotropic, restricted diffusion and flow. *J. Chem. Phys.* **43**(10), 3597–3603 (1965)
29. Pock, T., Cremers, D., Bischof, H., Chambolle, A.: An algorithm for minimizing the Mumford-Shah functional. In: 2009 IEEE 12th International Conference on Computer Vision (ICCV). Number 813396, IEEE, pp. 1133–1140 (2009)

30. Chambolle, A., Pock, T.: A first-order primal-dual algorithm for convex problems with applications to imaging. *J. Math. Imaging Vis.* **40**(1), 120–145 (2011)
31. Parikh, N., Boyd, S.: Proximal Algorithms. *Found. Trends Optim.* **1**, 123–231 (2014)
32. Yeh, F.-C., Wedeen, V.J., Tseng, W.-Y.I.: Generalized  $q$ -sampling imaging. *IEEE Trans Med Imaging* **29**(9), 1626–1635 (2010)
33. Golkov, V., Dosovitskiy, A., Sämann, P., Sperl, J.I., Sprenger, T., Czisch, M., Menzel, M.I., Gómez, P.A., Haase, A., Brox, T., Cremers, D.:  $q$ -Space deep learning for twelve-fold shorter and model-free diffusion MRI scans. In: MICCAI (2015)
34. Portegies, J.M., Fick, R.H.J., Sanguinetti, G.R., Meesters, S.P.L., Girard, G., Duits, R.: Improving fiber alignment in HARDI by combining contextual PDE flow with constrained spherical deconvolution. *PLoS ONE*. See <http://bmia.bmt.tue.nl/people/RDuits/mainJorg.pdf> (2015, submitted). Available on arXiv 2015

# Alzheimer's Disease Classification with Novel Microstructural Metrics from Diffusion-Weighted MRI

Talia M. Nir, Julio E. Villalon-Reina, Boris A. Gutman, Daniel Moyer, Neda Jahanshad, Morteza Dehghani, Clifford R. Jack Jr., Michael W. Weiner, and Paul M. Thompson, for the Alzheimer's Disease Neuroimaging Initiative (ADNI)

**Abstract** Alzheimer's disease (AD) deficits may be due in part to declining white matter (WM) integrity and disrupted connectivity. Numerous diffusion-weighted MRI (dMRI) studies of AD report WM deficits based on tensor model metrics. New microstructural measures derived from additional dMRI models may carry different information about WM microstructure including the geometry of diffusion anisotropy, diffusivity, complexity, estimated number of distinguishable fiber compartments, number of crossing fibers and neurite dispersion. Here we aimed to find the most helpful dMRI metrics and brain regions from a set of 17 dMRI-derived feature maps, to predict diagnostic group (AD or healthy control). The best metrics for classification were non-tensor metrics in the hippocampus and temporal lobes, areas consistently implicated in AD.

## 1 Introduction

On average, the world population is steadily aging, and, as a result, so is the incidence and prevalence of Alzheimer's disease (AD). Alzheimer's is the most common type of dementia, affecting one in eight (13 %) people age 65 and older

---

T.M. Nir (✉) • J.E. Villalon-Reina • B.A. Gutman • D. Moyer • N. Jahanshad • P.M. Thompson  
Imaging Genetics Center, University of Southern California, Marina del Rey, Los Angeles, CA,  
USA

e-mail: [Talia.m.nir@gmail.com](mailto:Talia.m.nir@gmail.com)

M. Dehghani

Brain and Creativity Institute, University of Southern California, Los Angeles, CA, USA

C.R. Jack Jr.

Department of Radiology, Mayo Clinic and Foundation, Rochester, MN, USA

M.W. Weiner

Department of Radiology, UCSF School of Medicine, San Francisco, CA, USA



in the U.S. alone [1]. AD is a neurodegenerative disease characterized by memory loss in its early stages, followed by a progressive decline in other behavioral and cognitive functions. Decline into AD is preceded by an intermediate stage called mild cognitive impairment (MCI). People with MCI convert to AD at a rate of about 10–15 % per year [2, 3]. Identifying biomarkers in these patients that might predict brain tissue loss is vital for drug trial enrichment, and to help identify those most likely to decline. Image-based predictors of decline may also offer new leads for understanding how AD develops.

AD is characterized by cortical and hippocampal neuronal loss and widespread gray matter atrophy driven by cortical plaque and tangle deposits, and vascular changes. However, there is also a progressive disconnection of cortical and sub-cortical regions due to white matter (WM) injury [4]. That is why, in addition to the more widely used anatomical MRI, FDG- and amyloid-PET, and CSF based measures of pathology, the Alzheimer’s Disease Neuroimaging Initiative (ADNI) has included diffusion weighted MRI (dMRI) in its second phase neuroimaging battery [5].

dMRI is a variant of MRI that measures the diffusion of water molecules in brain tissue. Due to the myelination of WM, water diffusion in the brain is hindered by hydrophobic myelin sheaths, promoting highly anisotropic water diffusion along axons. By characterizing the diffusion process at the voxel level, it is possible to make tentative inferences about the underlying WM microstructure [6].

Since the development of dMRI, along with improvements in acquisition protocols to increase angular, spatial, and spectral resolution, multiple mathematical models have been developed to describe the diffusion process. One of the first—and still most popular—methods developed to summarize diffusion properties in a specific voxel is the diffusion tensor model (DTI). This model is highly limited as it can only model a single fiber population at every voxel. It cannot resolve complex WM architecture, such as dispersing, crossing or kissing fibers. At the current resolution of dMRI, around two-thirds of WM voxels contain multiple fiber crossings [7, 8]. That said, the tensor-derived fractional anisotropy (FA) metric is still the scalar measure most widely used to characterize WM micro-architecture in disease [9, 10]. Furthermore, although FA is sensitive, it is somewhat non-specific as it depends on fiber diameter, packing density, membrane permeability, myelination, and intra-voxel orientation coherence [8].

In recent years a surge of new models have been proposed to overcome some of the tensor model limitations, including multi-tensor models, such as the tensor distribution function (TDF) [11],  $q$ -ball imaging and the orientation distribution function (ODF) [12], constrained spherical deconvolution [13], the “ball and stick” model [7], diffusion spectrum MRI (DSI) [14], and neurite orientation dispersion and density imaging (NODDI) [15], among many others. Not only do these models allow for the reconstruction of multiple underlying fibers, but they may give a richer understanding of the underlying structure than FA does, by providing information on diffusivity, complexity, estimated numbers of fiber compartments, number of crossing fibers and neurite dispersion.

Many studies describe WM microstructural differences between healthy aging controls (NC) and AD [9, 16–20], and some exploit WM metrics for classification [21–23]. But most use only basic tensor model metrics such as FA. Here we aimed to find the most helpful dMRI metrics to classify ADNI participants into diagnostic groups (AD or CN), from a set of 17 dMRI-derived feature maps, derived (DTI, CSA-ODF, TDF, and NODDI). We used a hierarchical logistic regression for classification, to determine the joint utility of the novel metrics.

## 2 Methods

### 2.1 Subject Information and Image Acquisition

Baseline MRI, DWI, and clinical data were downloaded from the ADNI database ([www.loni.usc.edu/ADNI](http://www.loni.usc.edu/ADNI)). Here we performed an initial analysis of 101 participants: 53 healthy controls (CN; mean age:  $72.4 \pm 6.0$  years; 24 M/29 F), and 48 AD patients (mean age:  $74.9 \pm 8.7$  years; 29 M/19 F). Detailed inclusion and exclusion criteria are found in the ADNI2 protocol ([http://adni-info.org/Scientists/Pdfs/ADNI2\\_Protocol\\_FINAL\\_20100917.pdf](http://adni-info.org/Scientists/Pdfs/ADNI2_Protocol_FINAL_20100917.pdf)).

All subjects underwent whole-brain MRI scanning on 3T GE Medical Systems scanners at 14 acquisition sites across North America. Anatomical T1-weighted SPGR (spoiled gradient echo) sequences ( $128 \times 128$  matrix; voxel size =  $1.2 \times 1.0 \times 1.0$  mm<sup>3</sup>; TI = 400 ms; TR = 6.98 ms; TE = 2.85 ms; flip angle = 11°), and dMRI ( $256 \times 256$  matrix; voxel size:  $2.7 \times 2.7 \times 2.7$  mm<sup>3</sup>; TR = 9000 ms; scan time = 9 min; more imaging details can be found at [http://adni.loni.ucla.edu/wp-content/uploads/2010/05/ADNI2\\_GE\\_3T\\_22.0\\_T2.pdf](http://adni.loni.ucla.edu/wp-content/uploads/2010/05/ADNI2_GE_3T_22.0_T2.pdf)) were collected. Forty-six separate images were acquired for each dMRI scan: five T2-weighted images with no diffusion sensitization ( $b_0$  images) and 41 diffusion-weighted images (DWI;  $b = 1000$  s/mm<sup>2</sup>).

### 2.2 Image Preprocessing

Images were preprocessed as in [24]. To summarize, raw DWI images were corrected for motion and eddy current distortions, while T1-weighted images underwent inhomogeneity normalization. Extra-cerebral tissue was removed from both scan types. Each T1-weighted anatomical image was linearly aligned to a standard brain template (the down-sampled Colin27 [25]:  $110 \times 110 \times 110$ , with 2 mm isotropic voxels). The diffusion images were linearly and then elastically registered [26] to their respective T1-weighted structural scans to correct for echo-planar imaging (EPI) induced susceptibility artifacts. To account for the linear registration of the DWI images to the structural T1-weighted scan, a corrected gradient table was calculated.

### 2.3 DWI Reconstruction Models and Scalar Maps


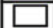















Seventeen DWI microstructural measures (Table 1) were computed per subject from four different reconstruction models: diffusion tensor (DTI), constant solid angle orientation distribution function (CSA-ODF), tensor distribution function (TDF), and neurite orientation dispersion and density imaging (NODDI).

**The Single Tensor Model** First, a single diffusion tensor [27], or ellipsoid, was modeled at each voxel in the brain from the corrected DWI scans using FSL ([http://fsl.fmrib.ox.ac.uk/fsl/fsl4.0/fdt/fdt\\_dtfitt.html](http://fsl.fmrib.ox.ac.uk/fsl/fsl4.0/fdt/fdt_dtfitt.html)), and scalar anisotropy and diffusivity maps were obtained from the resulting diffusion tensor eigenvalues ( $\lambda_1, \lambda_2, \lambda_3$ ). Fractional anisotropy (FA), a measure of the degree of diffusion anisotropy, is a normalized mean of the eigenvalues:

$$FA = \sqrt{\frac{3}{2}} \frac{\sqrt{(\lambda_1 - \langle \lambda \rangle)^2 + (\lambda_2 - \langle \lambda \rangle)^2 + (\lambda_3 - \langle \lambda \rangle)^2}}{\sqrt{\lambda_1^2 + \lambda_2^2 + \lambda_3^2}} \in [0, 1] \quad (1)$$

where  $\langle \lambda \rangle$  is the mean diffusivity (MD), or average rate of diffusivity in all directions.

**Table 1** Summary of 17 DWI measures derived from different reconstruction models: diffusion tensor (DTI), constant solid angle ODF (CSA-ODF), tensor distribution function (TDF), and neurite orientation dispersion and density imaging (NODDI)

	FA	Fractional Anisotropy
	MD	Mean Diffusivity
	RD	Radial Diffusivity
	AxD	Axial Diffusivity
	LIN	Linearity of the tensor
	PLA	Planarity of the tensor
	SPH	Sphericity of the tensor
	MOD	Mode of the tensor
	GA	Geodesic Fractional Anisotropy
	TDF-FA	Tensor Distribution Function FA
	TDF-MD	Tensor Distribution Function MD
	TDF-RD	Tensor Distribution Function RD
	TDF-AxD	Tensor Distribution Function AxD
	Peaks-4	Number of Peaks/Fiber Compartments (CSA based; threshold=0.4)
	Peaks-5	Number of Peaks/Fiber Compartments (CSA based; threshold=0.5)
	GFA	Generalized Fractional Anisotropy (CSA based)
	NODDI	Neurite Orientation Dispersion

Color key corresponds to Fig. 2

Axial diffusivity is defined as the primary (largest) eigenvalue ( $AxD = \lambda_1$ ), and is stipulated to capture the diffusivity parallel to the majority of axonal fibers. It has been associated with axonal injury, whereas radial diffusivity (RD) captures the average diffusivity perpendicular to AxD (the average of  $\lambda_2$  and  $\lambda_3$ ), and is believed to be associated with demyelination [28, 29].

A “geodesic” anisotropy (GA) map was also calculated for each participant. GA measures the geodesic distance between the tensor and the nearest isotropic tensor, computed intrinsically on the Lie group of symmetric positive-definite diffusion tensors, normalized by applying the hyperbolic tangent transform [30].

In addition to degree of anisotropy, the shape of the tensor ellipsoid may help to infer the underlying neurite organization. Linearity (LIN), planarity (PLA), and sphericity (SPH) capture the geometry of the tensor ellipsoid [31]. High FA may reflect increases in any of these three metrics. LIN assesses the uniformity of the diffusion direction along the main fiber direction (largest eigenvalue), while SPH is designed to measure a less uniform isotropic diffusion process, which implies more isotropic diffusion; PLA diffusion is restricted to a geometric plane spanned by the two largest eigenvalues, reflecting the existence of dispersed fibers along just two dimensions. Finally the diffusion tensor mode (MOD) helps to differentiate between these three types of anisotropy, approaching  $-1$  if diffusion is occurring along a geometric plane, and  $+1$  if diffusion is occurring along a single direction, with values approaching  $0$  indicating ortho- or iso-tropic diffusion.

$$\begin{aligned} \text{LIN} &= \frac{\lambda_1 - \lambda_2}{\lambda_1 + \lambda_2 + \lambda_3}, \quad \text{PLA} = \frac{2(\lambda_2 - \lambda_3)}{\lambda_1 + \lambda_2 + \lambda_3}, \quad \text{SPH} = \frac{3\lambda_3}{\lambda_1 + \lambda_2 + \lambda_3}, \\ \text{MOD} &= \frac{\lambda_1 \lambda_2 \lambda_3}{\left( \sqrt{(\lambda_1 - \mu)^2 + (\lambda_2 - \mu)^2 + (\lambda_3 - \mu)^2} \right)^3} \end{aligned} \quad (2)$$

**The Tensor Distribution Function** In contrast to the single tensor model, the tensor distribution function (TDF) represents the diffusion profile as a probabilistic mixture of tensors [32, 33] allowing for the reconstruction of multiple underlying fibers per voxel, together with a distribution of weights. We applied the framework proposed in [11] to the angular diffusion signal to compute the voxel-wise TDF- $P$  that describes the observed signal. TDF- $P$  is the probability distribution function defined on all feasible 3D Gaussian diffusion processes (in tensor space  $\mathbf{D}$ ) at each voxel. From the TDF at each voxel, the number of detected peaks was estimated by examining the local maxima of the tensor orientation distribution

$$\text{TOD}(\theta) = \int_{\lambda} P(D(\theta, \lambda)) d\lambda \quad (3)$$

The TDF-averaged eigenvalues of each fiber were calculated by computing the expected values along the principal direction of the fiber. From these eigenvalues, scalar TDF anisotropy and diffusivity measures (i.e. TDF-FA, TDF-MD, TDF-RD,

TDF-AxD) were calculated as below.

$$\begin{aligned}
 FA_{TDF} &= \int TOD(\theta) \cdot FA(\theta) d\theta \\
 FA(\theta) &= \sqrt{\frac{(\lambda'_1(\theta) - \lambda'_2(\theta))^2 + (\lambda'_1(\theta) - \lambda'_3(\theta))^2 + (\lambda'_2(\theta) - \lambda'_3(\theta))^2}{2[\lambda_1'^2(\theta) + \lambda_2'^2(\theta) + \lambda_3'^2(\theta)]}} \\
 \lambda'_i(\theta) &= \frac{\int P(D(\theta, \lambda)) \lambda_i d\lambda}{\int P(D(\theta, \lambda)) d\lambda}
 \end{aligned} \tag{4}$$

**Q-Ball Imaging Orientation Distribution Function** Q-ball imaging (QBI) was one of the first high angular resolution diffusion imaging (HARDI) techniques that allowed for the reconstruction of multiple fiber orientations in a given voxel [12]. QBI measures the diffusion function directly, and estimates a model-free diffusion orientation distribution (ODF) by estimating the radial integral of the diffusion propagator by applying the Funk-Radon transform (and does not require any assumptions on the diffusion process such as Gaussianity). Here, the ODFs were defined using a constant solid angle (CSA) factor, an improvement on the standard ODF computation, which results in less distorted, normalized, and sharper ODFs [34].

Scalar measures can be calculated from the ODF, such as the generalized FA (GFA)—analogous to the DTI FA metric which is defined by the standard deviation of each lambda over its root mean square of  $\text{std}(\lambda)/\text{rms}(\lambda)$ . We define the GFA as:

$$\text{GFA} = \frac{\text{std}(\psi)}{\text{rms}(\psi)} = \sqrt{\frac{n \sum_{i=1}^n (\psi(\mathbf{u}_i) - \langle \psi \rangle)^2}{(n-1) \sum_{i=1}^n \psi(\mathbf{u}_i)^2}} \tag{5}$$

where,  $\Psi(u)$  is the ODF,  $i$  is each diffusion direction and  $\langle \Psi \rangle = (1/n) \sum_{i=1}^n \Psi(u_i)$  is the mean of the ODF. We further calculated the number of dominant diffusion directions or distinguishable peaks of the ODF after normalizing the ODF (subtracting the baseline and rescaling) for which we selected two rescaling thresholds (relative peaks threshold = 0.4 and 0.5).

**Neurite Orientation Dispersion and Density Imaging (NODDI)** The NODDI model of tissue aims to differentiate between three microstructural environments that each uniquely affect water diffusion and in turn the MR signal: intra- and extra-cellular, and cerebrospinal fluid. The intra-neurite compartment is modeled as an orientation-dispersed distribution of cylinders or sticks, as myelin is known to restrict water diffusion [35]. The extra-neurite compartment is assumed to be Gaussian, because the diffusion is unrestricted [15]. NODDI allows for estimates of neurite density and orientation dispersion in dMRI data acquired with multiple shells (i.e., multiple  $b$ -values or gradient strengths). Due to the constraints of ADNI

data acquisition we could only reliably calculate the orientation dispersion index (ODI) and not the volume of the intra and extra-neurite fractions. NODDI can be more informative than DTI derived measures in areas with less organized patterns of axonal bundles. This opens a window to study diffusion properties towards the edges of the white matter and the cortex—as well as in subcortical gray matter structures.

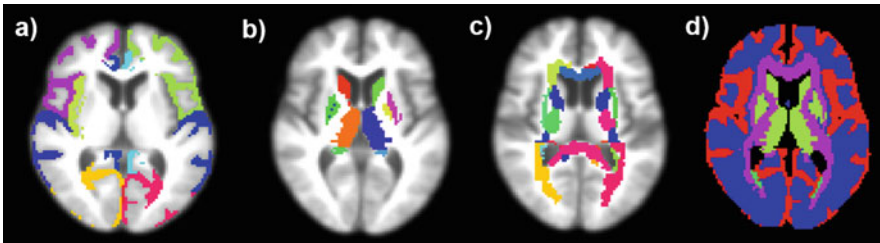
## 2.4 Template Creation and Spatial Normalization

Both FA and T1-weighted study-specific minimal deformation templates (MDT) were created from 29 cognitively healthy elderly control spatially aligned maps as in [24, 36]. Each subject's FA map was then elastically registered [26] to the FA-MDT. To ensure white matter alignment across subjects, registered FA maps were thresholded at  $FA > 0.2$  and elastically registered to the thresholded FA-MDT ( $FA > 0.2$ ). The resulting deformation fields from both elastic registrations were applied to all 17 DWI maps to align them to the same coordinate space for analysis.

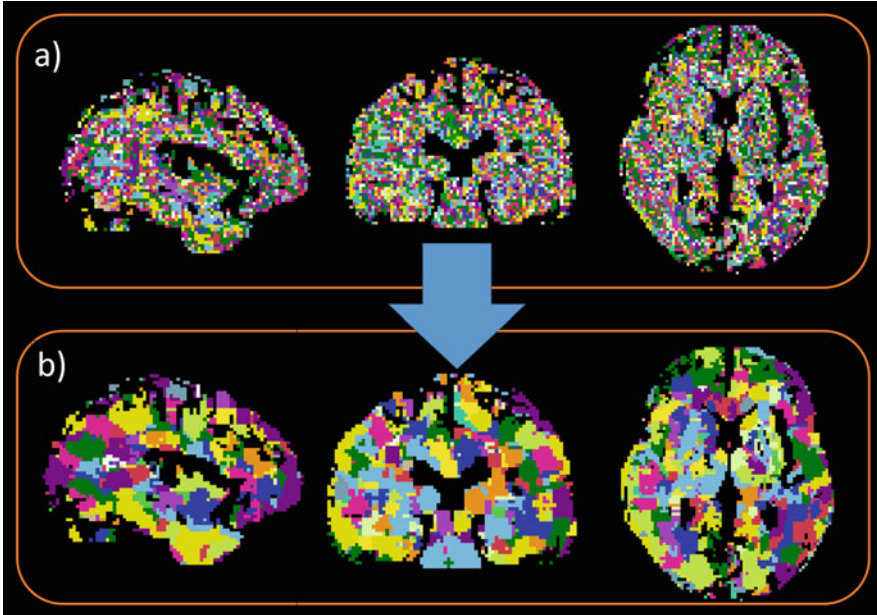
## 2.5 Atlas ROI Segmentation

We parcellated the T1-MDT and FA-MDT into several regions of interest (ROI) by using various software packages for different anatomical structures (Fig. 1).

**Cortical Gray Matter Segmentation** Using FreeSurfer [37], 34 cortical labels were automatically extracted per hemisphere from the T1-MDT. Regions were grouped into six lobes (Fig. 2a): frontal, parietal, temporal, occipital, insular, and cingulate cortex.



**Fig. 1** Automatically segmented regions of interest (ROIs). (a) Thirty-four cortical regions were parcellated in each hemisphere from the T1-MDT using FreeSurfer and grouped into six bilateral cortical lobes. (b) Seven bilateral subcortical structures were segmented from the T1-MDT with FSL FIRST. (c) Twenty-one major white matter tracts from the JHU atlas were elastically registered to the FA-MDT. (d) *Blue region* shows the external white matter or *corona radiata*



**Fig. 2** To avoid presenting ten maps from each fold, the classification process was additionally run on the entire data set for figures only. **(a)** ‘Best feature map’, where the dMRI measure with lowest classification MSE and  $p > 0.05$  was selected in each voxel. **(b)** Smoothing neighborhood search at a depth of three voxels, constrained by ROI boundaries, where the best measure for each voxel is changed to the measure most frequently found in the voxel’s neighborhood. Refer to Table 1 for corresponding metric color key

**Subcortical Gray Matter Structures** Subcortical regions were defined by segmenting the T1-MDT using the freely-available and automated FSL FIRST segmentation algorithm (Fig. 2b) [38]. These included the nucleus accumbens, amygdala, caudate, hippocampus, pallidum, putamen, and thalamus.

**Core White Matter Tract Atlas** We registered [26] the FA image from the JHU DTI atlas [39] to our FA-MDT to which all maps were spatially normalized. We then applied that deformation to the stereotaxic JHU “Eve” atlas WM labels (Fig. 2c). This atlas contains core WM structures representing large fiber bundles that traverse the brain.

**External White Matter/Corona Radiata** This region was generated by taking the full white matter parcellation computed with FreeSurfer (see above) and subtracting it from the core white matter tract atlas.



## 2.6 Hierarchical Logistic Regression Classification

**Test Each Measure on Each Voxel Independently** For each of the 193,586 voxels within the MDT mask, 17 separate logistic regression classifiers were run for each DWI measure to predict disease status (AD or CN). In each fold of a ten by ten-fold cross-validation, the DWI measure with the lowest mean squared error (MSE) and  $p > 0.05$  in each voxel was selected, resulting in ten 'best feature maps' (Fig. 2a).

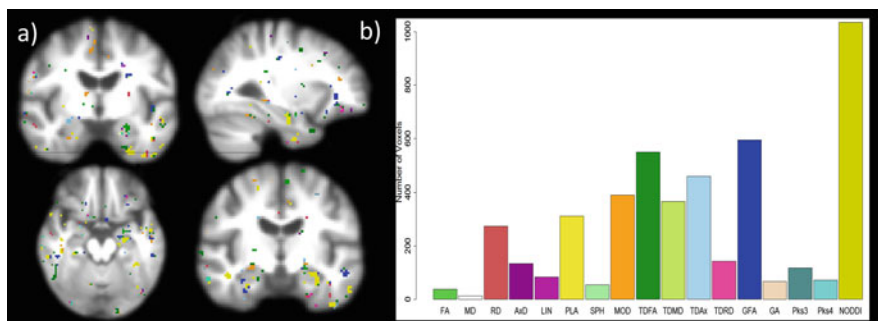
**Neighborhood Search to Smooth Best Feature Map** Individual voxels are noisy and not statistically independent. Neighboring anatomy, and therefore voxels, tend to have similar properties, yielding spatially correlated signals. As such, for each voxel a neighborhood search was performed, constraining the search to specific ROIs, (depth = 3 voxels for clusters of  $14 \times 14 \times 14$  mm), and the best measure for each voxel was then changed to the measure most frequently found in the given neighborhood (Fig. 2b).

**Hierarchical Classification on Best Feature Maps** A second logistic regression classifier was run on the best feature map. However, as there were  $\sim 200,000$  voxels/features per subject and only 101 subjects ( $p \gg n$ ), a regularized version of logistic regression was run using the *glmnet* package available on CRAN (<http://cran.r-project.org/web/packages/glmnet/index.html>). The most well-known penalty, the *L1* or LASSO penalty, encourages sparsity by setting most small coefficients to zero. This penalty function still suffers from some limitations when there is a large number of parameters  $p$  to fit, and few observations  $n$ , as LASSO selects at most  $n$  variables before it saturates. Also if there is a group of highly correlated variables, then the LASSO tends to select one variable from a group and ignore the others. Another common alternative is the *L2* or ridge penalty, which shrinks the coefficient estimates towards zero. However, this method never zeroes out any coefficients, leaving  $p$  coefficients. To overcome the limitations of both of these methods, the elastic net was introduced, to use both *L1* and *L2* tuned by a mixing parameter,  $0 \leq \alpha \leq 1$  [40].

$$\frac{1 - \alpha}{2\|\beta\|_2^2} + \alpha\|\beta\|_1 \quad (6)$$

When  $\alpha = 1$ , this is simply a LASSO and when  $\alpha = 0$ , it is the ridge penalty. On each of the ten 'best feature maps' from the ten-fold, a ten-fold cross validation was run to determine the best  $\alpha$  and tuning parameter  $\lambda$  to control the relative impact of the penalty on the coefficient estimates. Using accuracy, sensitivity, and specificity, we tested the relative utility of each map of features for distinguishing diagnostic groups.





**Fig. 3** To avoid presenting ten maps from each fold, the classification process was additionally run on the entire data set for figures only. **(a)** Voxels not zeroed out by the elastic net regularizer that contributed to classification. The voxels were largely found in the hippocampus and temporal lobe. **(b)** Most voxel clusters were NODDI, followed by GFA, TDF-FA, and TDF-AxD

### 3 Results

The mean MSE across all voxels from the ten ‘best feature maps’ was  $0.263 \pm 0.005$  (mean accuracy:  $\sim 74\%$ ). The final hierarchical logistic regression classification resulted in a mean accuracy of  $85\%$  (mean sensitivity =  $81\%$ , specificity =  $89\%$ ).

Voxels that were not zeroed out by the elastic net regularizer and that contributed to this classification were largely found in the hippocampus and temporal lobes (Fig. 3a), which makes sense, given the preferential involvement of these regions in AD. Most voxel clusters were NODDI, followed by GFA, TDF-FA, and TDF-AxD (Fig. 3b).

### 4 Discussion

In this article, we evaluated the utility of novel dMRI approaches for studying white matter (WM) microstructure in AD compared to healthy controls, by computing 17 dMRI metrics for each participant, and assessing which measures contribute most to disease classification.

There is a great deal of evidence that AD pathology includes disturbances in the brain’s WM pathways, perhaps secondary to cortical neuronal loss. WM neuropathology in AD includes partial loss of axons, myelin sheaths, and oligodendroglial cells [41, 42]. The growing imaging literature reports significant macrostructural WM atrophy [43, 44] as well as altered WM microstructure, as defined by dMRI metrics, with an emphasis on medial temporal lobe structures. Most of these findings, however, are derived from tensor-based metrics such as FA and MD [9, 16–20]. Fewer studies report disease-related changes in AxD and RD

tensor metrics, and almost none include dMRI measures derived from non-tensor models.

The scope of machine learning and classification dMRI findings is similarly limited. Volumetric measures, including hippocampal volume, gray matter volume from voxel-based morphometry, and cortical thickness [45–48], have effectively classified AD patients, but few studies have used dMRI derived biomarkers for classification purposes. The few that do, exclusively use the DTI model: several have used voxel-wise features derived from full DTI maps, using methods such as Pearson correlation and ReliefF for feature reduction [21–23], yielding accuracies of more than 90 %. In [49] tractography-based connectivity metrics based on fiber count, FA, and diffusivity were used for SVM classification, reporting an accuracy of 88 %, although clearly these accuracies depend on the problem and dataset used, and are not directly comparable with each other.

DTI metrics are sensitive enough to classify AD and identify related deficits, but the tensor model is limited as it only models a single fiber population per voxel, omitting information on complex WM architecture. While DTI metrics may sufficiently characterize the highly coherent fiber bundles at the core of the brain (Fig. 1c), they overlook information in the increasingly more complex peripheral structure, such as the crossing fibers of the *corona radiata*, and neurite dispersion near the cortex and gray matter. DTI metrics are non-specific as they are affected by fiber diameter, packing density, membrane permeability, myelination, and intra-voxel orientation coherence. It is therefore important to assess whether the wave of new models introduced in recent years offer any advantages or new information not previously captured on AD related microstructural changes.

Here we evaluated 101 subjects and were able to reach relatively high accuracy despite the heterogeneity of our multi-site sample. Although using novel metrics did not necessarily beat prior classification results, the goal was to compare the relative utility of metrics for classification, which leads to some insight on how the disease may affect different fiber properties. Moreover, it was important to see if these metrics might surpass tensor metrics in particular regions outside of the core, cohesive WM, and thus contribute extra information. Qualitatively, this seems to be the case in the best feature maps (Fig. 2b), as metrics such as NODDI (*mustard*), a measure of neurite dispersion, for example, was more prevalent as the “top metric” around the external cortical areas of the brain where fibers are more dispersed/diverted. TDF-AxD (*grey*) was more prevalent as the “top metric” toward the internal bundled structures. Even though all of the dMRI measures described are correlated with each other, each captures the microstructure in a slightly different way. Furthermore, clusters of surviving voxels from the hierarchical regularized logistic model were all non-tensor metric clusters largely in the temporal lobes and hippocampus (Fig. 3). While these regions are often implicated in AD pathology, the hippocampus is not a coherent WM structure, thus requiring a non-tensor model to pick up differences.

In conclusion, different reconstruction models and their respective scalar descriptors provide distinctive micro-anatomical features, which also differ in classification value by brain region. Future work should compare other classification methods (e.g., non-parametric SVM), and test if dMRI metrics can contribute to leading

classification approaches based on biomarkers such as hippocampal volume, amyloid deposition and tensor-based morphometry.

## References

1. Alzheimer's Disease Association: Alzheimer's disease facts and figures. *Alzheimers Dement.* **8**(2), 131–168 (2012)
2. Petersen, R.C., et al.: Current concepts in mild cognitive impairment. *Arch. Neurol.* **58**(12), 1985–1992 (2001)
3. Bruscoli, M., Lovestone, S.: Is MCI really just early dementia? A systematic review of conversion studies. *Int. Psychogeriatr.* **16**(2), 129–140 (2004)
4. Delbeck, X., et al.: Alzheimer's disease as a disconnection syndrome? *Neuropsychol. Rev.* **13**, 79e92 (2003)
5. Jack Jr., C.R., et al.: Update on the magnetic resonance imaging core of the Alzheimer's Disease Neuroimaging Initiative. *Alzheimers Dement.* **6**(3), 212–220 (2010)
6. Descoteaux, M., Poupon, C.: Diffusion-weighted MRI. In: Belvic, D., Belvic, K. (eds.) *Comprehensive Biomedical Physics*, vol. 3, no. 6, pp. 81–97. Elsevier, Oxford (2014)
7. Behrens, T.E.J., et al.: Probabilistic diffusion tractography with multiple fibre orientations. What can we gain? *Neuroimage* **34**(1), 144–155 (2007)
8. Descoteaux, M.: High angular resolution diffusion MRI: from local estimation to segmentation and tractography. Ph.D. Thesis, Université de Nice (2008)
9. Xie, S., et al.: Voxel-based detection of white matter abnormalities in mild Alzheimer disease. *Neurology* **66**(12), 1845–1849 (2006)
10. Canu, E., et al.: Microstructural diffusion changes are independent of macrostructural volume loss in moderate to severe Alzheimer's disease. *J. Alzheimers Dis.* **19**(3), 963–976 (2010)
11. Leow, A.D., et al.: The tensor distribution function. *Magn. Reson. Med.* **61**(1), 205–214 (2009)
12. Tuch, D.S.: Q-ball imaging. *Magn. Reson. Med.* **52**(6), 1358–1372 (2004)
13. Tournier, J.D., et al.: Direct estimation of the fiber orientation density function from diffusion-weighted MRI data using spherical deconvolution. *Neuroimage* **23**, 1176–1185 (2004)
14. Wedeen, V.J., et al.: Mapping complex tissue architecture with diffusion spectrum magnetic resonance imaging. *Magn. Reson. Med.* **54**, 1377–1386 (2005)
15. Zhang, H., et al.: NODDI: practical in vivo neurite orientation dispersion and density imaging of the human brain. *Neuroimage* **61**(4), 1000–1016 (2012)
16. Medina, D., et al.: White matter changes in mild cognitive impairment and AD: a diffusion tensor imaging study. *Neurobiol. Aging* **27**(5), 663–672 (2006)
17. Rose, S.E., et al.: Diffusion indices on magnetic resonance imaging and neuropsychological performance in amnesic mild cognitive impairment. *J. Neurol. Neurosurg. Psychiatry* **77**(10), 1122–1128 (2006)
18. Zhang, Y., et al.: Diffusion tensor imaging of cingulum fibers in mild cognitive impairment and Alzheimer disease. *Neurology* **68**(1), 13–19 (2007)
19. Kavcic, V., et al.: White matter integrity linked to functional impairments in aging and early Alzheimer's disease. *Alzheimers Dement.* **4**(6), 381–389 (2008)
20. Stebbins, G.T., Murphy, C.M.: Diffusion tensor imaging in Alzheimer's disease and mild cognitive impairment. *Behav. Neurol.* **21**(1), 39–49 (2009)
21. Graña, M., et al.: Computer aided diagnosis system for Alzheimer disease using brain diffusion tensor imaging features selected by Pearson's correlation. *Neurosci. Lett.* **502**, 225e229 (2011)
22. Haller, S., et al.: Individual prediction of cognitive decline in mild cognitive impairment using support vector machine-based analysis of diffusion tensor imaging data. *J. Alzheimers Dis.* **22**, 315e327 (2010)

23. O'Dwyer, L., et al.: Using support vector machines with multiple indices of diffusion for automated classification of mild cognitive impairment. *PLoS One* **7**, e32441 (2012)
24. Nir, T., et al.: Effectiveness of regional DTI measures in distinguishing Alzheimer's disease, MCI, and normal aging. *Neuroimage Clin.* **3**, 180–195 (2013)
25. Holmes, C.J., et al.: Enhancement of MR images using registration for signal averaging. *J. Comput. Assist. Tomogr.* **22**, 324–333 (1998)
26. Leow, A.D., et al.: Statistical properties of Jacobian maps and the realization of unbiased large-deformation nonlinear image registration. *IEEE Trans. Med. Imaging* **26**(6), 822–832 (2007)
27. Basser, P.J., et al.: MR diffusion tensor spectroscopy and imaging. *Biophys. J.* **66**(1), 259–267 (1994)
28. Song, S.K., et al.: Diffusion tensor imaging detects and differentiates axon and myelin degeneration in mouse optic nerve after retinal ischemia. *Neuroimage* **20**, 1714–1722 (2003)
29. Song, S.K., et al.: Demyelination increases radial diffusivity in corpus callosum of mouse brain. *Neuroimage* **26**(1), 132–140 (2005)
30. Batchelor, P.G., et al.: A rigorous framework for diffusion tensor calculus. *Magn. Reson. Med.* **53**, 221–225 (2005)
31. Ennis, D.B., Kindlmann, G.: Orthogonal tensor invariants and the analysis of diffusion tensor magnetic resonance images. *Magn. Reson. Med.* **55**, 136–146 (2006)
32. Jian, B., et al.: A novel tensor distribution model for the diffusion-weighted MR signal. *Neuroimage* **37**(1), 164–176 (2007)
33. Zhan, L., et al.: A novel measure of fractional anisotropy based on the tensor distribution function. *Med. Image Comput. Assist. Interv.* **12**(Pt 1), 845–852 (2009)
34. Aganj, I., et al.: Reconstruction of the orientation distribution function in single- and multiple-shell q-ball imaging within constant solid angle. *Magn. Reson. Med.* **64**(2), 554–466 (2010)
35. Zhang, H., et al.: Axon diameter mapping in the presence of orientation dispersion with diffusion MRI. *Neuroimage* **56**(3), 1301–1315 (2011)
36. Gutman, B., et al.: Creating Unbiased Minimal Deformation Templates for Brain Volume Registration. *Organization for Human Brain Mapping, Barcelona* (2010)
37. Fischl, B., et al.: Automatically parcellating the human cerebral cortex. *Cereb. Cortex* **14**(1), 11–22 (2004)
38. Patenaude, B., et al.: A Bayesian model of shape and appearance for subcortical brain segmentation. *Neuroimage* **56**, 907–922 (2011)
39. Mori, S., et al.: Stereotaxic white matter atlas based on diffusion tensor imaging in an ICBM template. *Neuroimage* **40**(2), 570–582 (2008)
40. Zou, H., Hastie, T.: Regularization and variable selection via the elastic net. *J. R. Statist. Soc. B* **67**(2), 301–320 (2005)
41. Brun, A., Englund, E.: White matter disorder in dementia of the Alzheimer type: a pathoanatomical study. *Ann. Neurol.* **19**(3), 253–262 (1986)
42. Sjobeck, M., et al.: Decreasing myelin density reflected increasing white matter pathology in Alzheimer's disease—a neuropathological study. *Int. J. Geriatr. Psychiatry* **20**(10), 919–926 (2005)
43. Hua, X., et al.: 3D characterization of brain atrophy in Alzheimer's disease and mild cognitive impairment using tensor-based morphometry. *Neuroimage* **41**(1), 19–34 (2008)
44. Migliaccio, R., et al.: White matter atrophy in Alzheimer's disease variants. *Alzheimers Dement.* **8**(5 Suppl.), S78–87 e71–72 (2012)
45. Desikan, R.S., et al.: An automated labeling system for subdividing the human cerebral cortex on MRI scans into gyral based regions of interest. *Neuroimage* **31**(3), 968–980 (2006)
46. Klöppel, S., et al.: Automatic classification of MR scans in Alzheimer's disease. *Brain* **131**, 681–689 (2008)

47. Lerch, J.P., et al.: Automated cortical thickness measurements from MRI can accurately separate Alzheimer's patients from normal elderly controls. *Neurobiol. Aging* **29**(1), 23–30 (2008)
48. Magnin, B., et al.: Support vector machine-based classification of Alzheimer's disease from whole-brain anatomical MRI. *Neuroradiology* **51**(2), 73–83 (2009)
49. Wee, C.Y., et al.: Enriched white matter connectivity networks for accurate identification of MCI patients. *Neuroimage* **54**(3), 1812–1822 (2011)

# Brain Tissue Micro-Structure Imaging from Diffusion MRI Using Least Squares Variable Separation

Hamza Farooq, Junqian Xu, Essa Yacoub, Tryphon Georgiou, and Christophe Lenglet

**Abstract** We introduce a novel data fitting procedure of multi compartment models of the brain white matter for diffusion MRI (dMRI) data. These biophysical models aim to characterize important micro-structure quantities like axonal radius, density and orientations. In order to describe the underlying tissue properties, a variety of models for intra-/extra-axonal diffusion signals have been proposed. Combinations of these analytic models are used to predict the diffusion MRI signal in multi-compartment settings. However, parameter estimation from these multi-compartment models is an ill-posed problem. Consequently, many existing fitting algorithms either rely on an initial grid search to find a good start point, or have strong assumptions like single fiber orientation to estimate some of these parameters from simpler models like the diffusion tensor (DT). In both cases, there is a trade-off between computational complexity and accuracy of the estimated parameters. Here, we describe a novel algorithm based on the separation of the Nonlinear Least Squares (NLLS) fitting problem, via Variable Projection Method, to search for non-linearly and linearly entering parameters independently. We use stochastic global search algorithms to find a global minimum, while estimating non-linearly entering parameters. The approach is independent of any starting point, and does not rely on estimates from simpler models. We show that the suggested algorithm is faster than algorithms involving grid search, and its greater accuracy and robustness are demonstrated on synthetic as well as ex-/in-vivo data.

---

H. Farooq (✉) • T. Georgiou  
Department of Electrical and Computer Engineering, University of Minnesota, Minneapolis, MN, USA  
e-mail: [faroo014@umn.edu](mailto:faroo014@umn.edu)

J. Xu  
Department of Radiology, Translational and Molecular Imaging Institute, Icahn School of Medicine at Mount Sinai, New York, NY, USA

E. Yacoub • C. Lenglet  
Department of Radiology, Center for Magnetic Resonance Research, University of Minnesota, Minneapolis, MN, USA

## 1 Introduction

Diffusion MRI quantifies the anisotropic displacement of water molecules during a certain time interval within a structure. This can be used to reveal tissue micro-structure information via biophysical models. The simplest of these models is the Diffusion Tensor[3], from which quantities like the Mean Diffusivity (MD) and Fractional Anisotropy (FA) can be computed. However, more specific markers like axon radius, density and volume fractions of different compartments can be estimated from more advanced multi-compartment models, as suggested for example in [12] and [2].

The problem of fitting diffusion MRI data to these biophysical models is not well posed in general because of the type of functions or models employed to describe diffusion in a certain geometry. These functions depend non-linearly on variables to be estimated, leading to a non-convex optimization problem and thus having many local optima. Any optimization algorithm using gradient based methods will largely depend upon a good starting point to reach a global optimum.

Initial grid search over a range of physically possible parameters can be performed, as done for example in NODDI[12] and ActiveAx[2] model fitting. This provides a starting point to subsequently solve a Gauss-Newton (GN) non-linear optimization problem and estimate parameters of interest. CAMINO[4] uses estimates from simpler models to find a starting point before solving a generic three-compartment model via the Levenberg Marquardt (LM) method. CAMINO needs to solve several simpler models to obtain an initial guess. Grid search and estimates from simpler models increase the possibility of reaching global optimum but add to the computational complexity and estimation time. Alternatively, AMICO[5] casts the multi-compartment models (as suggested in [12] and [2]) parameter estimation into a convex problem. For example, in case of ActiveAx, the problem is viewed as convex by estimating fiber orientation from the DT model and then searching for linearly entering parameters only, over a grid or dictionary of remaining two non-linearly entering parameters. The approach converges more quickly but still needs to be adapted in the presence of three or more non-linearly entering parameters.

We propose a novel algorithm for estimating any multi-compartment model parameters without requiring a grid or using simpler models for initial estimation. As further described in the following section, we focus on the Zeppelin-Cylinder-Dot model, identified as one of the best three-compartment white matter micro-structure models [7]. The problem is approached by separating linearly and non-linearly entering parameters. By exploiting variable separation and stochastic global search algorithms, we demonstrate that our method not only converges twice as fast as CAMINO, but also finds global minima for the non-linear parameters of interest more reliably, contrary to other existing methods. We present experiments both on synthetic and brain datasets, which illustrate the performance of the proposed method. Our improved fitting technique consistently leads to more robust and accurate estimates of axonal radius, density and fiber orientation.

## 2 Problem Formulation

A typical estimation problem for multi-compartment model parameters from diffusion MRI data in the presence of Rician noise [1] is of the following form:

$$\min_{x,f} \sum_{k=1}^N \sigma^{-2} (y(k) - \sum_{i=1}^n \sqrt{f_i e^{A_i(x)} + \sigma^2})^2 \quad (1)$$

where  $y$  represents normalized MRI measurements and  $N$  is the total number of measurements available.  $f = [f_1 \ f_2 \ \dots \ f_n]'$  is the vector containing volume fractions of  $n$  compartments.  $x = [x_1 \ x_2 \ \dots \ x_m]'$  is the vector containing  $m$  parameters on which functions describing the dMRI signal, in  $n$  compartments, depend.  $A_1, A_2 \dots A_n$  characterize the selected models for intra-axonal, extra-axonal, cerebrospinal fluid (CSF) and glial cells compartments etc. [7, 10].  $\sigma$  is the standard deviation of noise, which is estimated from  $b_0$  measurements of MRI.  $\sigma$  adds a constant bias to the objective functions, which can easily be taken care of. By dropping  $\sigma$ , we can rewrite the objective function in Eq. (1) including constraints as follows:

$$\min_{x,f} \| y - (f_1 e^{-A_1(x_1, \dots, x_{m1})} + f_2 e^{-A_2(x_{m1+1}, \dots, x_{m2})} + \dots + f_n e^{-A_n(x_{m2+1}, \dots, x_m)}) \|_2^2 \quad (2)$$

$$\text{such that } \sum_{i=1}^n f_i = 1, \quad f_i \geq 0 \quad i = 1, 2 \dots n$$

$$x_j^{\min} \leq x_j \leq x_j^{\max} \quad j = 1, 2 \dots m$$

where  $x_j^{\min}$  and  $x_j^{\max}$  represent lower bound and upper bound for unknown deterministic variables  $x$  respectively. Unknown parameters in  $x$  will vary with each choice of multi-compartment model.

## 3 Optimization via NLLS Variable Projection and Genetic Algorithm (GA)

We describe the four main steps of the proposed algorithm to solve Eq. (2).

- **Step 1. Variable projection for separating non-linearly entering parameters.** We can exploit the separable structure of the problem described in Eq. (1) by variable separation method as suggested in [8]. We can re-write our objective



function in the following form:

$$\min_{x,f} \|y - \Phi(x)f\|_2^2$$

$$\text{where } \Phi(x) = [e^{-A_1(x_1, \dots, x_{m1})} \quad e^{-A_2(x_{m1+1}, \dots, x_{m2})} \quad \dots \quad e^{-A_3(x_{m2+1}, \dots, x_m)}] \quad (3)$$

$$f = \Phi^\dagger(x)y \quad (4)$$

where  $\Phi^\dagger(x)$  is Moore-Penrose inverse of  $\Phi(x)$

$$\text{i.e., } \Phi^\dagger(x) = (\Phi(x)^T \Phi(x))^{-1} \Phi(x)^T \quad (5)$$

By substituting Eq. (4) in Eq. (3), our objective function takes the following form:

$$\min_x \|y - \Phi(x)(\Phi(x)^T \Phi(x))^{-1} \Phi(x)^T y\|_2^2 \quad (6)$$

$$\min_x \|(I - \Phi(x)(\Phi(x)^T \Phi(x))^{-1} \Phi(x)^T)y\|_2^2 \quad (7)$$

Eq. (7) is called the variable projection functional. Assuming that  $\Phi(x)$  has a locally constant rank, it has been proven in [8] that the global minimum of Eq. (7) remains the same as the global minimum of Eq. (3). The matrix  $\Phi(x)$  has number of measurements (rows) much larger than the number of compartments (columns). Further, the measurements are noisy. Thus, generically it will always have full column rank.

- **Step 2. Non-linear parameters estimation by GA.** It has been shown in [9] that GA can be used efficiently for NLLS estimation of  $x$ , while solving for a sum of exponentials models in time series. We extend the approach for solving Eq. (7) and employ elitism based method with population size of 24–40. Stopping criteria of 70–100 generations was found sufficient for convergence in this problem setting. Implementation was done by using the toolbox developed at the University of Sheffield.<sup>1</sup>
- **Step 3. Constrained linear parameters estimation.** Once non-linear parameters  $x$  are known, estimation of linear parameters is a linear least squares estimation problem as shown in (4).
- **Step 4. NLLS estimation using gradient based methods.** Estimates after step 3 are further refined by using gradient based methods (for example MATLAB's 'lsqcurvefit') by constrained NLLS estimation. In practice this allows the reduction of the number of generations used in the GA (step 2).

<sup>1</sup><http://codem.group.shef.ac.uk/index.php/ga-toolbox>.

## 4 Results

### 4.1 Experiment Using Synthetic Data

First the proposed algorithm was tested with synthetic data generated by the open source software CAMINO [4] using ‘datasynth’. For the purpose of this comparison, we used the Zeppelin-Cylinder-Dot model [7, 10] with Rician noise at different SNRs. Data was generated using 4 b-values each with 119 directions and 18 additional  $b_0$  volumes. Detail is given in Sect. 4.2 below.

#### Example Problem : dMRI Data Fitting to ‘Zeppelin-Cylinder-Dot’ Model

$$\min_{R, \theta, \phi, d_{\perp}, f} \| y - (f_1 e^{-A_{cylinder}(R, \theta, \phi)} + f_2 e^{-A_{zeppelin}(\theta, \phi, d_{\perp})} + f_3 e^{-A_{dot}}) \|_2^2 \quad (8)$$

$$\text{such that } \sum_{i=1}^3 f_i = 1, \quad f_i \geq 0 \quad i = 1, 2, 3.$$

$$0 \leq R \leq 20, \quad 0 \leq \theta \leq 2\pi, \quad 0 \leq \phi \leq \pi$$

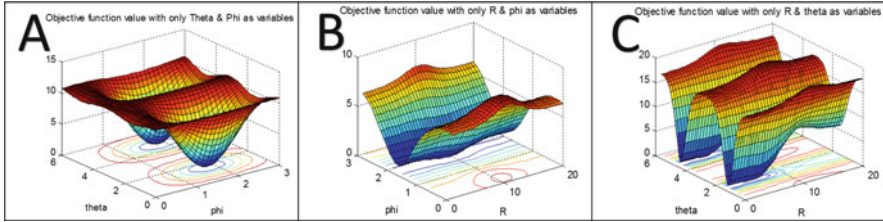
$$d_{\perp} = d_{\parallel}(1 - (f_1/(f_1 + f_2)))$$

$$\text{Fibre direction vector } n = [\cos \phi \sin \theta \quad \sin \phi \sin \theta \quad \cos \theta] \quad (9)$$

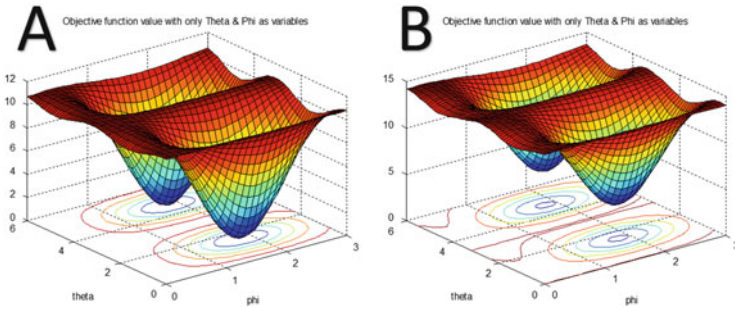
For simplicity, only unknown parameters have been shown in Eq.(8) and described as follows:  $f_1, f_2$  and  $f_3$  are intra-axonal, extra-axonal and CSF compartments volume fractions.  $d_{\parallel}$  (diffusion coefficient parallel to fiber orientation, fixed for in-vivo data to  $1.7e^{+3}$  ( $s/\mu m^2$ )),  $d_{\perp}$  ( $s/\mu m^2$ ) is the diffusion coefficient perpendicular to fiber orientation. The constraint given in Eq.(8) on  $d_{\perp}$ , is from a simple tortuosity model given in [11].  $R$  ( $\mu m$ ) denotes the average axonal radius, while  $\theta$  (rad) and  $\phi$  (rad) give the fiber orientation as in Eq. (9). Details about the functions describing  $e^{-A_{cylinder}}$ ,  $e^{-A_{zeppelin}}$  and  $e^{-A_{dot}}$  can be found in [10].

**Objective Function Analysis** Using the generated synthetic data, objective function given in Eq. (8) can be visualized by some of the plots as shown in Fig. 1. It can be seen in Fig. 1a, c that if  $\theta$  is constrained as in Eq.(8), there can be two distinct solutions for  $n$  ( $180^\circ$  apart). Figure 1c shows that if a gradient based method is used, any initial value of  $R$  greater than a certain point (approximately  $10 \mu m$  in this example), will never lead to a global minimum. Small axonal radii can therefore be over-estimated, should this type of situation arise. Figure 2 shows the effect of Rician noise on the objective function. Although the overall shape of the objective function remains approximately the same, extrema are elevated and exhibit less contrast, thereby possibly rendering the optimization procedure more complicated.

**Comparison of Results with CAMINO** For all parameter estimates ( $R, f_i, \theta$  and  $\phi$ ) and all SNR levels, the proposed method consistently yields greater accuracy and robustness than CAMINO on synthetic data. Figures 3, 4, 5, and 6 show the



**Fig. 1** Objective function plots when, (a)  $\theta$  and  $\phi$ , (b)  $R$  and  $\phi$ , (c)  $R$  and  $\theta$  are varying only



**Fig. 2** Objective function plots at (a)  $\text{SNR} = 200$ , (b)  $\text{SNR} = 12$  for  $\theta$  and  $\phi$  as only variables

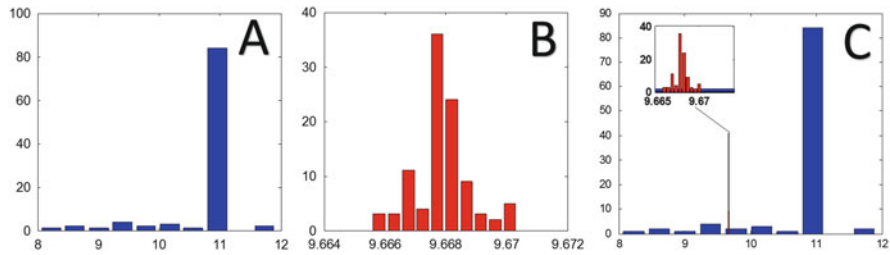
estimated parameters histograms for 100 runs at  $\text{SNR} = 25$ . Model fitting was done in CAMINO using the ‘modelfit’ function with 100 runs of the Levenberg-Marquardt algorithm. Particularly,  $R$  and orientation ( $\theta$ ,  $\phi$ ) estimates are very robust to noise using the proposed method. We find that  $R$  is slightly underestimated by only about  $0.05 \mu\text{m}$  at all SNR levels.

**Time Complexity** The estimation time depends upon the number of measurements. For CAMINO, it also increases with noise level. For this example, fitting time (per voxel) for CAMINO varied from 10 to 13 s while the proposed method took 4.8 s at the most. Time was calculated without any parallel processing on the same machine (Core i7 with 12 GB RAM).

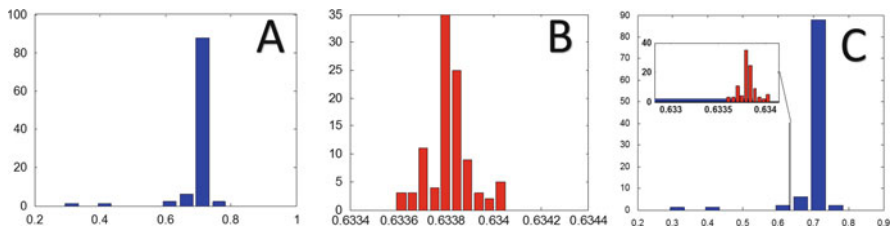
## 4.2 Experiments Using Real MRI Data

**Results Using Ex-Vivo Monkey Brain Data** A fixed monkey brain data set<sup>2</sup> [6], was used to compare results with CAMINO and AMICO. In CAMINO data fitting was performed using the ‘mmwmdfixed’ model, as detailed on the CAMINO

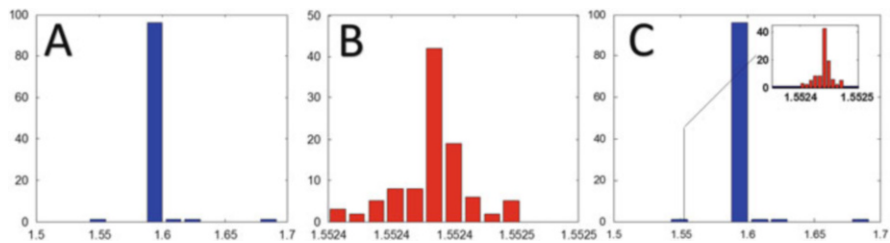
<sup>2</sup><http://dig.drcmr.dk/activeax-dataset/>.



**Fig. 3** Histogram of axon radius estimates using synthetic data SNR = 25 with true value of  $R = 10 \mu\text{m}$ . (a) CAMINO (8–12  $\mu\text{m}$ ). (b) Proposed algorithm (9.66–9.67  $\mu\text{m}$ ). (c) Histograms superimposed



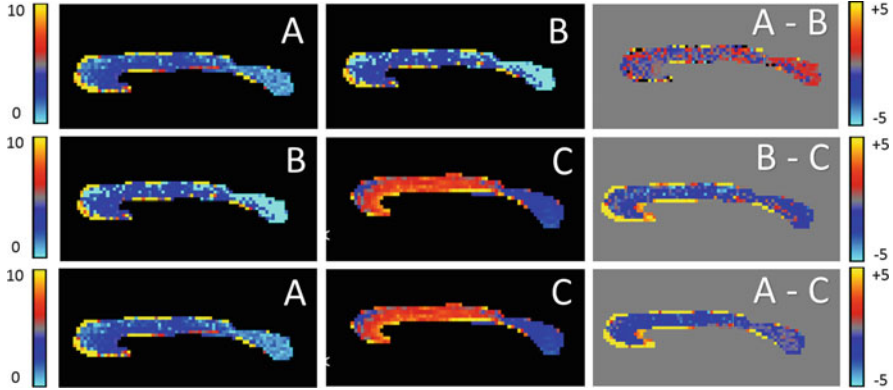
**Fig. 4** Histogram of  $v = f_1/(f_1 + f_2)$  estimates using synthetic data SNR = 25 with true value of  $v = 0.7$ . (a) CAMINO (0.3–0.8). (b) Proposed algorithm (0.633–0.634). (c) Histograms superimposed



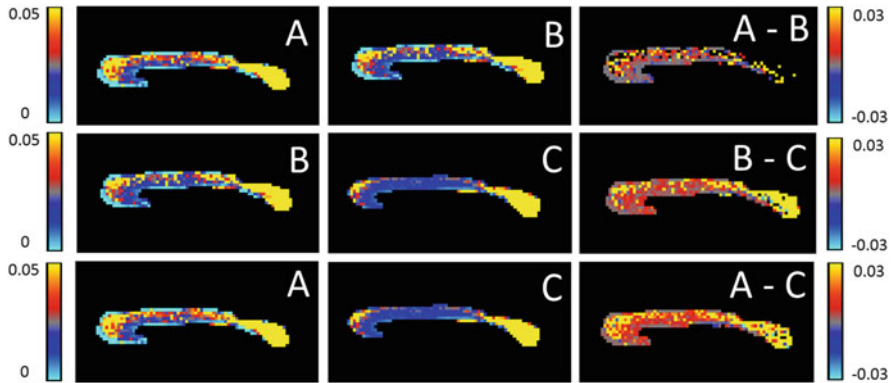
**Fig. 5** Histogram of  $\theta$  estimates using synthetic data SNR = 25 with true value of  $\theta = 1.54 \text{ rad}$ . (a) CAMINO (1.5–1.7 rad). (b) Proposed algorithm (1.5524–1.5525 rad). (c) Histograms superimposed

website.<sup>3</sup> AMICO results were generated as shown in [5]. Using proposed method, a four compartment model (‘Zeppelin-Cylinder-Ball-Dot’), as suggested in [12], was used to estimate parameters. Figure 6 shows radius estimates, while Fig. 7 shows density index ( $\rho'$ ) =  $f_1/(f_1 + f_2)\pi R^2$  estimates comparison. Figures 6 and 7 show a mid-sagittal slice of the corpus callosum.

<sup>3</sup><http://cmic.cs.ucl.ac.uk/camino/index.php?n=Tutorials.ActiveAx>.

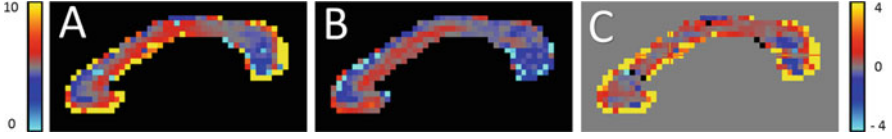


**Fig. 6** Radius estimates for ex-vivo monkey brain data. (A) CAMINO. (B) Proposed method. (C) AMICO (all units in  $\mu\text{m}$ )

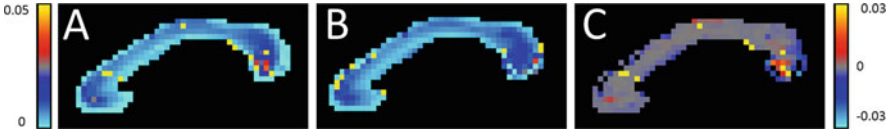


**Fig. 7** Density index  $\rho'$  estimates ex-vivo monkey brain data. (A) CAMINO. (B) Proposed method. (C) AMICO (no unit)

Results exhibit similar pattern throughout the corpus callosum i.e., densely packed small axon in genu and splenium, with larger axon and lower density in the mid-body. However, in comparison to the proposed method, CAMINO appears to over-estimate axon radii in both the genu and splenium (by about  $3 \mu\text{m}$ ) and under-estimates radii in the mid-body (by about  $2 \mu\text{m}$ ). AMICO almost uniformly over-estimates radii throughout corpus callosum by about  $2\text{--}3 \mu\text{m}$  as compared to both CAMINO and proposed method. The density index is over-estimated in the mid-body and under-estimated in the genu and splenium by CAMINO as compared to our proposed method. We hypothesize that such over-estimation for the radius may be related to the optimization issue illustrated in Fig. 1c. This result is also consistent with our analysis on synthetic data. AMICO as compared to CAMINO and proposed method, under-estimates density index by approximately 0.02 in mid-body, and 0.03 in genu and splenium.



**Fig. 8** Radius estimates for in-vivo human brain data. (a) CAMINO. (b) Proposed algorithm. (c) Difference (all units in  $\mu\text{m}$ )



**Fig. 9** Density index  $\rho'$  estimates for in-vivo human brain data. (a) CAMINO. (b) Proposed algorithm. (c) Difference (no unit)

**Results Using In-Vivo Human Brain Data** Diffusion MRI data was acquired on a healthy volunteer using a Siemens 3T Skyra system with voxel size  $2\text{ mm}^3$ , and four b-values, each with 119 directions and 18 additional  $b_0$  volumes. b-Values and corresponding parameters were chosen as follows:

$$\begin{aligned} b_1 &= 820\text{ s mm}^2 \quad (\Delta/\delta/|G|_{\max} = 17.6\text{ ms}/9\text{ ms}/98.5\text{ mT m}^{-1}); \\ b_2 &= 980\text{ s mm}^2 \quad (\Delta/\delta/|G|_{\max} = 55.5\text{ ms}/5.2\text{ ms}/97.1\text{ mT m}^{-1}); \\ b_3 &= 3010\text{ s mm}^2 \quad (\Delta/\delta/|G|_{\max} = 38.5\text{ ms}/22.2\text{ ms}/52.4\text{ mT m}^{-1}); \\ b_4 &= 7600\text{ s mm}^2 \quad (\Delta/\delta/|G|_{\max} = 37.8\text{ ms}/29.3\text{ ms}/66.6\text{ mT m}^{-1}). \end{aligned}$$

Only CAMINO has been used to compare results as AMICO does not implement ‘mmwmdin vivo’ model. A three-compartment model (Zeppelin-Cylinder-Ball, neglecting stationary compartment as suggested in [12]) was used to estimate parameters with our proposed method. Figure 8 shows radius estimates, while Fig. 9 shows  $\rho'$  estimates comparison in the corpus callosum.

Results are generally in close agreement for both methods. However, a few important differences can be identified. First, the proposed method is more robust to noise and partial volume effects, with less outlier values within (Fig. 9) and around (Fig. 8) the corpus callosum. Second, the proposed method is able to estimate smaller axonal radii and slightly higher density in the splenium area.

## 5 Conclusion

We have introduced a novel data fitting procedure for all multi-compartment models discussed in [10] using dMRI data. We have shown that the method is more reliable than other methods involving grid search and Markov Chain Monte Carlo (MCMC). It does not rely on any assumption such as single fiber orientation (for initialization), and directly estimates multi-compartment parameters from dMRI data.

Therefore, it can readily be applied to models with more than one fiber orientation and more than four compartments. We believe that there is a great potential for improved efficiency due to simple implementation in MATLAB (without requiring SPAMS and CAMINO). However, the strength of current implementation is not primarily the reduction in estimation time but the flexibility to handle more realistic models.

**Acknowledgements** Work partly supported by NIH grants P41 EB015894, P30 NS076408, R01 EB008432, Human Connectome Project (U54 MH091657) and Fulbright Program.

## References

1. Alexander, D.C.: Modelling, fitting and sampling of diffusion MRI. In: Visualization and Processing of Tensor Field. Mathematics and Visualization, pp. 3–20. Springer, Berlin (2009). [http://link.springer.com/chapter/10.1007%2F978-3-540-88378-4\\_1](http://link.springer.com/chapter/10.1007%2F978-3-540-88378-4_1)
2. Alexander, D.C., Hubbard, P.L., Hall, M.G., Moore, E.A., Ptito, M., Parker, G.J., Dyrby, T.B.: Orientationally invariant indices of axon diameter and density from diffusion. *MRI Neuroimage* **52**, 1374–1389 (2010)
3. Basser, J.P., Mattiello, J., LeBihan, D.: MR diffusion tensor spectroscopy and imaging. *Biophys. J.* **66**, 259–267 (1994)
4. Cook, P.A., Bai, Y., Nedjati-Gilani, S., Seunarine, K.K., Hall, M.G., Parker, G.J., Alexander, D.C.: Camino: open-source diffusion-MRI reconstruction and processing. In: 14th Scientific Meeting of the International Society for Magnetic Resonance in Medicine, Seattle, WA, May 2006, p. 2759
5. Daducci, A., Canales-Rodríguez, E., Zhang, H., Dyrby, T., Alexander, D.C., Thiran J.P.: Accelerated microstructure imaging via convex optimization (AMICO) from diffusion MRI data. *NeuroImage* **105**, 32–44 (2015)
6. Dyrby, T.B., Baaré, W.F., Alexander, D.C., Jelsing, J., Garde, E., Sjøgaard, L.V.: An ex vivo imaging pipeline for producing high-quality and high-resolution diffusion-weighted imaging datasets. *Hum. Brain Mapp.* **32**, 544–563 (2011)
7. Ferizi, U., Schneider, T., Panagiotaki, E., Nedjati-Gilani, G., Zhang, H., Wheeler-Kingshott, C.A., Alexander, D.C.: A ranking of diffusion MRI compartment models with in vivo human brain data. *Magn. Reson. Med.* **72**, 1785–1792 (2014)
8. Golub, G.H., Pereyra, V.: The differentiation of pseudo-inverses and nonlinear least squares problems whose variables separate. *SIAM J. Numer. Anal.* **10**, 413–432 (1973)
9. Mitra, S., Mitra, A.: A genetic algorithms based technique for computing the nonlinear least squares estimates of parameters of sum of exponentials model. *Expert Syst. Appl.* **39**, 6370–6379 (2012)
10. Panagiotaki, E., Schneider, T., Siow, B., Hall M.G., Lythgoe, M.F., Alexander, D.C.: Compartment models of the diffusion MR signal in brain white matter: a taxonomy and comparison. *NeuroImage* **59**, 2241–2254 (2012)
11. Szafer, A., Zhong, J., Gore, J.C.: Theoretical model for water diffusion in tissues. *Magn. Reson. Med.* **33**, 697–712 (1995)
12. Zhang, H., Schneider, T., Wheeler-Kingshott, C.A.M., Alexander, D.C.: NODDI: practical in vivo orientation dispersion and density imaging of the human brain. *NeuroImage* **61**, 1000–1016 (2012)

# Multi-Tensor MAPMRI: How to Estimate Microstructural Information from Crossing Fibers

Mauro Zucchelli, Lorenza Brusini, C. Andrés Méndez, and Gloria Menegaz

**Abstract** Diffusion Magnetic Resonance Imaging (dMRI) is able to detect the properties of tissue microstructure underneath the voxel through the imaging of water molecules diffusion. Many reconstruction methods have been proposed to calculate the Orientation Distribution Function (ODF) from the diffusion signal in order to distinguish between coherent fiber bundles and crossing fibers. The diffusion signal was also used to infer other microstructural information such as the axon diameter, but most often in areas with coherent fiber direction such as the *corpus callosum*. In this work, we developed a reconstruction model called Multi-Tensor MAPMRI (MT-MAPMRI) that is an extension of the MAPMRI model which improves the performance of MAPMRI for crossing fibers. In particular, it provides (a) enhanced signal fitting; (b) improved ODFs; (c) a more accurate diameter estimation. The model was tested and validated on both simulated and in-vivo data.

## 1 Introduction

Diffusion MRI is able to extract information on the cerebral tissue in vivo. From the diffusion weighted (DW) signal, it is possible to calculate the ensemble average propagator (EAP) under the long diffusion time assumption. The diffusion signal  $E(\mathbf{q})$  depends on the pulse width  $\delta$ , the pulse separation time  $\Delta$  and the gradient strength  $G$ . Since the number of points that is possible to acquire with diffusion MRI in practice is limited, analytical reconstruction models represent a mean of extrapolating missing data in a controlled way. These are thus fitted to the signal enabling the estimation of the tissue physical properties based on analytical expressions. One of the first reconstruction models was the Diffusion tensor (DTI) [4] in which the signal was modeled as a single multivariate Gaussian function

---

M. Zucchelli (✉) • L. Brusini • C.A. Méndez • G. Menegaz  
University of Verona, Verona, Italy  
e-mail: [mauro.zucchelli@univr.it](mailto:mauro.zucchelli@univr.it)



(diffusion tensor). This model has been proved suitable for describing diffusion in unconstrained conditions and in the case of single fiber bundles. Many attempts have been made to expand the single tensor to a double or multi-tensor [13] estimation in order to characterize more complex fiber topologies, like crossings, which normally occur in the majority of the white matter [8]. Other reconstruction techniques try to fit more complex basis functions to the signal in order to be able to naturally fit crossing fibers. The 3D Simple Harmonic Oscillator Based Reconstruction and Estimation (SHORE) introduced in [10] fits the diffusion signal as a series of Hermite polynomials and spherical harmonics, leading to good results in the calculation of the Orientation Distribution Function (ODF). The model further evolved in the Mean Apparent Propagator (MAP) MRI [12] in which the spherical harmonics were replaced by a set of orthogonal 1D-SHORE functions. In addition to the ODF, other micro-structural descriptors were introduced, including the Return To the Axis Probability (RTAP), an index characterizing the pore mean cross sectional area, under certain conditions. Previously this feature was only calculated in single fibers voxels using compartmental models such as the one proposed in [3, 15] or using 3D-SHORE and MAPMRI as in [5, 6].

In this paper, we propose an improvement of MAPMRI based on a multi-tensor fitting which is able to improve signal fitting and the calculation of EAP features like the ODF and the RTAP for voxel containing multiple crossings fibers.

## 2 Materials and Methods

### 2.1 MAPMRI

The SHORE basis was originally defined in [10] and expresses the 1D diffusion signal as

$$\Phi_n(u, q) = \frac{i^{-n}}{\sqrt{2^n n!}} e^{-2\pi^2 u^2 q^2} H_n(2\pi u q) \quad (1)$$

where  $u$  is a scale factor and  $H$  is the Hermite polynomial of order  $n$ . MAPMRI is a 3D SHORE basis where signal reconstruction is performed in two steps: in the first, a Gaussian function (tensor) is fitted to the signal and the tensor eigenvectors are used to rotate the reference frame in order to have the axis aligned with principal diffusion directions. The eigenvalues are then used to calculate the scale parameters of the three SHORE bases  $u_x$ ,  $u_y$  and  $u_z$ .

Since the basis is separable in the new reference frame, MAPMRI basis can be expressed as a 3D basis

$$\Phi_{n_1, n_2, n_3}(\mathbf{u}, \mathbf{q}) = \Phi_{n_1}(u_x, q_x) \Phi_{n_2}(u_y, q_y) \Phi_{n_3}(u_z, q_z) \quad (2)$$

with independent radial orders  $n_1, n_2, n_3$ . The diffusion signal  $E(\mathbf{q})$  can then be modeled as

$$E(\mathbf{q}) = \sum_{N=0}^{N_{max}} \sum_{n_1, n_2, n_3} c_{n_1, n_2, n_3} \Phi_{n_1, n_2, n_3}(\mathbf{q}) \quad (3)$$

where  $c_{n_1, n_2, n_3}$  are the basis coefficients. The coefficients vector  $\mathbf{c}$  can be obtained using the standard least-squares fit or, alternatively, using quadratic programming in order to add positivity constraints in the EAP space as in [12].

MAPMRI provides very accurate signal fitting in the case of voxels containing bundles of fibers aligned in a single direction [5]. RTAP is calculated as the integral of the signal in the plane orthogonal to the main axes of the pore [12]. There is an intrinsic problem in identifying the principal direction of a fiber crossing. MAPMRI identifies it as the main axis of the tensor that is usually placed between the axes of the fibers. Selecting only the principal axis of one of each fiber would not solve the problem because the signal originating in the second fiber would anyway contribute to the integral. The only way to calculate this index accurately for crossing fibers is to split the signal contributions of each fiber, as is explained below.

## 2.2 Multi-Tensor MAPMRI

In order to overcome the limitations of MAPMRI the initial tensor fitting is replaced with the fitting of  $m$  axially symmetric tensor  $\mathbf{D}_i$ . With this model the diffusion signal can be expressed as

$$E(\mathbf{q}) = \sum_{i=1}^m f_i \exp(-4\pi^2 \tau \mathbf{q}^T \mathbf{D}_i \mathbf{q}) \quad (4)$$

Finding the volume fraction coefficients,  $f_i$ , along with the tensor parameters is a nonlinear optimization problem that can not be solved by ordinary least squares. In order to find the coefficients, we implemented a Monte Carlo Markov Chain optimization algorithm maximizing the Rician log-likelihood of the fitting [9]. From the diffusion tensors, it is possible to derive multiple MAPMRI bases  $\Phi^i$ , using the respective eigenvalues and the eigenvector of  $\mathbf{D}_i$ . MT-MAPMRI basis signal reconstruction can then be calculated as

$$E(\mathbf{q}) = \sum_{i=1}^m \sum_{N=0}^{N_{max}} \sum_{n_1, n_2, n_3} c_{n_1, n_2, n_3}^i \Phi_{n_1, n_2, n_3}^i(\mathbf{q}) \quad (5)$$

The coefficients set  $\mathbf{c}^i$  can be fitted at the same time using ordinary least squares or quadratic programming. It is then possible to calculate the EAP and its features, like the ODF and the RTAP, as the sum of the contributions of each component.

For example, in the case of RTAP, it is possible to calculate each  $RTAP_i$  using the set of coefficients  $\mathbf{c}^i$  for all the  $m$  components. The final RTAP for MT-MAPMRI will be equal to  $\sum_{i=1}^m RTAP_i$ . This is a sum, and not a weighted average because the relative volume fraction of each component is already embedded in the basis coefficients.

Therefore, fitting the multi-tensor correctly is absolutely crucial, since a poor fit will lead to an even worse fitting of the SHORE basis. In order to ensure the robustness of the approach we try to fit at the same time: one isotropic tensor, one axially-symmetric tensor, two axially-symmetric tensors and three axially-symmetric tensors meanwhile selecting the best model using Akaike information criterion [2]. In addition, if the tensor fraction  $f_i$  is less than 0.15 the relative tensor is not used for the SHORE fitting. In the case of voxels containing single bundles of fibers the MT-MAPMRI basis is equivalent to the classical MAPMRI basis using a single axially-symmetric tensor.

### 2.3 Simulated Data

RTAP allows inferring the underlying pore cross-sectional area accurately only under three conditions: (a) the compartment is homogeneous (e.g. the pore is composed only of cylinders with the same radius and orientation), (b) the pulse separation time  $\Delta$  is much larger than the pulse width  $\delta$ , and (c), there are enough points in the  $q$ -space to provide a good fitting of the bases. We will refer to these conditions as ideal conditions for what concerns this work.

In order to have homogeneous compartments with known ground truth we calculate the diffusion signal inside the cylindrical pore of given radius  $r_0$  as described in [11] as  $E^{cy}(q_{\perp}, r_0) = (J_1(2\pi r_0 q_{\perp}) / (\pi r_0 q_{\perp}))^2$  where  $q_{\perp}$  is the plane perpendicular to the main cylinder axis and  $J_1$  is the Bessel function of the first kind.

The axis diffusivity  $E(q_{\parallel})$  is simulated as a 1D Gaussian function. The total 3D diffusivity can be calculated as  $E^{cy}(\mathbf{q}, r_0) = E(q_{\perp}, r_0)E(q_{\parallel})$ . This equation holds true only if  $\Delta \gg \delta$  which is the necessary condition for testing MAPMRI and MT-MAPMRI RTAP. In these conditions, the RTAP represents the inverse of the cross sectional area of the pore, and the cylinder diameter can thus be estimated as  $2\sqrt{1/(RTAP \cdot \pi)}$ .

We simulated three different sets of cylinders with radii of 4, 6 and 8  $\mu\text{m}$ , and with crossing angles of 0 (coherent fibers), 45°, 60° and 90°. For each of the crossing angles, we changed the orientation of the crossing fibers in 11 different directions. Rician noise was then added to the voxels at a signal to noise ratio (SNR) equal to 20, with ten different instances per voxel. The final dataset was composed of 1320 voxels.

## 2.4 *In Vivo* Data

The Human Connectome Project (HCP) [14] data results from a three-shell diffusion weighted acquisition with 1.25 mm isotropic voxels in a  $145 \times 174 \times 145$  matrix. A total of 288 DW measurements were acquired in each voxel with 90 gradients per shell, respectively, with  $b$ -values 1000, 2000 and 3000 s/mm<sup>2</sup> and 18 b0 images. Echo time and repetition time were respectively 78 ms, and 2.6 s, with pulse width  $\delta = 10.6$  ms, and pulse separation  $\Delta = 43.1$  ms.

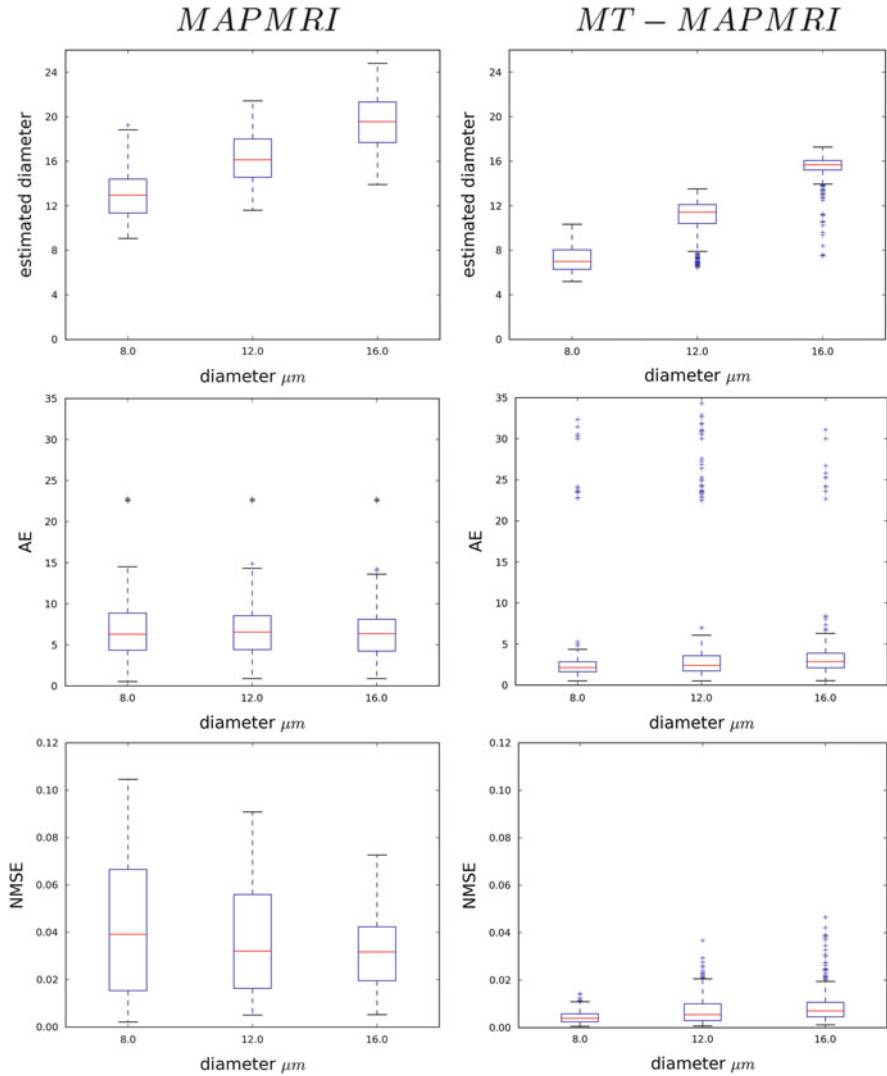
## 3 Results

Cylindrical signal was simulated as is explained in Sect. 2.3, using the HCP gradient table. MAPMRI and MT-MAPMRI were fitted on the signal, the maximal radial order  $N_{max}$  was set to 6 for MAPMRI (50 coefficients) and to 4 for MT-MAPMRI (22 coefficients times the number of tensors), respectively. From the signal fitting, it was possible to calculate the ODF, the RTAP and the normalized mean square error (NMSE). The latter was calculated by reconstructing the cylinders signal on a 10-shell ground truth, with  $b_{max} = 10,000$ , in order to benchmark the interpolation performance of the basis in points different from the one used for the fitting. The RTAP was then used to estimate the cylinders diameter while from the ODF it was possible to extract the principal directions that were used for calculating the angular error (AE) with respect to the ground truth directions.

An example of ODF for a simulated voxel featuring a crossing of 60° is presented in Fig. 1. As can be seen MAPMRI ODF tends to underestimate the crossing angle, which is actually 8° below the ground truth value [6]. On the contrary MT-MAPMRI recovers the crossing angle correctly. Figure 2, top row, shows the ability of the two bases to estimate the cylinder diameter under the ideal conditions. Since the single tensor can not adapt to the topology of the fibers configuration, MAPMRI introduces an error in the estimation of the RTAP, leading to an overestimation of the



**Fig. 1** Ground truth ODF, MAPMRI ODF and MT-ODF for a simulated two tensors crossing of 60°



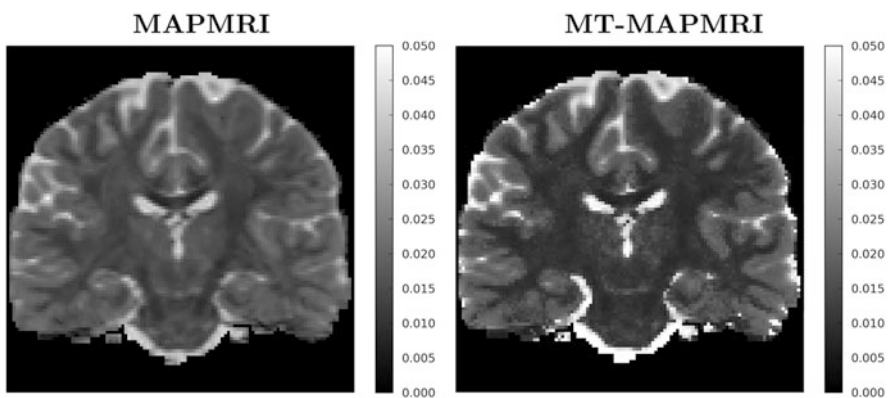
**Fig. 2** Estimated diameter (*top row*), angular error (*middle row*) and NMSE (*bottom row*) on pure cylinder voxels for MAPMRI (*left*) and MT-MAPMRI (*right*), grouped by the ground truth diameter

cylinders diameter. Instead, the multi-tensor of the MT-MAPMRI is able to detect the main diffusion directions and model the signal accordingly. In consequence, the diameter estimation is more accurate, outperforming MAPMRI. As stated in Sect. 2.1, MAPMRI tends to underestimate the crossing angles (Fig. 2, second row), while MT-MAPMRI is able to retrieve the orientation directions in a reliable way even for the majority of the  $45^\circ$  crossings. For the same reason the reconstruction

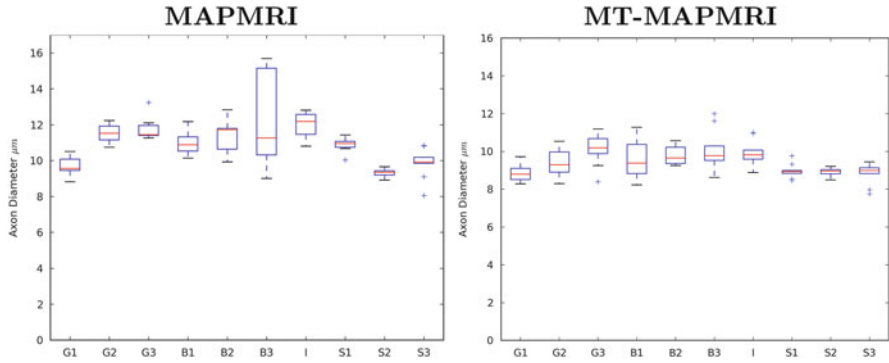
NMSE is lower for MT-MAPMRI than for MAPMRI. Although MT-MAPMRI is generally more robust than standard MAPMRI, with a narrower interquartile range, some outliers are still presents. These points represent voxels for which the initial multi-tensor fails to retrieve the correct fibers configuration, leading to a wrong MT-MAPMRI fitting.

Although it was possible to estimate the diameter under ideal conditions in these simulated voxels, a validation on in-vivo data is required. The real signal is the average of the signal contributions of all the water molecules trapped in the different compartments present in the voxel. Also, when we moving from the ideal condition  $\Delta \gg \delta$  to a more realistic  $\Delta \simeq \delta$  it is possible to observe an underestimation of the cylinder radius. The complete characterization of this behavior is beyond the scope of this paper. Figure 3 shows the values of the estimated mean diameter in a central coronal slice of HCP data for both MAPMRI and MT-MAPMRI. There are some little differences between the two techniques which are most probably due to the fact that in MT-MAPMRI the additional constraint of axially symmetric tensors is imposed for single fiber voxels, while MAPMRI uses classical DTI tensor. The corpus callosum (CC) presents an average apparent mean diameter of  $9.0 \mu\text{m}$  with both techniques (Fig. 4). The mean values in each section are higher than those reported in [1]. However, they are inline with those presented in [3]. This is due to different factors limiting the accuracy of the measure including partial volume effects. Fick et al. [5] were able to obtain a more accurate axon diameter estimation in CC but using a  $b_{max} = 10,000$  four shells acquisition, with 552 gradients.

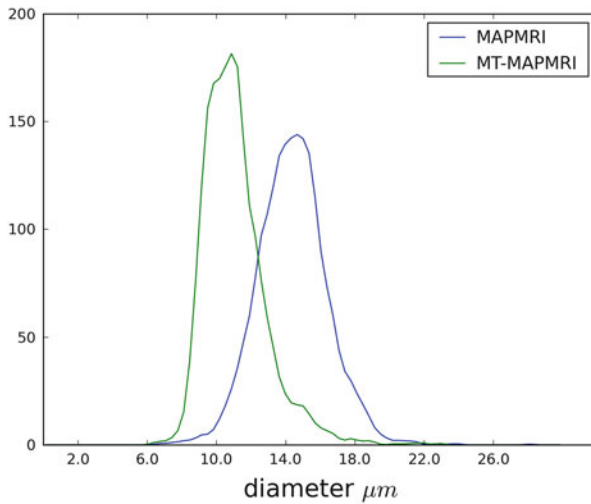
In the areas of crossings like the corona radiata (CR) MAPMRI diameter values ( $14.0 \mu\text{m}$  on average) are higher than the one obtained in the CC, in agreement with the results of the simulations showing that MAPMRI is prone to apparent mean diameter overestimation in case of crossing fibers. MT-MAPMRI values, on the contrary, are lower ( $10.4 \mu\text{m}$ ) and closer to those obtained in CC. The histogram of



**Fig. 3** Estimated diameter in one coronal slice of HCP in vivo data. As it is possible to observe MAPMRI (*left*) apparent mean diameter is higher in regions with crossing fibers, while MT-MAPMRI (*right*) estimated diameter appears steadier across the white matter



**Fig. 4** Estimated diameter in a corpus callosum ROI of HCP data



**Fig. 5** Profile of the histogram for the diameter estimation in white matter voxels for MPMRI (blue) and MT-MPMRI (green) for a slice of HCP brain

the white matter apparent mean diameter (Fig. 5) of MT-MPMRI shows that there is a higher number of voxels with low diameter with respect to the same histogram for MPMRI. This is due to the large amount of crossings present in brain white matter compared to pure single fiber voxels [8], highlighting the potential of MT-MPMRI in detecting white matter structural features in the presence of complex fiber topologies.

## 4 Conclusions

The apparent mean diameter for in vivo data is an index that is limited by three factors: (a) the compartments inside the voxel are not homogeneous, (b) the long diffusion time hypothesis is not verified, (c) the gradient strength used for in vivo studies is not high enough for characterizing small compartments [7]. Despite these limitations this index holds the potential to describe anomalies and peculiarities of the different brain tissues in vivo, in both pathological and healthy subjects. MT-MAPMRI expands the MAPMRI reconstruction technique adding the possibility to align the basis on multiple tensors if the voxel presents a high likelihood to contain more than one fiber bundles. This led to a better estimation of ODF and apparent mean diameter for such voxels, in both simulations and in-vivo data. The principal drawback of the technique is the fact that the fitting of multiple tensors is a non-linear problem with no easy solution. It can give unstable results (especially in the presence of noise) and that requires a longer computation time with respect to the single tensor (three seconds per voxel on an Intel Core I7-3610QM, 2.3 GHz). Future work will include the research of an improved and faster multi-tensor implementation, besides the complete characterization of MT-MAPMRI performance on an extended set of data and with respect to other state-of-the-art methods such as constrained spherical deconvolution and 3D-SHORE.

**Acknowledgements** Data were provided by the Human Connectome Project, WU-Minn Consortium (Principal Investigators: David Van Essen and Kamil Ugurbil; 1U54MH091657) funded by the 16 NIH Institutes and Centers that support the NIH Blueprint for Neuroscience Research; and by the McDonnell Center for Systems Neuroscience at Washington University.

## References

1. Aboitiz, F., Scheibel, A.B., Fisher, R.S., Zaidel, E.: Fiber composition of the human corpus callosum. *Brain Res.* **598**(12), 143–153 (1992)
2. Akaike, H.: Information theory and an extension of the maximum likelihood principle. In: Parzen, E., Tanabe, K., Kitagawa, G. (eds.) *Selected Papers of Hirotugu Akaike*. Springer Series in Statistics, pp. 199–213. Springer, New York (1998)
3. Alexander, D.C., Hubbard, P.L., Hall, M.G., Moore, E.A., Ptito, M., Parker, G.J., Dyrby, T.B.: Orientationally invariant indices of axon diameter and density from diffusion MRI. *NeuroImage* **52**(4), 1374–1389 (2010)
4. Basser, P., Mattiello, J., LeBihan, D.: Estimation of the effective self diffusion tensor from the nmr spin echo. *J. Magn. Reson.* **103**, 247–254 (1994)
5. Fick, R.H., Wassermann, D., Sanguinetti, G., Deriche, R.: Laplacian-regularized MAP-MRI: improving axonal caliber estimation. In: *International Symposium on Biomedical Imaging: From Nano to Macro*, Brooklyn, New York (April 2015). <https://hal.inria.fr/hal-01140021>
6. Fick, R.H., Zucchelli, M., Girard, G., Descoteaux, M., Menegaz, G., Deriche, R.: Using 3D-SHORE and MAP-MRI to obtain both tractography and microstructural contrast from a clinical DMRI acquisition. In: *International Symposium on Biomedical Imaging: From Nano to Macro*, Brooklyn, New York (April 2015)



7. Huang, S., Nummenmaa, A., Witzel, T., Duval, T., Cohen-Adad, J., Wald, L., McNab, J.: The impact of gradient strength on in vivo diffusion {MRI} estimates of axon diameter. *NeuroImage* **106**, 464–472 (2015). <http://www.sciencedirect.com/science/article/pii/S1053811914010003>
8. Jeurissen, B., Leemans, A., Tournier, J.D., Jones, D.K., Sijbers, J.: Investigating the prevalence of complex fiber configurations in white matter tissue with diffusion magnetic resonance imaging. *Hum. Brain Mapp.* **34**(11), 2747–2766 (2013). <http://dx.doi.org/10.1002/hbm.22099>
9. Landman, B., Bazin, P.L., Prince, J.: Diffusion tensor estimation by maximizing rician likelihood. In: IEEE 11th International Conference on Computer Vision, 2007. ICCV 2007, pp. 1–8 (October 2007)
10. Ozarslan, E., Koay, C., Shepherd, T., Blackband, S., Basser, P.: Simple harmonic oscillator based estimation and reconstruction for three-dimensional q-space MRI. *Proc. Int. Soc. Magn. Reson. Med.* **17**, 1396 (2009)
11. Ozarslan, E., Koay, C., Basser, P.: Simple harmonic oscillator based reconstruction and estimation for one-dimensional q-space magnetic resonance (1d-shore). In: Andrews, T.D., Balan, R., Benedetto, J.J., Czaja, W., Okoudjou, K.A. (eds.) *Excursions in Harmonic Analysis. Applied and Numerical Harmonic Analysis*, vol. 2, pp. 373–399. Birkhauser, Boston (2013)
12. Ozarslan, E., Koay, C., Shepherd, T., Komlosh, M., Irfanoglu, M., Pierpaoli, C., Basser, P.: Mean apparent propagator (map) MRI: a novel diffusion imaging method for mapping tissue microstructure. *NeuroImage* **78**, 16–32 (2013)
13. Scherrer, B., Warfield, S.: Why multiple b-values are required for multi-tensor models. evaluation with a constrained log-euclidean model. In: 2010 IEEE International Symposium on Biomedical Imaging: From Nano to Macro, pp. 1389–1392 (April 2010)
14. Sotiropoulos, S.N., Jbabdi, S., Xu, J., Andersson, J.L., Moeller, S., Auerbach, E.J., Glasser, M.F., Hernandez, M., Sapiro, G., Jenkinson, M., Feinberg, D.A., Yacoub, E., Lenglet, C., Essen, D.C.V., Ugurbil, K., Behrens, T.E.: Advances in diffusion {MRI} acquisition and processing in the human connectome project. *NeuroImage* **80**, 125–143 (2013). <http://www.sciencedirect.com/science/article/pii/S105381191300551X>. Mapping the Connectome
15. Zhang, H., Hubbard, P.L., Parker, G.J., Alexander, D.C.: Axon diameter mapping in the presence of orientation dispersion with diffusion {MRI}. *NeuroImage* **56**(3), 1301–1315 (2011)

# On the Use of Antipodal Optimal Dimensionality Sampling Scheme on the Sphere for Recovering Intra-Voxel Fibre Structure in Diffusion MRI

Alice P. Bates, Zubair Khalid, and Rodney A. Kennedy

**Abstract** In diffusion magnetic resonance imaging (dMRI), the diffusion signal can be reconstructed from measurements collected on single or multiple spheres in  $q$ -space using a spherical harmonic expansion. The number of measurements that can be acquired is severely limited and should be as small as possible. Previous sampling schemes have focused on using antipodal symmetry to reduce the number of samples and uniform sampling to achieve rotationally invariant reconstruction accuracy, but do not allow for an accurate or computationally efficient spherical harmonic transform (SHT). The recently proposed antipodal optimal dimensionality sampling scheme on the sphere requires the minimum number of samples, equal to the number of degrees of freedom for the representation of the antipodal symmetric band-limited diffusion signal in the spherical harmonic domain. In addition, it allows for the accurate and efficient computation of the SHT. In this work, we evaluate the use of this recently proposed scheme for the reconstruction of the diffusion signal and subsequent intra-voxel fibre structure estimation in dMRI. We show, through numerical experiments, that the use of this sampling scheme allows accurate and computationally efficient reconstruction of the diffusion signal, and improved estimation of intra-voxel fibre structure, in comparison to the antipodal electrostatic repulsion and spherical code sampling schemes with the same number of samples. We also demonstrate that it achieves rotationally invariant reconstruction accuracy to the same extent as the other two sampling schemes.

## 1 Introduction

Diffusion magnetic resonance imaging (dMRI) uses the intra-voxel diffusion characteristics of water molecules to determine the structure and connectivity of white matter in the brain. Diffusion signal measurements are collected on a single sphere

---

A.P. Bates (✉) • Z. Khalid • R.A. Kennedy  
Research School of Engineering, The Australian National University, Canberra, ACT 2601,  
Australia  
e-mail: [alice.bates@anu.edu.au](mailto:alice.bates@anu.edu.au); [zubair.khalid@anu.edu.au](mailto:zubair.khalid@anu.edu.au); [rodney.kennedy@anu.edu.au](mailto:rodney.kennedy@anu.edu.au)

or multiple spheres in  $q$ -space (known as  $q$ -shells) [8, 9]. The reconstruction of the diffusion signal on a sphere from these measurements is carried out by expanding the signal in terms of spherical harmonics [12, 14]. By choosing a sufficiently large band-limit in the spherical harmonic degree,  $L$ , the diffusion signal can be represented in terms of a finite number of coefficients in the spectral domain, enabled by spherical harmonic transform (SHT) [16]. Various techniques proposed in the literature for estimating the intra-voxel fibre structure in dMRI use the diffusion signal spherical harmonic coefficients, such as Q-ball imaging in constant solid angle (QBI<sub>CSA</sub>) [1, 11].

In order to facilitate accurate and fast estimation of fibre structure, a sampling scheme must support accurate and efficient computation of the SHT. It is also important that the scheme require as few measurements as possible in order to reduce scan times [2, 19]. Furthermore as fibre populations may assume any orientation within a voxel, the accuracy of the reconstruction of the diffusion signal should not change significantly if the diffusion signal (or sampling scheme) is rotated [7, 8]. As dMRI is an inherently noisy imaging technique, reconstruction should also be robust to noise [10].

**Novel Sampling Scheme** Many sampling schemes used in dMRI focus on uniform sampling on the sphere to achieve rotationally invariant reconstruction accuracy and antipodally symmetric sampling grids to reduce the number of samples, but do not consider accurate and efficient computation of the SHT [7, 8, 15]. Recently, the antipodal optimal dimensionality sampling scheme on the sphere [3] has been proposed for the reconstruction of antipodal symmetric signals. This scheme enables a SHT which is more computationally efficient than the other sampling schemes that use the least squares (LS) method of SHT computation, as we show later in the paper. It also requires the minimum number of samples, given by the degrees of freedom required to represent the antipodal symmetric signal in the spectral domain, for accurate computation of SHT of the signal.

The widely used antipodal electrostatic repulsion sampling scheme (ESR) [15] can be used with the minimum number of samples, however it does not allow accurate reconstruction of the diffusion signal with this number of points, as we later demonstrate in the paper. The sampling scheme [7] generalises the ESR scheme to multiple  $q$ -shells and reduces to the ESR scheme for a single  $q$ -shell. The ESR scheme is also extended to 3D  $q$ -space sampling in [17] and a generalised metric is defined. For single-shell  $q$ -space sampling, the energy measure used in ESR is suitable [17]. The scheme [8] is another scheme with a uniformly and antipodally symmetric distributing of samples on the sphere, it generalises the spherical code (SC) formulation (minimum angular distance between samples) to multiple shells and can be formed for any number of samples.

We note that the sampling scheme [6] uses spherical design to enable the accurate computation of the SHT, and has a uniform and antipodally symmetric arrangement of samples, however it requires more than the minimum number of samples. The equiangular sampling scheme proposed in [9] has an accurate and efficient SHT but requires approximately four times the minimum number of samples.

**Contributions** In this work, we evaluate the antipodal optimal dimensionality sampling scheme for estimating the intra-voxel fibre structure in dMRI. We address whether the sampling scheme: (a) enables the accurate reconstruction of the diffusion signal on the sphere and consequently improves estimation of fibre structure within each voxel, (b) has a reconstruction accuracy that does not vary significantly with rotation and (c) is computationally efficient.

In order to answer these questions, we evaluate the antipodal optimal dimensionality sampling scheme against other single  $\mathbf{q}$ -shell sampling schemes that can be used with the minimum number of samples; we analyse the reconstruction of the diffusion signal and the intra-voxel fibre structure estimation using  $\text{QBI}_{\text{CSA}}$  from measurements of the diffusion signal taken over the antipodal optimal dimensionality, ESR and SC sampling schemes. We demonstrate that the acquisition of measurements over the antipodal optimal dimensionality sampling scheme allows accurate and computationally efficient reconstruction of the diffusion signal, and better estimation of intra-voxel structure in dMRI.

## 2 Materials and Methods

### 2.1 Diffusion Signal on Sphere

Let the diffusion weighted signal at a fixed  $\mathbf{q}$ -space radius (or fixed diffusion weighting,  $b$ ) be denoted by  $S(\theta, \phi; b)$ , where the angles co-latitude  $\theta \in [0, \pi]$  and longitude  $\phi \in [0, 2\pi)$  parameterise a point  $\mathbf{u}(\theta, \phi) = (\sin \theta \cos \phi, \sin \theta \sin \phi, \cos \theta)'$  on the sphere  $\mathbb{S}^2$ .

The spherical harmonic functions (or spherical harmonics for short), denoted by  $Y_\ell^m(\theta, \phi)$  and defined for integer degree  $\ell \geq 0$  and integer order  $|m| \leq \ell$ , form a complete basis for the space of signals defined on the sphere. Since  $S(\theta, \phi; b)$  is antipodal symmetric, with  $S(\theta, \phi; b) = S(\pi - \theta, \phi + \pi; b)$  and  $Y_\ell^m(\theta, \phi) = Y_\ell^m(\pi - \theta, \pi + \phi)$  for even  $\ell$  and  $Y_\ell^m(\theta, \phi) = -Y_\ell^m(\pi - \theta, \pi + \phi)$  for odd  $\ell$ , the expansion of  $S(\theta, \phi; b)$  in the spherical harmonic basis only includes even degree spherical harmonics, that is,

$$S(\theta, \phi; b) = \sum_{\substack{\ell=0 \\ \ell \text{ even}}}^{L-1} \sum_{m=-\ell}^{\ell} (S)_\ell^m(b) Y_\ell^m(\theta, \phi), \quad L \text{ odd}, \quad (1)$$

where  $L$  represents the band-limit that depends on the  $b$ -value [9, 19], and  $(S)_\ell^m(b)$  denotes the spherical harmonic coefficient of degree  $\ell$  and order  $m$ , which is calculated using the SHT, given by

$$(S)_\ell^m(b) \triangleq \int_{\mathbb{S}^2} S(\theta, \phi; b) \overline{Y_\ell^m(\theta, \phi)} \sin \theta \, d\theta \, d\phi. \quad (2)$$

The spherical harmonic coefficients  $(S)_\ell^m(b)$  form the spectral domain representation of  $S(\theta, \phi; b)$ . In practise, (2) has to be calculated numerically; there exist sampling schemes, such as [3], that enable algorithms for accurately calculating the SHT (see [18] for a comprehensive review). For other schemes, such as [8] and [15],  $(S)_\ell^m(b)$  can also be calculated using LS where (1) is written as a system of linear equations.

The reconstruction of the signal  $S(\theta, \phi; b)$  from its spherical harmonic coefficients, as given in (1), is referred to as the inverse SHT. The diffusion signal is assumed to be band-limited at degree  $L$  such that  $(S)_\ell^m(b) = 0$  for  $\ell \geq L$ ; if this assumption does not hold, there is a truncation error.

**Diffusion-Weighted Data Synthesis** We use the commonly used Gaussian mixture model [2, 10] to obtain a diffusion weighted dataset. The diffusion weighted signal model for a voxel is given by

$$S(\theta, \phi; b) = S_0 \sum_{k=1}^M f_k e^{-bu(\theta, \phi)^T \mathbf{D}_k u(\theta, \phi)}, \quad (3)$$

where  $S_0$  is the baseline image at  $b = 0$ ,  $M$  is the number of fibres, the volume fractions  $f_k$  of each fibre population are normalized to ensure that  $\sum_{k=1}^M f_k = 1$  and  $\mathbf{D}_k$  is the diffusion tensor for the  $k$ th fibre in the voxel. Each fibre's tensor is computed from a rotated version of a tensor,  $\mathbf{D} = \text{diag}(\lambda_1, \lambda_2, \lambda_3)$ , with  $\mathbf{D}_k = \mathbf{R}_k^T \mathbf{D} \mathbf{R}_k$ , where  $\lambda_1$  is the diffusivity along the main axis of a fibre while  $\lambda_2$  and  $\lambda_3$  are the diffusivities in the plane perpendicular to it, and  $\mathbf{R}_k$  is the rotation matrix that rotates the  $k$ th fibre to the direction of the  $k$ th fibre population.

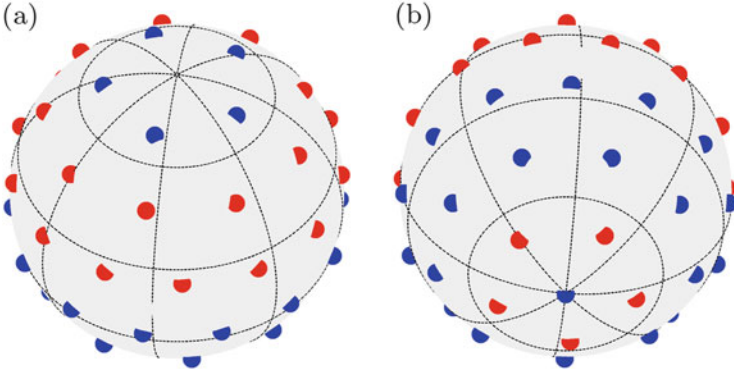
In the numerical experiments where the effect of noise is considered, we add Rician noise to the diffusion weighted signal as [13]

$$S(\theta, \phi; b)_n = \sqrt{(S(\theta, \phi; b) + \eta_1)^2 + \eta_2^2}, \quad (4)$$

with  $\eta_1, \eta_2 \sim \mathcal{N}(0, \sigma^2)$  and  $\sigma = S_0/\text{SNR}$ . The signal-to-noise ratio (SNR) controls the level of noise on the baseline image, assumed to be  $S_0 = 1$  [10].

## 2.2 Antipodal Optimal Dimensionality Sampling Scheme

The antipodal optimal dimensionality sampling scheme [3], which we denote by  $\mathfrak{S}_O(N_O)$  where  $N_O = L(L + 1)/2$ , has an iso-latitude sampling grid with  $L$  iso-latitude rings placed in antipodal pairs at  $[0, \dots, \pi - \theta_{L-3}, \theta_{L-3}, \pi - \theta_{L-1}, \theta_{L-1}]$ ,  $L$  odd and equiangular sampling along longitude with the points placed so that the samples in ring  $\theta_n$  are antipodal to those in ring  $\theta_{n-1}$  (Fig. 1 shows  $\mathfrak{S}_O(28)$  which has  $L = 7$  rings). The antipodal nature of  $\mathfrak{S}_O(N_O)$  means that measurements only need to be taken over the rings  $\theta_n$  for  $n = 0, 2, \dots, L - 1$ ; the value of the diffusion signal over the remaining points can be determined using the antipodal symmetry of the diffusion signal.



**Fig. 1** The antipodal optimal dimensionality sampling scheme for  $L = 7$ ,  $\mathfrak{S}_O(28)$ . (a) North and (b) south pole view. Points where measurements are taken are shown in *blue* and points where antipodal symmetry is used to evaluate  $S(\theta, \phi; b)$  are shown in *red*

The number of measurements required by this scheme is  $N_O$ , which is the minimum number of samples attainable by any sampling scheme as there are  $N_O$  degrees of freedom required to represent the antipodal band-limited signal in the spectral domain [as can be seen from Eq. (1)]. More details of  $\mathfrak{S}_O(N_O)$ , including the precise location of samples, can be found in [3]. The design of  $\mathfrak{S}_O(N_O)$  enables a SHT (described in [3]) which is accurate and efficient, unlike other schemes that focus on uniform sampling of the sphere which use LS.

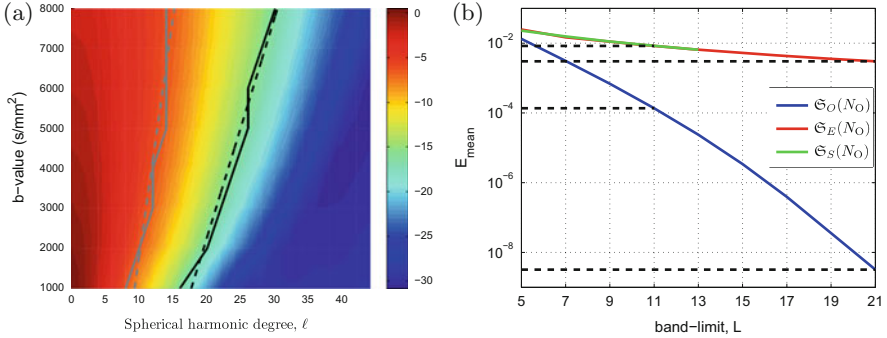
### 3 Diffusion Signal Reconstruction

In this section, we analyse the reconstruction of the diffusion signal from its samples taken over  $\mathfrak{S}_O(N_O)$ . We obtain a diffusion weighted dataset using the diffusion signal model (3), with  $\lambda_1 = 1.7 \times 10^{-3} \text{ mm}^2/\text{s}$  and  $\lambda_2 = \lambda_3 = 0.3 \times 10^{-3} \text{ mm}^2/\text{s}$  which are values typically observed in the human brain [5].

#### 3.1 Evaluation of Band-Limit of Diffusion Signal

It has been demonstrated that  $\mathfrak{S}_O(N_O)$  allows accurate computation of the SHT of any band-limited antipodal symmetric signal on the sphere in [3]; we therefore evaluate whether the assumption that the diffusion signal is band-limited holds. In order to study the band-limit of the diffusion signal, we define the per-degree energy spectrum  $P(b, \ell)$  of the diffusion signal (3) as

$$P(b, \ell) \triangleq \sum_{m=-\ell}^{\ell} |(S)_{\ell}^m(b)|^2, \quad (5)$$



**Fig. 2** (a) Per-degree energy spectrum  $P(b, \ell)$  (5), is plotted as  $\log_{10} P(b, \ell)$  for  $0 \leq \ell < 45$ ,  $\ell$  odd and  $1000 \leq b \leq 8000$  s/mm<sup>2</sup>. Black and grey lines indicate where  $P(b, \ell)$  drops below  $10^{-15}$  and  $10^{-6}$  respectively, and dashed lines show linear relationship between  $b$  and  $L$ . (b) Mean reconstruction error  $E_{\text{mean}}$  for  $5 \leq L \leq 21$  for  $\mathfrak{S}_O(N_O)$ ,  $\mathfrak{S}_E(N_O)$  and  $\mathfrak{S}_S(N_O)$

which is plotted for  $1000 \leq b \leq 8000$  s/mm<sup>2</sup> and  $0 \leq \ell \leq 45$  in Fig. 2a, where it can be observed that the energy spectrum  $P(b, \ell)$  decreases gradually with the increase in spherical harmonic degree  $\ell$ .

The threshold lines on the surface plot in Fig. 2a for which  $P(b, \ell)$  drops below  $10^{-15}$  (black) and  $10^{-6}$  (grey) can guide us in choosing the band-limit of the diffusion signal. For example,  $L = 21$  and  $L = 11$  for  $b = 3000$  s/mm<sup>2</sup> as indicated by black and grey line, respectively. For  $L = 21$ , we require  $N_O = 231$  samples, which may be too large as it is common for around 60 samples to be taken at  $b = 3000$  s/mm<sup>2</sup> [10]. For  $L = 11$ , we need  $N_O = 66$  samples. Using a smaller  $L$  (larger threshold) means less samples are required but will result in a larger truncation error, as we demonstrate in the next section.

The approximately linear relationship between  $b$  and  $L$  is indicated by dashed lines in Fig. 2a. Figure 2a shows  $P(b, \ell)$  for a synthetic diffusion signal obtained from (3) with  $M = 2$  fibres and a crossing angle of  $25^\circ$ , however we observed insignificant variation in  $P(b, \ell)$  for different  $M$  and fibre orientations.

### 3.2 Reconstruction Accuracy

In order to evaluate whether  $\mathfrak{S}_O(N_O)$  allows for the accurate reconstruction of  $S(\theta, \phi; b)$ , we compare it with the ESR scheme [15] composed of  $N_O$  samples, denoted by  $\mathfrak{S}_E(N_O)$  and the SC scheme [8] composed of  $N_O$  samples, denoted by  $\mathfrak{S}_S(N_O)$ .<sup>1</sup> In order to compute the SHT of a signal from its samples taken

<sup>1</sup>The best known solutions of the SC problem [8] are available at <http://neilsloane.com/grass/dim3/> for up to 100 antipodal pairs, hence we are only able to show results obtained using SC for  $L < 15$  ( $N_O = 91$ ) in this paper.

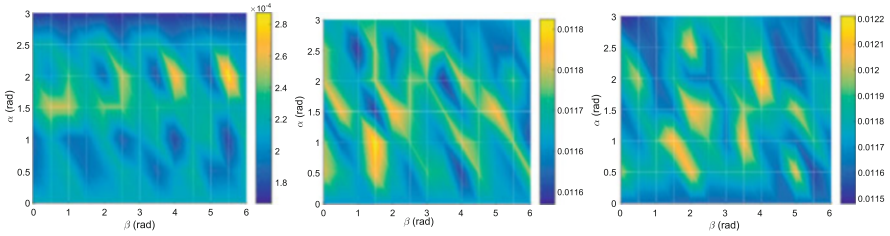
over  $\mathfrak{S}_E(N_O)$  and  $\mathfrak{S}_S(N_O)$ , regularised LS is used with regularisation parameter  $\lambda = 0.006$  (used in [11, 20]) to improve the condition number of the matrix involved in the computation of the SHT. Due to space constraints, here and in the rest of the paper we only show results for  $b = 3000 \text{ s/mm}^2$ , which is commonly used to obtain  $S(\theta, \phi)$  measurements [10].

We conduct the following experiment to determine the reconstruction accuracy. For a given  $b$ -value, synthetic measurements of the diffusion signal, using (3), are first obtained over the sampling grid  $\mathfrak{S}_O(N_O)$  or  $\mathfrak{S}_E(N_O)$  or  $\mathfrak{S}_S(N_O)$ . The spherical harmonic coefficients  $(S)_\ell^m(b)$  are then calculated using the SHT proposed in [3] or the regularised LS method [11]. Finally, the spherical harmonic coefficients  $(S)_\ell^m(b)$  are used to reconstruct the diffusion signal over a high resolution uniform grid (consisting of 2562 points which are the vertices of a fourth-order icosahedron). We analyse the mean reconstruction error,  $E_{\text{mean}} \triangleq \text{mean}(|S_A(\theta, \phi; b) - S_r(\theta, \phi; b)|)$ , between the reconstructed and analytical value of the diffusion signal calculated over the 2562 points.

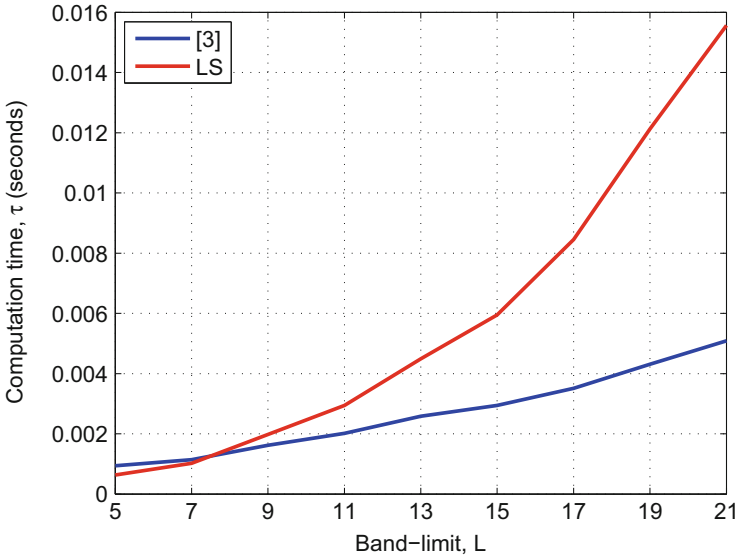
The mean reconstruction error  $E_{\text{mean}}$  for band-limits  $5 \leq L \leq 21$  is shown in Fig. 2b, where it is evident that taking measurements over  $\mathfrak{S}_O(N_O)$ , in comparison to  $\mathfrak{S}_E(N_O)$  and  $\mathfrak{S}_S(N_O)$ , enables significantly more accurate reconstruction of the diffusion signal. For example at  $L = 21$  ( $N_O = 231$ ), the mean error  $E_{\text{mean}}$  is on the order of  $10^{-9}$  and  $10^{-4}$  for  $\mathfrak{S}_O(N_O)$  and  $\mathfrak{S}_E(N_O)$  respectively, while at  $L = 11$  ( $N_O = 66$ ), it is on the order of  $10^{-4}$  for  $\mathfrak{S}_O(N_O)$ , and  $10^{-2}$  for  $\mathfrak{S}_E(N_O)$  and  $\mathfrak{S}_S(N_O)$ . Figure 2b shows  $E_{\text{mean}}$  for a synthetic diffusion signal obtained from (3) with  $M = 2$  fibres and a crossing angle of  $25^\circ$  as in Sect. 3.1, however we again observed insignificant variation in  $E_{\text{mean}}$  for different  $M$  and fibre orientations. In summary, the use of the sampling scheme  $\mathfrak{S}_O(N_O)$  greatly reduces the diffusion signal reconstruction error compared with  $\mathfrak{S}_E(N_O)$  and  $\mathfrak{S}_S(N_O)$ .

**Rotational Invariance**  $\mathfrak{S}_E(N_O)$  and  $\mathfrak{S}_S(N_O)$  focus on uniform sampling of the sphere to ensure rotationally invariant reconstruction accuracy [8, 15], that is the accuracy of reconstruction does not significantly vary if the diffusion signal (or sampling scheme is rotated) [7].  $\mathfrak{S}_O(N_O)$  is not uniform by design, however, it does not have dense sampling on any region of the sphere. For all three sampling schemes  $\mathfrak{S}_O(N_O)$ ,  $\mathfrak{S}_E(N_O)$  and  $\mathfrak{S}_S(N_O)$ , we analyse the rotational invariance of the reconstruction accuracy; we change the orientation of a fibre centered at  $z$ -axis by rotating the fibre by  $\beta \in [0, \pi]$  around  $y$ -axis and then by  $\alpha \in [0, 2\pi]$  around  $x$ -axis, and compute the mean reconstruction error  $E_{\text{mean}}$  for different orientations/rotations. In Fig. 3a–c it can be observed that the mean error  $E_{\text{mean}}$  does not change significantly for any of the schemes (the reconstruction error remains on the order of  $10^{-4}$  for  $\mathfrak{S}_O(N_O)$ , and on the order of  $10^{-2}$  for  $\mathfrak{S}_E(N_O)$  and  $\mathfrak{S}_S(N_O)$  for all rotations), showing that all schemes enable rotationally invariant reconstruction accuracy to the same extent.





**Fig. 3** Mean reconstruction error  $E_{\text{mean}}$  varies insignificantly for different fibre orientations, given by  $\alpha \in [0, \pi]$  and  $\beta \in (0, 2\pi]$ , for (a)  $\mathfrak{S}_O(66)$ , (b)  $\mathfrak{S}_E(66)$  and (c)  $\mathfrak{S}_S(66)$



**Fig. 4** The computation time  $\tau$  in seconds for the SHT in [3] and for LS to compute the spherical harmonic coefficients of the diffusion signal for  $5 \leq L \leq 21$

### 3.3 Computation Time

We investigate the computational complexity of the SHT of  $\mathfrak{S}_O(N_O)$  [3] compared to the LS method of SHT computation employed by  $\mathfrak{S}_E(N_O)$  and  $\mathfrak{S}_S(N_O)$  by measuring the time it takes for both methods to calculate the spherical harmonic coefficients of the diffusion signal for band-limits  $5 \leq L \leq 21$ . It can be seen in Fig. 4 that for  $L > 7$ , [3] allows for faster computation of the SHT and that the time taken by the LS method increases much faster with  $L$ ; this is due to the computational complexity of the LS being  $O(L^6)$  while the SHT proposed in [3] has asymptotic complexity  $O(L^4)$  [3]. Hence,  $\mathfrak{S}_O(N_O)$  allows for a SHT which is significantly more efficient compared with the LS method of SHT used by  $\mathfrak{S}_E(N_O)$  and  $\mathfrak{S}_S(N_O)$ .

## 4 Application: Intra-Voxel Fibre Structure Estimation Using $\text{QBI}_{\text{CSA}}$

In this section, we show that the acquisition of diffusion signal measurements over  $\mathfrak{S}_O(N_O)$  allows accurate estimation of the intra-voxel structure in dMRI. In our analysis, we use  $\text{QBI}_{\text{CSA}}$  [1],<sup>2</sup> one of the intra-voxel structure estimation techniques that uses the spherical harmonic coefficients of the diffusion signal, that has been compared in the 2012 High Angular Resolution Diffusion (HARDI) Reconstruction Challenge [11]. We use the structured field testing data set,<sup>3</sup> that consists of 1280 voxels, where each voxel is constructed using the diffusion signal model given in (3) (see [10] for the values of parameters). To compare the performance of  $\mathfrak{S}_O(N_O)$  with  $\mathfrak{S}_E(N_O)$  and  $\mathfrak{S}_S(N_O)$  we use the following two metrics: success rate (SR) defined as the percentage of voxels in which the correct number of fibre populations are detected and mean average angular error per voxel, denoted by  $\text{mean}(\bar{\theta})$ , defined as the average error between the estimated fibre directions and the true ones in each voxel, averaged over all voxels.

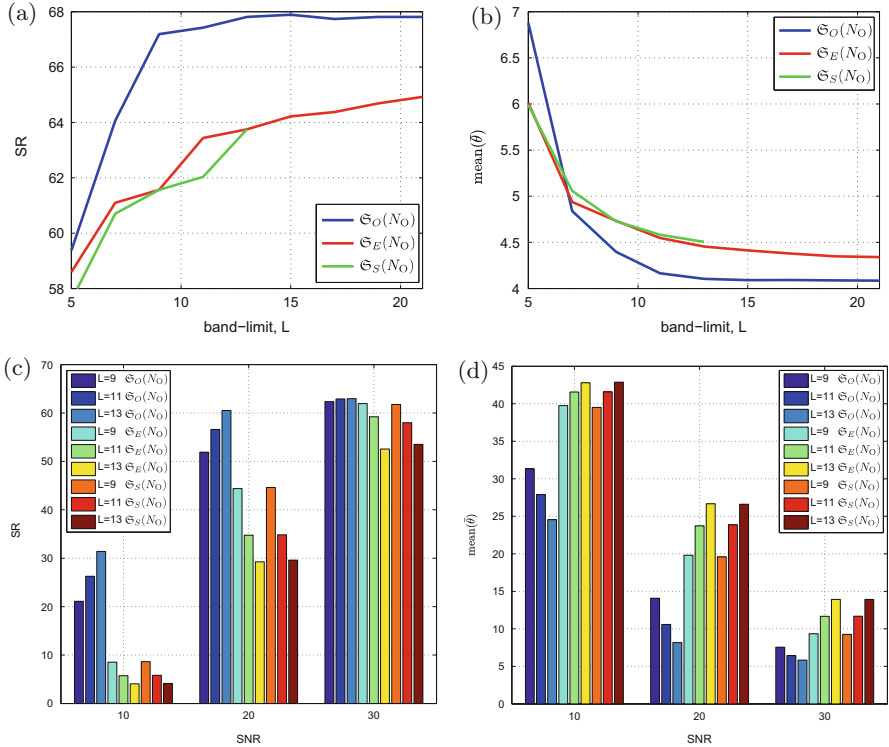
**Noise Free** We have plotted the performance metrics, SR and  $\text{mean}(\bar{\theta})$ , Fig. 5a, b for noise free measurements obtained using  $\mathfrak{S}_O(N_O)$ ,  $\mathfrak{S}_E(N_O)$  and  $\mathfrak{S}_S(N_O)$ . It is evident that the higher diffusion signal reconstruction accuracy of  $\mathfrak{S}_O(N_O)$ , compared with  $\mathfrak{S}_E(N_O)$  and  $\mathfrak{S}_S(N_O)$ , results in a higher SR and lower  $\text{mean}(\bar{\theta})$ . In the absence of noise,  $\mathfrak{S}_O(N_O)$  therefore enables more accurate intra-voxel fibre structure estimation compared with  $\mathfrak{S}_E(N_O)$  and  $\mathfrak{S}_S(N_O)$ .

**With Noise** We use 2012 HARDI Challenge Data with SNR = 10, 20 and 30 (4) to evaluate the intra-voxel fibre structure estimation performance of  $\mathfrak{S}_O(N_O)$  used with  $\text{QBI}_{\text{CSA}}$  in the presence of noise. The regularisation parameter in LS used for  $\mathfrak{S}_E(N_O)$  and  $\mathfrak{S}_S(N_O)$  filters the noise [11]. For  $\mathfrak{S}_O(N_O)$ , we use a Gaussian kernel given by  $e^{-\ell(\ell+1)t}$  [4], with parameter  $t = 0.032$  (empirically chosen to maximise SR), to low pass filter the noisy signal. More sophisticated filtering techniques that take into account the noise statistics is future work.

Figure 5c, d show the SR and  $\text{mean}(\bar{\theta})$  respectively for different SNR averaged over 10 realisations of the noise for  $\mathfrak{S}_O(N_O)$ ,  $\mathfrak{S}_E(N_O)$  and  $\mathfrak{S}_S(N_O)$  for  $L = 9, 11, 13$  ( $N_O = 45, 66, 91$ ), which are typical numbers for single-shell sampling).  $\mathfrak{S}_O(N_O)$  has a higher SR and lower  $\text{mean}(\bar{\theta})$  than  $\mathfrak{S}_E(N_O)$  and  $\mathfrak{S}_S(N_O)$  for all SNR, demonstrating that the estimation of fibre structure from noisy measurements taken over  $\mathfrak{S}_O(N_O)$  is more accurate.

<sup>2</sup>The orientation distribution function (ODF) peaks are extracted using finite differences over a 724 point grid mesh as in [11].

<sup>3</sup>Available at [http://hardi.epfl.ch/static/events/2012\\_ISBI/](http://hardi.epfl.ch/static/events/2012_ISBI/).



**Fig. 5** Fibre reconstruction metrics, **(a)** SR and **(b)**  $\text{mean}(\bar{\theta})$ , obtained by sampling over  $\mathfrak{S}_O(N_O)$ ,  $\mathfrak{S}_E(N_O)$  and  $\mathfrak{S}_S(N_O)$  for  $5 \leq L \leq 21$  in the absence of noise. **(c)** SR and **(d)**  $\text{mean}(\bar{\theta})$  for  $L = 9, 11$  and  $13$ , and SNR = 10, 20 and 30, and sampling schemes  $\mathfrak{S}_O(N_O)$ ,  $\mathfrak{S}_E(N_O)$  and  $\mathfrak{S}_S(N_O)$

## 5 Conclusions

In this work, we have evaluated the antipodal optimal dimensionality sampling scheme on the sphere for the reconstruction of the diffusion signal and subsequent intra-voxel structure estimation in dMRI. Unlike other schemes in the literature, this scheme allows for the accurate and efficient computation of the SHT with the minimum number of measurements. The antipodal optimal dimensionality scheme achieved a greater diffusion signal reconstruction and intra-voxel fibre structure estimation accuracy in the absence and presence of noise, in comparison to the antipodal electrostatic repulsion and spherical code sampling schemes when the minimum number of samples were used. It has also been shown that all three schemes give rotationally invariant reconstruction accuracy to the same extent. Extension of the work to multiple  $q$ -shell sampling and the analysis of the scheme with real data is being carried out.

## References

1. Aganj, I., Lenglet, C., Sapiro, G., Yacoub, E., Ugurbil, K., Harel, N.: Reconstruction of the orientation distribution function in single- and multiple-shell Q-ball imaging within constant solid angle. *Magn. Reson. Med.* **64**(2), 554–566 (2010)
2. Assemlal, H.E., Tschumperlé, D., Brun, L.: Evaluation of q-space sampling strategies for the diffusion magnetic resonance imaging. In: *Medical Image Computing and Computer-Assisted Intervention - MICCAI'2009*, London, vol. 12, pp. 406–414 (2009)
3. Bates, A.P., Khalid, Z., Kennedy, R.A.: An optimal dimensionality sampling scheme on the sphere for antipodal signals in diffusion magnetic resonance imaging. Arxiv preprint physics.med-ph/1502.07099 presented at ICASSP'2015 (2015)
4. Bülow, T.: Multiscale image processing on the sphere. In: *Proceedings of the 24th DAGM Symposium on Pattern Recognition*, London, pp. 609–617 (2002)
5. Canales-Rodríguez, E.J., Melie-García, L., Iturria-Medina, Y.: Mathematical description of q-space in spherical coordinates: exact Q-ball imaging. *Magn. Reson. Med.* **61**(6), 1350–1367 (2009)
6. Caruyer, E., Deriche, R.: A computational framework for experimental design in diffusion MRI. In: *MICCAI Workshop on Computational Diffusion MRI, CDMRI'2012*, Nice (October 2012)
7. Caruyer, E., Lenglet, C., Sapiro, G., Deriche, R.: Design of multishell sampling schemes with uniform coverage in diffusion MRI. *Magn. Reson. Med.* **69**(6), 1534–1540 (2013)
8. Cheng, J., Shen, D., Yap, P.T.: Designing single- and multiple-shell sampling schemes for diffusion MRI using spherical code. In: *Medical Image Computing and Computer-Assisted Intervention - MICCAI'2014*, Boston, MA, vol. 8675, pp. 281–288 (2014)
9. Daducci, A., McEwen, J.D., Ville, D.V.D., Thiran, J.P., Wiaux, Y.: Harmonic analysis of spherical sampling in diffusion MRI. In: *Proceedings of 19th Annual Meeting of the International Society for Magnetic Resonance Medicine* (June 2011)
10. Daducci, A., Canales-Rodríguez, E.J., Descoteaux, M., Garyfallidis, E., Gur, Y., Lin, Y.C., Mani, M., Merlet, S., Paquette, M., Ramirez-Manzanares, A., Reisert, M., Reis Rodrigues, P., Sepelband, F., Caruyer, E., Choupan, J., Deriche, R., Jacob, M., Menegaz, G., Prčkovska, V., Rivera, M., Wiaux, Y., Thiran, J.P.: Quantitative comparison of reconstruction methods for intra-voxel fiber recovery from diffusion MRI. *IEEE Trans. Med. Imag.* **33**(2), 384–399 (2014)
11. Descoteaux, M., Boré, A.: Testing classical single-shell HARDI techniques. In: *Proceedings of the 2012 ISBI Diffusion MRI Reconstruction Contest/Workshop*, Barcelona, p. 5 (2012)
12. Descoteaux, M., Angelino, E., Fitzgibbons, S., Deriche, R.: Regularized, fast, and robust analytical Q-ball imaging. *Magn. Reson. Med.* **58**(3), 497–510 (2007)
13. Gudbjartsson, H., Patz, S.: The rician distribution of noisy MRI data. *Magn. Reson. Med.* **34**(6), 910–914 (1995)
14. Hess, C.P., Mukherjee, P., Han, E.T., Xu, D., Vigneron, D.B.: Q-ball reconstruction of multimodal fiber orientations using the spherical harmonic basis. *Magn. Reson. Med.* **56**(1), 104–117 (2006)
15. Jones, D.K., Horsfield, M.A., Simmons, A.: Optimal strategies for measuring diffusion in anisotropic systems by magnetic resonance imaging. *Magn. Reson. Med.* **42**(3), 515–525 (1999)
16. Kennedy, R.A., Sadeghi, P.: *Hilbert Space Methods in Signal Processing*. Cambridge University Press, Cambridge (2013)
17. Knutsson, H., Westin, C.F.: Tensor metrics and charged containers for 3d q-space sample distribution. In: *Medical Image Computing and Computer-Assisted Intervention - MICCAI'2013*, Nagoya, vol. 16, pp. 679–86 (September 2013)
18. McEwen, J.D., Wiaux, Y.: A novel sampling theorem on the sphere. *IEEE Trans. Signal Process.* **59**(12), 5876–5887 (2011)

19. Tournier, J.D., Calamante, F., Connelly, A.: Determination of the appropriate b value and number of gradient directions for high-angular-resolution diffusion-weighted imaging. *NMR Biomed.* **26**(12), 1775–1786 (2013)
20. Wilkins, B., Lee, N., Rajagopalan, V., Law, M., Leporé, N.: Effect of data acquisition and analysis method on fiber orientation estimation in diffusion MRI. In: Schultz, T., Nedjati-Gilani, G., Venkataraman, A., O'Donnell, L., Panagiotaki, E. (eds.) *Computational Diffusion MRI and Brain Connectivity: MICCAI Workshops, Nagoya, 22 September 2013*, pp. 13–24. Springer, Cham (2014)

# Estimation of Fiber Orientations Using Neighborhood Information

Chuyang Ye, Jiachen Zhuo, Rao P. Gullapalli, and Jerry L. Prince

**Abstract** Diffusion magnetic resonance imaging (dMRI) has been used to noninvasively reconstruct fiber tracts. Fiber orientation (FO) estimation is a crucial step in the reconstruction, especially in the case of crossing fibers. In FO estimation, it is important to incorporate spatial coherence of FOs to reduce the effect of noise. In this work, we propose a method of FO estimation using neighborhood information. The diffusion signal is modeled by a fixed tensor basis. The spatial coherence is enforced in weighted  $\ell_1$ -norm regularization terms, which contain the interaction of directional information between neighbor voxels. Data fidelity is ensured by the agreement between raw and reconstructed diffusion signals. The resulting objective function is solved using a block coordinate descent algorithm. Experiments were performed on a digital crossing phantom, ex vivo tongue dMRI data, and in vivo brain dMRI data for qualitative and quantitative evaluation. The results demonstrate that the proposed method improves the quality of FO estimation.

## 1 Introduction

Diffusion magnetic resonance imaging (dMRI) has been used to noninvasively reconstruct fiber tracts by imaging the anisotropy of water diffusion in tissue [11]. A major topic in dMRI is the estimation of fiber orientations (FOs), especially

---

C. Ye (✉)

Brainnetome Center, Institute of Automation, Chinese Academy of Sciences, Beijing, China

Department of Electrical and Computer Engineering, Johns Hopkins University, Baltimore, MD, USA

e-mail: [chuyang.ye@nlpr.ia.ac.cn](mailto:chuyang.ye@nlpr.ia.ac.cn)

J. Zhuo • R.P. Gullapalli

Department of Radiology, University of Maryland School of Medicine, Baltimore, MD, USA

J.L. Prince

Department of Electrical and Computer Engineering, Johns Hopkins University, Baltimore, MD, USA

in situations where fibers cross. For example, constrained spherical deconvolution [17],  $q$ -ball reconstruction [6], multi-tensor models [3, 10, 20], and spherical ridgelet models [13] have been proposed to estimate crossing FOs.

Successful resolution of crossing FOs may require a large number of diffusion gradient directions, which takes a long acquisition time and limits the use in clinical practice [4]. To reduce the required number of gradient directions, with the assumption that the number of FOs in a voxel is small, methods have been proposed to model the diffusion signals using a basis and solve the FO estimation with sparsity regularization [5, 10, 12, 13, 15, 20]. For example, the basis can be diffusion tensors [5, 10, 15, 20], spherical ridgelets [13], or spherical polar Fourier basis [12].

Besides sparsity assumption, it is also important to consider spatial coherence of FOs to reduce the effect of noise and improve FO estimation. For example, in [2] the diffusion weighted images (DWIs) are smoothed before FO estimation whereas in [16] smoothing of FOs is performed after FO estimation. Several works have placed spatial regularization of tensors on the multi-tensor model to estimate FOs, but the sparsity assumption was not used [7, 14]. There are also methods that have combined spatial continuity with sparsity and seek to simultaneously estimate and smooth FOs. In [13], the TV-norm of DWIs is incorporated in the objective function for FO estimation. In [15] and [20], spatial consistency of FOs is enforced by adding the smoothness of the mixture fraction of each basis tensor as regularization terms in the FO estimation. However, in [15] and [20], the FO coherence is ensured in a relatively indirect way in the sense that directional information in FOs is not explicitly modeled in the objective functions. FO estimation incorporating both sparsity and spatial coherence is still an open problem.

In this work, we propose a method of FO estimation using both sparsity assumption and neighborhood information. The diffusion signal is modeled by a fixed tensor basis. In contrast to previous works, we directly incorporate the directional information in the neighborhood into the objective function to encode spatial coherence. Spatial coherence and sparsity are enforced in weighted  $\ell_1$ -norm regularization terms, which contain the interaction of directional information between neighbor voxels. Data fidelity is ensured by the agreement between raw and reconstructed diffusion weighted signals. The resulting objective function is solved using a block coordinate descent algorithm. Experiments were performed on a digital crossing phantom, ex vivo tongue dMRI data, and in vivo brain dMRI data for evaluation.

## 2 Methods

### 2.1 Background: Multi-Tensor Model with a Fixed Tensor Basis

As discussed in [8], the diffusion weighted signal at each voxel can be modeled using a unified framework,

$$S(\mathbf{q}) = S_0 \int_{\mathcal{M}} f(x)R(\mathbf{q}, x)dx, \quad (1)$$

where  $\mathcal{M}$  is a smooth manifold,  $x$  is a point on  $\mathcal{M}$ ,  $S(\mathbf{q})$  is the diffusion weighted signal with the diffusion gradient  $\mathbf{q}$ ,  $S_0$  is the signal without diffusion weighting,  $R(\mathbf{q}, x)$  is a kernel function, and  $f(x)$  is a probability density function. As in [10] and [20], we use a fixed tensor basis to represent diffusion signals, which has the advantage of explicit relationship between the basis and FOs. In this work, the basis comprises  $N = 289$  prolate tensors  $\mathbf{D}_i$  whose primary eigenvectors (PEVs)  $\mathbf{v}_i$  are approximately evenly oriented over the sphere. Each  $\mathbf{D}_i$  represents an FO given by its PEV  $\mathbf{v}_i$ . The eigenvalues ( $\lambda_1 \geq \lambda_2 \geq \lambda_3 > 0$ ) determine the shape of the basis tensor, and they are determined by examining the diffusion tensors of a noncrossing fiber tract [10].

With this tensor basis, we have  $\mathcal{M} = \mathcal{S}^2$  (a unit sphere),  $x = \mathbf{v}$  (a unit vector),  $f(\mathbf{v}) = f_i \delta(\mathbf{v}; \mathbf{v}_i)$ , and  $R(\mathbf{q}, \mathbf{v}_i) = e^{-\mathbf{q}^T \mathbf{D}_i \mathbf{q}}$  [8]. If we normalize the diffusion gradient as  $\tilde{\mathbf{q}} = \mathbf{q}/|\mathbf{q}|$ , then  $\tilde{\mathbf{q}}$  is associated with a constant  $b$  determined by the imaging sequence. Then, taking noise  $n(\mathbf{q})$  into account, (1) becomes [10]

$$S(\mathbf{q}) = S_0 \sum_{i=1}^N f_i e^{-b \tilde{\mathbf{q}}^T \mathbf{D}_i \tilde{\mathbf{q}}} + n(\mathbf{q}), \quad (2)$$

where  $f_i$  ( $\sum_i f_i = 1$ ) is the unknown nonnegative mixture fraction (MF) for  $\mathbf{D}_i$ .

By defining  $y(\mathbf{q}) = S(\mathbf{q})/S_0$  and  $\eta(\mathbf{q}) = n(\mathbf{q})/S_0$ , (2) can be written as

$$\mathbf{y} = \mathbf{G}\mathbf{f} + \boldsymbol{\eta}, \quad (3)$$

where  $\mathbf{y} = (y(\mathbf{q}_1), y(\mathbf{q}_2), \dots, y(\mathbf{q}_K))^T$  ( $K$  is the number of DWIs),  $\mathbf{G}$  is a  $K \times N$  matrix comprising the attenuation terms  $G_{ki} = e^{-b \tilde{\mathbf{q}}_k^T \mathbf{D}_i \tilde{\mathbf{q}}_k}$ ,  $\mathbf{f} = (f_1, f_2, \dots, f_N)^T$ , and  $\boldsymbol{\eta} = (\eta(\mathbf{q}_1), \eta(\mathbf{q}_2), \dots, \eta(\mathbf{q}_K))^T$ . Because the number of FOs in each voxel is small, it makes sense to estimate the MFs using sparse reconstruction:

$$\hat{\mathbf{f}} = \arg \min_{\mathbf{f} \geq \mathbf{0}, \|\mathbf{f}\|_1=1} \|\mathbf{G}\mathbf{f} - \mathbf{y}\|_2^2 + \beta \|\mathbf{f}\|_0. \quad (4)$$



By relaxing the constraint of  $\sum_{i=1}^N f_i = 1$  and replacing the  $\ell_0$ -norm with the  $\ell_1$ -norm [10, 20], we have

$$\hat{\mathbf{f}} = \arg \min_{\mathbf{f} \geq \mathbf{0}} \|\mathbf{G}\mathbf{f} - \mathbf{y}\|_2^2 + \beta \|\mathbf{f}\|_1, \quad (5)$$

Then, the estimated  $\mathbf{f}$  is projected onto the unit sphere  $\|\mathbf{f}\|_1 = 1$  by normalization [10]. Basis directions with nonzero MFs are interpreted as estimated FOs. Thus, we will use FO estimation and MF estimation interchangeably.

## 2.2 FO Estimation Using Neighborhood Information

Because of image noise, it is important to incorporate spatial coherence of FOs to improve FO estimation [13]. An intuitive way of incorporating neighborhood information can be based on the smoothness of MFs [15, 20]. But establishing smooth MFs does not mean that the FO angles are smooth. For example, let  $\mathbf{f}_a = (1, 0, \dots, 0)^T$ ,  $\mathbf{f}_b = (0, 1, 0, \dots, 0)^T$ , and  $\mathbf{f}_c = (0, 0, 1, 0, \dots, 0)^T$ . The difference between  $\mathbf{f}_a$  and  $\mathbf{f}_b$  ( $\|\mathbf{f}_a - \mathbf{f}_b\|$ ) is the same as that between  $\mathbf{f}_a$  and  $\mathbf{f}_c$  ( $\|\mathbf{f}_a - \mathbf{f}_c\|$ ), while the desired difference is clearly related to the basis directions represented by the nonzero entries in the MFs. In this work, we seek to explicitly incorporate the directional information from neighbor voxels into FO estimation.

**FO Estimation with Known Neighborhood Information** First we consider a simplified case of estimating FOs in a single voxel with known neighbor information. Let the MFs at voxel  $m$  be  $\mathbf{f}_m$ . A voxel  $n$  is in the neighborhood  $N_m$  of  $m$  and has FOs  $\{\mathbf{v}_{n,j}\}_{j=1}^{V_n}$ , where  $V_n$  is the number of FOs at  $n$ . Suppose  $\{\mathbf{v}_{n,j}\}_{j=1}^{V_n}$  were known, and we want to estimate  $\mathbf{f}_m$  given the neighbor FOs.

We assume that a majority of neighbor voxels  $n \in N_m$  have similar FO patterns as the desired one at  $m$ . Then, a set of *likely FO*  $\{\mathbf{u}_{m,p}\}_{p=1}^{U_m}$  for  $m$  can be obtained from the neighbor voxels (details will be introduced later), where  $U_m$  is the number of likely FOs at  $m$ . Motivated by Ye et al. [18], where fixed pre-determined prior directions at each voxel are encoded in the sparse reconstruction of FOs from dMRI, a weighted  $\ell_1$ -norm regularized least squares problem derived from a Bayesian perspective can be solved to encode the information of likely FOs:

$$\hat{\mathbf{f}}_m = \arg \min_{\mathbf{f}_m \geq \mathbf{0}} \|\mathbf{G}\mathbf{f}_m - \mathbf{y}_m\|_2^2 + \beta \|\mathbf{C}_m \mathbf{f}_m\|_1. \quad (6)$$

Here,  $\mathbf{C}_m$  is a diagonal weighting matrix encoding likely FOs. The basis directions closer to likely FOs are weighted less in the weighted  $\ell_1$ -norm, and thus they are less penalized in the objective function. We set the diagonal entries as

$$C_{m;ii} = \left(1 - \alpha \max_p |\mathbf{v}_i \cdot \mathbf{u}_{m,p}|\right) / \min_q \left(1 - \alpha \max_p |\mathbf{v}_q \cdot \mathbf{u}_{m,p}|\right), \quad (7)$$

where  $\alpha \in [0, 1)$  is a constant. Since  $\mathbf{v}_i$  and  $\mathbf{u}_{m,p}$  are unit vectors,  $0 \leq |\mathbf{v}_i \cdot \mathbf{u}_{m,p}| \leq 1$  and  $C_{m:ii}$  is positive. In this way, the penalty for basis directions that are closest to likely FOs is the same as that when no information on likely FOs is used.

Note that our application of FO estimation with spatial coherence is fundamentally different than [18] in two aspects: (1) likely FOs are computed based on neighbor FOs while in [18] an anatomical atlas is needed to provide prior directions specified at each voxel; (2) since the FOs in the neighbors are also to be estimated, voxelwise FO estimation in (6) is inappropriate. The proposed approach to likely FO computation and FO estimation is introduced below.

**Likely FO Computation** At voxel  $m$  we first consider one neighbor voxel  $n$ . Between each basis direction  $\mathbf{v}_i$  and the neighbor  $n$ , we define a *basis-neighbor similarity*  $r_m(i, n) = w_{m,n} \max_j |\mathbf{v}_i \cdot \mathbf{v}_{n,j}|$ . Here,  $w_{m,n}$  is a weighting coefficient, which represents the similarity between  $m$  and  $n$ . It is defined as  $w_{m,n} = e^{-\mu d^2(\mathbf{D}_m, \mathbf{D}_n)}$  ( $\mu$  is a constant).  $\mathbf{D}_m$  and  $\mathbf{D}_n$  are the diffusion tensors fitted from DWIs at  $m$  and  $n$ , respectively, and  $d(\mathbf{D}_m, \mathbf{D}_n)$  is a distance metric for tensors  $\mathbf{D}_m$  and  $\mathbf{D}_n$ :  $d(\mathbf{D}_m, \mathbf{D}_n) = \sqrt{\text{Trace}\{\log(\mathbf{D}_m) - \log(\mathbf{D}_n)\}^2}$  [1]. For each  $\mathbf{v}_i$ , the max function in  $r_m(i, n)$  measures the similarity between  $\mathbf{v}_i$  and its closest FO in  $n$ , and this similarity is further weighted by the voxel similarity  $w_{m,n}$ . In this way, given one neighbor  $n$ , we can measure how similar  $\mathbf{v}_i$  is to the FOs at  $n$ .

To consider all neighbor voxels, an *aggregate basis-neighbor similarity* for  $\mathbf{v}_i$  at voxel  $m$  is defined as  $R_m(i) = \sum_{n \in N_m} r_m(i, n)$ . We can extract likely FOs for  $m$  by finding the basis directions with local maximal  $R_m$  values:

$$\{\mathbf{u}_{m,p}\}_{p=1}^{U_m} = \{\mathbf{v}_i | R_m(i) \geq R_m(j), \forall j \neq i : \arccos(|\mathbf{v}_i \cdot \mathbf{v}_j|) \leq \frac{\theta\pi}{180^\circ}\}. \quad (8)$$

Here,  $\theta$  is a threshold and we empirically choose  $\theta = 20^\circ$ .

**FO Estimation for All Voxels** With the likely FOs, the weighting matrix can then be obtained. Note that we have assumed known neighbor information to obtain (6). However, the FOs in the neighbors are also to be estimated. Thus the FOs in all the voxels should be estimated simultaneously. For a total number of  $M$  voxels of interest, where the MFs  $\mathbf{f} = (\mathbf{f}_1^T, \mathbf{f}_2^T, \dots, \mathbf{f}_M^T)^T$  (and thus the FOs) are unknown, the FO estimation can be achieved as

$$\hat{\mathbf{f}} = \arg \min_{\mathbf{f} \geq \mathbf{0}} E(\mathbf{f}) = \arg \min_{\mathbf{f}_1, \mathbf{f}_2, \dots, \mathbf{f}_M \geq \mathbf{0}} \sum_{m=1}^M \|\mathbf{G}\mathbf{f}_m - \mathbf{y}_m\|_2^2 + \beta \|\mathbf{C}_m \mathbf{f}_m\|_1. \quad (9)$$

Note that  $\mathbf{C}_m$  contains the interaction between neighbors and it is also dependent on  $\alpha$ . Greater  $\alpha$  leads to more influence from neighbors.  $\beta$  controls the sparsity. In this work,  $\alpha$  and  $\beta$  were chosen empirically.

### 2.3 Minimization of the Objective Function

Because each voxel  $m$  is coupled with its neighbors in  $\mathbf{C}_m$  in (9), we use a block coordinate descent (BCD) optimization strategy. At iteration  $k + 1$ ,

$$\begin{aligned}\hat{\mathbf{f}}_m^{k+1} &= \arg \min_{\mathbf{f}_m \geq \mathbf{0}} E(\hat{\mathbf{f}}_1^{k+1}, \dots, \hat{\mathbf{f}}_{m-1}^{k+1}, \mathbf{f}_m, \hat{\mathbf{f}}_{m+1}^k, \dots, \hat{\mathbf{f}}_M^k) \\ &= \arg \min_{\mathbf{f}_m \geq \mathbf{0}} \|\mathbf{G}\mathbf{f}_m - \mathbf{y}_m\|_2^2 + \beta \|\mathbf{C}_m^{k+1} \mathbf{f}_m\|_1.\end{aligned}\quad (10)$$

Using (8), the likely FOs  $\mathbf{u}_{m,p}^{k+1}$  are obtained by finding the local maxima from  $R_m^{k+1}(i) = \sum_{n \in N_m} w_{m,n} \max_j |\mathbf{v}_i \cdot \mathbf{v}_{n,j}^{k+1} \mathbb{1}_{n < m}|$ , where  $\mathbb{1}$  is an indicator function. Then,  $\mathbf{C}_m^{k+1}$  can be determined with  $\mathbf{u}_{m,p}^{k+1}$  using (7).

To solve (10), we define  $\mathbf{g}_m^{k+1} = \mathbf{C}_m^{k+1} \mathbf{f}_m$ . Since  $\mathbf{C}_m^{k+1}$  is diagonal and  $C_m^{k+1:ii} > 0$ ,  $\mathbf{C}_m^{k+1}$  is invertible and  $\mathbf{f}_m = (\mathbf{C}_m^{k+1})^{-1} \mathbf{g}_m^{k+1}$ . By defining  $\tilde{\mathbf{G}}_m^{k+1} = \mathbf{G}(\mathbf{C}_m^{k+1})^{-1}$ ,

$$\hat{\mathbf{g}}_m^{k+1} = \arg \min_{\mathbf{g}_m^{k+1} \geq \mathbf{0}} \|\tilde{\mathbf{G}}_m^{k+1} \mathbf{g}_m^{k+1} - \mathbf{y}_m\|_2^2 + \beta \|\mathbf{g}_m^{k+1}\|_1.\quad (11)$$

We find  $\hat{\mathbf{g}}_m^{k+1}$  using the method in [9] and the MFs are estimated as

$$\hat{\mathbf{f}}_m^{k+1} = (\mathbf{C}_m^{k+1})^{-1} \hat{\mathbf{g}}_m^{k+1}.\quad (12)$$

Then, we project  $\hat{\mathbf{f}}_m^{k+1}$  back onto the unit sphere by normalization:  $\tilde{\mathbf{f}}_{m,i}^{k+1} = \hat{\mathbf{f}}_{m,i}^{k+1} / \sum_j \hat{\mathbf{f}}_{m,j}^{k+1}$ , and the FOs at  $m$  at iteration  $k + 1$  are the basis directions with  $\tilde{\mathbf{f}}_{m,i}^{k+1} > t$  ( $t = 0.1$  in this work), because FOs with small MFs are interpreted as components of isotropic diffusion [10, 18].

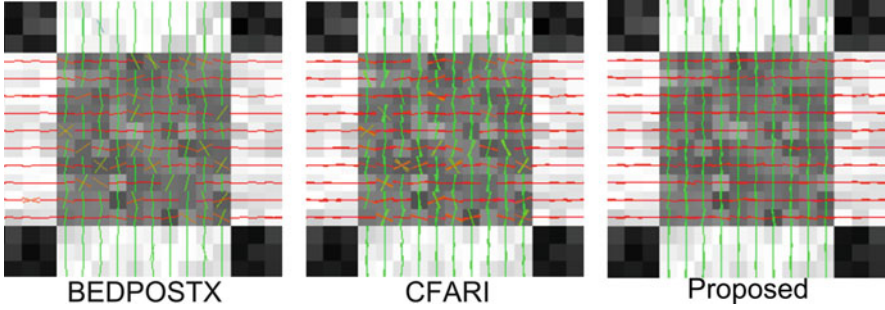
The FOs are initialized by Landman et al. [10]. Iterative update is terminated if the FO difference between successive iterations is small or the maximum iteration is reached.

## 3 Experiments

### 3.1 3D Digital Crossing Phantom

A 3D digital crossing phantom was generated to simulate two tracts crossing at  $90^\circ$ , where one  $b_0$  image and 30 gradient directions ( $b = 700 \text{ s/mm}^2$ ) were used. Rician noise ( $\sigma/S_0=0.05$ ) was added to the DWIs.

The proposed method with  $(\alpha, \beta, \mu) = (0.4, 0.5, 1.0)$  was compared with BEDPOSTX [3] and CFARI [10], which are commonly used with around 30



**Fig. 1** FO estimation overlaid on the FA map of the 3D crossing phantom

**Table 1** The mean errors of FO estimation (with standard deviations in parentheses)

	Noncrossing region		Crossing region	
	$e_1$	$e_2$	$e_1$	$e_2$
BEDPOSTX	3.26° (3.58°)	2.80° (1.89°)	12.12° (8.92°)	13.72° (11.66°)
CFARI	3.41° (1.73°)	0.79° (1.88°)	12.23° (7.79°)	12.21° (11.52°)
Proposed	3.08° (1.63°)	0.58° (1.64°)	5.57° (2.24°)	3.89° (2.65°)

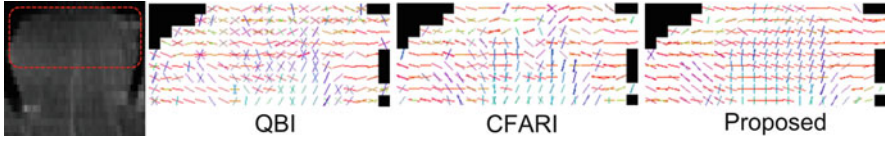
gradient directions. The results are overlaid on the fractional anisotropy (FA) map in Fig. 1. Compared with BEDPOSTX and CFARI, the proposed method produces smoother FOs and better identifies crossing FOs. We then compared the results quantitatively by using the two error measures proposed in [18], where the first measure ( $e_1$ ) represents how close each estimated FO is to its ground truth FO, and the second one ( $e_2$ ) measures how accurately each ground truth FO is represented. The results are listed in Table 1. The proposed method estimates FOs more accurately in both noncrossing and crossing regions.

### 3.2 Real Data

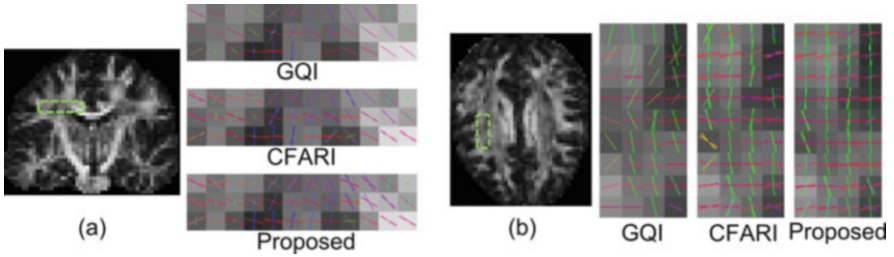
**Ex Vivo Tongue dMRI** Nine  $b_0$  images and 64 gradient directions ( $b = 2000 \text{ s/mm}^2$ ) were acquired on a 3T MRI scanner (Magnetom Trio, Siemens, Erlangen, Germany). The resolution is 2 mm isotropic.

The proposed method with  $(\alpha, \beta, \mu) = (0.4, 0.5, 3.0)$  was compared with  $q$ -ball imaging (QBI) using spherical harmonics based transformation [6] and CFARI [10]. The eigenvalues of the basis tensors are  $\lambda_1 = 7.0 \times 10^{-4} \text{ mm}^2/\text{s}$  and  $\lambda_2 = \lambda_3 = 3.0 \times 10^{-4} \text{ mm}^2/\text{s}$ . We focus on the crossing region of the genioglossus (GG) and transverse (T) muscle in Fig. 2, where the proposed method better estimates the crossing FOs and produces smoother FOs than QBI and CFARI.

**In Vivo Brain dMRI** Two  $b$ -values ( $b = 1000 \text{ s/mm}^2$  and  $2000 \text{ s/mm}^2$ ) were used in the acquisition. Each  $b$ -value is associated with 30 gradient directions and



**Fig. 2** FO estimation on the ex vivo tongue in the coronal view, which is focused on the crossing of the GG and T muscle (the tongue area is indicated by the white mask). A high resolution structural image (*left*) is shown for location reference



**Fig. 3** FO estimation on brain dMRI (overlaid on the FA map), which is focused on the crossing of (a) CC and CST (coronal view) and (b) CC and SLF (axial view)

each DWI has two repeated scans. Twelve  $b_0$  images were also acquired. The images were acquired on a 3T MRI scanner (Magnetom Trio, Siemens, Erlangen, Germany). The resolution is 2.7 mm isotropic.

The proposed method with  $(\alpha, \beta, \mu) = (0.4, 0.5, 1.0)$  was compared with CFARI [10] and generalized  $q$ -sampling imaging (GQI) [19]. GQI is a generalization of QBI [6] and can reconstruct FOs from multi-shell (multiple  $b$ -values) dMRI. The eigenvalues of the basis tensors are  $\lambda_1 = 2.0 \times 10^{-3} \text{ mm}^2/\text{s}$  and  $\lambda_2 = \lambda_3 = 5.0 \times 10^{-4} \text{ mm}^2/\text{s}$ . We highlight two regions for evaluation: the crossing region of the corpus callosum (CC) and the corticospinal tract (CST) and the crossing region of CC and the superior longitudinal fasciculus (SLF), which are shown in Fig. 3. It can be seen that the proposed method is able to better reconstruct the crossing FOs and has smoother results than CFARI and GQI.

## 4 Conclusion

We have proposed an FO estimation algorithm using neighborhood information. The diffusion signal is modeled by a tensor basis. Directional information in neighbors is modeled in weighted  $\ell_1$ -norm regularization terms to ensure spatial coherence. FO estimation is achieved using a BCD strategy. The proposed method was applied to simulated and real dMRI data. The results indicate that the proposed method improves FO estimation by using neighborhood information.

**Acknowledgements** This work is supported by NIH/NINDS 5R01NS056307, and NIH/NINDS IR21NS082891.

## References

1. Arsigny, V., Fillard, P., Pennec, X., Ayache, N.: Log-Euclidean metrics for fast and simple calculus on diffusion tensors. *Magn. Reson. Med.* **56**(2), 411–421 (2006)
2. Becker, S., Tabelow, K., Mohammadi, S., Weiskopf, N., Polzehl, J.: Adaptive smoothing of multi-shell diffusion weighted magnetic resonance data by msPOAS. *NeuroImage* **95**, 90–105 (2014)
3. Behrens, T.E.J., Berg, H.J., Jbabdi, S., Rushworth, M.F.S., Woolrich, M.W.: Probabilistic diffusion tractography with multiple fibre orientations: what can we gain? *NeuroImage* **34**(1), 144–155 (2007)
4. Bilgic, B., Setsompop, K., Cohen-Adad, J., Yendiki, A., Wald, L.L., Adalsteinsson, E.: Accelerated diffusion spectrum imaging with compressed sensing using adaptive dictionaries. *Magn. Reson. Med.* **68**(6), 1747–1754 (2012)
5. Daducci, A., Van De Ville, D., Thiran, J.P., Wiaux, Y.: Sparse regularization for fiber ODF reconstruction: from the suboptimality of  $\ell_2$  and  $\ell_1$  priors to  $\ell_0$ . *Med. Image Anal.* **18**(6), 820–833 (2014)
6. Descoteaux, M., Angelino, E., Fitzgibbons, S., Deriche, R.: Regularized, fast, and robust analytical q-ball imaging. *Magn. Reson. Med.* **58**(3), 497–510 (2007)
7. Hao, X., Fletcher, P.: Joint fractional segmentation and multi-tensor estimation in diffusion MRI. In: Gee, J., Joshi, S., Pohl, K., Wells, W., Zillei, L. (eds.) *Information Processing in Medical Imaging. Lecture Notes in Computer Science*, vol. 7917, pp. 340–351. Springer, Berlin (2013). [http://dx.doi.org/10.1007/978-3-642-38868-2\\_29](http://dx.doi.org/10.1007/978-3-642-38868-2_29)
8. Jian, B., Vemuri, B.C.: A unified computational framework for deconvolution to reconstruct multiple fibers from diffusion weighted MRI. *IEEE Trans. Med. Imaging* **26**(11), 1464–1471 (2007)
9. Kim, S.J., Koh, K., Lustig, M., Boyd, S.: An efficient method for compressed sensing. In: *IEEE International Conference on Image Processing*, vol. 3, pp. 117–120 (2007)
10. Landman, B.A., Bogovic, J.A., Wan, H., ElShahaby, F.E.Z., Bazin, P.L., Prince, J.L.: Resolution of crossing fibers with constrained compressed sensing using diffusion tensor MRI. *NeuroImage* **59**(3), 2175–2186 (2012)
11. Le Bihan, D.: Looking into the functional architecture of the brain with diffusion MRI. *Nat. Rev. Neurosci.* **4**(6), 469–480 (2003)
12. Merlet, S.L., Deriche, R.: Continuous diffusion signal, EAP and ODF estimation via compressive sensing in diffusion MRI. *Med. Image Anal.* **17**(5), 556–572 (2013)
13. Michailovich, O., Rathi, Y., Dolui, S.: Spatially regularized compressed sensing for high angular resolution diffusion imaging. *IEEE Trans. Med. Imaging* **30**(5), 1100–1115 (2011)
14. Pasternak, O., Assaf, Y., Intrator, N., Sochen, N.: Variational multiple-tensor fitting of fiber-ambiguous diffusion-weighted magnetic resonance imaging voxels. *Magn. Reson. Imaging* **26**(8), 1133–1144 (2008). <http://www.sciencedirect.com/science/article/pii/S0730725X08000490>
15. Ramirez-Manzanares, A., Rivera, M., Vemuri, B.C., Carney, P., Mareci, T.: Diffusion basis functions decomposition for estimating white matter intravoxel fiber geometry. *IEEE Trans. Med. Imaging* **26**(8), 1091–1102 (2007)
16. Sigurdsson, G.A., Prince, J.L.: Smoothing fields of weighted collections with applications to diffusion MRI processing. In: *SPIE Medical Imaging*, pp. 90342D–90342D (2014)
17. Tournier, J., Calamante, F., Connelly, A.: Robust determination of the fibre orientation distribution in diffusion MRI: non-negativity constrained super-resolved spherical deconvolution. *NeuroImage* **35**(4), 1459–1472 (2007)

18. Ye, C., Carass, A., Murano, E., Stone, M., Prince, J.L.: A Bayesian approach to distinguishing interdigitated muscles in the tongue from limited diffusion weighted imaging. In: Bayesian and Graphical Models for Biomedical Imaging. Lecture Notes in Computer Science, vol. 8677, pp. 13–24. Springer, Berlin (2014)
19. Yeh, F.C., Wedeen, V., Tseng, W.Y.: Generalized  $q$ -sampling imaging. *IEEE Trans. Med. Imaging* **29**(9), 1626–1635 (2010)
20. Zhou, Q., Michailovich, O., Rathi, Y.: Resolving complex fibre architecture by means of sparse spherical deconvolution in the presence of isotropic diffusion. In: SPIE Medical Imaging, pp. 903425–903425 (2014)

# **Part II**

## **Posters**



# A Framework for Creating Population Specific Multimodal Brain Atlas Using Clinical T1 and Diffusion Tensor Images

Vikash Gupta, Grégoire Malandain, Nicholas Ayache, and Xavier Pennec

**Abstract** Spatial normalization is one of the most important steps in population based statistical analysis of brain images. This involves normalizing all the brain images to a pre-defined template or a population specific template. With multiple emerging imaging modalities, it is quintessential to develop a method for building a joint template that is a statistical representation of the given population across different modalities. It is possible to create different population specific templates in different modalities using existing methods. However, they do not give an opportunity for voxelwise comparison of different modalities. A multimodal brain template with probabilistic region of interest (ROI) definitions will give opportunity for multivariate statistical frameworks for better understanding of brain diseases. In this paper, we propose a methodology for developing such a multimodal brain atlas using the anatomical T1 images and the diffusion tensor images (DTI), along with an automated workflow to probabilistically define the different white matter regions on the population specific multimodal template. The method will be useful to carry out ROI based statistics across different modalities even in the absence of expert segmentation. We show the effectiveness of such a template using voxelwise multivariate statistical analysis on population based group studies on HIV/AIDS patients.

---

Vikash Gupta is presently at Imaging Genetics Center, University of Southern California, Los Angeles, CA, USA

Grégoire Malandain is presently at MORPHENE team, INRIA Sophia-Antipolis, Sophia Antipolis, France

V. Gupta (✉) • G. Malandain • N. Ayache • X. Pennec  
INRIA Sophia Antipolis - ASCLEPIOS Project, 06902 Sophia Antipolis Cedex, France  
e-mail: [vikash.gupta@inria.fr](mailto:vikash.gupta@inria.fr)

## 1 The Need for a Probabilistic Multimodal Atlas

The growth in brain imaging data across different modalities gives an opportunity to understand the disease progression and make correlations across them. Statistical analysis across different modalities and across population require spatial normalization. All the brain images are often normalized to a pre-defined template, for example the ICBM-152 or MNI template. However in [1, 2], the authors have shown that choosing a generic template biases the statistical results. For example, if one intends to do statistical analysis on a population of children, choosing an MNI template will involve an unintended scaling of all the brain images in the population adding a bias to the results. Moreover the generic MNI-T1 template is not a statistical representation of the population under consideration. The importance of multimodal brain atlases is discussed in detail in [3]. We support the need of such a multimodal template by comparing two groups of population. One of the groups comprises 18 healthy controls without any episodes of neurological disorder and another group of 30 patients with HIV associated neurocognitive disorder.

Some of the most common atlases being used today for spatial normalization are the ICBM (International Consortium of Brain Mapping), the MNI (Montreal Neuroimaging Institute) atlas and the FMRIB58\_FA atlases. The ICBM initiative has provided the neuroimaging community with a number of brain atlases. The three atlases which we will like to discuss here are the nonlinear version of ICBM T1 atlas, ICBM DTI-81 atlas and the white matter parcellation map (WMPM) [4]. It should be noted that though the atlases are in the MNI coordinate space, they are not necessarily built with the same population. Thus, the DTI atlas and the T1 atlas do not represent the variability across different modalities in the same population and so are not suited for a multimodal statistical analysis. There are two different versions of the ICBM T1 template. The first one was built in 2001 using an affine registration which was followed by another one built in 2009 using affine and nonlinear image registration. The 2009 version presents a more detailed outline of different brain structures as compared to its previous version.<sup>1</sup> Some of the drawbacks of the present ICBM atlases are as follows,

1. The DTI atlas was affinely aligned with the 2001 affine version of ICBM T1 template.
2. For creating the DTI atlas, scalar averaging of tensor elements was performed.
3. The DTI-81 data is normalized using an affine registration which increases the chances of misalignment of different brain structures.
4. The ICBM DTI-81 and ICBM 152 nonlinear atlases are independent atlases in their own right. However, the atlases cannot be used for a multimodal study because they are not aligned in the same geometrical space.

---

<sup>1</sup>The ICBM family of templates are available for download at [http://www.loni.usc.edu/atlas/Atlas\\_Detail.php?atlas\\_id=5](http://www.loni.usc.edu/atlas/Atlas_Detail.php?atlas_id=5).

In the following sections, we present an automated workflow to build a multimodal brain atlas using DTI and T1 images. Unlike the ICBM atlases, this atlas is in the same coordinate space which allows voxelwise comparison across the two modalities. In addition to the multimodal template we also present a method to probabilistically transfer the white matter labels in our template space. This opens further room for ROI based statistics on white matter region. Out of many possible applications to the presented atlas, we illustrate the applicability and relevance of the method by building a multimodal template to compare groups of HIV/AIDS patients with controls.

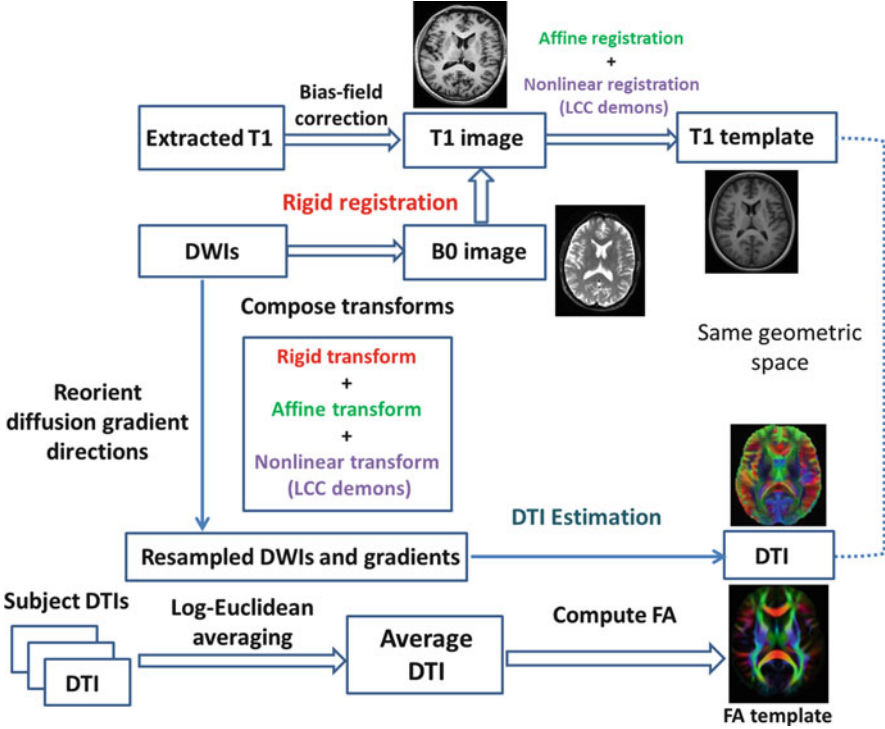
## 2 Atlas Construction

### 2.1 Joint T1 and DTI Template

An unbiased T1 atlas is constructed using the methodology outlined in [5, 6]. In principle, a similar method can be used to make a DTI template from a given population. However, in such a case the DTI template and the T1 template will be in different spaces and a comparative study across different modalities cannot be performed. For constructing a joint T1 and DTI template, we propose a workflow that takes into account physically plausible transformations that exists in the image space and across modalities. The workflow is shown in Fig. 1. The dicom images were extracted using the MRICron software into a nifti image format. The diffusion weighted images (DWIs) are corrected for eddy currents distortions and head motion using the FSL toolbox. N4ITK bias correction tool [7] was used for intensity bias correction in the T1 images. The undiffused ( $B_0$ ) images and the T1 images are rigidly registered using FSL's *flirt* tool using seven degrees of freedom and mutual information cost function to take into account the multimodality of the images. Seven degrees of freedom for the registration takes into account the rigid motion of the head (rotation and translation) along with the scaling of the voxels that is present due to differences in the field of view of the  $B_0$  and the T1 images during image acquisition. The T1 images were first aligned to the T1 template using an affine followed by a nonlinear registration using LCC-demons algorithm [8]. The rigid transform between the subject's  $B_0$  and T1 images, the affine and nonlinear deformation field are composed in order to produce the net deformation field. The diffusion images are then resampled into the T1 template image space using the composed deformation field. The combined deformation field can be expressed using a displacement field ( $u$ ). The local linear transformation can be described as

$$T = I + \frac{du}{dx},$$

where  $I$  is the identity matrix and  $\frac{du}{dx}$  Jacobian of the deformation field at the point  $x$ . The Jacobian matrix can be decomposed into a rotation component  $R$  and a



**Fig. 1** Workflow for generating joint T1 and DTI brain atlas. Registrations and the corresponding transforms are color matched

deformation component  $P$  using the polar decomposition theorem. Using singular value decomposition (SVD), the rotation matrix  $R$  can be computed as

$$R = UV^T,$$

where  $F = UWV^T$  is the singular value decomposition of the matrix  $F$ . The diffusion gradient directions are then transformed to the new space using the rotational component of the transformation for each voxel as

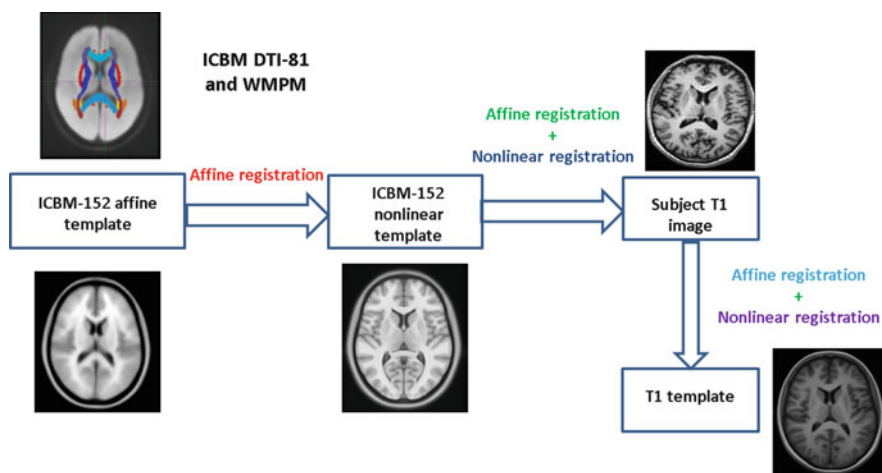
$$g_v = Rg^T,$$

where  $g$  is the diffusion gradient direction and  $g_v$  is the transformed gradient direction. The diffusion tensors are then estimated in the template space using the algorithm presented in [9]. Once the diffusion tensors are estimated, they are averaged using the Log-Euclidean framework [10] to compute the DTI template. This workflow produces a combined T1 and DTI template in a common geometrical space.

## 2.2 Probabilistic White Matter

For computing ROI based statistical analysis, it is important to have an accurate segmentation of the white matter regions. However, an accurate segmentation is a difficult problem because of the partial volume effects in the images which makes the segmentation task particularly difficult. In such a scenario it is desirable to have an automated probabilistic segmentation of the ROIs. A probabilistic segmentation allows us to attach an additional level of accuracy depending on how conservative one is in choosing the ROIs, thus mitigating the problems due to misregistration to certain extent. For generating a probabilistic parcellation of the white matter, we used the celebrated ICBM-WMPM as a prior. The WMPM is defined in the ICBM-DWI template space. The ICBM-DTI and the ICBM-152 affine template are aligned and share the same geometric space. Thus a registration using the ICBM-152 template will approximate a registration between the ICBM-DWI and the ICBM-152 nonlinear template. The workflow for transferring the labels is shown in Fig. 2. The different steps involved in the transferring the labels is enumerated as,

1. The ICBM-152 affine template is affinely aligned with the 2009 ICBM-152 nonlinear template.
2. The ICBM-152 nonlinear template (moving image) is registered with the T1 image (fixed image) of each of the subject using an affine and nonlinear registration. The target image for the registration is the T1 image.



**Fig. 2** Workflow for transferring white matter labels in ICBM-WMPM to a population specific multimodal atlas. The ICBM DTI-81 and the ICBM 152-affine atlas are defined in the same geometry. The ICBM-152 affine template is affinely registered with the ICBM-152 nonlinear template. The ICBM nonlinear template is then registered with each of the subject's T1 image which is again registered with the population specific T1 templated. The arrows show the registration paths and the corresponding registration methods are shown above the arrows.

3. Similarly, the subject T1 image (moving image) is registered with the population-specific template (fixed image) created before.
4. All the transformations are composed in the same order for each subject.
5. The respective transformations for each subject are applied to the ICBM-WMPM for transferring the labels.
6. All the transferred labels are averaged to produce the probabilistic parcellation map.

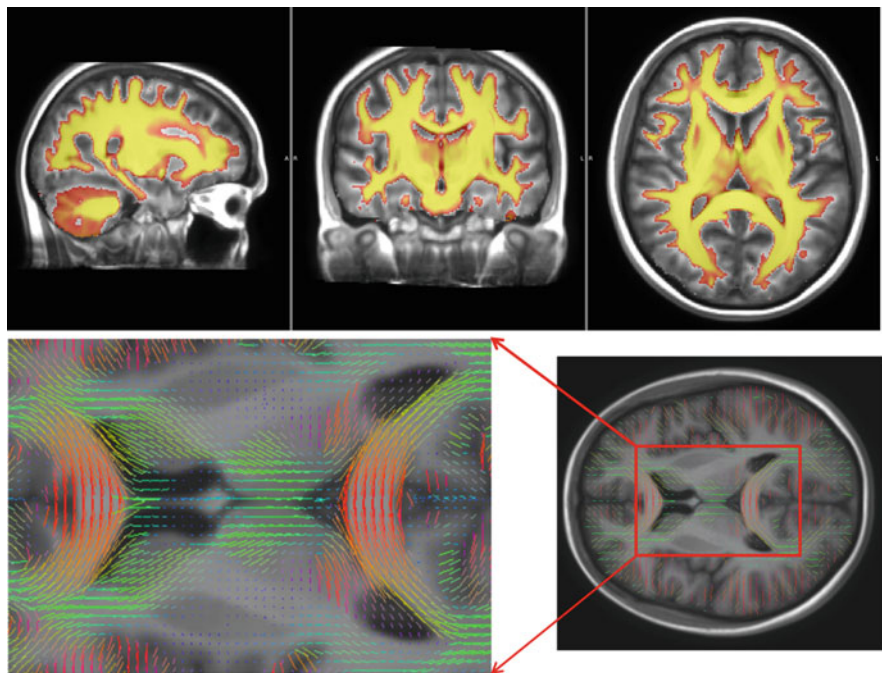
All the anatomical T1 registrations are carried out using LCC-demons algorithm in both the workflows.

### 3 Results

A total of 18 controls and 30 patients with HIV associated neurocognitive disorder (HAND) were chosen for the study. The images were acquired using a 1.5 T MRI scanner (GE Signa HDxt<sup>®</sup>). T1-weighted images were acquired using a magnetization prepared 3D Spoiled Gradient Recalled (SPGR) sequence (TR = 12.4 ms, TE = 5.2 ms, TI = 300 ms, flip angle = 18°, FOV = 240 mm). The T1 images have 256×256×248 voxels, with an isotropic voxel size of 0.6 mm. The DTI data was acquired with 23 encoding gradient direction and one undiffused B0 image. The diffusion weighted images has 256×256×26 voxels with sizes 0.9375×0.9375×5.5 mm<sup>3</sup>. The *b*-value for the acquisition was 700 s/mm<sup>2</sup>.

#### 3.1 Multimodal Template and Probabilistic ROIs

Figure 3 shows the multimodal template. The different structures across the two modalities T1 and DTI are in good agreement as shown in the figure. The top row shows the FA template (in red-yellow) overlayed on the anatomical T1 image. In the bottom row we show good agreement between the DTI and T1 templates. A close-up shows the diffusion tensors in genu and splenium of the corpus callosum in detail. In order to facilitate ROI based statistics, all the 52 white matter labels defined in ICBM-WMPM are transferred to this population specific template. In Fig. 4 probabilistic ROIs for external and internal capsule, middle cerebellar peduncle (MCP) and corpus callosum is shown. It also shows a probabilistic iso-surface rendition of the MCP and corpus callosum. The probability of a voxel being classified in a certain ROI is highest in the center and decreases outwards as expected from blue to red. Such renditions can be used for shape analysis of individual white matter structures.

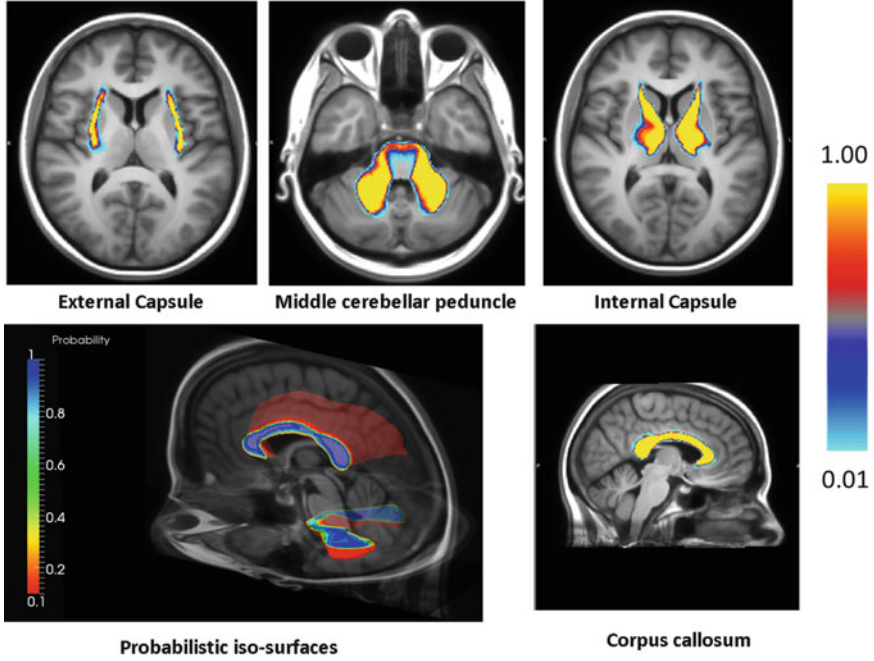


**Fig. 3** The multimodal brain template. *Top row*: FA template overlaid on the T1 template. *Bottom row*: DTI template is overlaid on top of T1 template. The zoomed section shows good alignment of diffusion tensors along the corpus callosum above and below the ventricles

### 3.2 Statistical Analyses on HIV Patients

A multimodal population specific brain atlas can be used for multivariate statistical analysis. As opposed to the univariate analysis, in this case it is possible to combine information from different modalities which increases the statistical power of the test. In univariate analysis like tract based spatial statistics (TBSS) or voxel based morphometry, the focus of study is to find changes in a single tissue type. In order to illustrate one possible application of such a multimodal template, we use the FA images from the DTIs and log-Jacobian from the T1 registration. FA images contain information about the white matter integrity, whereas the logarithm of the Jacobian determinant of the deformation field gives information about local volume shrinkage or expansion. For conducting the statistical test, first a multimodal template is created as mentioned above. All DTIs and T1 images are registered to the common template space. FA maps are computed from the registered DTIs and the log-Jacobian maps are computed from the deformation field resulting from T1 image registration. Thus, we have a voxelwise multi-channel information. A non-parametric distribution free permutation test is used for comparing the control group





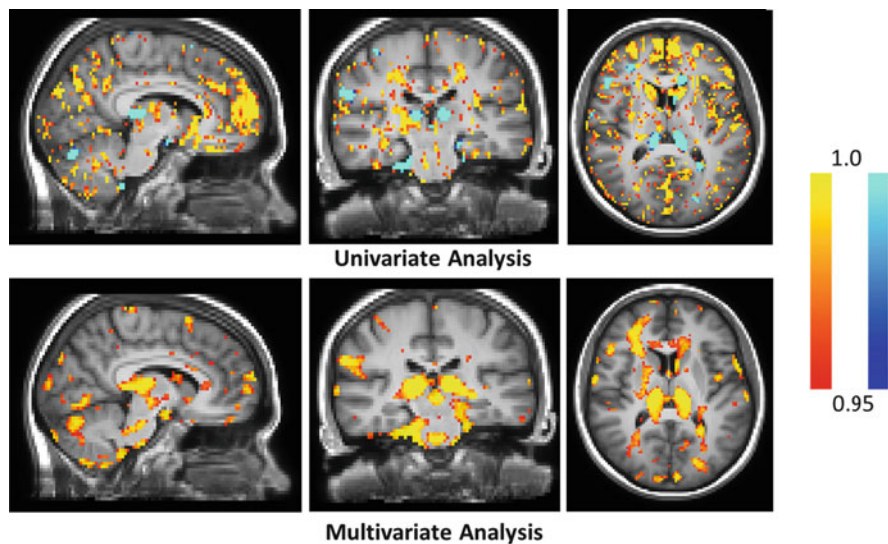
**Fig. 4** Probabilistic ROIs for some of the representative white matter structures are shown overlaid on the T1 image for anatomical reference. *Bottom-right* image shows 3D probabilistic iso-surfaces for corpus callosum and middle cerebral peduncle

against the patients. The test-statistic as suggested in [11] is used for the permutation test.

$$T_{n_1, n_2} = \frac{n_1 n_2}{n_1 + n_2} \left[ \frac{1}{n_1 n_2} \sum_{i=1}^{n_1} \sum_{j=1}^{n_2} \|\mathbf{V}_{1,i} - \mathbf{V}_{2,j}\| - \frac{1}{2n_1^2} \sum_{i=1}^{n_1} \sum_{j=1}^{n_1} \|\mathbf{V}_{1,i} - \mathbf{V}_{1,j}\| - \frac{1}{2n_2^2} \sum_{i=1}^{n_2} \sum_{j=1}^{n_2} \|\mathbf{V}_{2,i} - \mathbf{V}_{2,j}\| \right],$$

where  $\|\cdot\|$  is the Euclidean distance,  $n_1$  and  $n_2$  are the sizes of control and HAND patients respectively.  $\mathbf{V}$  and is the vector of two elements as described above. We used 1000 random permutations to generate the distribution. Figure 5 compares the result of univariate analysis against the multivariate analysis. In the top row red-yellow and blue-lightblue shows the statistically significant regions at 5% significance level for FA and log-Jacobian respectively. The bottom row shows the significantly different regions for multivariate tests. It should be noted that with the multivariate tests, we are able to detect more regions of differences between the





**Fig. 5** Statistically significant regions of difference. *Top row:* Univariate results on FA (red-yellow) and log-Jacobian (blue-lightblue) of the deformation field from T1 registration. *Bottom row:* Multivariate (red-yellow) statistical test. The images show the test-statistic values between 0.95 and 1 corresponding to 5% significance level

controls and HAND patients and thus attributing a higher detection power to such multivariate treatment of images.

## 4 Conclusion

In this paper we have presented a novel workflow for creating a multimodal T1 and DTI template which can be used for population based statistical studies. In our knowledge, there have been very few attempts in the past to perform group study by fusing multiple modalities and making a true multimodal brain atlas. The main idea of the paper is to combine the well accepted existing tools in order to make a workflow and suggest methods for multimodal statistical analysis. We created a probabilistic atlas of white matter regions using the ROI definitions from the WMPM labels. The multimodal atlas will have a wide variety of applications in the future. For example, one can use the probabilistic ROI definition as a prior for manual segmentation. It will be possible to correlate measures across different modalities giving us a better understanding of neuro-pathologies and possibly seek for biomarkers. We already showed an illustration of the possible applications in the case of HAND patients. The multivariate framework seems to have a higher detection power. However, the clinical relevance of these findings remain to be seen. The methods presented in this paper can easily be adopted to create any

other population specific multimodal templates. However, we are intending to make this atlas public for research purposes. In the future, it will interesting to look into building a spatio-temporal population specific brain atlases. Such an atlas will give deep insights into disease progression in case of progressive neuro-degenerative diseases like AIDS, Alzheimer's disease and ALS. One of the major contributions of this work is that with the presented method, it is possible to combine well accepted pre-existing tools for creating a population specific multimodal brain atlas and use the same for multimodal statistical analysis.

**Acknowledgements** We would like to acknowledge Nice University Hospital (CHU) and the NEURADAPT study for collecting the data. The work was partly supported by the European Research Council through the ERC Advanced Grant MedYMA 2011-291080.

## References

1. Thompson, P.M., Toga, A.W.: Detection, visualization and animation of abnormal anatomic structure with a deformable probabilistic brain atlas based on random vector field transformations. *Med. Image Anal.* **1**(4), 271–294 (1997)
2. Joshi, S., Davis, B., Jomier, M., Gerig, G.: Unbiased diffeomorphic atlas construction for computational anatomy. *NeuroImage* **23**, S151–S160 (2004)
3. Toga, A.W., Thompson, P.M., et al.: Towards multimodal atlases of the human brain. *Nat. Rev. Neurosci.* **7**(12), 952–966 (2006)
4. Mori, S., et al.: Stereotaxic white matter atlas based on diffusion tensor imaging in an ICBM template. *Neuroimage* **40**(2), 570–582 (2008)
5. Guimond, A., Meunier, J., Thirion, J.P.: Average brain models: a convergence study. *Comput. Vis. Image Underst.* **77**(2), 192–210 (2000)
6. Commowick, O., Malandain, G.: Efficient selection of the most similar image in a database for critical structures segmentation. In: *Medical Image Computing and Computer-Assisted Intervention - MICCAI 2007*, pp. 203–210. Springer, Berlin (2007)
7. Tustison, N.J., Avants, B.B., et al.: N4ITK: improved N3 bias correction. *Trans. Med. Imaging* **29**(6), 1310–1320 (2010)
8. Lorenzi, M., et al.: LCC-Demons: a robust and accurate symmetric diffeomorphic registration algorithm. *NeuroImage* **81**, 470–483 (2013)
9. Fillard, P., Pennec, X., et al.: Clinical DT-MRI estimation, smoothing, and fiber tracking with log-Euclidean metrics. *IEEE Trans. Med. Imaging* **26**(11), 1472–1482 (2007)
10. Arsigny, V., Commowick, O., Pennec, X., Ayache, N.: A log-Euclidean framework for statistics on diffeomorphisms. In: *MICCAI 2006*, pp. 924–931. Springer, Berlin (2006)
11. Baringhaus, L., Franz, C.: On a new multivariate two-sample test. *J. Multivar. Anal.* **88**(1), 190–206 (2004)

# Alignment of Tractograms as Linear Assignment Problem

Nusrat Sharmin, Emanuele Olivetti, and Paolo Avesani

**Abstract** Diffusion magnetic resonance imaging (dMRI) offers a unique approach to study the structural connectivity of the brain. DMRI allows to reconstruct the 3D pathways of axons within the white matter as a set of polylines (*streamlines*), called the *tractogram*. Tractograms of different brains need to be aligned in a common representation space for various purposes, such as group-analysis, segmentation or atlas construction. Typically, such alignment is obtained with affine registration, through which tractograms are globally transformed, with the limit of not reconciling local differences. In this paper, we propose to improve registration-based alignment by what we call *mapping*. The goal of mapping is to find the correspondence between streamlines across brains, i.e. to find the map of which streamline in one tractogram correspond to which streamline in the other tractogram. We frame the mapping problem as a *rectangular linear assignment problem (RLAP)*, a cornerstone of combinatorial optimization. We adopt a variant of the famous Hungarian method to get the optimal solution of the RLAP. We validate the proposed method with a tract alignment application, where we register two tractograms and, given one anatomical tract, we segment the corresponding one in the other tractogram. On dMRI data from the Human Connectome Project, we provide experimental evidence that mapping, implemented as a RLAP, can vastly improve both the true positive rate and false discovery rate of registration-based alignment, establishing a strong argument in favor of what we propose. We conclude by discussing the limitations of the current approach, which gives perspective for future work.

---

N. Sharmin (✉) • E. Olivetti • P. Avesani

NeuroInformatics Laboratory (NILab), Bruno Kessler Foundation, Trento, Italy

Center for Mind and Brain Sciences (CIMEC), University of Trento, Trento, Italy

e-mail: [nusrat.sharmin@unitn.it](mailto:nusrat.sharmin@unitn.it); <http://nilab.fbk.eu>

## 1 Introduction

Diffusion magnetic resonance imaging (dMRI) [1] provides information about the local orientation of white matter axons in each voxel of a brain image. Reconstruction and tracking algorithms aim at connecting voxels, based on the orientation within each voxel, in order to reconstruct the approximate trajectories of fibers as 3D polylines, called *streamlines*. A streamline, is a vectorial representation of thousands of neuronal axons following the same pathway. The whole set of streamlines is called *tractogram* and it represents the anatomical connectivity of the brain.

Tracts are sets of streamlines with specific neuroanatomical meaning. A manual procedure of virtual dissection allows the segmentation of streamlines for a given tract of interest. For example, shape and size of a tract can be helpful for a neurologist to assess the progress of a neurodegenerative disease [5]. Such analysis compares the tract from a tractogram of a patient to that healthy subjects, or atlas [13]. The common practice is based on the quantifying the number of voxels shared by the two tracts [7], which requires that the two tracts are first aligned in a common representation space.

The alignment of two tractograms is still an open problem. The best practice is based on the affine registration of the corresponding structural images, such as T1 or FA (Fractional Anisotropy) [1], and by applying the estimated transformation to the coordinates of streamlines. Improvements of these methods have been proposed by using more informative volumetric images, such as the orientation distribution functions (ODFs) [14]. More recently, a new approach has been investigated by computing the affine transformation directly in the space of the streamlines [6]. The intuitive idea is to find the affine transformation that minimizes a loss function based on the distance between streamlines. Computational issues prevent the use a whole tractogram, i.e. the registration is usually based on a small subset of the streamlines.

We claim that the alignment of tractograms based on registration methods has two main limitations. The first is concerned with the affine transformation, which is a global one. Local anatomical differences between two subjects/tractograms cannot be reconciled by a global linear transformation. Non-linear/elastic registration methods may overcome this limitation, but it is not straightforward how to preserve the orientation information of dMRI images after the distortion of the volumetric space. Evidence of this problem is the absence of literature on this topic. The second limitation is related to the use of transformations for alignment, that indeed reduces the differences between tractograms, but it is still not able to provide the correspondence between anatomical structures at the local level. We claim that alignment can provide more useful information when enriched with correspondence of streamlines across tractograms.

In this work we propose to overcome these limitations by introducing the notion of *mapping*. We claim that, when the ultimate goal is alignment and comparison of tracts across subjects, the registration in a common space is not enough and the additional step of finding which streamline in a tractogram correspond to which streamline in another tractogram should be computed.

In principle, the correspondence between streamlines across tractograms can be one-to-one, one-to-many or many-to-many. Here we restrict to the one-to-one case, and defer the other more general cases to future work. Under this assumption, the problem of finding corresponding streamlines can be cast as an *assignment problem* [4]. The assignment problem is a fundamental combinatorial optimization problem. Given two sets of objects, A and B, and a cost function to assign one element of A to one of B, the goal is to find the injective assignments of each element of A, to one of B, such that the total cost of the assignments is minimized. If the numbers of items are equal and the total cost is given by the sum of each assignment cost, the problem is called linear assignment problem (LAP). When  $|A| \neq |B|$ , the problem is called rectangular LAP (RLAP) [2], which is a generalization of the LAP.

Efficient and well known algorithms for solving the LAP are the Hungarian method [11] and Jonker-Volgenant algorithm (LAPJV) [9], both giving the optimal solution with complexity  $\mathcal{O}(n^3)$ ,  $n = |A|$ . For the rectangular case, where  $m = |B| > n$ , efficient variants of the previous algorithms are available in the literature, such as [3] which has complexity  $\mathcal{O}(n^2m)$  and provide the optimal solution. In this work we adopt that algorithm.

We designed an experiment about segmenting a desired tract in a tractogram. On dMRI data from the Human Connectome Project [15], we show experimental evidence that mapping through the RLAP greatly improves the quality of segmentation, both in terms of true positive rate (TPR) and false discovery rate (FDR), with respect to that of affine registration. This result confirms that the concept of mapping should be considered as a new useful tool in the context of alignment of tractograms and that its implementation as an assignment problem is effective, despite some limitations.

The paper is structured as follows. In Sect. 2 we define the notation and formally introduce mapping and the RLAP, together with the algorithm adopted here. In Sect. 3 we describe the details of the experiment and its results. A brief discussion about the merits a limitations is reported in Sect. 4.

## 2 Methods

In this section we briefly introduce the notation, the concept of mapping and the formal description of the linear assignment problem (LAP), with details of its *rectangular* (RLAP) version and references to efficient solutions.

### 2.1 Notation and Streamline Distance

Let the polyline  $s = \{\mathbf{x}_1, \mathbf{x}_2, \dots\}$ , where  $\mathbf{x}_i \in \mathbb{R}^3$ , be a *streamline*, reconstructed from dMRI data through reconstruction and tractography algorithms. Let the *tractogram*,  $T = \{s_1, s_2, \dots, s_M\}$  be defined as a set of  $M$  streamlines, where

$M \approx 10^5$ . Let  $t = \{s_1, s_2, \dots, s_k\} \subset T$ , be a subset of the tractogram, called *tract*, usually with a specific anatomical meaning, e.g. the cortico-spinal tract (CST).

Multiple distance functions between streamlines have been proposed in the literature [18]. Here we adopt the most common one, i.e. the symmetric minimum average distance (MAM). Given two streamlines,  $s_a$  and  $s_b$ :

$$d_{MAM}(s_a, s_b) = \frac{1}{2}(D(s_a, s_b) + D(s_b, s_a)) \quad (1)$$

where

$$D(s_a, s_b) = \frac{1}{|s_a|} \sum_{i=1}^{|s_a|} d(\mathbf{x}_i^a, s_b) \quad (2)$$

and

$$d(\mathbf{x}, s_b) = \min_{j=1, \dots, |s_b|} \|\mathbf{x} - \mathbf{x}'_j\|_2 \quad (3)$$

## 2.2 Mapping

The alignment of two tractograms,  $T_A$  and  $T_B$ , is usually implemented through registration algorithms, that transform the coordinates of the streamlines into a common space. Here we propose a different way of aligning tractograms, based on finding corresponding streamlines across two tractograms, without operating any transformation. The problem of finding which streamline  $s_j^B \in T_B$  correspond to a given streamline  $s_i^A \in T_A$  is a combinatorial one and its solution is a correspondence map between the two sets. For this reason, we call this kind of alignment as *mapping*. We denote the map as a binary matrix  $P = [p_{ij}]_{ij} \in \{0, 1\}^{|T_A| \times |T_B|}$ , that we call *mapping matrix*, such that  $p_{ij}$  is 1 when streamline  $s_i^A \in T_A$  corresponds to streamline  $s_j^B \in T_B$ , and 0 otherwise.

In practical cases, it is common to observe that different tractograms have different number of streamlines, i.e.  $|T_A| \neq |T_B|$ . Moreover, corresponding tracts across different subjects may have different size, meaning that different streamlines of one tractogram may correspond to the same streamline in the other one. For these reasons, in general, the correspondence between streamlines cannot be a bijective or an injective map but a many-to-one or many-to-many map. A very simple many-to-one greedy solution to the mapping problem is assigning the nearest streamline of the second tractogram to each streamline of the first tractogram, after affine registration in a common space. We refer to this baseline solution as *registration + nearest neighbor* (NN). The main limitation of this solution is that it strongly rely on the assumption that the affine registration reconciles most of the differences between the two tractograms, which is generally not true.

In order to propose an improvement over NN, in this work, we add the restrictive assumption that different streamlines in  $T_A$  correspond to different streamlines in  $T_B$ , i.e. we assume the mapping to be injective.<sup>1</sup> In Sects. 3 and 4 we show that this restriction does not prevent the proposed approach to reach major improvements over NN. Under the assumption just mentioned, and in order to find the desired mapping between two tractograms, we cast the mapping problem into a well known optimization problem, called *assignment problem* [4]. In the following we formally introduce the linear assignment problem along with its rectangular version.

### 2.3 The Linear Assignment Problem

Given two sets of objects of the *same size*,  $T_A = \{s_1^A, \dots, s_n^A\}$  and  $T_B = \{s_1^B, \dots, s_n^B\}$ , the problem of finding the optimal bijective assignment of each  $s_i^A$  to one element in  $T_B$ , given the cost matrix  $C = [c_{ij}]_{ij} \in \mathbb{R}^{n \times n}$ , where  $c_{ij}$  is the cost of assigning  $s_i^A$  to  $s_j^B$ , is called *linear assignment problem* (LAP). In our case, the cost is the distance between streamlines. The bijective assignment between the streamlines of two tractograms can be represented by permutation matrix  $P = [p_{ij}]_{ij} \in \{0, 1\}^{n \times n}$ , where  $p_{ij} = 1$  if  $s_i^A$  is assigned to  $s_j^B$ , and 0 otherwise. Notice that, since  $P$  represents a bijective correspondence, then  $\forall i \in \{1, \dots, n\}$ ,  $\sum_j p_{ij} = 1$  and  $\forall j \in \{1, \dots, n\}$ ,  $\sum_i p_{ij} = 1$ . The formal definition of the LAP is then:

$$P^* = \operatorname{argmin}_{P \in \mathcal{P}} \sum_{i,j=1}^n c_{ij} p_{ij} \quad (4)$$

where  $\mathcal{P}$  is the set of all possible  $n \times n$  permutation matrices and  $P^*$  is the optimal assignment with lowest overall cost.

Among the most efficient algorithm in the literature to find  $P^*$ , the Hungarian method is the most famous one. Its first formulation [10] had time complexity  $\mathcal{O}(n^4)$ , which was later improved to  $\mathcal{O}(n^3)$  by Munkres [11]. Another prominent algorithm in this group is LAPJV [9] which has the same complexity,  $\mathcal{O}(n^3)$ .

### 2.4 Rectangular Assignment Problem

When  $|A| \neq |B|$ , LAP is called *rectangular assignment problem* [2] (RLAP). In that case, let  $n = |A|$  and  $m = |B|$  and  $n \leq m$ , the problem consists in finding the

---

<sup>1</sup>Additionally we introduce the technical assumption that  $|T_A| \leq |T_B|$ .

injective assignment of all  $s_i^A \in A$  within  $B$ . Formally:

$$P^* = \operatorname{argmin}_{P \in \mathcal{P}} \sum_{i=1}^n \sum_{j=1}^m c_{ij} p_{ij} \quad (5)$$

where  $[p_{ij}]_{ij} = P \in \mathcal{P}$  is a *partial* permutation matrix<sup>2</sup> and  $C = [c_{ij}]_{ij}$  is the cost matrix.

The literature about algorithms to find the optimal solution to the RLAP is much smaller than then one on the LAP. See [2] for a brief review, with adaptations of the most effective LAP algorithms to the RLAP case.

A common solution for the RLAP is adding  $m - n$  dummy entries, so that the RLAP becomes a LAP with  $(m - n)!$  optimal solutions. The time complexity of this solution is then  $\mathcal{O}(m^3)$ . In this paper we adopt a more efficient algorithm [3], which is a rectangular extension of the Munkres algorithm. Its time complexity is  $\mathcal{O}(n^2m)$ , which is convenient in the setting of our experiments where  $m \gg n$  (see Sect. 3).

### 3 Experiments

Experiments were performed on 10 randomly selected subjects from the Human Connectome Project (HCP) [15, 16] dMRI datasets. We preprocessed the data with single shell ( $b = 1000$ ) and isometric up-scaling (2 mm). The tractography was reconstructed using a diffusion tensor model (DTI) and the tracking was computed with the Euler Delta Crossing (EuDX) algorithm, using the DiPy toolbox.<sup>3</sup> We used the white matter query language (WMQL)[17], a parcellation-based method, to virtually dissect several types of neuroanatomical tracts: arcuate fasciculus (AF), corticospinal tract (CST), cingulum (CG), uncinate fasciculus (UF) optical radiation (OR), medial longitudinal fasciculus (MDLF), inferior longitudinal fasciculus (ILF), inferior occipitofrontal fasciculus (IFOF). Considering both left and right hemispheres, we obtained 16 different tracts for all the 10 subjects. A summary of the information after the virtual dissection are reported in Table 1, specifically the average and standard deviation of the number of streamlines and the number of voxels of all tracts.

The purpose of the experiment was to collect empirical evidence that exploiting the correspondence of streamlines across tractograms improves the alignment of tracts with respect to what affine registration can do. The experiment was conceived in the following way: after alignment, given a tract, its corresponding voxels were extracted, as well as those of the same tract in the second tractogram. The

<sup>2</sup>A partial permutation matrix is a rectangular version of the permutation matrix, i.e.  $P = [p_{ij}]_{ij} \in \{0, 1\}^{n \times m}$  and  $\sum_{j=1}^n p_{ij} = 1$  but  $\sum_{i=1}^m p_{ij} \leq 1$ .

<sup>3</sup><http://dipy.org>.



**Table 1** Data description.  
For each tract, the table reports the average and standard deviation of the number of streamlines and of voxels over ten subjects

Tract name	# Streamline	# Voxels
CST_LEFT	50 ± 41	1478 ± 725
CST_RIGHT	23 ± 17	1075 ± 478
CG_LEFT	947 ± 135	12075 ± 1602
CG_RIGHT	833 ± 100	10920 ± 1507
AF_LEFT	290 ± 107	5437 ± 1617
AF_RIGHT	186 ± 144	4046 ± 1916
UF_LEFT	189 ± 71	2913 ± 932
UF_RIGHT	171 ± 87	2583 ± 1117
OR_LEFT	78 ± 68	1547 ± 2171
OR_RIGHT	83 ± 22	2246 ± 418
MDLF_LEFT	195 ± 116	4152 ± 2022
MDLF_RIGHT	180 ± 119	3339 ± 1482
ILF_LEFT	199 ± 82	2568 ± 1923
ILF_RIGHT	133 ± 115	2475 ± 1283
IFOF_LEFT	175 ± 58	4794 ± 1068
IFOF_RIGHT	145 ± 88	4681 ± 1636

overlap over the two sets of voxels [7], in terms of true positive rate (TPR) and false discovery rate (FDR), was computed. We considered three scenarios: (1) registration-only alignment, without additional mapping of streamlines; (2) registration and mapping as nearest-neighbor (NN); (3) registration and mapping as optimal solution of the RLAP.

In each scenario, the first step was the projection of the two tractograms in a common space. The registration was performed with respect to the standard MNI space using FSL FLIRT, that implements a voxel-based affine registration [8].

For scenarios (2) and (3), the second step was concerned with the computation of the correspondence among streamlines, from a source tract  $t_A$  to a target tractogram  $T_B$ . We call the *true* target tract, as obtained through WMQL segmentation, as  $t_B$  and its approximation, through mapping or registration, as  $\hat{t}_B$ . For each tract in Table 1, we computed TPR and FDR for all possible pairs over the 10 subjects, i.e. 45 pairs. We excluded those pairs where the difference in the number of streamlines was  $\geq 60\%$ . We may reasonably assume that such extreme differences in the number of streamlines for the same tract were related to limitations in the virtual dissection with the WMQL.

**Table 2** Average, over multiple pairs of subjects, of true positive rate (TPR, higher is better) and false discovery rate (FDR, lower is better) for three methods: Registration, Registration+NN (nearest neighbor), Registration+RLAP. Each row corresponds to a different anatomical tract

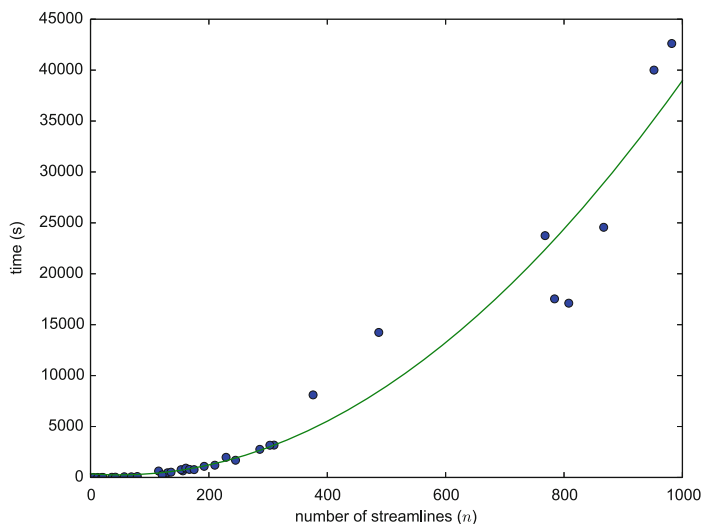
Tract name	Registration		Registration +NN		Registration +Assignment	
	TPR	FDR	TPR	FDR	TPR	FDR
CST_LEFT	0.10	0.63	0.24	0.64	<b>0.38</b>	<b>0.11</b>
CST_RIGHT	0.06	0.76	0.21	0.70	<b>0.32</b>	<b>0.32</b>
CG_LEFT	0.24	0.38	0.33	0.62	<b>0.67</b>	<b>0.20</b>
CG_RIGHT	0.25	0.37	0.36	0.56	<b>0.69</b>	<b>0.14</b>
AF_LEFT	0.15	0.55	0.27	0.69	<b>0.69</b>	<b>0.18</b>
AF_RIGHT	0.11	0.57	0.31	0.67	<b>0.67</b>	<b>0.15</b>
UF_LEFT	0.24	0.45	0.37	0.57	<b>0.71</b>	<b>0.21</b>
UF_RIGHT	0.32	0.31	0.39	0.56	<b>0.80</b>	<b>0.18</b>
OR_LEFT	0.06	0.75	0.14	0.75	<b>0.23</b>	<b>0.26</b>
OR_RIGHT	0.07	0.64	0.13	0.77	<b>0.27</b>	<b>0.30</b>
MDLF_LEFT	0.13	0.68	0.24	0.66	<b>0.53</b>	<b>0.18</b>
MDLF_RIGHT	0.15	0.48	0.24	0.70	<b>0.57</b>	<b>0.16</b>
ILF_LEFT	0.18	0.61	0.29	0.64	<b>0.67</b>	<b>0.26</b>
ILF_RIGHT	0.07	0.66	0.18	0.75	<b>0.39</b>	<b>0.13</b>
IFOF_LEFT	0.16	0.59	0.29	0.65	<b>0.66</b>	<b>0.17</b>
IFOF_RIGHT	0.16	0.31	<b>0.60</b>	0.64	0.56	<b>0.28</b>

Denoted as  $v(t)$  the set of voxels corresponding to a tract  $t$ , the quantification of the overlap between  $\hat{t}_B$  and  $t_B$  was the following:

$$\text{TPR} = \frac{|v(\hat{t}_B) \cap v(t_B)|}{|v(t_B)|} \quad (6)$$

$$\text{FDR} = \frac{|v(\hat{t}_B) \setminus v(t_B)|}{|v(\hat{t}_B)|} \quad (7)$$

In Table 2 are reported the results, in term of TPR and FDR for the three methods. We highlight in bold face the best results, i.e. highest TPR and lowest FDR for each row. The results clearly show that the computation of the correspondence of streamlines between tracts is beneficial for alignment. Even the simplest implementation of mapping, i.e. the NN heuristic explained in Sect. 2, introduces a consistent improvement over affine registration. Such improvement is much greater when adopting the optimal solution of the RLAP. The results of RLAP are consistently better for all tracts, except for the TPR of IFOF RIGHT. However, for IFOF RIGHT, the TPR of RLAP is similar to that of NN and the TDR is much lower. We noticed that the NN mapping, which computes a many-to-one correspondence, tends to underestimate the number of streamlines, i.e usually  $|\hat{t}_B| < |t_B|$ . For this reason and for the strong assumption that the affine registration is able to reduce the local and global differences, the alignment based on NN achieves lower values of TPR with respect to the RLAP.



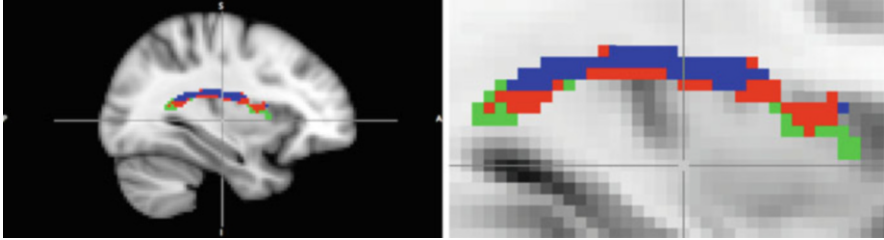
**Fig. 1** Time, in seconds, required to solve the RLAP with the rectangular version of the Munkres algorithm [3], for tracts with various sizes ( $n$ ). The quadratic dependence of the time complexity term is shown in *green*. Notice that  $m \approx 10^5$

While RLAP looks effective for tract alignment, the same solution is not viable for full tractograms alignment, because of the computational cost. In Fig. 1 it is reported the time required by the rectangular Munkres algorithm of [3], as implemented in Scikit-Learn,<sup>4</sup> to compute the optimal solution for the tracts for some of the cases in our experiments. For low values of  $n$  ( $<50$ ), the computation required less than a minute, while for large values of  $n$  ( $>600$ ) it required several hours.

In Fig. 2 we report a visual snapshot of the alignment of the arcuate fasciculus (AF) between two subjects. The picture<sup>5</sup> shows the voxels correctly mapped both by NN and RLAP (blue), those correctly mapped by only the RLAP (red), and the ones missed by both (green). In this example, no correct voxel was found by NN and not by RLAP. The benefit of RLAP with respect to NN is illustrated as a meaningful increment of the number of voxels correctly aligned (red).

<sup>4</sup><http://scikit-learn.org>.

<sup>5</sup>For simplicity we limit the view to one slice only.



**Fig. 2** Mapping of Arcuate Fasciculus (AF). The pictures (*left*: whole brain; *right*: zoomed detail) report one slice ( $x = 61, y = 53, z = 37$ ) of the projection of the AF tract from a source subject (ID=124422) to a target subject (ID=239944) of the Human Connectome Project dataset. Voxels in *blue* are the ones correctly detected by NN and RLAP, in *red* by only RLAP and in *green* the missed ones. No correct voxel was found by NN and not by RLAP

## 4 Conclusion and Future Work

In the present work we addressed the task of aligning sets of streamlines. We introduced the notion of correspondence between streamlines, that we call *mapping*, as additional step to improve the registration of tractograms based on affine transformation. We proposed to recast the problem of computing the correspondence as a rectangular linear assignment problem (RLAP). We performed an experimental assessment on real data from the Human Connectome Project dataset and, in Sect. 3, we provided strong empirical evidence of the improvement for tract alignment.

Despite the very positive results presented in Sect. 3, many questions require further investigation. First of all, the RLAP approach presented here is based on the assumptions that the mapping is injective and that the distance function between streamlines across different tractograms is meaningful. The first assumption, even though quite restrictive in principle (see Sect. 2.2), provides clearly better results than the nearest neighbor (NN) solution, which is a many-to-one mapping. Nevertheless, investigating more refined many-to-one and many-to-many solutions seems to be more anatomically meaningful. The second assumption requires that the affine registration is sufficient to make the streamline distance function meaningful across tractograms. Given that without initial registration such distance may be non-informative, this step requires further understanding on when and how registration becomes crucial. This issue provides motivation for completely avoiding the computation of streamline distances across tractograms, a direction that we recently proposed using a graph matching approach [12].

In the short term, the solution presented in this work can be improved on at least two levels: reducing the computational time and investigating the effect of different streamlines distance functions. We plan to investigate sub-optimal solutions to the RLAP, in order to reduce the computational complexity so to address the problem of mapping whole tractograms.

**Acknowledgements** The research was funded by the Autonomous Province of Trento, Call “Grandi Progetti 2012”, project “Characterizing and improving brain mechanisms of attention - ATTEND”.

Data were provided [in part] by the Human Connectome Project, WU-Minn Consortium (Principal Investigators: David Van Essen and Kamil Ugurbil; 1U54MH091657) funded by the 16 NIH Institutes and Centers that support the NIH Blueprint for Neuroscience Research; and by the McDonnell Center for Systems Neuroscience at Washington University.

## References

1. Basser, P.J., Mattiello, J., LeBihan, D.: MR diffusion tensor spectroscopy and imaging. *Biophys. J.* **66**(1), 259–267 (1994). [http://dx.doi.org/10.1016/s0006-3495\(94\)80775-1](http://dx.doi.org/10.1016/s0006-3495(94)80775-1)
2. Bijstervosch, J., Volgenant, A.: Solving the rectangular assignment problem and applications. *Ann. Oper. Res.* (2010). <http://dx.doi.org/10.1007/s10479-010-0757-3>
3. Bourgeois, F., Lassalle, J.C.: An extension of the Munkres algorithm for the assignment problem to rectangular matrices. *Commun. ACM* **14**(12), 802–804 (1971)
4. Burkard, R., Dell’Amico, M., Martello, S.: *Assignment Problems*. Society for Industrial and Applied Mathematics, 2nd edn. (2012). <http://dx.doi.org/10.1137/1.9781611972238>
5. Catani, M., Allin, M.P.G., Husain, M., Pugliese, L., Mesulam, M.M., Murray, R.M., Jones, D.K.: Symmetries in human brain language pathways correlate with verbal recall. *Proc. Natl. Acad. Sci.* **104**(43), 17163–17168 (2007)
6. Garyfallidis, E., Wassermann, D., Descoteaux, M.: Direct native-space fiber bundle alignment for group comparisons. In: *International Society for Magnetic Resonance Imaging (ISMRM)*. Milan, Italy (2014). <https://hal.inria.fr/hal-00991740>
7. Golding, D., Tittgemeyer, M., Anwender, A., Douglas, T.: A comparison of methods for the registration of tractographic fibre images. In: Robinson, P., Nel, A. (eds.) *Proceedings of the Twenty-Second Annual Symposium of the Pattern Recognition Association of South Africa*, pp. 55–59 (2011)
8. Jenkinson, M., Smith, S.: A global optimisation method for robust affine registration of brain images. *Med. Image Anal.* **5**(2), 143–156 (2001). <http://view.ncbi.nlm.nih.gov/pubmed/11516708>
9. Jonker, R., Volgenant, A.: A shortest augmenting path algorithm for dense and sparse linear assignment problems. *Computing* **38**(4), 325–340 (1987). <http://dx.doi.org/10.1007/bf02278710>
10. Kuhn, H.W.: The Hungarian method for the assignment problem. *Nav. Res. Logist.* **2**(1–2), 83–97 (1955). <http://dx.doi.org/10.1002/nav.3800020109>
11. Munkres, J.: Algorithms for the assignment and transportation problems. *J. Soc. Ind. Appl. Math.* **5**(1), 32–38 (1957)
12. Nguyen, T.B., Olivetti, E., Avesani, P.: Mapping tractography across subjects (2014). 4th NIPS Workshop on Machine Learning and Interpretation in Neuroimaging (MLINI). Accepted (forthcoming)
13. O’Donnell, L.J., Wells, W.M., Golby, A.J., Westin, C.F.F.: Unbiased groupwise registration of white matter tractography. In: *Medical Image Computing and Computer-Assisted Intervention: MICCAI - International Conference on Medical Image Computing and Computer-Assisted Intervention*, vol. 15(Pt 3), pp. 123–130 (2012). <http://www.ncbi.nlm.nih.gov/pmc/articles/PMC3638882/>
14. Raffelt, D., Tournier, J.D., Frupp, J., Crozier, S., Connelly, A., Salvado, O.: Symmetric diffeomorphic registration of fibre orientation distributions. *NeuroImage* (2011). <http://dx.doi.org/10.1016/j.neuroimage.2011.02.014JD>

15. Sotiropoulos, S.N., Jbabdi, S., Xu, J., Andersson, J.L., Moeller, S., Auerbach, E.J., Glasser, M.F., Hernandez, M., Sapiro, G., Jenkinson, M., Feinberg, D.A., Yacoub, E., Lenglet, C., Van Essen, D.C., Ugurbil, K., Behrens, T.E.: WU-Minn HCP consortium: advances in diffusion MRI acquisition and processing in the human connectome project. *NeuroImage* **80**, 125–143 (2013). <http://view.ncbi.nlm.nih.gov/pubmed/23702418>
16. Van Essen, D.C., Smith, S.M., Barch, D.M., Behrens, T.E., Yacoub, E., Ugurbil, K., Consortium, W.M.H., et al.: The Wu-Minn human connectome project: an overview. *Neuroimage* **80**, 62–79 (2013)
17. Wassermann, D., Makris, N., Rathi, Y., Shenton, M., Kikinis, R., Kubicki, M., Westin, C.F.F.: On describing human white matter anatomy: the white matter query language. In: *Medical Image Computing and Computer-Assisted Intervention: MICCAI - International Conference on Medical Image Computing and Computer-Assisted Intervention*, vol. 16(Pt 1), pp. 647–654 (2013). <http://www.ncbi.nlm.nih.gov/pmc/articles/PMC4029160/>
18. Zhang, S., Correia, S., Laidlaw, D.H.: Identifying white-matter fiber bundles in DTI data using an automated proximity-based fiber-clustering method. *IEEE Trans. Vis. Comput. Graph.* **14**(5), 1044–1053 (2008). <http://dx.doi.org/10.1109/tvcg.2008.52>

# Accelerating Global Tractography Using Parallel Markov Chain Monte Carlo

Haiyong Wu, Geng Chen, Zhongxue Yang, Dinggang Shen,  
and Pew-Thian Yap

**Abstract** Global tractography estimates brain connectivity by determining the optimal configuration of signal-generating fiber segments that best describes the measured diffusion-weighted data, promising better stability than local greedy methods with respect to imaging noise. However, global tractography is computationally very demanding and requires computation times that are often prohibitive for clinical applications. We present here a reformulation of the global tractography algorithm for fast parallel implementation amenable to acceleration using multi-core CPUs and general-purpose GPUs. Our method is motivated by the key observation that each fiber segment is affected by a limited spatial neighborhood. That is, a fiber segment is influenced only by the fiber segments that are (or can potentially be) connected to its both ends and also by the diffusion-weighted signal in its proximity. This observation makes it possible to parallelize the Markov chain Monte Carlo (MCMC) algorithm used in the global tractography algorithm so that updating of independent fiber segments can be done concurrently. The experiments show that the proposed algorithm can significantly speed up global tractography, while at the same time maintain or improve tractography performance.

---

H. Wu

Key Laboratory of Trusted Cloud Computing and Big Data Analysis, Xiaozhuang University, Nanjing, China

Department of Radiology and BRIC, UNC Chapel Hill, Chapel Hill, NC, USA

G. Chen

Data Processing Center, Northwestern Polytechnical University, Xi'an, China

Department of Radiology and BRIC, UNC Chapel Hill, Chapel Hill, NC, USA

Z. Yang

Key Laboratory of Trusted Cloud Computing and Big Data Analysis, Xiaozhuang University, Nanjing, China

D. Shen • P.-T. Yap (✉)

Department of Radiology and BRIC, UNC Chapel Hill, Chapel Hill, NC, USA

e-mail: [ptyap@med.unc.edu](mailto:ptyap@med.unc.edu)

## 1 Introduction

Diffusion magnetic resonance imaging (DMRI) is a key imaging technique for *in vivo* investigation of white matter pathways in the brain. It probes water diffusion in various directions and at various diffusion scales to characterize micro-structural compartments that are much smaller than the voxel size and presents unique opportunities for non-invasive investigation of white matter connectivity [1–8]. To trace white matter brain connections, local [9–12] or global [13, 14] tractography algorithms can be utilized.

In local algorithms [9, 10], fibers are initiated from a random or predetermined region and are then traced point-by-point using a greedy approach via small successive steps by following local voxel-wise distributions of axonal directions. These algorithms are hence susceptible to error accumulation, which might cause the reconstructed trajectories to deviate from the true trajectories [15]. On the other hand, global tractography (GT) approaches try to reconstruct all fiber trajectories simultaneously by considering their agreement with the underlying diffusion data [13, 14]. They are more resilient to error accumulation and are more robust to imaging noise and artifacts. While effective, the reconstruction of white matter trajectories for the whole brain via GT approaches usually requires much longer time than the local approaches. It was reported in [16, 17] that the computation can take up to one day on a standard PC. This high computational cost reduces the applicability of GT approaches in clinical settings.

Several algorithms were applied to accelerate local deterministic and probabilistic tractography methods via parallelization [18, 19]. They typically spawn an independent thread for each seed voxel so that the tracing of different fiber tracts can be performed in parallel. To the best of our knowledge, there is no existing discussion in the literature about the parallelization of the GT algorithm. In this paper, our goal is to leverage recent advancements in parallel big-data MCMC techniques [20] to improve the speed of the original GT algorithm proposed by Reisert and his colleagues [14], which at its core uses a popular MCMC technique called the Metropolis-Hastings algorithm. As the number of posterior samples grows, MCMC techniques guarantee asymptotically exact recovery of the posterior distribution. However, MCMC methods can be prohibitively slow, since for  $N$  data points, most methods must perform  $\mathcal{O}(N)$  operations to draw a sample. Furthermore, MCMC methods might require a large number of “burn-in” steps before producing representative samples.

Recently, an *embarrassingly parallel* approach was proposed in [20] to parallelize burn-in and sampling in MCMC. The key idea is to apply any MCMC method independently to subsets of data without requiring much communication between them. First, the data are partitioned in multiple subsets. Then an MCMC method is used to draw samples from the posterior distribution associated with each data subset. Finally, the samples resulting from all subsets are combined to form samples from the full posterior. This method is termed *embarrassingly parallel* because the processing of each subset is performed independently without communication with other subsets until the final combination stage.



Building on this concept, we provide a proof of concept in this work that the GT algorithm can be improved significantly in terms of speed by MCMC parallelization. The key observation is that the spatial extent of the influence of each fiber segment is limited. In other words, each fiber segment depends only on the fiber segments that are connected (or can potentially be connected) to its both ends and also on the diffusion-weighted signal that is in its proximity. That is, despite the fact we are trying to decrease the total fitting energy in a global sense, the influence of each fiber segment on the variation of the energy is in fact *local*. Based on this observation, significant parallelism can be harnessed for improving the speed of the GT algorithm. The data can be partitioned into statistically independent subsets similar to [20] and processed separately before combining the results to form samples for the original problem. Experimental results confirm the effectiveness of the proposed method and demonstrate that similar tractography performance can be achieved in a significantly reduced amount of time.

## 2 Method

### 2.1 Background

The goal of GT [14] is to determine the optimal configuration  $\mathcal{M}$  of a set of signal-generating fiber segments given the measured diffusion-weighted signals  $\mathcal{D}$ . That is, one is interested in determining the  $\mathcal{M}$  that maximizes the posterior probability  $P(\mathcal{M}|\mathcal{D})$  defined as

$$P(\mathcal{M}|\mathcal{D}) = \frac{1}{Z} \exp(-E_{\text{int}}(\mathcal{M}) - E_{\text{ext}}(\mathcal{M}, \mathcal{D})), \quad (1)$$

where  $E_{\text{int}}(\mathcal{M})$  and  $E_{\text{ext}}(\mathcal{M}, \mathcal{D})$  are the internal energy and the external energy, respectively,  $Z$  is the partition function. The internal energy characterizes the smoothness of the fibers and is defined as the sum of all the interaction potentials between two connected segments:

$$E_{\text{int}}(\mathcal{M}) = \lambda_{\text{int}} \sum_{(e_i^{\alpha_i \rightarrow j}, e_j^{\alpha_j \rightarrow i})} \frac{1}{l^2} (\|e_i^{\alpha_i \rightarrow j} - \bar{x}_{ij}\|^2 + \|e_j^{\alpha_j \rightarrow i} - \bar{x}_{ij}\|^2) - L, \quad (2)$$

where  $\alpha \in \{+, -\}$  indicates the positive or negative endpoint of a segment,  $e_i^{\alpha_i \rightarrow j}$  is the location of the endpoint of the  $i$ th segment that is connected to the  $j$ th fiber segment, and  $\bar{x}_{ij}$  represents the midpoint of the line that connects these two segments. Parameter  $l$  is the half length of a fiber segment and the bias  $L$  affects

the probability of connections between segments. The external energy measures the difference between the observed data  $\mathcal{D}$  and the predicted signal given by the configuration  $\mathcal{M}$ :

$$E_{\text{ext}}(\mathcal{M}, \mathcal{D}) = \lambda_{\text{ext}} \|F_{\mathcal{M}} - \mathcal{D}\| = \lambda_{\text{ext}} \int_{\mathbb{R}^3 \times \mathcal{S}^2} |F_{\mathcal{M}}(\mathbf{x}, \mathbf{n}) - \mathcal{D}(\mathbf{x}, \mathbf{n})|^2 d^3 \mathbf{x} d^2 \mathbf{n} \quad (3)$$

where  $\lambda_{\text{ext}}$  is a weighting for the external energy. Let  $\mathbf{x}_i$  and  $\mathbf{n}_i$  be respectively the position and the orientation of  $i$ th fiber segment, the signal predicted by the fiber segments at location  $\mathbf{x}$  and orientation  $\mathbf{n}$  is defined as

$$F_{\mathcal{M}}(\mathbf{x}, \mathbf{n}) = w \sum_{i=1}^N \exp(-c(\mathbf{n}^T \mathbf{n}_i)^2) \exp\left(\frac{-|\mathbf{x} - \mathbf{x}_i|^2}{\sigma^2}\right). \quad (4)$$

The constant  $w$  controls the amount of signal contribution from each fiber segment. Parameter  $\sigma > 0$  controls the spatial extent of the influence of each fiber segment. Parameter  $c > 0$  controls the shape of the signal profile generated by each fiber segment [14]. The goal of GT is to determine a configuration  $\mathcal{M}$  that maximizes the posterior distribution

$$P(\mathcal{M}|\mathcal{D}) \propto P(\mathcal{D}|\mathcal{M})P(\mathcal{M}) = \exp\left(\frac{-E(\mathcal{M}, \mathcal{D})}{T}\right), \quad (5)$$

where  $E(\mathcal{M}, \mathcal{D}) = E_{\text{int}}(\mathcal{M}) + E_{\text{ext}}(\mathcal{M}, \mathcal{D})$  is the total energy and  $T$  is the temperature associated with simulated annealing [21].

## 2.2 Parallel Global Tractography (PGT)

To maximize the posterior probability, an MCMC method called the Metropolis-Hastings (MH) algorithm [22] is employed in [14]. The MH algorithm draws samples from the posterior distribution defined in Eq. (5). However, MCMC methods usually take a long time to draw a sample, proportional to the number of data points [20]. In view of this, we randomly partition the image data into  $K$  regions that are mutually non-influential and statistically independent. Then the MH algorithm is applied in parallel by proposing changes to the fiber segments in these regions based on the corresponding transition probabilities. The proposals in these regions are accepted/rejected based on their individual acceptance ratios. The independence condition ensures that the proposals for each of the  $K$  regions can be accepted and rejected separately but in parallel. The details are described next.

We first partition the posterior density into subposterior densities [20] based on  $K$  randomly determined and statistically independent subregions:

$$P(\mathcal{M}|\mathcal{D}) = P(\mathcal{M}_0|\mathcal{D}) \prod_{k=1}^K P(\mathcal{M}_k|\mathcal{D}, \mathcal{M}_0), \quad (6)$$

where  $\mathcal{M}_0$  denotes configuration of the fiber segmentations in the region that separates the  $K$  regions to ensure their independence, and  $\mathcal{M}_k$  denotes the configuration of the fiber segments in the  $k$ -th region, including their existence, spatial positions, orientations, and connections at both ends to other fiber segments. Proposals for modification of configuration are made for the fiber segments in each region according to its subposterior density by randomly selecting at each time a fiber segment, perturbing it using a creation/deletion and shifting mechanism, and examining if the regional energy can be decreased. In this process,  $\mathcal{M}_0$  remains fixed and  $\{\mathcal{M}_k\}$  are updated. After  $\{\mathcal{M}_k\}$  are sufficiently updated, they are combined to form  $\mathcal{M}$ . The random partitioning of the image space into subregions is performed iteratively so that each time the fiber configurations of a different set of  $K$  random subregions can be updated.

The decision of whether to accept a proposal is based on the individual Green's ratio of the  $k$ -th region

$$R_k = \frac{P(\mathcal{M}'_k|\mathcal{D}, \mathcal{M}_0)Q(\mathcal{M}_k|\mathcal{M}'_k)}{P(\mathcal{M}_k|\mathcal{D}, \mathcal{M}_0)Q(\mathcal{M}'_k|\mathcal{M}_k)}, \quad (7)$$

where  $Q(\mathcal{M}'_k|\mathcal{M}_k)$  is the transition probability associated with the MH algorithm. The internal energy contributed by the fiber segments in the  $k$ -th region alone is

$$E_{\text{int}}(\mathcal{M}_k) = \lambda_{\text{int}} \sum_{(e_i^{\alpha_i \rightarrow j}, e_j^{\alpha_j \rightarrow i}), i, j \in \mathcal{N}_k} \frac{1}{l^2} (||e_i^{\alpha_i \rightarrow j} - \bar{x}_{ij}||^2 + ||e_j^{\alpha_j \rightarrow i} - \bar{x}_{ij}||^2) - L \quad (8)$$

and the external energy is

$$E_{\text{ext}}(\mathcal{M}_k, \mathcal{D}) = \lambda_{\text{ext}} \int_{\mathcal{N}_k \times S^2} |F_{\mathcal{M}}(\mathbf{x}, \mathbf{n}) - \mathcal{D}(\mathbf{x}, \mathbf{n})|^2 d\mathbf{x}^3 d\mathbf{n}^2. \quad (9)$$

where  $\mathcal{N}_k$  is the index set containing the indices of all fiber segments in the  $k$ -th region. The subposterior distribution is

$$P(\mathcal{M}_k|\mathcal{D}, \mathcal{M}_0) \propto P(\mathcal{M}_k, \mathcal{M}_0)P(\mathcal{D}|\mathcal{M}_k, \mathcal{M}_0). \quad (10)$$

Note that some proposals are parallelizable and some are not. For each fiber segment, the change in internal energy associated with the creation/deletion and shifting proposals is affected only by the fiber segments it is (or will be) connected to.

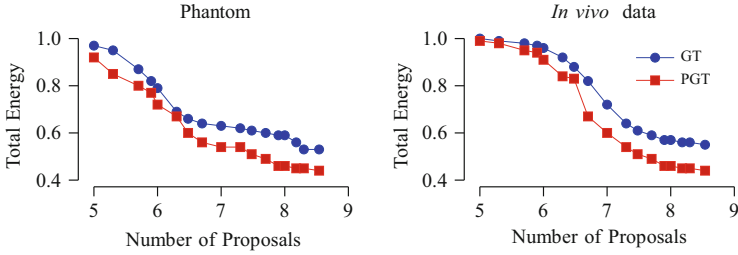
The change in external energy involves only the diffusion signals in a localized neighborhood surrounding the fiber segment. Hence, the creation/deletion and shifting proposals can be performed independently and simultaneously in different subregions. However, the connection/disconnection proposals, which attempt to determine new fibers with lower energy, involve a larger spatial extent and are hence more difficult to parallelize. To overcome this problem, we alternate between parallel proposals (i.e., creation/deletion and shifting) and serial proposals (i.e., connection/disconnection) according to MH transition probabilities assigned to them. In summary, the PGT algorithm involves repeating the following steps until convergence.

1. **Data Partitioning:** Randomly partitioning the image space into  $K$  subregions, between which the configurations of the fiber segments are not dependent.
2. **Parallel Proposals:** Make creation/deletion and shifting proposals in parallel for the fiber segments in these regions according to the corresponding transition probabilities and accept/reject the proposals based on their acceptance ratios. Repeat this step for a sufficient number of times.
3. **Serial Proposals:** Make connection/disconnection proposals and determine fiber tracts that better explain the data.

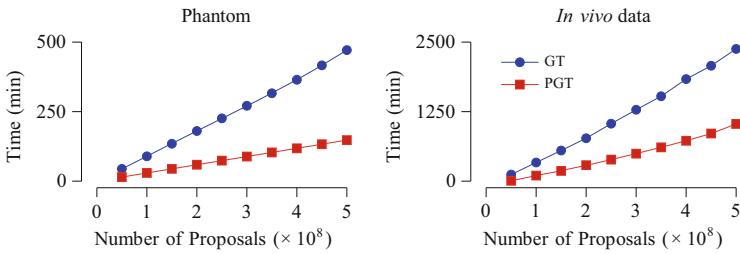
### 3 Evaluation

We report here preliminary results from our evaluation of the PGT algorithm using synthetic and in vivo data. The synthetic data consist of a set of  $60 \times 60$  diffusion-weighted images, simulating fiber bundles crossing at  $90^\circ$ . The signal at each voxel was generated using a tensor model or its mixture with principal diffusivities [23]  $\lambda_1 = 1.5 \times 10^{-3} \text{ mm}^2/\text{s}$ ,  $\lambda_2 = \lambda_3 = 1.0 \times 10^{-3} \text{ mm}^2/\text{s}$  and diffusion weighting  $b = 2000 \text{ s}/\text{mm}^2$ . The in vivo dataset for an adult subject was acquired with  $(2 \text{ mm})^3$  resolution using a Siemens 3T TIM Trio MR scanner. Diffusion gradients were applied in 120 non-collinear directions with diffusion weighting  $b = 2000 \text{ s}/\text{mm}^2$ .

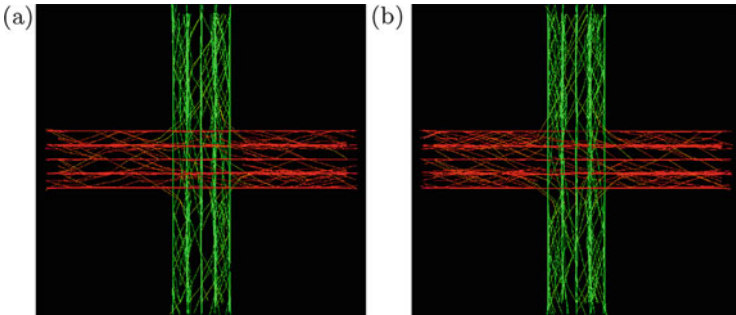
First, we compared the convergence of GT (PGT with one thread) and PGT (eight threads). The parameters used for GT and PGT were set as suggested in [14]. Figure 1 shows the plots of the total energy against the number of proposals for the synthetic and in vivo data. The total energy decreases rapidly at the beginning when less proposals have been made and when the configuration of the fiber segments is more arbitrary. The decrease slows down and flattens when the configuration becomes stable. It can also be observed that PGT is slightly advantageous over GT in its ability to yield lower total energy. This can be attributed to the fact that multiple adjustments of fiber segments are done concurrently, making it easier and faster to reach a configuration with lower energy.



**Fig. 1** Normalized total energy plotted against the number of proposals (in logarithmic scale)



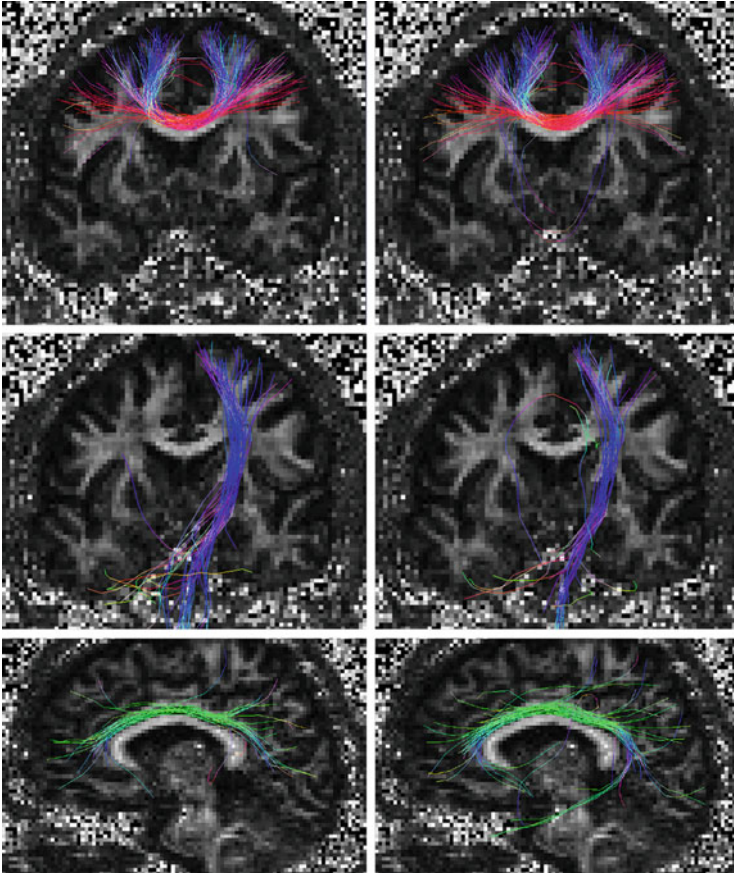
**Fig. 2** Time costs of GT and PGT



**Fig. 3** Tractography results on synthetic data using (a) GT and (b) PGT

Next, we evaluated the speed improvement given by PGT over GT. The evaluation was performed using an iMac with Intel 4-Core i7 CPU (3.4 GHz each) and 8 GB of DDR3 RAM. Figure 2 shows that, on both synthetic and in vivo data, PGT always consumes less than approximately 1/3 the time required by GT. Note that it is not possible to achieve the ideal 8× speed increase because the GT algorithm is only partially parallelized, as discussed in Sect. 2.2. Part of the time also goes to the computational overhead involved in the parallelized implementation.

Figure 3 shows the tractography results of GT and PGT on the synthetic data after  $2 \times 10^8$  proposals. Both GT and PGT create reasonable fiber tracts that are in agreement with the data. The normalized total energy values for GT and PGT



**Fig. 4** Fiber bundles given by GT (*left*) and PGT (*right*)

are 0.56 and 0.45, respectively. For the in vivo data, fiber bundles extracted with multiple ROIs [24] are shown in Fig. 4. These fiber bundles are similar to those in [14]: the part of the callosal fibers coming from the left motor cortex (CCtoM1), corticospinal tracts to the left motor cortex (CST), and the cingulum (CG). These are shown from top to bottom in the figure. PGT results in fiber bundles that are similar to GT, but in a fraction of time.

## 4 Discussion and Future Work

The proposed algorithm helps to reduce the time cost associated with the global optimization process required in global tractography. We run in parallel multiple independent chains of MCMC on a number of dynamically determined subregions,

resulting in faster convergence and producing results that are comparable to the non-parallelized version. Future implementation based on GPUs will further improve the speed of global tractography and hence its feasibility in large-scale studies.

**Acknowledgements** This work was supported in part by an Educational Science in Jiangsu Province grant (D201501125), a UNC BRIC-Radiology start-up fund, and NIH grants (EB006733, EB008374, EB009634, MH088520, AG041721, and MH100217).

## References

1. Basser, P.J., Pajevic, S., Pierpaoli, C., Duda, J., Aldroubi, A.: In vivo fiber tractography using DT-MRI data. *Magn. Reson. Med.* **44**(4), 625–632 (2000)
2. Yap, P.T., Wu, G., Shen, D.: Human brain connectomics: networks, techniques, and applications. *IEEE Signal Process. Mag.* **27**(4), 131–134 (2010)
3. Yap, P.T., Fan, Y., Chen, Y., Gilmore, J., Lin, W., Shen, D.: Development trends of white matter connectivity in the first years of life. *PLoS ONE* **6**(9), e24678 (2011)
4. Wee, C.Y., Yap, P.T., Li, W., Denny, K., Browndyke, J.N., Potter, G.G., Welsh-Bohmer, K.A., Wang, L., Shen, D.: Enriched white matter connectivity networks for accurate identification of MCI patients. *NeuroImage* **54**(3), 1812–1822 (2011)
5. Wee, C.Y., Yap, P.T., Zhang, D., Denny, K., Browndyke, J.N., Potter, G.G., Welsh-Bohmer, K.A., Wang, L., Shen, D.: Identification of MCI individuals using structural and functional connectivity networks. *NeuroImage* **59**(3), 2045–2056 (2012)
6. Shi, F., Yap, P.T., Gao, W., Lin, W., Gilmore, J.H., Shen, D.: Altered structural connectivity in neonates at genetic risk for schizophrenia: a combined study using morphological and white-matter networks. *NeuroImage* **62**(3), 1622–1633 (2012)
7. Jin, Y., Shi, Y., Zhan, L., de Zubicaray, G., McMahon, K.L., Martin, N.G., Wright, M.J., Thompson, P.M., et al.: Labeling white matter tracts in HARDI by fusing multiple tract atlases with applications to genetics. In: *IEEE International Symposium on Biomedical Imaging (ISBI)* (2013)
8. Jin, Y., Shi, Y., Zhan, L., Gutman, B.A., de Zubicaray, G.I., McMahon, K.L., Wright, M.J., Toga, A.W., Thompson, P.M.: Automatic clustering of white matter fibers in brain diffusion MRI with an application to genetics. *NeuroImage* **100**, 75–90 (2014)
9. Mori, S., Crain, B.J., Chacko, V., Van Zijl, P.: Three-dimensional tracking of axonal projections in the brain by magnetic resonance imaging. *Ann. Neurol.* **45**(2), 265–269 (1999)
10. Zhang, F., Hancock, E.R., Goodlett, C., Gerig, G.: Probabilistic white matter fiber tracking using particle filtering and von Mises-Fisher sampling. *Med. Image Anal.* **13**(1), 5–18 (2009)
11. Yap, P.T., Gilmore, J.H., Lin, W., Shen, D.: Longitudinal tractography with application to neuronal fiber trajectory reconstruction in neonates. In: *Medical Image Computing and Computer-Assisted Intervention (MICCAI)*, vol. 14(Pt 2), pp. 66–73 (2011)
12. Yap, P.T., Gilmore, J., Lin, W., Shen, D.: PopTract: population-based tractography. *IEEE Trans. Med. Imaging* **30**(10), 1829–1840 (2011)
13. Kreher, B., Mader, I., Kiselev, V.: Gibbs tracking: a novel approach for the reconstruction of neuronal pathways. *Magn. Reson. Med.* **60**(4), 953–963 (2008)
14. Reisert, M., Mader, I., Anastasopoulos, C., Weigel, M., Schnell, S., Kiselev, V.: Global fiber reconstruction becomes practical. *NeuroImage* **54**, 955–962 (2011)
15. Fillard, P., Descoteaux, M., Goh, A., Gouttard, S., Jeurissen, B., Malcolm, J., Ramirez-Manzanares, A., Reisert, M., Sakaie, K., Tensaouti, F., Yo, T., Mangin, J., Poupon, C.: Quantitative evaluation of 10 tractography algorithms on a realistic diffusion MR phantom. *NeuroImage* **56**(1), 220–234 (2011)

16. Reisert, M., Mader, I., Kiselev, V.: Global reconstruction of neuronal fibres. In: Proceedings of MICCAI Workshop on Diffusion Modelling (2009)
17. Neher, P.F., Stieltjes, B., Reisert, M., Reicht, I., Meinzer, H.P., Fritzsche, K.H.: MITK global tractography. In: SPIE Medical Imaging, pp. 83144–83149. International Society for Optics and Photonics, SPIE, San Diego (2012)
18. McGraw, T., Nadar, M.: Stochastic DT-MRI connectivity mapping on the GPU. *IEEE Trans. Vis. Graph.* **13**(6), 1504–1511 (2007)
19. Jungsoo, L., Dae-Shik, K.: Acceleration of DTI tractography using multi GPU- parallel processing. *Int. J. Imaging Syst. Technol.* **23**(3), 256–264 (2013)
20. Neiswanger, W., Wang, C., Xing, E.: Asymptotically exact, embarrassingly parallel MCMC. In: The Annual Conference on Uncertainty in Artificial Intelligence (UAI), pp. 623–632 (2013)
21. Aarts, E., Korst, J.: *Simulated Annealing and Boltzmann Machines: A Stochastic Approach to Combinatorial Optimization and Neural Computing*. Wiley, New York (1988)
22. Hastings, W.K.: Monte Carlo sampling methods using Markov chains and their applications. *Biometrika* **57**(1), 97–109 (1970)
23. Yap, P.T., Shen, D.: Spatial transformation of DWI data using non-negative sparse representation. *IEEE Trans. Med. Imaging* **31**(11), 2035–2049 (2012)
24. Wakana, S., Caprihan, A., Panzenboeck, M.M., Fallon, J.H., Perry, M., Gollub, R.L., Hua, K., Zhang, J., Jiang, H., Dubey, P., Blitz, A., van Zijl, P., Mori, S.: Reproducibility of quantitative tractography methods applied to cerebral white matter. *NeuroImage* **36**, 630–644 (2007)



# Adaptive Enhancement in Diffusion MRI Through Propagator Sharpening

Tom Dela Haije, Neda Sepasian, Andrea Fuster, and Luc Florack

**Abstract** In this short note we consider a method of enhancing diffusion MRI data based on analytically deblurring the ensemble average propagator. Because of the Fourier relationship between the normalized signal and the propagator, this technique can be applied in a straightforward manner to a large class of models. In the case of diffusion tensor imaging, a commonly used ‘ad hoc’ min-normalization sharpening method is shown to be closely related to this deblurring approach. The main goal of this manuscript is to give a formal description of the method for (generalized) diffusion tensor imaging and higher order apparent diffusion coefficient-based models. We also show how the method can be made adaptive to the data, and present the effect of our proposed enhancement on scalar maps and tractography output.

## 1 Introduction

Many advanced tractography techniques allow tracts to deviate from the principal direction of diffusion. This can be advantageous in terms of robustness to noise, but if the diffusion profile is not sufficiently sharp the tracts can still deviate significantly from the main diffusion direction. This is just one example of issues that inspired various preprocessing techniques that have been proposed, such as the log-Euclidean framework to handle noisy data [1], spherical deconvolution of the diffusion tensor to enhance the anisotropy [10], and sharpening by raising the diffusion tensors to a certain power [19].

The purpose of this manuscript is the introduction of a simple enhancement method based on deblurring the ensemble average propagator. The theoretical basis of the method is described in Sect. 2, and explicit expressions for specific models

---

T. Dela Haije (✉) • N. Sepasian • A. Fuster • L. Florack  
Eindhoven University of Technology, Den Dolech 2, P.O. Box 513, 5600MB Eindhoven,  
Noord-Brabant, The Netherlands  
e-mail: [T.C.J.Dela.Haije@tue.nl](mailto:T.C.J.Dela.Haije@tue.nl)

are presented in Sect. 2.2. We perform some basic experiments on diffusion tensor imaging to illustrate the potential of the method (Sect. 3) of which the results are presented in Sect. 4.

## 2 Theory

### 2.1 The Enhanced Diffusion Signal

The ensemble average propagator  $P_\Delta(\mathbf{r})$  represents the likelihood of a displacement  $\mathbf{r}$  occurring in a voxel within diffusion time  $\Delta$ , which is assumed to satisfy  $P_\Delta(-\mathbf{r}) = P_\Delta(\mathbf{r})$ . Under the narrow-pulse approximation, i.e., when the duration  $\delta$  of the applied<sup>1</sup> diffusion encoding gradients  $\mathbf{g}$  is much smaller than  $\Delta$ ,  $P_\Delta$  is related to the normalized signal  $S_\Delta(\mathbf{q})$  through a Fourier transform [4]:

$$S_\Delta(\mathbf{q}) = \mathcal{F}^{-1}\{P_\Delta\}(\mathbf{q}) := \int_{\mathbb{R}^3} e^{i2\pi \mathbf{q}\mathbf{r}} P_\Delta(\mathbf{r}) d\mathbf{r}. \quad (1)$$

Here  $\mathbf{q} := (2\pi)^{-1}\gamma\delta\mathbf{g}$  is the wave vector encoding information regarding the applied gradients, with  $\gamma$  the gyromagnetic ratio. In the typical situation where  $\delta \approx \Delta$ , a relation analogous to Eq. (1) holds [22, 24]. One generally acquires a number of samples of  $S_\Delta$  for various  $\mathbf{q}$  in each voxel, though we will not state this voxel dependence explicitly until Sect. 4.

Interesting features of the propagator, like differences between angular diffusivities, can be difficult to detect. This difficulty is aggravated by e.g. sparse sampling of the Fourier space, which has a blurring effect. To this end we consider what happens when the propagator  $P_\Delta$  is blurred with a Gaussian  $G_\sigma(\mathbf{r}) := \frac{1}{(\sqrt{2\pi}\sigma)^3} e^{-\frac{\|\mathbf{r}\|^2}{2\sigma^2}}$ ,  $\sigma \geq 0$ , and define  $Q_\Delta$  as the deconvolution of  $P_\Delta$ , i.e., such that  $P_\Delta = G_\sigma * Q_\Delta$ . Consequently,

$$S_\Delta = \mathcal{F}^{-1}\{G_\sigma * Q_\Delta\} = \mathcal{F}^{-1}\{G_\sigma\} \mathcal{F}^{-1}\{Q_\Delta\}. \quad (2)$$

Using  $\mathcal{F}^{-1}\{G_\sigma\}(\mathbf{q}) = e^{-2\pi^2\sigma^2\|\mathbf{q}\|^2}$  we obtain

$$\rho_\sigma(S_\Delta)(\mathbf{q}) := \mathcal{F}^{-1}\{Q_\Delta\}(\mathbf{q}) = e^{2\pi^2\sigma^2\|\mathbf{q}\|^2} S_\Delta(\mathbf{q}), \quad (3)$$

where  $\rho_\sigma$  is the effective deblurring operator acting on the signal.

We note that  $\sigma$  is constrained by the fact that the signal  $S_\Delta$ , and thus also the sharpened signal  $\rho_\sigma(S_\Delta)(\mathbf{q})$ , is required to be strictly less than 1 everywhere except

---

<sup>1</sup>We assume a standard pulsed gradient spin echo sequence.

in the origin.<sup>2</sup> This means that  $\sigma$  should be chosen such that

$$\forall \mathbf{q} \neq \mathbf{0} \quad e^{2\pi^2 \sigma^2 \|\mathbf{q}\|^2} S_\Delta(\mathbf{q}) < 1. \quad (4)$$

Equation (3) can be used to process raw diffusion MRI data, but this should be avoided due to ill-posedness. Note for example that for large values of  $\|\mathbf{q}\|$ , the presence of noise means Eq. (4) will impose  $\sigma^2 = 0$ . In fact, it is desirable to apply the sharpening after  $S_\Delta$  is expressed in terms of a specific model, the specific structure of which can be exploited to simplify Eq. (3). In the following section we present details for three commonly used models.

## 2.2 Simplified Deconvolution for Specific Models

### Diffusion Tensor Imaging

In Diffusion Tensor Imaging (DTI) [3], the ensemble average propagator is assumed to be a multivariate normal distribution. The signal model is of the form

$$S_\Delta(\mathbf{q}) = e^{-\tau \mathbf{q}^T \mathbf{D} \mathbf{q}}, \quad (5)$$

with a constant  $\tau := 4\pi^2 (\Delta - \frac{\delta}{3})$  and with  $\mathbf{D}$  the positive-definite second order diffusion tensor. It follows that the signal corresponding to the sharpened propagator is given by

$$\rho_\sigma(S_\Delta)(\mathbf{q}) = e^{-\tau \mathbf{q}^T \mathbf{D} \mathbf{q} + 2\pi^2 \sigma^2 \mathbf{q}^T \mathbf{I} \mathbf{q}} = e^{-\tau \mathbf{q}^T (\mathbf{D} - \frac{2\pi^2 \sigma^2}{\tau} \mathbf{I}) \mathbf{q}} \quad (6)$$

with  $\mathbf{I}$  the  $3 \times 3$  identity matrix. In this case the sharpening consists therefore simply of subtracting a constant value (depending on the chosen  $\sigma$ ) from the diagonal elements of the diffusion tensor  $\mathbf{D}$ .

Note that the diffusion tensor is required to be positive-definite, which imposes a cap on the allowed values for  $\sigma$ :

$$\frac{2\pi^2 \sigma^2}{\tau} < \lambda_{\min}. \quad (7)$$

Here  $\lambda_{\min}$  is the smallest eigenvalue. This constraint corresponds exactly to Eq. (4).

---

<sup>2</sup>This follows from Eq. (1) under some regularity conditions.

## Apparent Diffusion Coefficient Models

For higher order models based on the apparent diffusion coefficient, the signal is described by [11, 25]

$$S_{\Delta}(\mathbf{q}) = e^{-\tau ADC(\mathbf{q})}, \quad (8)$$

in which the apparent diffusion coefficient  $ADC(\mathbf{q})$  is assumed to satisfy

$$ADC(\lambda \mathbf{q}) = \lambda^2 ADC(\mathbf{q}) \quad (9)$$

for  $\lambda \in \mathbb{R}$ . Applying Eq. (3) to this model gives

$$\rho_{\sigma}(S_{\Delta})(\mathbf{q}) = e^{-\tau ADC(\mathbf{q}) + 2\pi^2 \sigma^2 \|\mathbf{q}\|^2}, \quad (10)$$

a common ‘ad-hoc’ enhancement principle already adopted in practice [26]. The  $ADC$  is typically expressed in terms of a fully symmetric higher order (Cartesian) tensor or in terms of real-valued spherical harmonic functions, both of which transform in a straightforward manner under the proposed enhancement.

In the case of a tensor expansion the  $ADC$  is parameterized by symmetric coefficients  $T^{i_1 \dots i_{2L}}$ .  $L$  is called the order of the expansion. By defining  $\hat{\mathbf{q}} := \mathbf{q}/\|\mathbf{q}\| \in S^2$  as the direction of the wave vector, we can write the tensor expansion of the  $ADC$  as

$$ADC(\mathbf{q}) = \|\mathbf{q}\|^2 \sum_{i_1, \dots, i_{2L}=1}^3 T^{i_1 \dots i_{2L}} \hat{q}_{i_1} \dots \hat{q}_{i_{2L}}, \quad (11)$$

where  $\hat{q}_i$  denotes the  $i$ th component of  $\hat{\mathbf{q}}$  in Cartesian coordinates. Plugging Eq. (11) into Eq. (9) gives

$$\rho_{\sigma}(S_{\Delta})(\mathbf{q}) = e^{-\tau \|\mathbf{q}\|^2 \left[ \sum_{i_1, \dots, i_{2L}=1}^3 \left( T^{i_1 \dots i_{2L}} - \frac{2\pi^2 \sigma^2}{\tau} I^{i_1 \dots i_{2L}} \right) \hat{q}_{i_1} \dots \hat{q}_{i_{2L}} \right]}, \quad (12)$$

in which the tensor with components  $I^{i_1 \dots i_{2L}}$  has the property that it produces one when contracted with any unit vector  $\hat{\mathbf{q}}$ , viz.

$$I^{i_1 \dots i_{2L}} = \delta^{(i_1 i_2} \dots \delta^{i_{2L-1} i_{2L})}. \quad (13)$$

Here  $\delta^{ij}$  is 1 for  $i = j$  and 0 otherwise, and parentheses denote index symmetrization [21, p. 126]. For  $L = 2$  for example, the only non-zero components (excluding symmetries) are given by Özarlsan et al. [27]

$$I^{1111} = I^{2222} = I^{3333} = 3I^{1122} = 3I^{1133} = 3I^{2233} = 1. \quad (14)$$

The real-valued and symmetrical spherical harmonics are defined [8] for  $l = 0, 2, \dots$  and  $-l \leq m \leq l$  as

$$\tilde{Y}_l^m(\hat{\mathbf{q}}) := \begin{cases} \sqrt{2} \operatorname{Re} [Y_l^m(\hat{\mathbf{q}})] & m < 0 \\ Y_l^0(\hat{\mathbf{q}}) & m = 0 \\ \sqrt{2} \operatorname{Im} [Y_l^m(\hat{\mathbf{q}})] & m > 0 \end{cases}, \quad (15)$$

in which  $\operatorname{Re}$  and  $\operatorname{Im}$  extract the real and imaginary parts of the spherical harmonics basis function  $Y_l^m$  (seismological convention) respectively. The  $ADC$  is then parameterized by the spherical harmonics coefficients  $c_l^m$  giving

$$ADC(\mathbf{q}) = \|\mathbf{q}\|^2 \sum_{l=0}^L \sum_{m=-2l}^{2l} c_{2l}^m \tilde{Y}_{2l}^m(\hat{\mathbf{q}}), \quad (16)$$

with  $2L$  again the maximum order of the expansion. Since  $\tilde{Y}_0^0(\hat{\mathbf{q}}) = (2\sqrt{\pi})^{-1}$  is the only constant basis function, sharpening in the spherical harmonics basis has the simple form

$$\rho_\sigma(S_\Delta)(\mathbf{q}) = e^{-\tau \|\mathbf{q}\|^2} \left[ (c_0^0 - \frac{4\pi^{5/2}\sigma^2}{\tau}) \tilde{Y}_0^0(\hat{\mathbf{q}}) + \sum_{l=1}^L \sum_{m=-2l}^{2l} c_{2l}^m \tilde{Y}_{2l}^m(\hat{\mathbf{q}}) \right], \quad (17)$$

and so sharpening boils down to subtracting the constant  $\frac{4\pi^{5/2}\sigma^2}{\tau}$  from the coefficient  $c_0^0$ .

There are no known conditions on the coefficients (independent of the chosen basis) that impose the constraint in Eq. (4) exactly, so one would have to solve Eq. (4) numerically when explicit constraints are needed. The constraint does simplify significantly though:

$$\sigma^2 < \min_{\{\mathbf{q} \mid \|\mathbf{q}\|=1\}} \left[ \frac{\tau}{2\pi^2} ADC(\mathbf{q}) \right]. \quad (18)$$

Alternatively one could check if the coefficients satisfy a sufficient (but *not* necessary) condition for positive-definiteness [14].

## Generalized Diffusion Tensor Imaging

The last model we consider is another generalization of DTI proposed by Liu et al. [20]. In this case the signal is modeled as

$$S_\Delta(\mathbf{q}) = e^{-\sum_{i=2}^L \tau_i \sum_{j_1, \dots, j_i=1}^3 D^{j_1 \dots j_i} q_{j_1} \dots q_{j_i}}, \quad (19)$$

with  $\tau_i := (2\pi)^i (\Delta - \frac{i-1}{i+1} \delta)$  and  $D^{j_1 \dots j_i}$  the components of the generalized diffusion tensor, and now  $L$  the maximum order considered (in this case not forced to be

even). In this case the analogy with DTI is immediately apparent, and we observe that the sharpening is achieved by subtracting the value  $\frac{2\pi^2\sigma^2}{\tau}$  from the coefficients  $D^{11}$ ,  $D^{22}$ , and  $D^{33}$ . The same holds for more specific models of this general form, like diffusional kurtosis imaging [18].

Again there are no known conditions on the coefficients  $D^{j_1 \dots j_i}$  that enforce Eq. (4) generally, and unlike in the previous section Eq. (4) does not simplify. There do exist similar sufficient conditions that can be useful in this context [7, 15].

### 2.3 Adaptive Enhancement

To apply enhancement the user would have to select a reasonable value for  $\sigma$ . We know from Eq. (4) that if we allow the sharpening parameter  $\sigma$  to surpass the given limit, then the sharpening will produce incorrect results. A single globally optimal value for  $\sigma$  will thus, provided it exists, be based on a fraction of the globally smallest eigenvalue. Let us define the theoretical bound on  $\sigma$  as

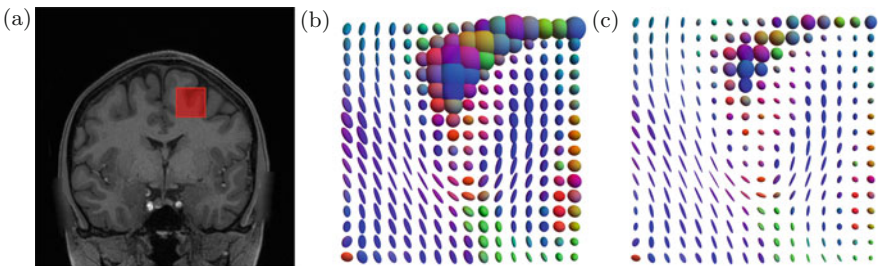
$$\epsilon := \min_{\mathbf{x} \in \Omega} \max_{\sigma \in \mathbb{R}} \left\{ \sigma \mid \forall_{\mathbf{q} \neq \mathbf{0}} \rho_{\sigma}(S_{\Delta})(\mathbf{x}, \mathbf{q}) < 1 \right\}, \quad (20)$$

where  $\mathbf{x} \in \Omega \subset \mathbb{R}^3$  specifies a voxel in the region  $\Omega$ , which will typically comprise all voxels in the brain, and where we include the  $\mathbf{x}$ -dependence of the signal  $S_{\Delta}$ . The enhancement operator is then defined as

$$\rho_f^{\text{global}}(S_{\Delta})(\mathbf{x}, \mathbf{q}) := \rho_{f\epsilon}(S_{\Delta})(\mathbf{x}, \mathbf{q}), \quad (21)$$

where  $f \in [0, 1]$  is a user-selected fraction of  $\epsilon$  that determines the sharpening strength. The effect of sharpening for a number of DTI tensors is shown in Fig. 1.

Though a single parameter value for an entire data set makes sense from a theoretical perspective, in practice it can be rather limiting. Therefore we propose to



**Fig. 1** Illustration of adaptive enhancement for DTI in the cortex (Human Connectome Project data set, see Sect. 3). (a) T1 weighted data with the *red box* indicating the investigated region. (b) The tensors in the region indicated in (a). (c) The enhanced tensors of (b) after applying Eq. (22) with  $f = 0.5$

select a global fraction  $f$  of the *local* bound  $\epsilon(\mathbf{x})$ . This locally adaptive enhancement can be defined as

$$\rho_f^{\text{local}}(S_\Delta)(\mathbf{x}, \mathbf{q}) := \rho_{f \cdot \epsilon(\mathbf{x})}(S_\Delta)(\mathbf{x}, \mathbf{q}). \quad (22)$$

In this case  $f$  is still a global parameter, but the bound  $\epsilon$  is now a function of position:

$$\epsilon(\mathbf{x}) := \max_{\sigma \in \mathbb{R}} \left\{ \sigma \mid \forall \mathbf{q} \neq \mathbf{0} \quad \rho_\sigma(S_\Delta)(\mathbf{x}, \mathbf{q}) < 1 \right\}. \quad (23)$$

The effect this operator has depends on the type of diffusion in a voxel, and we can make the following observations, see also Fig. 1.

1. Voxels with large and relatively isotropic diffusion (e.g. in the ventricles) are affected the strongest; the amount of diffusion is decreased while the anisotropy is increased slightly.
2. In areas where the diffusion is anisotropic (white matter), the amount of diffusion decreases a little bit, while anisotropy increases far more significantly.
3. With small isotropic diffusion, both the (absolute) amount of diffusion and the anisotropy remain relatively untouched.

## 2.4 Relation to Other Sharpening Methods

The sharpening method discussed here is similar to, but distinctly different from techniques like spherical deconvolution [9, 10]. A precise description of their relation is subject of future work. The method also has obvious ties to the work of Canales-Rodríguez et al. [5], who looked at deconvolving a fully reconstructed propagator (based on diffusion spectrum imaging) with a sinc function.

## 3 Methods

The first experiment we present in the next section illustrates the effect of the method on scalar maps, where it provides a simple means to improve contrast. As a preliminary investigation into its use as a pre-processing step for further analysis, we additionally present results on DTI tractography. For this second experiment we select two deterministic tractography algorithms; a streamline method that traces the vector field defined by the main eigenvector of the diffusion tensor, and a multi-valued geodesic tractography method.

Since the enhancement presented here does not change the main directions of diffusivity, its use in streamline tractography is limited to a modification of the boundary conditions (like the stopping criterion). In geodesic tractography fibers are reconstructed as minimum length paths, i.e., the geodesics in a given metric

space, where the main assumption is that the fibers tend to follow the path of the most efficient diffusion propagation [16]. Specifically, we use a recently introduced geodesic tractography technique that obtains these pathways as solutions of Euler-Lagrange equations in Riemannian or Finslerian manifolds [29]. This approach can capture (multivalued) geodesics connecting two given points or regions by considering the geodesics as functions of position and orientation. Since in this case tractography relies on the entire diffusion profile instead of just the main directions of diffusion, enhancement has a more pronounced effect. Though there are alternatives [12, 13, 17, 28], we use the inverse of the diffusion tensor as the metric as it is the most well-known definition.

Apart from the proposed enhancement we use a simple power transform as an alternative diffusion tensor imaging pre-processing step for a comparison [19, 30]. The power sharpening depends on the parameter  $s$ , and is given by the matrix power of the diffusion tensor:

$$(\mathbf{D}, s) \mapsto \mathbf{D}^s. \quad (24)$$

We use two data sets to perform the experiments. The first data set (referred to as the Siemens data set) was acquired with a 3T Siemens scanner at a resolution of  $1 \times 1 \times 1 \text{ mm}^3$  and a  $b$ -value of  $1000 \text{ s/mm}^2$  (66 gradient directions). The second data set is provided by the Human Connectome Project (subject ID 100307, preprocessed, weighted linear least squares DTI reconstruction based on the  $b = 1000 \text{ s/mm}^2$  shell), WU-Minn Consortium (Principal Investigators: David Van Essen and Kamil Ugurbil; 1U54MH091657) funded by the 16 NIH Institutes and Centers that support the NIH Blueprint for Neuroscience Research; and by the McDonnell Center for Systems Neuroscience at Washington University [32].

The regions of interest are selected within the corpus callosum and derived from the expert-annotated Mori tract atlas [23]. Experiments were performed with in-house software and with the vIST/e software framework.<sup>3</sup> With geodesic tractography two seed points are placed in each voxel, and we assign four random orientations to each seed point from an elliptic cone around the main eigenvector [29]. In all tracking experiments the algorithms terminate once the fractional anisotropy gets below 0.1.

Since there is no ground truth available to quantify the tractography, we look at the true positive percentile defined as the percentage of fibers which connect a seed region with given regions of interest selected using available white matter bundle atlases [6, 23].

---

<sup>3</sup><http://bmia.bmt.tue.nl/software/viste/>.



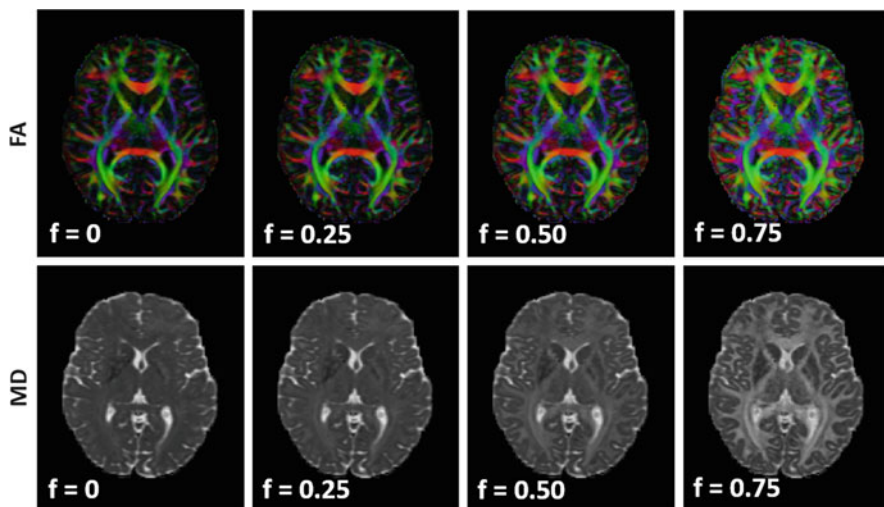
## 4 Results

### 4.1 Adaptive Sharpening of Scalar Maps

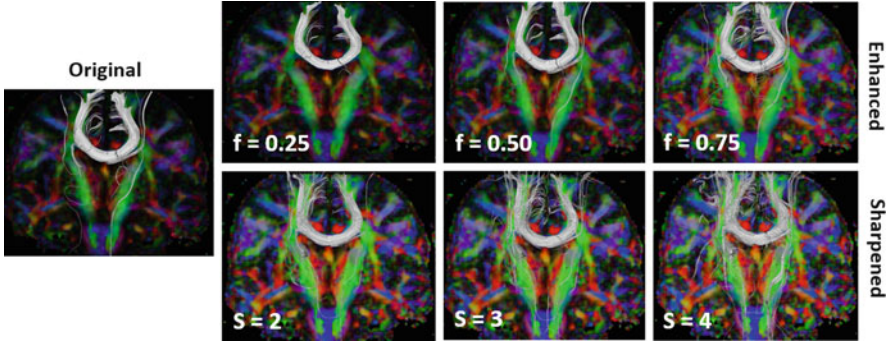
One interesting and illustrative application of enhancement pertains to scalar maps. We look at the effect of enhancement on the Fractional Anisotropy (FA) and Mean Diffusivity (MD) indices for diffusion tensor imaging [2]. The results are shown in Fig. 2, and showcase the effects listed at the end of Sect. 2.3. In both cases contrast improves markedly, but concomitant changes such as a strong decrease in MD for areas of large and isotropic diffusivity may, depending on the application, be undesirable.

### 4.2 The Effect of Adaptive Sharpening on DTI Tractography

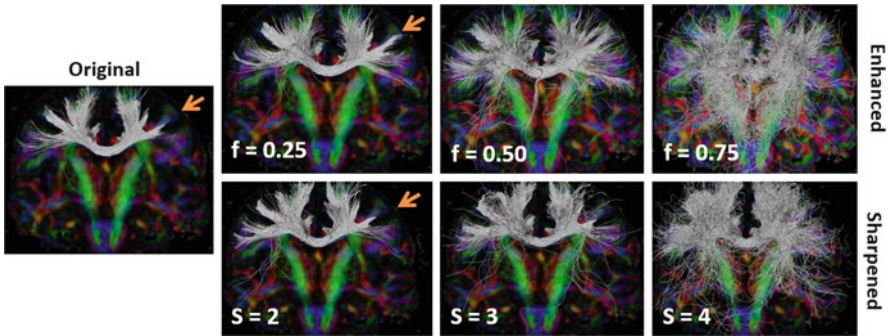
In Fig. 3 the seed region is placed in the postcentral gyri areas of the corpus callosum, Siemens data set (Sect. 3), and tractography is done using streamlining. The resulting tracts are known to correspond fairly well to the anatomy, even in the case of DTI tractography. As such we would like the enhancement not to change the tracts too much, which we indeed see in the top row. Note also that the tracts are recovered consistently while varying  $f$ . Additionally we find that tracts continue a little bit farther into the gray matter compared to the original data due to the



**Fig. 2** DTI-based FA and MD scalar maps of the Human Connectome Project data after adaptive enhancement, for increasing values of  $f$  (Eq. (22))



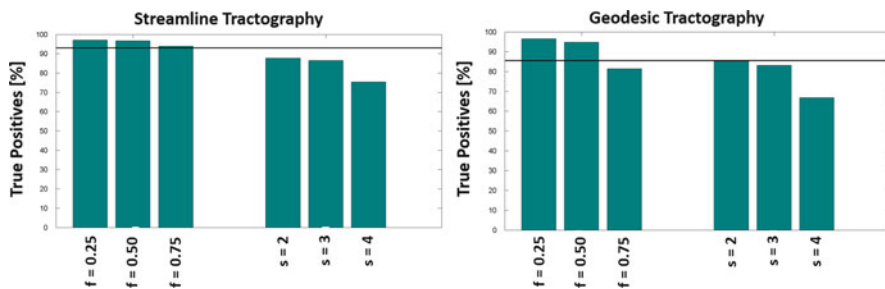
**Fig. 3** The results of streamline tractography seeded from the postcentral gyri areas of the corpus callosum (Siemens data), using no additional preprocessing (*left*), the presented deconvolution enhancement with  $f = 0.25, 0.50, 0.75$  [*top row*, Eq. (22)], and sharpened diffusion tensors with powers 2, 3, and 4 [*bottom row*, Eq. (24)]



**Fig. 4** The results of geodesic tractography seeded from the postcentral gyri areas of the corpus callosum (Siemens data), using no additional preprocessing (*left*), the presented deconvolution enhancement with  $f = 0.25, 0.50, 0.75$  [*top row*, Eq. (22)], and sharpened diffusion tensors with powers 2, 3, and 4 [*bottom row*, Eq. (24)]. The *orange arrows* point to regions where symmetry of the tracts, lacking in the original and the power sharpened data, is partly recovered after enhancement

increased anisotropy. The second row shows that sharpening with a power transform produces a number of incoherent tracts even for low powers.

More interesting are the results of geodesic tractography, seen in Fig. 4, for the same data set and seed region. In this case we see that after enhancement, we obtain much denser, more coherent, and generally more cogent tracts. The number of spurious fibers increases as expected with increasing  $f$ , with the best results apparently attained with  $f \approx 0.25$ . Of particular interest are the areas indicated with the orange arrows, where we recover tracts that are missing in the tractography based on the original data. These fibers are expected to be present from known anatomy and from symmetry arguments. For reference we include the results obtained when applying a power transform to the tensors, Eq. (24), which introduces far more



**Fig. 5** The true positive percentile of fibers connecting the given regions in the postcentral gyri part of the corpus callosum in the Siemens data. The *horizontal solid black lines* indicate the true positive percentiles obtained when using the original data

spurious fibers and does not recover any tracts in the indicated region. As a very simple quantification we show the true positive percentiles in Fig. 5, as explained in Sect. 3.

## 5 Discussion

Regarding the method, we have presented in Sect. 2.2 simple expressions that follow when modeling the diffusion weighted signal in a particular way. For many models not considered here the resulting expressions will be equally uninvolved, e.g. multi-compartment models in which the compartments are modeled by tensors. In other models (e.g. fiber orientation distribution models [31]) application of the enhancement might range from difficult to extraneous.

The experiments presented here illustrate that the method has some positive effects on tractography in the simple DTI case. Though the presented experiments are quite straightforward, combined with the fact that the method is fairly easy even for more advanced models they demonstrate potential. Generally speaking though, the method remains to be validated for each model in which it is to be applied, including DTI. In addition to this there are still model-dependent open questions, like the proper range of  $f$ , that would have to be considered.

One final point we have not discussed in depth concerns the computation of  $\epsilon(\mathbf{x})$ , Eq. (23). In the experiments presented here simple analytical formulae provided an unambiguous choice for this value, but for some other models this value may have to be approximated numerically. This will complicate the implementation, and in some cases may even be a limiting factor. We plan to address this issue in future work.

## 6 Conclusion

In this work we propose a new method to enhance diffusion MRI data by deconvolving the central quantity in diffusion MRI, the ensemble average propagator. The method is shown to produce very simple algorithms for a number of models, namely apparent diffusion coefficient based models and (generalized) diffusion tensor imaging, and a preliminary valuation is done by investigating its effect on scalar maps and on tractography. Improvement is shown in preliminary tractography experiments, both quantitative by tallying the number of true positive connections found, and qualitative by the recovery of a reasonable fiber tract not obtained using the original data.

**Acknowledgements** Tom Dela Haije gratefully acknowledges The Netherlands Organisation for Scientific Research (NWO) for financial support. Neda Sepasian and Tom Dela Haije are equal first authors.

## References

1. Arsigny, V., Fillard, P., Pennec, X., Ayache, N.: Log-Euclidean metrics for fast and simple calculus on diffusion tensors. *Magn. Reson. Med.* **56**(2), 411–421 (2006)
2. Basser, P.J., Pierpaoli, C.: Microstructural and physiological features of tissues elucidated by quantitative-diffusion-tensor MRI. *J. Magn. Reson. Ser. B* **111**(3), 209–219 (1996)
3. Basser, P.J., Mattiello, J., Le Bihan, D.: Estimation of the effective self-diffusion tensor from the NMR spin echo. *J. Magn. Reson. Ser. B* **103**(3), 247–254 (1994)
4. Callaghan, P.T.: *Principles of Nuclear Magnetic Resonance Microscopy*. Clarendon Press, Oxford (1991)
5. Canales-Rodríguez, E.J., Iturria-Medina, Y., Alemán-Gómez, Y., Melie-García, L.: Deconvolution in diffusion spectrum imaging. *NeuroImage* **50**(1), 136–149 (2010)
6. Catani, M., Thiebautdeschotten, M.: A diffusion tensor imaging tractography atlas for virtual in vivo dissections. *Cortex* **44**(8), 1105–1132 (2008)
7. Dela Haije, T.C.J., Fuster, A., Florack, L.M.J.: Reconstruction of convex polynomial diffusion MRI models using semi-definite programming. In: *Proceedings of the 23rd Annual Meeting of the ISMRM, Toronto*, p. 2821 (2015)
8. Descoteaux, M., Angelino, E., Fitzgibbons, S., Deriche, R.: Apparent diffusion coefficients from high angular resolution diffusion imaging: estimation and applications. *Magn. Reson. Med.* **56**(2), 395–410 (2006)
9. Descoteaux, M., Lenglet, C., Deriche, R.: Diffusion tensor sharpening improves white matter tractography. *Proc. SPIE (Med. Imaging 2007: Image Process.)* **6512**, 65121J (2007)
10. Florack, L., Astola, L.: A multi-resolution framework for diffusion tensor images. In: *IEEE Computer Society Conference on Computer Vision and Pattern Recognition Workshops, 2008. CVPRW'08*, pp. 1–7 (2008)
11. Florack, L.M.J., Fuster, A.: Riemann-Finsler geometry for diffusion weighted magnetic resonance imaging. In: Westin, C.F., Vilanova, A., Burgeth, B. (eds.) *Visualization and Processing of Tensors and Higher Order Descriptors for Multi-Valued Data*, pp. 189–208. *Mathematics and Visualization*, vol. XV. Springer, Berlin (2014)
12. Fuster, A., Tristán-Vega, A., Dela Haije, T., Westin, C.-F., Florack, L.: A novel Riemannian metric for geodesic tractography in DTI. In: *Computational Diffusion MRI and Brain Connectivity*, pp. 97–104. Springer, Berlin (2014)

13. Fuster, A., Dela Haije, T., Tristán-Vega, A., Plantinga, B., Westin, C.-F., Florack, L.: Adjugate diffusion tensors for geodesic tractography in white matter. *J. Math. Imaging Vision* **54**(1), 1–14 (2016). doi:[10.1007/s10851-015-0586-8](https://doi.org/10.1007/s10851-015-0586-8)
14. Ghosh, A., Deriche, R., Moakher, M.: Ternary quartic approach for positive 4th order diffusion tensors revisited. In: *IEEE International Symposium on Biomedical Imaging: From Nano to Macro, 2009. ISBI'09*, pp. 618–621 (2009)
15. Ghosh, A., Milne, T., Deriche, R.: Constrained diffusion kurtosis imaging using ternary quartics & MLE. *Magn. Reson. Med.* **71**(4), 1581–1591 (2014)
16. Hao, X., Whitaker, R., Fletcher, P.: Adaptive Riemannian metrics for improved geodesic tracking of white matter. In: *Information Processing in Medical Imaging*, pp. 13–24 (2011)
17. Hao, X., Zygmunt, K., Whitaker, R.T., Fletcher, P.T.: Improved segmentation of white matter tracts with adaptive Riemannian metrics. *Med. Image Anal.* **18**(1), 161–175 (2014)
18. Jensen, J.H., Helpert, J.A., Ramani, A., Lu, H., Kaczynski, K.: Diffusional kurtosis imaging: the quantification of non-Gaussian water diffusion by means of magnetic resonance imaging. *Magn. Reson. Med.* **53**(6), 1432–1440 (2005)
19. Lazar, M., Weinstein, D.M., Tsuruda, J.S., Hasan, K.M., Arfanakis, K., Meyerand, M.E., Badie, B., Rowley, H.A., Haughton, V., Field, A., Alexander, A.L.: White matter tractography using diffusion tensor deflection. *Hum. Brain Mapp.* **18**(4), 306–321 (2003)
20. Liu, C., Bammer, R., Acar, B., Moseley, M.E.: Characterizing non-Gaussian diffusion by using generalized diffusion tensors. *Magn. Reson. Med.* **51**(5), 924–937 (2004)
21. Misner, C.W., Thorne, K.S., Wheeler, J.A.: *Gravitation*. W.H. Freeman, San Francisco, CA (1973)
22. Mitra, P.P., Halperin, B.I.: Effects of finite gradient-pulse widths in pulsed-field-gradient diffusion measurements. *J. Magn. Reson. Ser. A* **113**(1), 94–101 (1995)
23. Mori, S., Crain, B.J.: *MRI Atlas of Human White Matter*. Elsevier, Amsterdam, Boston (2005)
24. Novikov, D.S., Kiselev, V.G.: Effective medium theory of a diffusion-weighted signal. *NMR Biomed.* **23**(7), 682–697 (2010)
25. Özarlan, E., Mareci, T.H.: Generalized diffusion tensor imaging and analytical relationships between diffusion tensor imaging and high angular resolution diffusion imaging. *Magn. Reson. Med.* **50**(5), 955–965 (2003)
26. Özarlan, E., Vemuri, B.C., Mareci, T.H.: Fiber orientation mapping using generalized diffusion tensor imaging. In: *IEEE International Symposium on Biomedical Imaging: Nano to Macro, 2004*, pp. 1036–1039 (2004)
27. Özarlan, E., Vemuri, B.C., Mareci, T.H.: Generalized scalar measures for diffusion MRI using trace, variance, and entropy. *Magn. Reson. Med.* **53**(4), 866–876 (2005)
28. Schober, M., Kasenburg, N., Feragen, A., Hennig, P., Hauberg, S.: Probabilistic shortest path tractography in DTI using Gaussian process ODE solvers. In: *Medical Image Computing and Computer-Assisted Intervention-MICCAI 2014*, Nagoya (2014)
29. Sepasian, N., ten Thije Boonkkamp, J.H.M., Ter Haar Romeny, B.M., Vilanova, A.: Multi-valued geodesic ray-tracing for computing brain connections using diffusion tensor imaging. *SIAM J. Imag. Sci.* **5**(2), 483–504 (2012)
30. Tournier, J.D., Calamante, F., Gadian, D.G., Connelly, A.: Diffusion-weighted magnetic resonance imaging fibre tracking using a front evolution algorithm. *NeuroImage* **20**(1), 276–288 (2003)
31. Tournier, J.D., Calamante, F., Gadian, D.G., Connelly, A.: Direct estimation of the fiber orientation density function from diffusion-weighted MRI data using spherical deconvolution. *NeuroImage* **23**(3), 1176–1185 (2004)
32. Van Essen, D.C., Smith, S.M., Barch, D.M., Behrens, T.E., Yacoub, E., Ugurbil, K.: The WU-Minn human connectome project: an overview. *NeuroImage* **80**, 62–79 (2013)

# Angular Resolution Enhancement of Diffusion MRI Data Using Inter-Subject Information Transfer

Geng Chen, Pei Zhang, Ke Li, Chong-Yaw Wee, Yafeng Wu, Dinggang Shen, and Pew-Thian Yap

**Abstract** Diffusion magnetic resonance imaging is widely used to investigate diffusion patterns of water molecules in the human brain. It provides information that is useful for tracing axonal bundles and inferring brain connectivity. Diffusion axonal tracing, namely tractography, relies on local directional information provided by the orientation distribution functions (ODFs) estimated at each voxel. To accurately estimate ODFs, data of good signal-to-noise ratio and sufficient angular samples are desired, but unfortunately, are not always practically available. In this paper, we propose to improve ODF estimation by using inter-subject correlation. Specifically, diffusion-weighted images acquired from different subjects, when transformed to the space of a target subject, can not only provide signal denoising with additional information, but also drastically increase the number of angular samples for better ODF estimation. This is largely because of the incoherence of the angular samples generated when the diffusion signals are reoriented and warped to the target space. Experiments on both synthetic data and real data show that our method can reduce noise-induced artifacts, such as spurious ODF peaks, and yield more coherent orientations.

---

G. Chen

Data Processing Center, Northwestern Polytechnical University, Xi'an, China

Department of Radiology and BRIC, UNC Chapel Hill, Chapel Hill, NC, USA

P. Zhang • C.-Y. Wee • D. Shen • P.-T. Yap (✉)

Department of Radiology and BRIC, UNC Chapel Hill, Chapel Hill, NC, USA

e-mail: [ptyap@med.unc.edu](mailto:ptyap@med.unc.edu)

K. Li

Fundamental Science on Ergonomics and Environment Control Laboratory, Beihang University, Beijing, China

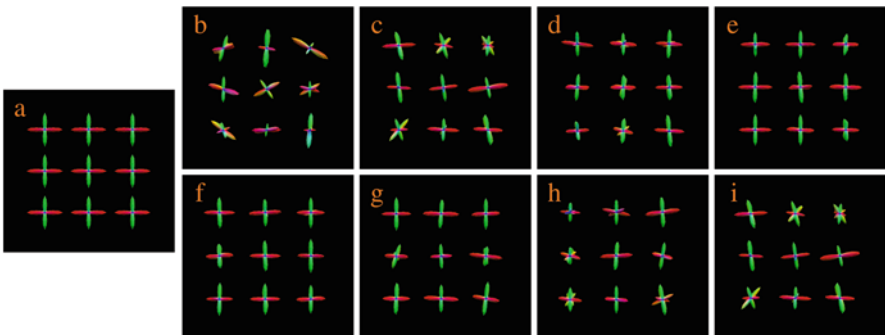
Y. Wu

Data Processing Center, Northwestern Polytechnical University, Xi'an, China

## 1 Introduction

Diffusion magnetic resonance imaging (MRI) provides information on brain circuitry by observing the diffusion patterns of water molecules in the human brain. To trace the brain connections, diffusion tractography algorithms rely on information provided by local fiber orientations, which are often represented by a quantity called the orientation distribution function (ODF). Accurate ODF estimation is key to successful tractography. Precise tractography can be used to study the integrity and changes of white matter tracts in relation to development and disorders [1–8]. Two major factors affect the estimation of ODFs: (1) The number of diffusion-sensitizing gradient directions used to acquire the diffusion data, and (2) The signal-to-noise ratio (SNR) of the data. Figure 1 shows that ODF estimation improves when a sufficient number of gradient directions are used (top row), and gets worse with heavy noise (bottom row).

Varentsova et al. [9] introduced a post-processing approach to increase the number of gradient directions for improving ODF estimation in an atlas. The key idea is to make use of the orientation incoherence of the diffusion signals when they are reoriented and warped to a common space. This incoherence is a direct result of the variation of brain shape and the position of the head when scanned. A major drawback of this approach is that only rotation is considered when reorienting the diffusion signals. We show that this deteriorates ODF estimation when transformations such as shearing are involved. This approach is also limited due to its implicit assumption that the images are perfectly aligned after spatial registration. This assumption almost never holds in the real-world scenario and will cause blurring of structures that are misaligned.

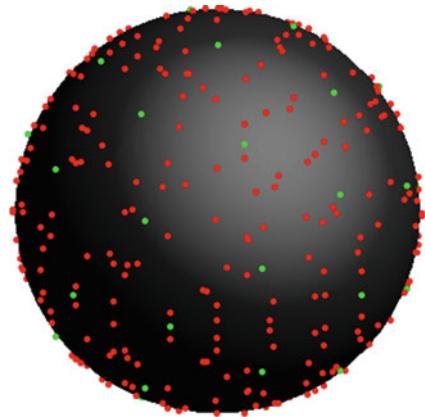


**Fig. 1** Influence of the number of gradient directions and noise on ODF estimation. (a) Ground truth. (b)–(e) ODFs estimated using 6, 21, 81, and 321 gradient directions with 9% noise. (f)–(i) ODFs estimated using 21 diffusion directions with 3%, 5%, 7%, and 9% noise. Gaussian noise (i.e.  $\mathcal{N}(0, v(p/100))$ ) is added in the complex domain of the signal, determined by the percentage  $p$ , where  $v$  is the maximum signal value (150 in our case)



A number of methods for denoising the diffusion MRI data have been proposed [10, 11]. These methods are effective for enhancing the signal SNR, but to improve the ODF estimation, removing noise is not sufficient—another important aspect is to enhance angular resolution. In this paper we seek to better estimate ODFs by concurrent edge-preserving signal denoising and angular resolution enhancement. Inspired by our previous work in MRI denoising [12], we extend the non-local means (NLM) algorithm [13] to leverage both self and inter-subject similarity. The underlying assumption is that the possibility of finding repeating structures from a collection of scans of different individuals is higher than a single scan from the same individual. In transferring information from images of multiple individuals to the space of the target individual for denoising, we make available signals from incoherent gradient directions for improving ODF estimation. This is illustrated in Fig. 2, where we show that the effective number of gradient directions can be significantly increased by inter-subject information transfer. For this purpose, we propose a signal reorientation method that utilizes the full affine transform estimated locally from a non-linear deformation field. This differs from [9], which uses only the rotation component of the affine transform. Finally, we integrate both block-matching based denoising and angular resolution enhancement into a unified framework to improve ODF estimation.

**Fig. 2** Angular resolution enhancement using inter-subject information transfer. The *green points on the sphere* indicate the original gradient directions. Transferring incoherent samples from ten other images increases the effective number of gradient directions, as indicated by the *red points*





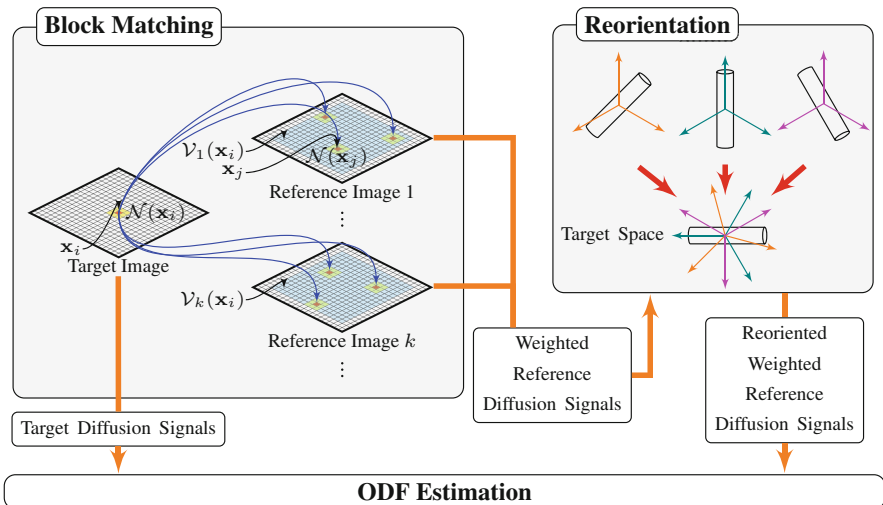
## 2 Method

### 2.1 Overview

Suppose we have a group of reference images acquired from different individuals (possibly also including the target individual), the goal is to improve ODF estimation for the target image with the help of the reference images. This is achieved in three steps: (1) block matching, (2) reorientation, and (3) ODF estimation. Each step is detailed below. See Fig. 3 for an overview.

### 2.2 Block Matching

We first warp all the reference images to the target space. For each voxel in the target image, we then determine the matching voxels in the reference images via robust block matching, similar to that used in NLM [13]. A similarity weight is determined for each matching voxel and will be used for ODF estimation. NLM relies on repeating structures in an image. However, this might be challenging due to the complex anatomy of the human brain and fine unique structures might not find matching candidates. To address this issue, we extend NLM by performing block matching across images, significantly increasing the chance of finding similar



**Fig. 3** Overview. Three components of our method: (1) block matching for identifying corresponding voxels from the reference images, (2) reorientation of the reference diffusion signals, and (3) ODF estimation

structures. Gross misalignment between images is first dealt with using non-linear registration and residual misalignment is then overcome using block matching.

Let  $\mathcal{N}(\mathbf{x}_i)$  be a 3D block neighbourhood centered at  $\mathbf{x}_i \in \mathbb{R}^3$ . The size of  $\mathcal{N}(\mathbf{x}_i)$  is  $(2d + 1)^3$ , where  $d$  is the neighborhood radius. Let  $\mathcal{V}_k(\mathbf{x}_i)$  be the search volume centered at  $\mathbf{x}_i$  in reference image  $k$ . The size of  $\mathcal{V}_k(\mathbf{x}_i)$  is  $(2M + 1)^3$ , where  $M$  is the search radius. Let  $u(\mathbf{x}_i)$  be the intensity value at  $\mathbf{x}_i$ , then  $u(\mathcal{N}(\mathbf{x}_i))$  is a vector that represents the intensity values of all voxels within  $\mathcal{N}(\mathbf{x}_i)$ . The unnormalized weight, indicating similarity between the neighborhoods of a voxel,  $\mathbf{x}_i$ , in the target image, and a voxel,  $\mathbf{x}_j \in \mathcal{V}_k(\mathbf{x}_i)$ , in the reference image is computed as  $w_{\text{NLM}}(\mathbf{x}_i, \mathbf{x}_j) = \exp \left\{ -\frac{\|u(\mathcal{N}(\mathbf{x}_i)) - u(\mathcal{N}(\mathbf{x}_j))\|_2^2}{h_i^2} \right\}$ , where  $h_i$  controls the attenuation of the exponential function. Coupé et al. [14] suggested to set  $h_i = \sqrt{2\beta\hat{\sigma}_i^2 |\mathcal{N}(\mathbf{x}_i)|}$ , where  $|\mathcal{N}(\mathbf{x}_i)|$  is the cardinality of  $\mathcal{N}(\mathbf{x}_i)$ ,  $\beta$  is a constant that is set to 1,  $\hat{\sigma}_i$  is an estimate of the standard deviation of the noise at  $\mathbf{x}_i$ , which is spatial-adaptively estimated following the method described in [15].

For each voxel in the target image, block matching leads to a set of corresponding voxels and associated similarity weights in the reference images. Specifically, given  $\mathbf{x}_i$  in the target, we have  $\Omega(\mathbf{x}_i) = \bigcup_k \{ (S(\mathbf{q}, \mathbf{x}_j; k), w_{\text{NLM}}(\mathbf{x}_i, \mathbf{x}_j; k)) \}_{\mathbf{x}_j \in \mathcal{V}_k} \cup \{ (S(\mathbf{q}, \mathbf{x}_i; 0), 1) \}$ , where  $S(\mathbf{q}, \mathbf{x}_j; k)$ ,  $k > 0$  is the diffusion-attenuated signal collected at  $\mathbf{x}_j$  with wavevector  $\mathbf{q}$  in the  $k$ th reference dataset, and  $S(\mathbf{q}, \mathbf{x}_i; 0)$  is the signal measured in the target dataset.

### 2.3 Reorientation

The diffusion signal  $S(\mathbf{q}, \mathbf{x}_j)$  in  $\Omega(\mathbf{x}_i)$  has to be reoriented before it can be used for ODF estimation. We note that the MR signal attenuation  $E(\mathbf{q}, \mathbf{x}_j) = S(\mathbf{q}, \mathbf{x}_j)/S_0(\mathbf{x}_j)$ , where  $S_0(\mathbf{x}_j)$  is the base signal without diffusion-sensitizing gradient. Then, the ODF  $\psi(\hat{\mathbf{u}}, \mathbf{x}_j, q')$ , contributed by the sampling shell with radius  $q'$  in  $q$ -space can be computed as [16]

$$\psi(\hat{\mathbf{u}}, \mathbf{x}_j, q') \approx \int E(\mathbf{q}, \mathbf{x}_j) \delta(\hat{\mathbf{q}}^T \hat{\mathbf{u}}) \delta(\|\mathbf{q}\| - q') d\mathbf{q}, \quad (1)$$

where  $\hat{\mathbf{q}} = \mathbf{q}/\|\mathbf{q}\|$ ,  $\hat{\mathbf{u}}$  is a unit vector that represents a spatial direction, and  $\delta(\cdot)$  is the Dirac delta function. Given a local affine matrix  $\mathbf{A}(\mathbf{x}_j)$  computed at  $\mathbf{x}_j$ , the integral of the ODF must be maintained after transformation

$$\int \psi(\hat{\mathbf{u}}, \mathbf{x}_j, q') d\hat{\mathbf{u}} = \int |\mathbf{A}^{-1}(\mathbf{x}_j)| |\mathbf{J}_{\mathbf{A}^{-1}(\mathbf{x}_j)\hat{\mathbf{u}}}| \psi \left( \frac{\mathbf{A}^{-1}(\mathbf{x}_j)\hat{\mathbf{u}}}{\|\mathbf{A}^{-1}(\mathbf{x}_j)\hat{\mathbf{u}}\|}, q' \right) d\hat{\mathbf{u}}, \quad (2)$$

where  $\mathbf{J}_{\mathbf{A}^{-1}(\mathbf{x}_j)\hat{\mathbf{u}}}$  is a transformation associated with  $\hat{\mathbf{u}} \rightarrow \frac{\hat{\mathbf{u}}}{\|\mathbf{A}^{-1}(\mathbf{x}_j)\hat{\mathbf{u}}\|}$ . After applying  $\mathbf{A}^{-1}(\mathbf{x}_j)$  to  $\hat{\mathbf{u}}$  on both sides of (1) and simplifying, we have

$$|\mathbf{A}^{-1}(\mathbf{x}_j)| |\mathbf{J}_{\mathbf{A}^{-1}(\mathbf{x}_j)\hat{\mathbf{u}}}| \psi \left( \frac{\mathbf{A}^{-1}(\mathbf{x}_j)\hat{\mathbf{u}}}{\|\mathbf{A}^{-1}(\mathbf{x}_j)\hat{\mathbf{u}}\|}, q' \right) \approx \underbrace{\int E \left( \frac{\mathbf{A}^T(\mathbf{x}_j)\hat{\mathbf{q}}}{\|\mathbf{A}^T(\mathbf{x}_j)\hat{\mathbf{q}}\|} \|\mathbf{q}\|, \mathbf{x}_j \right) \delta(\hat{\mathbf{q}}^T \hat{\mathbf{u}}) \delta(\|\mathbf{q}\| - q') \, d\mathbf{q}}_{\text{Reoriented Signal Profile}}, \quad (3)$$

where  $|\cdot|$  denotes the determinant and  $\|\cdot\|$  is the  $\ell_2$  norm. If we let

$$\hat{E}(\mathbf{q}, \mathbf{x}_j) = E \left( \frac{\mathbf{A}^T(\mathbf{x}_j)\hat{\mathbf{q}}}{\|\mathbf{A}^T(\mathbf{x}_j)\hat{\mathbf{q}}\|} \|\mathbf{q}\|, \mathbf{x}_j \right) \rightarrow \hat{E} \left( \frac{\mathbf{A}^{-T}(\mathbf{x}_j)\hat{\mathbf{q}}}{\|\mathbf{A}^{-T}(\mathbf{x}_j)\hat{\mathbf{q}}\|} \|\mathbf{q}\|, \mathbf{x}_j \right) = E(\mathbf{q}, \mathbf{x}_j), \quad (4)$$

we can see that the reorientation involves transforming the signal measured at  $\mathbf{q}$ , i.e.,  $E(\mathbf{q}, \mathbf{x}_j)$ , to  $\frac{\mathbf{A}^{-T}(\mathbf{x}_j)\hat{\mathbf{q}}}{\|\mathbf{A}^{-T}(\mathbf{x}_j)\hat{\mathbf{q}}\|} \|\mathbf{q}\|$ . The reoriented signal is hence  $\hat{S}(\mathbf{q}, \mathbf{x}_j) = \hat{E}(\mathbf{q}, \mathbf{x}_j) S_0(\mathbf{x}_j)$ . We denote the reoriented version of  $\Omega(\mathbf{x}_i)$  as  $\hat{\Omega}(\mathbf{x}_i)$ .

## 2.4 ODF Estimation

To estimate the ODF at  $\mathbf{x}_i$ ,  $\hat{\Omega}(\mathbf{x}_i)$  is decomposed into a linear combination of diffusion basis functions (DBFs). By dropping off  $\mathbf{x}_i$  for simplicity, the decomposition is given by

$$S(\mathbf{q}) = \sum_{j=0}^N \alpha_j f_j(\mathbf{q} | \lambda_1, \lambda_2, \lambda_3), \quad (5)$$

where  $\alpha_j$  is the volume fraction associated with the  $j$ th tensor DBF  $f_j(\cdot)$  and  $\{\lambda_1, \lambda_2, \lambda_3\}$  are the three eigenvalues of the tensor. The DBF is defined as  $f_j(\mathbf{q} | \lambda_1, \lambda_2, \lambda_3) = \exp(-t\mathbf{q}^T \mathbf{D}_j \mathbf{q}) = \exp(-b\hat{\mathbf{q}}^T \mathbf{D}_j \hat{\mathbf{q}})$ , where  $\mathbf{D}_j$  is a tensor defined by  $\{\lambda_1, \lambda_2, \lambda_3\}$  and principal diffusion direction  $\boldsymbol{\mu}_j$ ,  $t$  is the diffusion time, and  $b$  is the diffusion weighting. For  $1 \leq j \leq N$ , the tensors are anisotropic with principal diffusion directions distributed uniformly on a unit sphere. For  $j = 0$ , the tensor is isotropic to model free water diffusion. By representing each element of set  $\hat{\Omega}(\mathbf{x}_i)$  as  $(\mathbf{s}_n, w_n)$  and each DBF as a column of matrix  $\mathbf{F}_n$ , we can solve for the volume

fraction vector  $\boldsymbol{\alpha} = [\alpha_0, \dots, \alpha_N]^T$  using  $\ell_1$ -penalized weighted least-squares [17]:

$$\arg \min_{\boldsymbol{\alpha}} \left\{ \sum_n w_n \|(\mathbf{s}_n - \mathbf{F}_n \boldsymbol{\alpha})\|_2^2 + \gamma \|\boldsymbol{\alpha}\|_1 \right\} \text{ s.t. } \boldsymbol{\alpha} \geq \mathbf{0}, \quad (6)$$

where  $\|\cdot\|_1$  is the  $\ell_1$ -norm and  $\gamma \geq 0$  is a tuning parameter.  $\mathbf{F}_n$  is the DBF matrix corresponding to  $\mathbf{s}_n$ , computed based on its reoriented gradient directions. If no reorientation is applied,  $\mathbf{F}_n$  is identical for all  $n$ . The ODF can then be computed as

$$\psi(\hat{\mathbf{u}}) = \frac{1}{S_0} \sum_{j=0}^N \alpha_j \phi(\hat{\mathbf{u}}, \mathbf{D}_j). \quad (7)$$

When  $\phi(\hat{\mathbf{u}}, \mathbf{D}_j) = \frac{1}{4\pi Z} |\mathbf{D}_j|^{-\frac{1}{2}} (\hat{\mathbf{u}}^T \mathbf{D}_j^{-1} \hat{\mathbf{u}})^{-\frac{1}{2}}$ , with  $Z$  being the normalization constant, we have the diffusion ODF proposed by Tuch [16]. When  $\phi(\hat{\mathbf{u}}, \mathbf{D}_j) = \frac{1}{4\pi} |\mathbf{D}_j|^{-\frac{1}{2}} (\hat{\mathbf{u}}^T \mathbf{D}_j^{-1} \hat{\mathbf{u}})^{-\frac{3}{2}}$ , we have the constant-solid-angle diffusion ODF [18]. Finally, when  $\phi(\hat{\mathbf{u}}, \mathbf{D}_j) = \delta(|\hat{\mathbf{u}}^T \hat{\mathbf{v}}_j| - 1)$ , with  $\hat{\mathbf{v}}_i$  being the eigenvector of  $\mathbf{D}_j$  corresponding to the largest eigenvalue, we have the fiber ODF [19, 20].

## 3 Experiments

### 3.1 Data

#### Synthetic Dataset

A set of single pixel images were generated to evaluate the performance of our method in reconstructing ODFs from low angular resolution noisy data. Both single-direction and two-direction cases were considered. For the latter, the angular separation between two directions was set to  $45^\circ$  and  $90^\circ$ . Six ground truth images for these two cases were generated using 6 and 21 gradient directions. Ten reoriented images were generated for each ground truth image by applying affine transformations to the principal directions of the tensors. The affine transformations include random rotation ( $[-90^\circ, 90^\circ]$ ) around the axis perpendicular to the image plane and shearing ( $[-0.5, 0.5]$ ) within the image plane. Four levels of Rician noise (3%, 5%, 7% and 9%) were added to the ground truth image and the reoriented images. The noise-perturbed ground truth image was used as the target image and the noisy reoriented images were the reference images.

## Real Dataset

The real dataset consists of diffusion-weighted (DW) images from 11 subjects. One subject was used as the target and the whole subjects as references. All images were acquired using a Siemens 3T TRIO MR scanner following a standard imaging protocol: 30 diffusion directions isotropically distributed on a hemisphere,  $b = 1000 \text{ s/mm}^2$ , one image with no diffusion weighting,  $128 \times 128$  imaging matrix, voxel size of  $2 \times 2 \times 2 \text{ mm}^3$ , TE= 81 ms, TR= 7618 ms, 1 average.

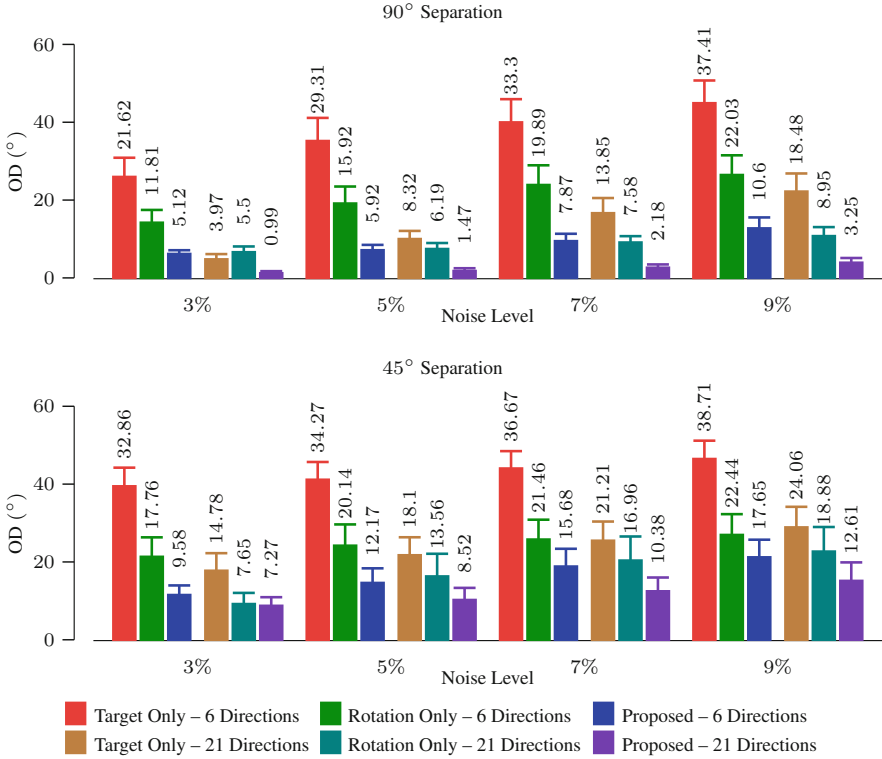
## 3.2 Results

In all experiments, we set block radius  $d = 1$  and search radius  $M = 2$  for block matching and tuning parameter  $\gamma = 0.01$  for sparse estimation. The number of reference images was 11, including the target image. The diffusivities of the anisotropic tensors  $\lambda_1, \lambda_2, \lambda_3$  were estimated from the corpus callosum. Those of the isotropic tensor were estimated from the ventricles. A total of 321 orientations, generated by subdividing the faces of an icosahedron three times and discarding antipodal symmetric directions, were used as the principal diffusion directions of the DBFs.

For the synthetic dataset, we utilized our reorientation algorithm described in Sect. 2.3, we applied the affine transformation to the tensors in the reference images. For the real dataset, the reference DW images were registered to the target space by diffeomorphic demons [21] using the reference and target fractional anisotropy (FA) images, though other non-rigid registration algorithms [22] may be used. Based on the estimated deformation field, the reference DW images were warped to the target space using a DW spatial warping method [17]. The warped reference DW images were then used for multi-channel block matching with respect to the target DW images.

For quantitative evaluation, Orientational Discrepancy (OD) measure [23] was used. OD is a measure of the angular difference between two sets of directions. After calculating the ODFs for the diffusion MRI data, the ODF peaks were detected following the method described in [17] and then the resulting peaks were compared with the ground truth using OD as the metric. We repeatedly generated the synthetic data and ran the experiment 900 times. The mean and standard deviation of OD values were reported.

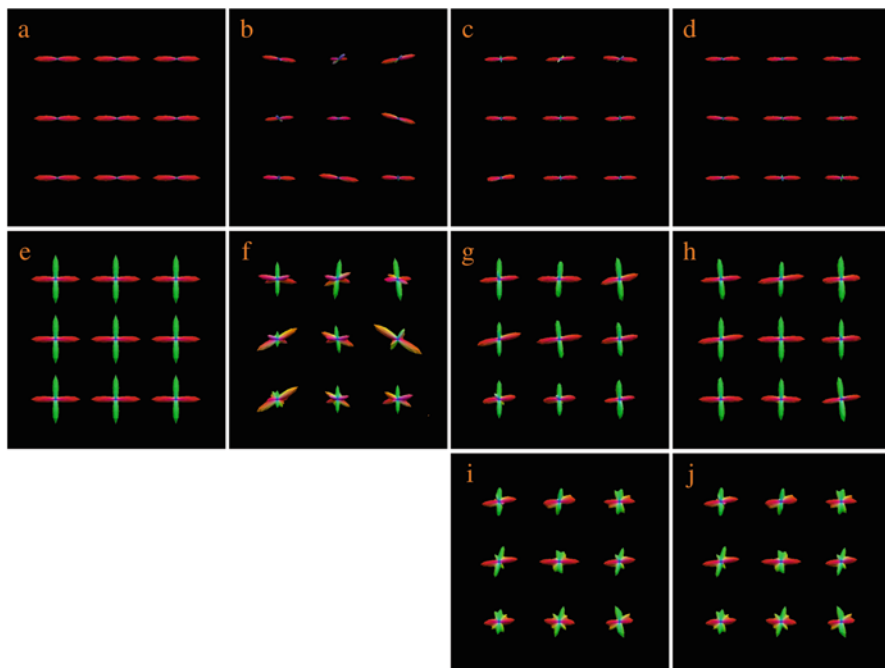
Figure 4 shows that our method significantly reduces the mean OD on the two-direction crossing synthetic data. The small mean OD indicates that the estimated peaks are close to the ground truth. Compared with the results given by using the



**Fig. 4** Average OD comparison using two-direction synthetic data. Three cases were compared: (1) using only the target image; (2) using the proposed method; and (3) using the proposed method but only rotation was used for reorientation. Four noise levels and two sets of gradient directions were involved. The error bars indicate the standard deviations. For the proposed method, ten reference images were used

target image only, the maximum improvement is 26.81° when the noise level is 9%. This is for the case of 6 gradient directions, where each pair of directions are separated by an angle of 90°.

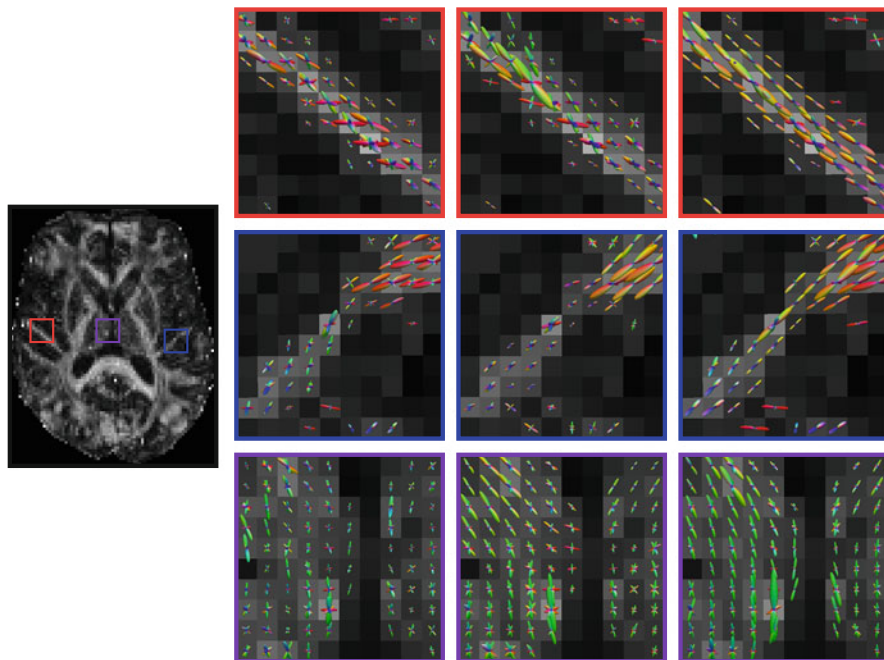
The ODF glyphs are shown for visual inspection in Fig. 5. The estimated ODF glyphs look very similar to the ground truth. We ran the same experiment by performing only rotation for reorientation, as done in [9]. The results, shown in Fig. 5, indicate that this will cause spurious peaks that are not observed in the ground truth. The superiority of our method over the rotation-only approach is confirmed in Fig. 4.



**Fig. 5** Comparison of ODFs. (a) and (e) Ground truth ODFs. (b) and (f) ODFs estimated using only the target, which was generated using 5 % noise and six gradient directions; (e) and (g) ODFs estimated using the proposed method with five reference images. (d) and (h) ODFs estimated using the proposed method with ten reference images. (i) and (j) Results when only rotation was used for reorientation

For the real data, the ODFs are shown in Fig. 6. We can observe that the ODFs estimated using the target alone and with the reference images but without block matching exhibit spurious peaks. The ODFs are also not as coherent as those estimated using the proposed method.

Tractography results, shown in Fig. 7, indicate that the proposed method gives cleaner and richer fiber tracts compared with the other two methods. When block matching is not used, a significant amount of fiber tracts are missing. The proposed method gives fuller and smoother fiber tracts.

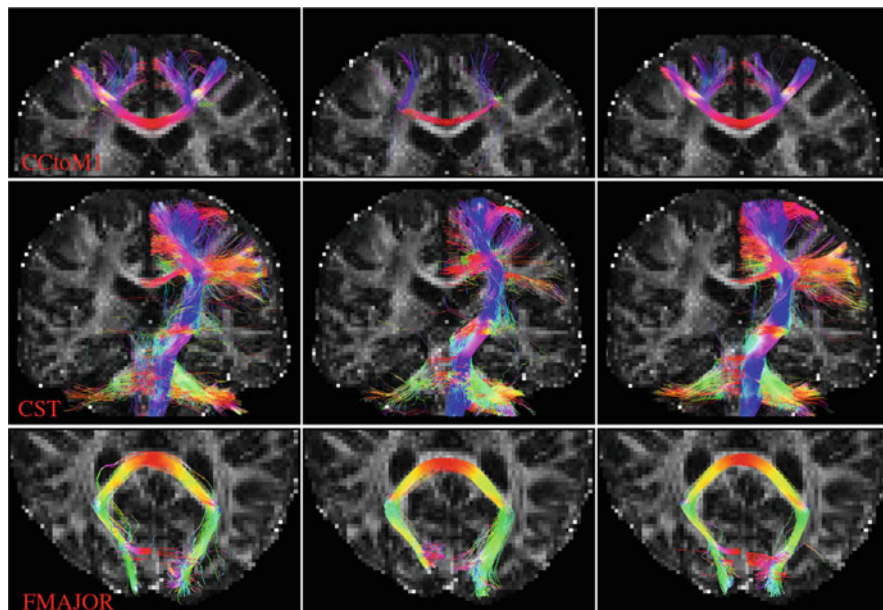


**Fig. 6** ODF results for the real data. (*Far left*) Reference FA image. ODFs estimated using (*left*) the target dataset only, (*middle*) 11 reference images but without block matching, and (*right*) the proposed method with 11 reference images

## 4 Conclusion

We have proposed a method for improving ODF estimation by using correlated information between subjects. Information from multiple reference datasets is used to simultaneously remove noise and to enhance angular resolution. Extensive experiments on both synthetic and real data show improved ODF estimation, despite using noisy data with insufficient angular sampling. Further validation on tractography performance demonstrates the efficacy of our approach in reconstructing clean and rich fiber tracts.





**Fig. 7** Tractography. Three representative sets of tractography results using (*Left*) the target dataset only, (*Middle*) the proposed method without block matching, and (*Right*) the proposed method. The fiber bundles are extracted using different ROIs, including CCtoM1: precentral gyrus and corpus callosum, CST: precentral gyrus and posterior limb of the internal capsule, FMAJOR: occipital cortex and corpus callosum

**Acknowledgements** This work was supported in part by a UNC BRIC-Radiology start-up fund and NIH grants (EB006733, EB008374, EB009634, MH088520, AG041721, and MH100217). The first author was supported by a scholarship from the China Scholarship Council.

## References

1. Yap, P.T., Wu, G., Shen, D.: Human brain connectomics: networks, techniques, and applications. *IEEE Signal Process. Mag.* **27**(4), 131–134 (2010)
2. Yap, P.T., Fan, Y., Chen, Y., Gilmore, J., Lin, W., Shen, D.: Development trends of white matter connectivity in the first years of life. *PLoS ONE* **6**(9), e24678 (2011)
3. Wee, C.Y., Yap, P.T., Li, W., Denny, K., Browndyke, J.N., Potter, G.G., Welsh-Bohmer, K.A., Wang, L., Shen, D.: Enriched white matter connectivity networks for accurate identification of MCI patients. *NeuroImage* **54**(3), 1812–1822 (2011)
4. Wee, C.Y., Yap, P.T., Zhang, D., Denny, K., Browndyke, J.N., Potter, G.G., Welsh-Bohmer, K.A., Wang, L., Shen, D.: Identification of MCI individuals using structural and functional connectivity networks. *NeuroImage* **59**(3), 2045–2056 (2012)
5. Shi, F., Yap, P.T., Gao, W., Lin, W., Gilmore, J.H., Shen, D.: Altered structural connectivity in neonates at genetic risk for schizophrenia: a combined study using morphological and white-matter networks. *NeuroImage* **62**(3), 1622–1633 (2012)

6. Jin, Y., Shi, Y., Zhan, L., Gutman, B.A., de Zubicaray, G.I., McMahon, K.L., Wright, M.J., Toga, A.W., Thompson, P.M.: Automatic clustering of white matter fibers in brain diffusion MRI with an application to genetics. *NeuroImage* **100**, 75–90 (2014)
7. Dennis, E.L., Jin, Y., Villalón-Reina, J.E., Zhan, L., Kernan, C.L., Babikian, T., Mink, R.B., Babbitt, C.J., Johnson, J.L., Giza, C.C., Thompson, P.M., Asanow, R.F.: White matter disruption in moderate/severe pediatric traumatic brain injury: advanced tract-based analyses. *NeuroImage: Clinical* **7**, 493–505 (2015)
8. Zhan, L., Zhou, J., Wang, Y., Jin, Y., Jahanshad, N., Prasad, G., Nir, T.M., Leonardo, C.D., Ye, J., Thompson, P.M.: Comparison of nine tractography algorithms for detecting abnormal structural brain networks in Alzheimer’s disease. *Front. Aging Neurosci.* **7**, 48 (2015)
9. Varentsova, A., Zhang, S., Arfanakis, K.: Development of a high angular resolution diffusion imaging human brain template. *NeuroImage* **91**, 177–186 (2014)
10. McGraw, T., Vemuri, B.C., Chen, Y., Rao, M., Mareci, T.: DT-MRI denoising and neuronal fiber tracking. *Med. Image Anal.* **8**(2), 95–111 (2004)
11. Chen, B., Hsu, E.W.: Noise removal in magnetic resonance diffusion tensor imaging. *Magn. Reson. Med.* **54**(2), 393–401 (2005)
12. Chen, G., Zhang, P., Wu, Y., Shen, D., Yap, P.T.: Collaborative non-local means denoising of magnetic resonance images. In: *IEEE International Symposium on Biomedical Imaging (ISBI)*, pp. 564–567 (2015)
13. Buades, A., Coll, B., Morel, J.M.: A review of image denoising algorithms, with a new one. *Multiscale Model. Simul.* **4**(2), 490–530 (2005)
14. Coupé, P., Yger, P., Prima, S., Hellier, P., Kervrann, C., Barillot, C.: An optimized blockwise nonlocal means denoising filter for 3-D magnetic resonance images. *IEEE Trans. Med. Imaging* **27**(4), 425–441 (2008)
15. Commowick, O., Stamm, A.: Non-local robust detection of DTI white matter differences with small databases. In: *Medical Image Computing and Computer-Assisted Intervention (MICCAD)*, pp. 476–484. Springer, Berlin (2012)
16. Tuch, D.S.: Q-ball imaging. *Magn. Reson. Med.* **52**(6), 1358–1372 (2004)
17. Yap, P.T., Shen, D.: Spatial transformation of DWI data using non-negative sparse representation. *IEEE Trans. Med. Imaging* **31**(11), 2035 (2012)
18. Aganj, I., Lenglet, C., Sapiro, G.: ODF reconstruction in q-ball imaging with solid angle consideration. In: *IEEE International Symposium on Biomedical Imaging (ISBI)*, pp. 1398–1401 (2009)
19. Tournier, J.D., Calamante, F., Gadian, D.G., Connelly, A.: Direct estimation of the fiber orientation density function from diffusion-weighted MRI data using spherical deconvolution. *NeuroImage* **23**(3), 1176–1185 (2004)
20. Jian, B., Vemuri, B.C.: A unified computational framework for deconvolution to reconstruct multiple fibers from diffusion weighted MRI. *IEEE Trans. Med. Imaging* **26**(11), 1464–1471 (2007)
21. Vercauteren, T., Pennec, X., Perchant, A., Ayache, N.: Diffeomorphic demons: efficient non-parametric image registration. *NeuroImage* **45**(1), S61–S72 (2009)
22. Zhang, P., Niethammer, M., Shen, D., Yap, P.T.: Large deformation diffeomorphic registration of diffusion-weighted imaging data. *Med. Image Anal.* **18**(8), 1290–1298 (2014)
23. Yap, P.T., Chen, Y., An, H., Yang, Y., Gilmore, J.H., Lin, W., Shen, D.: SPHERE: spherical harmonic elastic registration of HARDI data. *NeuroImage* **55**(2), 545–556 (2011)

# Crossing Versus Fanning: Model Comparison Using HCP Data

Aurobrata Ghosh, Daniel Alexander, and Hui Zhang

**Abstract** This paper assesses the importance of modelling fiber dispersion in brain regions with complex fiber configurations using a model comparison approach. It is well known that DTI, although popular, is insufficient for describing complex fiber configurations that exist in the brain—such as crossings, bendings and fannings. “Higher order” models have been proposed to overcome this limitation by modelling crossings with greater accuracy and recent works have reported that up to 90 % of white matter voxels contain crossings. However, since these models do not account for bending and fanning, i.e. *dispersion*, it is unknown if some fiber configurations are better explained by dispersion or by crossing (or by both). To address this problem, we take a model comparison approach on the publicly available state-of-the-art HCP dataset. We consider compartment based single fiber, crossing fiber and dispersion models, which are fitted to the data and ranked using several model selection and validation metrics, such as AIC, BIC and k-fold cross-validation. We generate maps of the brain based on these rankings which quantify the voxels where a single fiber or crossing or dispersion is the preferred model. The results show that 45–50 % of the brain’s parenchyma, including the white matter, are better explained by dispersion models, indicating the importance of modelling dispersion in addition to crossings.

## 1 Introduction

Diffusion MRI (dMRI) is unique in its ability to measure the Brownian motion of water molecules within the geometry of biological tissue, allowing us to gain insights into the microstructure of the brain in vivo and non-invasively. Diffusion Tensor Imaging (DTI) [2] is today the de facto dMRI reconstruction technique. However, it is well known that DTI, based on a Gaussian diffusion assumption, has

---

A. Ghosh (✉) • D. Alexander • H. Zhang  
Centre for Medical Image Computing, University College London, London, UK  
e-mail: [aurobrata.ghosh@ucl.ac.uk](mailto:aurobrata.ghosh@ucl.ac.uk)

limitations in describing complex fiber configurations in the brain such as crossings, bendings or fannings. Thus numerous “higher order” models have been proposed to improve the ability to resolve crossing configurations with greater accuracy [1, 4, 7]. Using these models, studies have reported that up to  $\sim 90\%$  [7] of white matter voxels contain crossing configurations in the brain.

However, in general, most higher order models do not explicitly attempt to model bending and fanning structures, i.e. *dispersion*, which may lead to an overestimation of the percentage of crossing voxels. Only recently a new group of compartment based parametric models have proposed to model dispersion explicitly [8, 11, 13]. Studies based on these models indicate the relevance of modelling dispersion when interpreting the dMRI signal. Surprisingly, even the signal from regions widely considered to contain only parallel fibers or a single coherent fiber bundle, such as the corpus callosum (CC), is modelled favourably by dispersion [6]. Thus it is important to gauge the pertinence of the dispersion model in the brain.

To address this problem, in this paper, we attempt to answer the question—whether some complex fiber configurations (or the dMRI signals in the voxels) are better explained by dispersion than crossing—from a data driven perspective. Similar studies have been conducted before [6, 9], but in [9], the authors used ex-vivo data from rat brains and in [6], the authors used specially acquired data and conducted their experiments only in a targetted region of the brain—the corpus callosum. We revisit the model comparison problem on the publicly available state-of-the-art HCP dataset [12] in regions known to be rich in complex fiber configurations. Thus, the added values of this study is twofold—one, it is conducted on a widely available, high resolution and high quality dataset, and two, we compare the models in various regions of the brain that contain a variety of simple to complex fiber configurations.

In this study, we consider compartment based models that can be classified as single or crossing or dispersed fiber models and compare them using various well known model selection and validation metrics, such as Akaike information criterion (AIC), Bayesian information criterion (BIC) and cross validation (CV) [6, 10]. We fit the models on a subset of the rich HCP acquisition protocol and repeat the experiments for different subsets numerous times and generate average ranking results in the form of brain maps. These maps quantify the regions of the brain where the single fiber or crossing or dispersion is the preferred model for explaining the dMRI signal. The results indicate the importance of modelling both dispersion and crossing and where each is relevant.

## 2 Materials and Methods

This section presents the procedural details of this study. We begin by describing the models and their constituent compartments, then we describe the experimental setup and finally provide the criteria for ranking the models.

In compartment based modelling the diffusion signal is assumed to be a sum of signals from various tissue compartments, often classified as intracellular, extracellular and free diffusion (to model the cerebrospinal fluid, CSF):  $E = v_{iso}E_{iso} + (1 - v_{iso})(v_{ic}E_{ic} + (1 - v_{ic})E_{ec})$ .  $E$ ,  $E_{iso}$ ,  $E_{ic}$  and  $E_{ec}$  are the normalised measured, CSF, intracellular and extracellular compartment signals respectively, while  $v_{iso}$  and  $v_{ic}$  are the normalized volume fractions of the CSF and intracellular compartments.

A detailed taxonomy of signal models for various tissue compartments is described in [9]. Borrowing from this taxonomy we list out the signal models used in this study. The most flexible is the DTI model:  $E = \exp(-\mathbf{b}\mathbf{g}^T\mathbf{D}\mathbf{g})$ , parametrized by the symmetric 2nd order tensor  $\mathbf{D}$  with eigenvalues  $\lambda_1 \geq \lambda_2 \geq \lambda_3 \geq 0$ . The ‘‘Tensor’’ model is often used to model the extracellular tissue compartment. The constraint  $\lambda_2 = \lambda_3$  gives rise to the more constrained ‘‘Zeppelin’’ model, which is also often used to model extracellular tissue compartment. The ‘‘Ball’’ or isotropic model arises with the double constraints  $\lambda_1 = \lambda_2 = \lambda_3$  and, depending on its diffusivity, can model either the CSF or the extracellular compartment. Finally, the ‘‘Stick’’,  $\lambda_2 = \lambda_3 = 0$ , is used to model the intracellular tissue compartment. Two or more Sticks can be used to model crossing fibers. The Tensor and Zeppelin models can also model CSF or intracellular compartments.

From these compartments, we construct a set of 11 representative models: 2 dispersion, 4 crossing and 5 single fibers models.

**Dispersion Models** To model dispersed fibers, we picked two well established dispersion models from the literature—NODDI-Watson [13] and NODDI-Bingham [11]. Both the models contain three compartments—a Ball for CSF, a tortuosity constrained Zeppelin (extracellular) and a Stick (intracellular). In NODDI-Watson, the Zeppelin and Stick compartments are orientationally dispersed following a Watson distribution (instead of a discrete sum for crossings), while in NODDI-Bingham they follow a Bingham distribution.

**Crossing Models** To model crossing fibers, we picked the well known Stick-Stick-Ball model [4] as a starting point and explored alternative models that can account for CSF, including Stick-Stick-CSF, a highly flexible Zeppelin-Zeppelin-CSF and a triple crossing configuration with Stick-Stick-Stick-CSF.

**Single Fiber Models** To model single fibers, we selected four two-compartment models with increasing complexity—Stick-Ball [3], Stick-CSF, Stick-Zeppelin and Tensor-CSF and a three-compartment model—Stick-Tensor-CSF.

**Model Fitting** The model parameters were estimated from the signal using the same detailed procedure described in [13], which was shown to be robust. The scheme consisted of a non-linear optimization using a maximum likelihood estimation (MLE) for a Rice distributed noise model, where the noise variance  $\sigma^2$  was estimated from the  $b_0$  images. Some of the diffusivities were fixed to likely in vivo values:  $d_{\parallel} = 1.7 \times 10^{-3} \text{ mm}^2/\text{s}$  for the Stick and  $d_{iso} = 3 \times 10^{-3} \text{ mm}^2/\text{s}$  for the CSF-Ball [13].

## 2.1 Data and Experimental Design

The HCP dataset has 288 acquisitions with 18  $b_0$  images and 270 diffusion weighted images (DWIs) distributed evenly over 3  $b$ -shells—with 90 DWIs in each shell. The shells have  $b$ -values of 1000, 2000 and 3000 s/mm<sup>2</sup>. The 90 diffusion gradient directions differ for each shell to provide a maximum isotropic sampling of directions on the sphere both intra-shells and inter-shells [12].

To evaluate the models from a data driven perspective, we conducted bootstrapping experiments with multiple trials. To setup the experiments we divided each of the 90 gradient directions for the three shells into six subsets of 15 isotropically distributed directions. These subsets were computed using the *subsetpoints* algorithm from the Camino toolbox [5], which uses simulated annealing to compute subset directions that are distributed as isotropically as possible. This resulted in a total of 18 subsets, six per shell, each containing 15 gradient directions. From these we created new protocols with 225 gradient directions by removing one subset of 15 gradients from each shell (a total of 45 isotropic gradient directions were removed). By choosing different subsets (of the six) in each shell, we created 216 possible k-fold cross-validation protocols, each containing 225 gradients and missing 45. From these 216 protocols we randomly selected 50 for our experiments.

For each of these 50 trials we computed various model selection and validation metrics (described below) for all the above models. Then we computed the average for each metric over all the trials to rank the models. Finally, we selected the model with the highest average score for each metric in each voxel as the best model. Thus, we created maps (for each metric), which quantitatively identify the most likely model that best explains the diffusion signal in a voxel.

We stress here the computationally demanding requirements of this experimental design. We considered 11 non-linear models (that use Rician ML estimation), with fifty cross-validation experiments each, where each trial had 243 DWIs (225 gradient directions and 18  $b_0$  images). We found that a single slice (axial or coronal), from a HCP dataset, required, on an average, up to 2 days of computation time on a shared high performance computing cluster with 42 parallel processing units running our MATLAB code. An additional 2 days were required to set up each dataset for the experiments. Hence, we only computed the rankings on individual slices of the brain. Nonetheless, to produce robust estimates, we conducted the experiments on two slices (one axial and one coronal) on two separate HCP subjects (a total of four slices from two subjects). The slices were chosen from the coloured FA maps to contain a rich variety of complex fiber configurations.

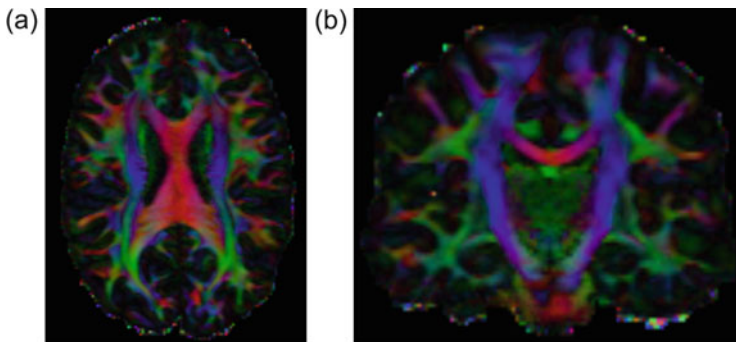
**Model Selection Metrics** We computed several model selection metrics so as not to rely on any single ranking criterion. The models were compared in each voxel by three metrics—AIC, BIC and CV—or prediction error on the unseen part of the protocol (the 45 gradient directions left out in each protocol). AIC and BIC are widely used as model selection metrics that guard against data overfitting by penalising model complexity, with BIC penalising more than AIC. Cross-validation is a model validation metric that helps assess how a model's performance will generalise to unseen data.

Finally, to compute the predicted error for CV, we computed a (negative) Rice log-likelihood value of the predicted signal given the measured signal along the unseen 45 gradient directions. We justify this choice over a mean squared error since the signal is assumed to be corrupted by Rician noise.

### 3 Results

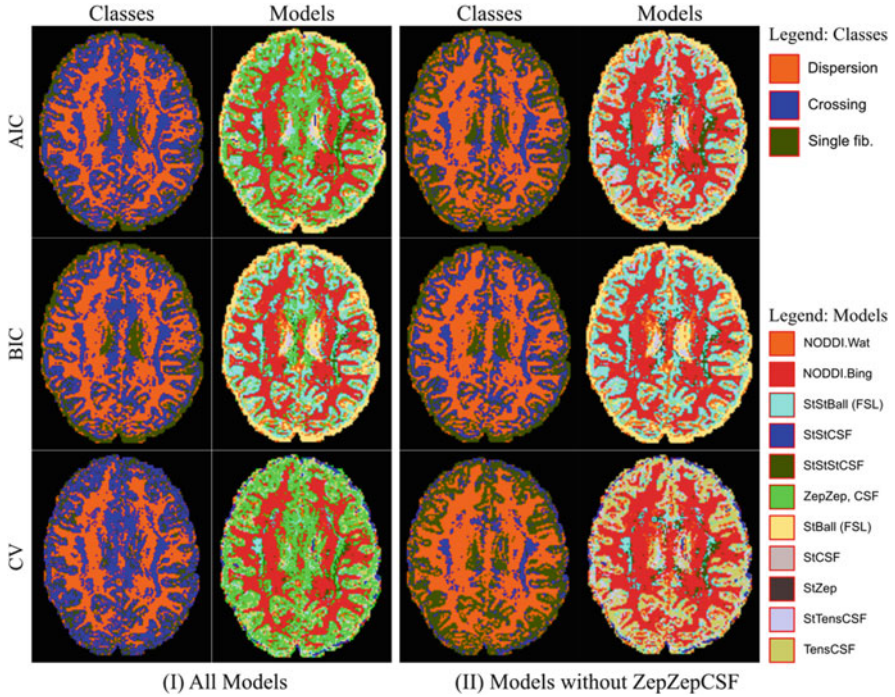
This section presents the final rankings from the three metrics: AIC, BIC and CV after bootstrapping. The results are organised into two parts: (I) where we consider all models of the previous section and (II) where we exclude the ZeppelinZeppelinCSF crossing model. This is motivated by the fact that the Zeppelin compartment, due to its number of free parameters, can model any tissue—CSF, extracellular or intracellular. Hence, although we consider the ZeppelinZeppelinCSF as a crossing model it can very well adapt to fit the signal in a way where one Zeppelin models the extracellular signal while the second Zeppelin models the intracellular signal—effectively becoming a single fiber or dispersion model. This effect can be seen in the results presented in Figs. 2 and 3.

Figure 1 presents two slices as colour-FA maps that were chosen in subject 1 (axial) and subject 2 (coronal). Although, we present only two slices here, we worked on a total of four slices with an axial and a coronal slice in each of the two subjects. In the following, we only present representative results from the slices shown in Fig. 1. The outcome of the other two slices are similar and are not shown. These slices contain regions rich in complex fiber configurations. In particular, these slices contain the corpus callosum (CC), the corticospinal tract (CST) and the superior longitudinal fasciculus (SLF). The cingulum bundle is also visible. The slices also contain the complex crossing configurations between the CC, CST and



**Fig. 1** Colour-FA maps of example slices. (a) Subject-1 axial slice, (b) Subject-2 coronal slice. These are example slices—we worked on two slices for each subject: one axial and one coronal. These slices contain typical fiber bundles such as the corpus callosum (CC), corticospinal tract (CST), the superior longitudinal fasciculus (SLF) and their crossing regions



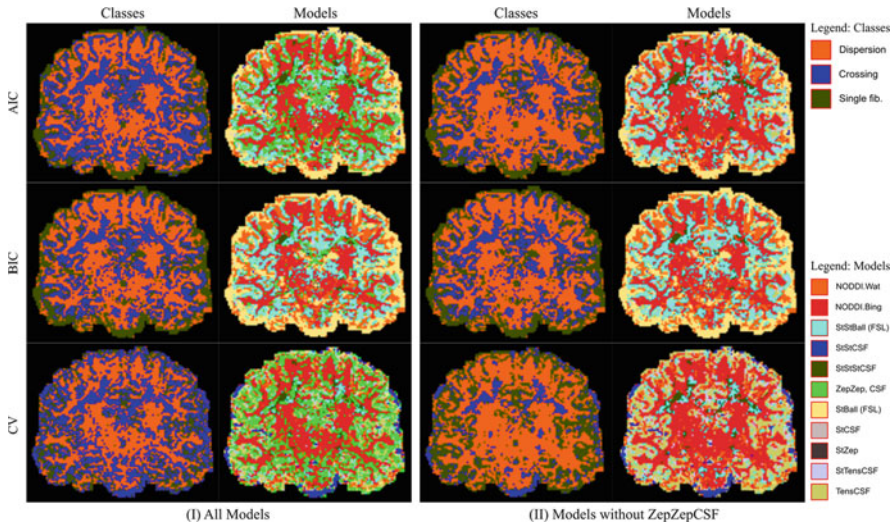


**Fig. 2** Subject-1 (axial slice), see Table 1. Final rankings presented as a *colour* coded brain map. A large portion of the white matter is better explained by dispersion models based on all three metrics of AIC, BIC and CV. Known regions of crossings between the CST and CC are better modelled by crossing models. Greater details are visible in Cols-3,4 without ZepZepCSF than in Cols-1,2 which includes ZepZepCSF. Columns-1,3: rankings aggregated into *classes* of dispersion, crossing and single fiber models. Columns-2,4: rankings of individual models. Columns-1,2: rankings considering all 11 models. Columns-3,4: rankings of ten models without ZepZepCSF. Row-1: AIC. Row-2: BIC. Row-3: CV

SLF. Hence, these mid-brain slices are commonly chosen to identify complex fiber configurations.

Figure 2 presents the ranking results of the 11 models as colour coded maps of the axial slice of subject 1. The maps from the three metrics AIC, BIC and CV are each presented in a separate row. Columns 1 and 2 present the results from (I)—all the models, and columns 3 and 4 present the results from (II)—the set of models not containing ZepZepCSF. Columns 1 and 3 present the rankings aggregated into classes of dispersion, crossing and single fiber models, while columns 2 and 4 present the rankings of the individual models per voxel. It is clear that a large portion of the white matter is modelled better by dispersion models, including in the CC, which is in agreement with [6]. Furthermore, known regions with crossings between major fiber bundles (e.g. CST and CC), which can be located in Fig. 1, are found to favour crossing fiber models. Finally, from column 2, we see that the ZepZepCSF model can fit any kind of tissue (CSF, grey matter and white





**Fig. 3** Subject-2 (coronal slice), see Table 2. Final rankings presented as a *colour* coded brain map. Again a large portion of the white matter is better explained by dispersion models based on all three metrics of AIC, BIC and CV. Known regions of crossings between the CST, CC and SLF are better modelled by crossing models. Greater details are visible in Cols-3,4 without ZepZepCSF than in Cols-1,2 which includes ZepZepCSF. Columns-1,3: rankings aggregated into *classes* of dispersion, crossing and single fiber models. Columns-2,4: rankings of individual models. Columns-1,2: rankings considering all 11 models. Columns-3,4: rankings of ten models without ZepZepCSF. Row-1: AIC. Row-2: BIC. Row-3: CV

matter), making it difficult to discern the underlying tissue type. In contrast, greater tissue details become visible in column 4 by excluding the ZeppelinZeppelinCSF model. This effect is less pronounced in the BIC metric, which penalises model complexity more than AIC, but nonetheless it is still present.

Corresponding results from the coronal slice of subject 2 are presented in Fig. 3. The layout of Fig. 3 is similar to the layout of Fig. 2. Again, it is clear that large portions of the white matter are better explained by dispersion models rather than crossing fiber or even single fiber models. Also regions, such as the centrum semiovale, where the CC, the CST and the SLF are known to cross, are clearly better explained by crossing fiber models. Finally, as seen in Fig. 2, the ZeppelinZeppelinCSF model seems to fit all tissue types, making it hard to discern them in column 2. Excluding the model reveals greater tissue details as seen in column 4.

In both Figs. 2 and 3, the ventricles are better explained by single fiber models. Although this may seem surprising, as seen from the colour maps containing the rankings of the individual models (columns 2,4), the ventricles are best explained by single fiber models that contain a CSF or a Ball compartment.

Tables 1 and 2 present the quantitative results from the experiments and show the statistics that accompany Figs. 2 and 3. Table 1 shows the results of the axial

**Table 1** Subject-1 (axial slice, 10,618 voxels), see Fig. 2

I. Ranking with all models (% of voxels)											
Dispersion		Crossing						Single fiber			
AIC	40.49	39.4						20.1			
BIC	45.0	30.69						24.3			
CV	39.7	41.7						18.64			
NODDI.B		NODDI.W		StStBall		StStCSF		ZepZepCSF		StCSF	
AIC	34.1	6.39	9.11	0.26	2.18	27.85	0.03	9.0	5.57	0.03	5.49
BIC	33.94	11.06	20.2	0.03	1.01	9.45	0.09	16.29	3.73	0.19	4.01
CV	36.91	2.79	2.96	2.15	1.74	34.85	0.06	0.06	1.03	4.28	13.14
II. Ranking models without ZepZepCSF (% of voxels)											
Dispersion		Crossing						Single fiber			
AIC	48.16	18.16						33.69			
BIC	48.11	24.49						27.4			
CV	49.76	11.12						39.11			
NODDI.B		NODDI.W		StStBall		StStCSF		ZepZepCSF		StCSF	
AIC	39.71	8.45	15.15	0.3	3.71	-	0.03	9.09	11.47	0.07	13.03
BIC	35.94	12.17	23.07	0.04	1.38	-	0.09	16.39	5.14	0.4	5.38
CV	44.36	5.4	5.93	2.19	3.0	-	0.06	1.18	10.13	0.14	27.6

Final ranking of models presented as percentage of total voxels in the chosen slice of the HCP data

**Table 2** Subject-2 (coronal slice, 7356 voxels), see Fig. 3

I. Ranking with all models (% of voxels)											
Dispersion		Crossing						Single fiber			
AIC	43.67	35.87						20.5			
BIC	46.38	27.0						26.61			
CV	42.0	38.11						19.88			
NODDI.B		NODDI.W	StStBall	StStCSF	StStStCSF	ZepZepCSF	StCSF	StBall	StTenCSF	StZep	TenCSF
AIC	31.38	12.29	13.3	0.37	1.93	20.27	0.01	13.06	3.52	0.15	3.72
BIC	27.92	18.46	21.47	0.01	0.83	4.70	0.01	22.72	1.97	0.18	1.73
CV	35.54	6.48	4.31	3.33	1.88	28.59	0.08	1.45	3.74	0.10	14.51
II. Ranking models without ZepZepCSF (% of voxels)											
Dispersion		Crossing						Single fiber			
AIC	51.84	20.11						28.06			
BIC	48.81	23.53						27.66			
CV	53.62	12.81						33.58			
NODDI.B		NODDI.W	StStBall	StStCSF	StStStCSF	ZepZepCSF	StCSF	StBall	StTenCSF	StZep	TenCSF
AIC	37.48	14.36	16.71	0.38	3.02	-	0.01	13.15	6.80	0.19	7.91
BIC	29.45	19.36	22.36	0.01	1.16	-	0.01	22.74	2.49	0.19	2.23
CV	43.67	9.95	6.61	3.44	2.76	-	0.08	1.69	7.40	0.12	24.29

Final ranking of models presented as percentage of total voxels in the chosen slice of the HCP data

slice of subject 1, where 10,618 voxels were processed and Table 2 shows the results of the coronal slice of subject 2, where 7356 voxels were processed. Both the results for (I)—all the models, and (II)—the set of models not containing ZeppelinZeppelinCSF are presented. The tables contain the final rankings of the models as a percentage value of the total number of voxels, where the final rankings are the average over 50 trials.

From these statistics, it is evident that up to 40–45 % of the brain's parenchyma is better described by dispersion models. Hence, it is important to model dispersion in the brain—even in the white matter. The remaining voxels are shared between crossing fiber models and single fiber (or CSF) models. The ZeppelinZeppelinCSF model represents a large percentage of all crossing fiber voxels. However, as seen in Figs. 2 and 3, the spatial distribution of the ZeppelinZeppelinCSF model suggests that it is a confounding model that can describe all tissue types, including CSF, white matter and grey matter. Hence, it is not a good representative model for a particular tissue type and cannot be used to discern only crossing fibers. We note, that although we did not include the simpler ZeppelinCSF as a single fiber model, we did test the TensorCSF, which is almost the same. The results indicate that the TensorCSF, when favourable, fits best grey matter areas with partial voluming effects. Excluding the ZeppelinZeppelinCSF model results in an increase of up to 50 % dispersion voxels and a larger percentage of single fiber (or CSF) voxels. More importantly, other crossing fiber models also become more evident. The corresponding colour maps (Figs. 2 and 3, columns 3 and 4) are also more coherent and show greater tissue details.

## 4 Discussion and Conclusion

In this study, we attempted to address the question of whether complex fiber configurations in the brain are better described by dispersion or crossing, from a data driven perspective. We conducted 50 k-fold cross-validation trials and used three metrics, namely AIC, BIC and CV, to compare and rank 11 compartment based models of dispersion, crossing and single fibers on two subjects of the rich HCP dataset. The results indicate that it is important to consider dispersion models since they are ranked favourably in a large portion of the brain's parenchyma (up to 45–50 %), which also includes the CC and other regions of the white matter with complex fiber configurations. The results also showed that compartment based crossing fiber models were better at describing the data from voxels known to contain major fiber bundle crossings such as between the CC, CST and SLF. This is in agreement with the known literature on fiber crossings in dMRI.

This preliminary study has some limitations. Due to long computation times, we were constrained to consider only two slices of the brain and only two subjects in the HCP dataset. Furthermore, we did not include model-free approaches [1, 7] to

detect crossings. We plan to overcome these limitations in the future. Nevertheless, we generated quantitative maps of the brain for each metric, which indicate the importance of modelling dispersion in addition to crossings and where each model is relevant.

**Acknowledgements** The authors were supported by the EPSRC grant: EP/L022680/1. Data were provided by the Human Connectome Project, WU-Minn Consortium (Principal Investigators: David Van Essen and Kamil Ugurbil; 1U54MH091657) funded by the 16 NIH Institutes and Centers that support the NIH Blueprint for Neuroscience Research; and by the McDonnell Center for Systems Neuroscience at Washington University.

## References

1. Aganj, I., et al.: Reconstruction of the ODF in single and multiple shell q-ball imaging within constant solid angle. *Magn. Reson. Med.* **64**(2), 554–566 (2010)
2. Basser, P.J., Mattiello, J., Le Bihan, D.: Estimation of the effective self-diffusion tensor from the NMR spin echo. *J. Magn. Res. B* **103**, 247–254 (1994)
3. Behrens, T.E.J., Woolrich, M.W., Jenkinson, M., Johansen-Berg, H., Nunes, R.G., Clare, S., Matthews, P.M., Brady, J.M., Smith, S.M.: Characterization and propagation of uncertainty in diffusion-weighted MR imaging. *Magn. Res. Med.* **50**, 1077–1088 (2003)
4. Behrens, T.E.J., Berg, H.J., Jbabdi, S., Rushworth, M.F.S., Woolrich, M.W.: Probabilistic diffusion tractography with multiple fibre orientations: What can we gain? *Neuroimage* **34**, 144–155 (2007)
5. Cook, P.A., Bai, Y., Gilani, N.S., Seunarine, K.K., Hall, M.G., Parker, G.J., Alexander, D.C.: Camino: open-source diffusion-MRI reconstruction and processing. In: *ISMRM*, p. 2759 (2006)
6. Ferizi, U., Schneider, T., Tariq, M., Wheeler-Kingshott, C.A., Zhang, H., Alexander, D.C.: The importance of being dispersed: a ranking of diffusion MRI models for fibre dispersion using in vivo human brain data. In: *MICCAI 2013*, pp. 74–81. Springer, Berlin/Heidelberg (2013)
7. Jeurissen, B., Leemans, A., Tournier, J.D., Jones, D.K., Sijbers, J.: Investigating the prevalence of complex fiber configurations in white matter tissue with diffusion magnetic resonance imaging. *Hum. Brain Mapp.* **34**(11), 2747–2766 (2013)
8. Kaden, E., Knoesche, T.R., Anwender, A.: Parametric spherical deconvolution: inferring anatomical connectivity using diffusion MR imaging. *Neuroimage* **37**(2), 474–488 (2007)
9. Panagiotaki, E., Schneider, T., Siow, B., Hall, M.G., Lythgoe, M.F., Alexander, D.C.: Compartment models of the diffusion mr signal in brain white matter: a taxonomy and comparison. *Neuroimage* **59**, 2241–2254 (2012)
10. Scherrer, B., Schwartzman, A., Taquet, M., Prabhu, S.P., Sahin, M., Akhondi-Asl, A., Warfield, S.K.: Characterizing the distribution of anisotropic micro-structural environments with diffusion-weighted imaging (DIAMOND). In: *MICCAI*, vol. 8151, pp. 518–526 (2013)
11. Tariq, M., Schneider, T., et al.: In vivo estimation of dispersion anisotropy of neurites using diffusion MRI. In: Golland, P., Hata, N., Barillot, C., Hornegger, J., Howe, R. (eds.) *MICCAI LNCS*, vol. 8675, pp. 241–248 (2014)
12. Van Essen, D.C., Ugurbil, K., Auerbach, E., et al.: The human connectome project: a data acquisition perspective. *Neuroimage* **62**(4), 2222–2231 (2012)
13. Zhang, H., Schneider, T., Wheeler-Kingshott, C.A., Alexander, D.C.: NODDI: practical in vivo neurite orientation dispersion and density imaging of the human brain. *Neuroimage* **61**(4), 1000–1016 (2012)

# White Matter Fiber Set Simplification by Redundancy Reduction with Minimum Anatomical Information Loss

Gali Zimmerman Moreno, Guy Alexandroni, and Hayit Greenspan

**Abstract** Advanced Diffusion Weighted Imaging (DWI) techniques and leading tractography algorithms produce dense fiber sets of hundreds of thousands of fibers, or more. In order to make fiber based analysis more practical, the fiber set needs to be preprocessed to eliminate redundancies and to keep only essential representative fibers. In this paper we evaluate seven commonly used distance metrics for fiber clustering and present a novel approach for comparing the metrics as well as estimating the anatomical information loss as a function of the reduction rate. The framework includes pre-clustering into sub-groups using K-means, followed by further decomposition using Hierarchical Clustering, each time with a different distance metric. Finally, volume histograms comparison is used to compare the reduction quality with the different metrics. The proposed comparison was applied to a dataset containing tractographies of four healthy individuals. Each set contains around 600k fibers.

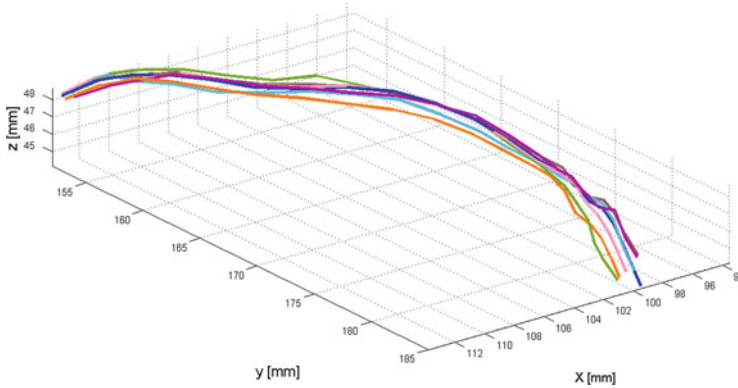
## 1 Introduction

Diffusion Weighted Imaging (DWI) characterizes the diffusion of water in the tissues and is sensitive to the microstructural density, spacing, and orientational organization of tissue membranes, including myelin [1]. Fiber tracking or tractography exploits the measured orientation distribution of water diffusion to follow specific white matter pathways from voxel to voxel through the brain [2]. This information is useful when studying the organization of white matter in the brain as well as the microstructural changes that occur with neuropathology and

---

G.Z. Moreno (✉) • H. Greenspan  
Department of Biomedical Engineering, Tel Aviv University, 69978 Tel Aviv, Israel  
e-mail: [zimer@post.tau.ac.il](mailto:zimer@post.tau.ac.il)

G. Alexandroni  
Department of Electrical Engineering, Tel Aviv University, 69978 Tel Aviv, Israel



**Fig. 1** A set of almost identical fibers which is typical in dense datasets

treatment. Advanced acquisition techniques, such as High Angular Resolution Imaging (HARDI) in conjunction with appropriate tractography algorithms (here q-ball tractography with residual bootstrap [2]) produce highly dense fiber datasets, which can hold millions of fibers. Working with such huge datasets can be quite challenging, especially for algorithms that are supposed to perform highly complex operations on the data. Hence, one can ease the analysis of brain fibers by exploiting the redundancies of the sets, namely the presence of almost identical fibers. This is achieved by compressing the overall fiber set and keeping only unique representatives. Smart reduction should lead to minimum anatomical information loss. Figure 1 shows a set of almost identical fibers which is typical in dense datasets.

The reduced fiber set can be utilized for various purposes:

- It can be used as a pre-processing stage for sophisticated algorithms that cannot deal with huge number of fibers, for example in atlas construction.
- The reduced set may be sufficient for detection of various diseases and thus can ease the computational burden, as long as the reduction is performed efficiently.
- Since there are many DTI datasets of low resolution taken over the years, if one wants to compare new, high resolution acquisitions with an old one, using this tool as a pre-processing may result in better comparison (for example, when an intra-subject follow-up is needed).
- The reduced set should be sufficient to construct a connectivity map between distinct brain regions and thus may serve connectome studies or help determine structural integrity of distinct white matter pathways.

The notion of simplifying the dataset has been around in recent years and different frameworks have been suggested in order to address this issue. These frameworks are usually based on combination of clustering technique and a distance metric. For example, Guevara et al. [5] presented a preprocessing step to be used before further analysis of huge fiber datasets, in which hierarchical decomposition is applied on the fiber set. At first, the set is split according to location and fiber

length, the voxels are clustered into parcels using Kmeans and a parcel connectivity matrix is computed according to the number of tracts passing through each pair of parcels. The parcels are clustered using Hierarchical Clustering (HC) and fiber bundles are inferred. Those bundles are further split, centroids are computed and merged using HC and Hausdorff (HD) distance. Silless et al. [10] performed a comparison of metrics and algorithms for fiber clustering. They used Kmeans and QuickBundle [4] along with several distance metrics: Point Density Model (PDM), Undirected Euclidean (EUC) and HD. Doderio et al. [3] presented a novel clustering approach based on the Dominant Sets framework, in which the white matter fibers are segmented into bundles in order to untangle the complex skein of fibers. This framework is robust to noise and to outliers and the number of clusters it produces is driven by the underlying natural similarity of the data. DTI fiber clustering is also common in fibers segmentation frameworks. In this case it is usually highly desired that the resulting clusters represent anatomical bundles. For example, Ros et al. [8] offered a novel atlas guided clustering framework for exploratory data analysis of large tractography datasets. The framework uses a hierarchical cluster analysis approach that exploits the inherent redundancy in large datasets to time-efficiently group fiber tracts. White matter atlas is incorporated into the clustering to achieve an anatomically correct grouping of fiber tracts. In another paper [7], the shared nearest neighbor clustering algorithm has been applied on DTI fibers along with an evaluation framework based on the manual classification of the fibers into a number of anatomical structures. The authors identify HC as the preferred clustering algorithm for this framework.

To our knowledge, in most frameworks no more than a couple of distance metrics are evaluated. In this work we utilize and compare between various state-of-the-art distance metrics that have been used with WM fibers [3–5, 8, 10]. We suggest a novel approach for comparing the metrics and estimating the anatomical information loss as a function of reduction rate. We do not strive to classify the fibers into tracts, but rather reduce the number of fibers while preserving as much of the fiber set characteristics as possible.

## 2 Methods

The metrics we are evaluating [3–5, 8, 10] are defined in Table 1 along with their main characteristics. Each metric computes a distance between two fibers denoted by  $p$  and  $q$ . A fiber,  $p$ , is represented as a sequence of  $k$  points in a 3-dimensional space, sampled equidistantly:  $p = \{p_1, p_2, \dots, p_k\}$  where  $p_i \in \mathfrak{R}^3$  and  $k = 20$  for all fibers. The choice of  $k$  is motivated by previous research [11] which has shown this to be a good compromise between the dimensionality and fidelity to the original representation.

We use the Complete Linkage Hierarchical Clustering (HC) [6] in order to compare the different distance metrics in conjunction with several reduction rates. This method allows examining multiple reduction rates simultaneously. The input to



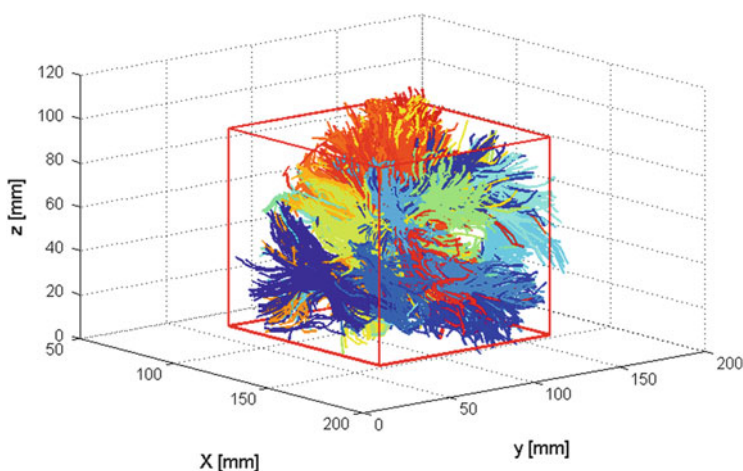
**Table 1** Metrics under evaluation and their characteristics (taken from works [3–5, 8, 10])

Metric	Characteristics
<b>Undirected Euclidean (EUC)</b> $d_{euc}(p, q) = \min(d_{direct}(p, q), d_{flipped}(p, q))$ where: $d_{direct}(p, q) = d(p, q) = \ p - q\ _2$ $d_{flipped}(p, q) = d(p, q^F) = d(p^F, q)$	<ul style="list-style-type: none"> <li>– Fast to compute <math>O(k)</math></li> <li>– Assumes both fibers have <math>k</math> points</li> <li>– Hence, two similar and close fibers, where one is shorter (i.e due to faulty tractography), will automatically be far from each other</li> </ul>
<b>Minimum average Direct-Flip (MDF)</b> $d_{MDF}(p, q) = \min_{direct}(d(p, q), d_{flipped}(p, q))$ where: $d_{direct}(p, q) = d(p, q) = \frac{1}{k} \sum_{i=1}^k \ p_i - q_i\ _2$ $d_{flipped}(p, q) = d(p, q^F) = d(p^F, q)$	<ul style="list-style-type: none"> <li>– Fast to compute <math>O(k)</math></li> <li>– Assumes both fibers have <math>k</math> points</li> <li>– Penalizes distance between curves of different lengths (corresponding points may not be close to each other)</li> </ul>
<b>Hausdorff</b> $d_{HD}(p, q) = \max\{sup_{p_i \in p} inf_{q_i \in q} \ p_i - q_i\ _2, sup_{q_i \in q} inf_{p_i \in p} \ p_i - q_i\ _2\}$	<ul style="list-style-type: none"> <li>– Slow computing time <math>O(k^2)</math></li> <li>– Commonly used for measuring similarity between two curves</li> <li>– Takes into account only one pair of points and neglects all other points along the curves</li> <li>– Hence, penalizes distances between curves of different lengths</li> </ul>
<b>Cosine</b> $d_{cosine}(p, q) = 1 - \frac{pq^T}{\sqrt{(pp^T)(qq^T)}}$	<ul style="list-style-type: none"> <li>– Fast to compute <math>O(k)</math></li> <li>– Reflects orientation and not magnitude</li> </ul>
<b>Shorter mean of Closest distances (DSC)</b> $d_{sc}(p, q) = \min(d_m(p, q), d_m(q, p))$ where: $d_m(p, q) = \text{mean}_{p_i \in p} \min_{q_i \in q} \ p_i - q_i\ _2$	<ul style="list-style-type: none"> <li>– Slow computing time <math>O(k^2)</math></li> <li>– Doesn't penalize distance between curves of different lengths. Hence good for cases in which one of the fibers is broken</li> </ul>
<b>Longer mean of Closest distances (DLC)</b> $d_{lc}(p, q) = \max(d_m(p, q), d_m(q, p))$ where: $d_m(p, q) = \text{mean}_{p_i \in p} \min_{q_i \in q} \ p_i - q_i\ _2$	<ul style="list-style-type: none"> <li>– Slow computing time <math>O(k^2)</math></li> <li>– Penalizes distance between curves of different lengths</li> </ul>
<b>Point Density Model (PDM)</b> Let $K_\sigma$ be a Gaussian kernel with scale parameter $\sigma$ Let define the scalar product between 2 fibers: $\langle p, q \rangle = \frac{1}{k^2} \sum_{i=1}^k \sum_{j=1}^k K_\sigma(p_i, q_j)$ hence $d_{PDM\sigma}^2(p, q) = \ p\ _2 + \ q\ _2 - \langle p, q \rangle$	<ul style="list-style-type: none"> <li>– Slow computing time <math>O(k^2)</math></li> <li>– Sensitive to the fibers form and position and quite robust to missing fiber segments</li> <li>– Captures misalignment and shape dissimilarities at the resolution <math>\sigma</math></li> </ul>

HC is a dissimilarities matrix between all sample couples. The output is a clustering tree (dendrogram) that may be “sliced” at different levels and thus create different numbers of clusters. The first step in the hierarchical clustering process is to look for the pair of samples that are the most similar, having the lowest dissimilarity value, let's say  $d$ . These two samples are then joined at a level of  $d$  in the first step of the dendrogram. This step is repeated iteratively until all the samples are joined into a single cluster. The only open issue is how to calculate the dissimilarity

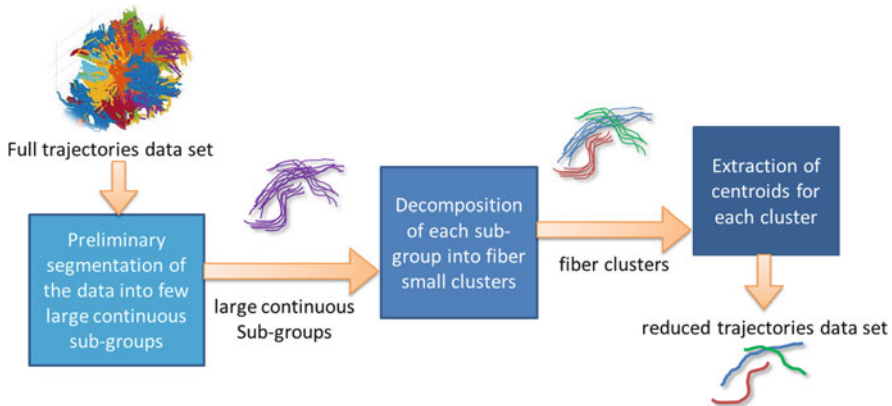
between merged samples and the other samples. This decision determines what type of hierarchical clustering we intend to perform. In this paper we used one of the most common choices, called the maximum, or complete linkage, method: the dissimilarity between two sample groups is the maximum dissimilarity that exists between a pair of samples—one from each group. The number of steps in this clustering technique is one less than the number of samples. Using the maximum method, all samples clustered below a particular level of dissimilarity would have inter-sample dissimilarities less than that level. The use of dissimilarity matrix as the input to HC limits the maximum size of fiber sets it can handle, due to performance issues. Therefore, in order to process substantial amount of fibers, a preliminary clustering stage was needed. For this purpose an efficient version of Kmeans was used (vlkmeans, implemented by VLfeat<sup>1</sup>). Approximated nearest neighbours (ANN) algorithm was used to accelerate the sample-to-center comparison. The full brain fiber set was thus divided into 100 sub-groups of fibers, each containing around 6000 fibers. Then, only the groups with a center of mass that is located inside a predefined bounding box, were chosen. This way the dataset was reduced to fiber groups inside a quarter of the brain. This was done to reduce run time on one hand, but also to conserve the full density of a fiber set, on the other hand. An example of such a quarter-brain set is presented in Fig. 2, where each Kmeans cluster has a different color.

The HC was conducted on each sub-group in the bounding box, using seven distance metrics. Overall, ten reduced sets were inferred, each representing a different reduction rate. The reduced set is made of the centroids of all clusters



**Fig. 2** An example of one quarter of a brain that was used in this work. Each *color* represents different sub-group of fibers that was clustered using Kmeans

<sup>1</sup><http://www.vlfeat.org/>.



**Fig. 3** The proposed framework

inherent from the HC at a given level. The reduced set size varied between 10 % and 100 % of the original set size. Overall, we achieved a reduction rate between 1 and 10 (number of fibers at original set divided by the number of fibers at the reduced set). A block diagram of the proposed framework is shown in Fig. 3.

### 3 Evaluation of Reduced Datasets

We wish to compare between the original, full set of fibers, and the different sets produced by the fibers reduction framework depicted in Fig. 3 (hereafter termed reduced sets). Each set is produced using a combination of different distance metric and reduction rate. A novel approach is proposed for comparing the metrics and estimating the loss of anatomical information as a function of the reduction rate: The volume containing the brain is divided into  $2 \times 2 \times 2 \text{ mm}^3$  cells. Next, for each reduced set and the original set of fibers, two histograms are computed:

- **Binary volume histogram**, in which cells receive the value 1 if any fiber passes through them, 0 otherwise. The concept is illustrated in Figs. 4 and 5. The first exemplifies several axial slices with fibers passing through them while the second shows a representative slice of the binary histogram with several different reduction rates.

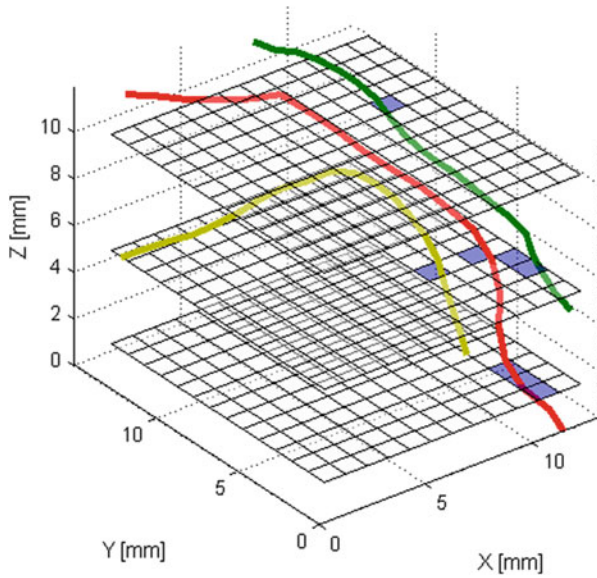


Fig. 4 Illustration of the construction of a binary histogram. *White cell—zero, blue cell—one*

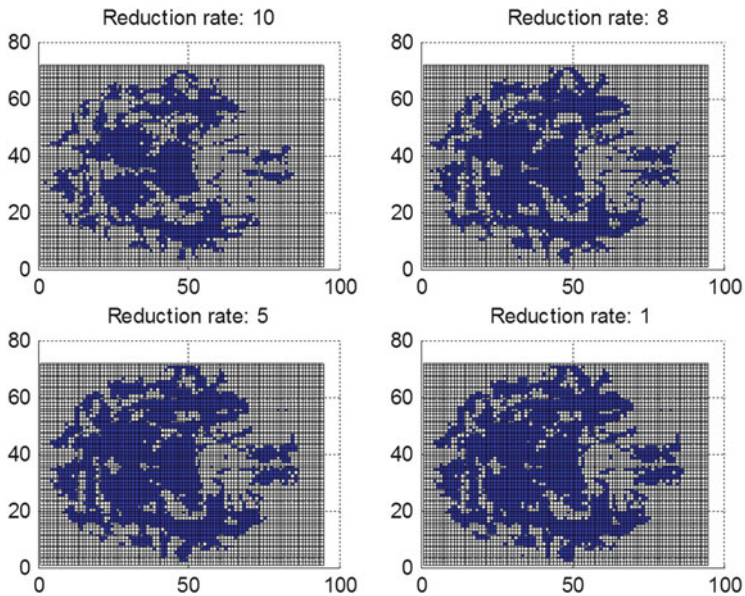


Fig. 5 Representative slice of the binary histogram with different reduction rates. *White cell—zero, blue cell—one*

- **Full volume histogram**, in which each cell value is determined according to the number of fibers that pass through the cell. The fibers in a reduced set are in fact the centroids of the clusters achieved by HC. When assessing the number of fibers passing through a given cell each fiber (centroid) is weighted according to the number of fibers in the cluster it was inferred from. For example, if one centroid originating from four fibers, passes through a given cell, the cell value is 4.

Comparison between the histograms of full and reduced sets:

- (a) Using the Binary Volume Histograms, the Hamming distance was calculated between the original set and the reduced sets histograms. Hamming distance between two binary vectors of equal length is the number of positions in which the corresponding symbols are different. In this paper the result is presented as percentage of total number of voxels.
- (b) Using the Full Volume Histogram, histogram intersection measure was calculated between the original set and the reduced sets histograms:

$d_{\text{histogram intersection}} = \frac{\sum_i \min(a_i, b_i)}{\min(\sum_i a_i, \sum_i b_i)}$ , where  $a$  and  $b$  are the two histograms and  $i$  is the index of histogram bin.

## 4 Experiments and Results

### 4.1 Data

The data used here belongs to four healthy individuals. The scans were acquired at the Memory and Aging Center (MAC) at the University of California San Francisco (UCSF). Subjects were scanned on a Siemens TrioTim syngo 3 T MR scanner equipped with an eight-channel head coil. A high angular resolution diffusion-weighted imaging (HARDI) dataset was acquired using a single-shot spin-echo echo-planar imaging (SE-EPI) sequence including 55 contiguous axial slices acquired in an interleaved order with in-plane resolution of  $2.2 \text{ mm}^2$ , slice thickness of  $2.2 \text{ mm}$ ,  $TR/TE = 8000/109 \text{ ms}$ , flip angle =  $90^\circ$ , matrix =  $100 \times 100$ , 64 noncollinear diffusion sensitization directions at  $b = 2000 \text{ s/mm}^2$ , 1 at  $b = 0$ , and an integrated parallel acquisition technique acceleration factor of 2. Initial image preprocessing was performed using the FMRIB Software Library (FSL<sup>2</sup>). This included skull stripping and eddy currents and motion distortions correction. WM fibers in an entire brain were reconstructed with a probabilistic streamline tractography algorithm in combination with a residual bootstrap Q-ball imaging

---

<sup>2</sup><http://www.fmrib.ox.ac.uk/fsl/>.

method [2] developed in Dipy.<sup>3</sup> Streamline propagation continued until reaching a voxel with  $FA < 0.15$  or a turning angle  $> 60^\circ$ . The resulting sets contains around 600,000 fibers each.

## 4.2 Experiments

The fibers of the four brains were clustered using the scheme described in Sect. 2. Each set was reduced by reduction factors in the range 1–10 using different metrics (Table 1). As a sanity check, the results of different metrics were compared to a simple down-sampled set. For example, at reduction rate 4, every fourth fiber was sampled from the original set. The PDM distance has a parameter that needs to be configured—the sigma factor of the Gaussian kernel. We have tested on the first brain three possible values: 0.5, 2 and 5. The best result was for the 0.5 value; this is the value we used for the rest of the brains.

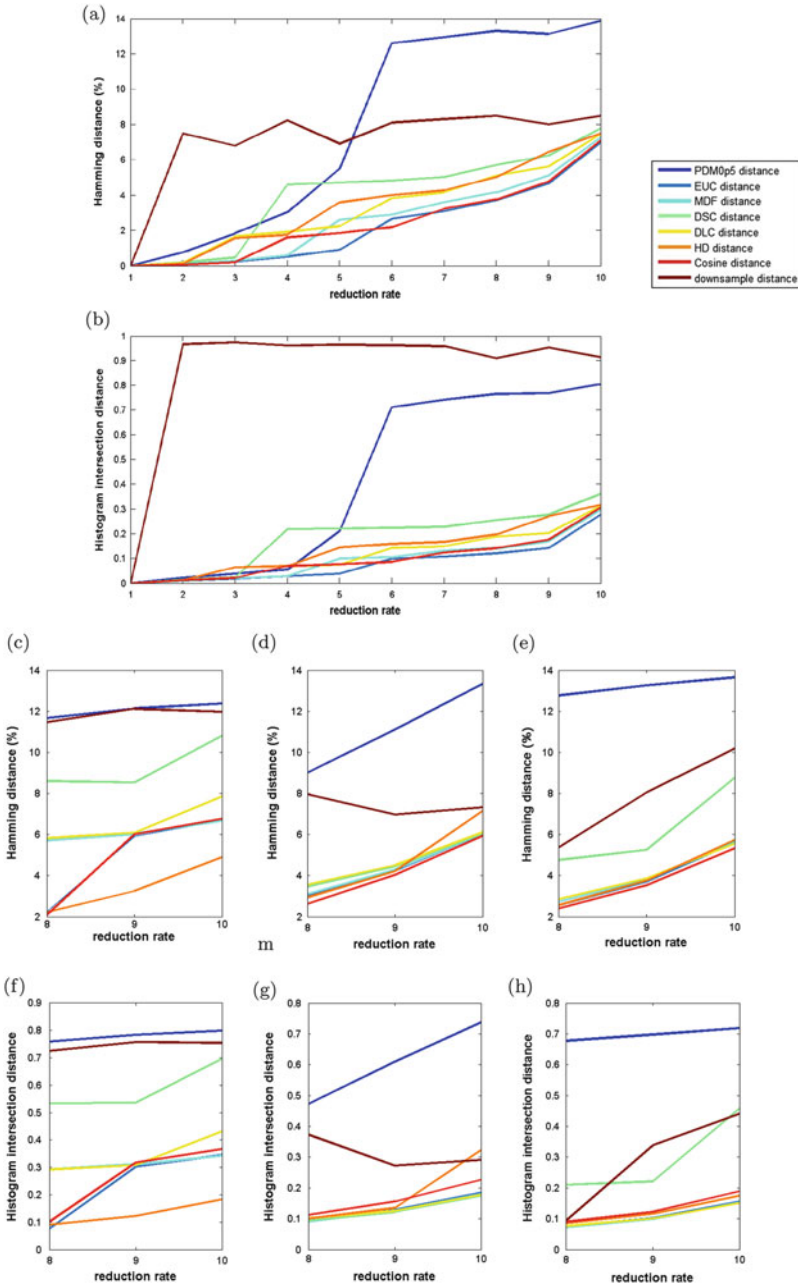
## 4.3 Results

Figure 6 shows the metrics and reduction rate evaluation on the above dataset. Tables 2 and 3 present the Histogram Intersection and the Hamming metrics for reduction rate = 9. This rate exhibits the largest deviation between the metrics. It is clear that by applying clustering, the reduced set remains much more similar to the original set than what we would get by performing a simple down-sampling operation. When comparing the binary histograms (Table 2) the smallest differences are achieved once for EUC, once for HD and in two cases for cosine distance. The fact that HD is the most computationally intensive metric between the three makes cosine the leading choice for a clustering metric. Another interesting insight is that the distance metrics start to behave differently around reduction rate 8 and up. Therefore if there is no need for reduction rate greater than 8, any of the tested metrics may be used (with the exception of down-sampling).

When comparing the full histograms (Table 3), the smallest distance is received for different metric in each case. In this type of comparison all of the distances are much smaller, which is to be expected since the weighting of the fibers in the reduced set makes the full histogram of this set very similar to the full histogram of the original set. For this reason Table 3 does not provide clear indication of the best metric.

---

<sup>3</sup><http://nipy.sourceforge.net/dipy/>.



**Fig. 6** (a) Binary volume histograms comparison between seven different distance metrics and down-sampling, at ten reduction rates. (b) Full volume histograms comparison between seven different distance metrics and down-sampling, at ten reduction rates. (c)–(e) Hamming distance comparison for the remaining three brains, at reduction rates 8–10, (f)–(h) Intersection distance comparison for the remaining three brains, at reduction rates 8–10



**Table 2** Hamming distance values at reduction rate 9 for all metrics and brains, the smallest distance for each brain is in bold

	PDM	EUC	MDF	DSC	DLC	HD	Cosine	d.sampl.
Brain1	13.4	<b>4.7</b>	5.1	6.2	5.6	6.5	4.8	8
Brain2	12.1	5.9	6	8.5	6.1	<b>3.3</b>	6	12.1
Brain3	11.1	4.3	4.3	4.5	4.5	4.2	<b>4</b>	7
Brain4	13.3	3.7	3.8	5.3	3.9	3.8	<b>3.5</b>	8

**Table 3** Histogram Intersection distance values at reduction rate 9 for all metrics and brains, the smallest distance for each brain is in bold

	PDM	EUC	MDF	DSC	DLC	HD	Cosine	d.sampl.
Brain1	0.769	<b>0.142</b>	0.17	0.277	0.203	0.271	0.177	0.953
Brain2	0.785	0.304	0.312	0.537	0.309	<b>0.123</b>	0.312	0.758
Brain3	0.609	0.13	0.126	<b>0.122</b>	0.126	0.136	0.156	0.273
Brain4	0.699	0.102	<b>0.099</b>	0.222	0.101	0.117	0.123	0.339

## 5 Discussion and Future Work

In this paper we evaluated a variety of state-of-the-art distance metrics for fiber clustering and presented a novel approach for comparing the metrics and estimating the anatomical information loss as a function of the reduction rate. For both comparison methods the worst performance was received when using simple downsampling or the PDM metric. In addition, in all cases the differences in performance of the various metrics become more significant at higher reduction rates (8 and up). The results of comparison by Hamming distance lean in favour of cosine distance as a leading metric for fibers set reduction by clustering. This is based on the relatively low Hamming distances and the low computational cost.

There are several open issues that should be covered in future work: From the histograms comparison plots it seems that when the reduction rate is higher than 10, the clustering techniques performance converges to what one can get by down-sampling. Additional testing may be conducted with higher reduction rates in order to define the range in which clustering is preferable to simple down-sampling. Quantifying the success of fiber reduction is highly dependent on the purpose of the reduction. Additional comparison methods may be useful; for example we can use network measures of brain connectivity in order to quantify the effect of fiber reduction on brain connectivity networks [9]. Another quantification method would be to use labeled sets of fibers in order to check if all of the anatomical tracts are adequately represented following the reduction. Finally in this study we used the HC clustering method. Alternative clustering methods can be examined and compared per given task.



**Acknowledgements** We would like to thank our colleagues for providing the data and tractography for this work: Marilu Gorno-Tempini, MD, Ph.D., Language and Neurobiology Laboratory at the UCSF Memory and Aging Center, Roland Henry Ph.D., department of Neurology, UCSF, as well as Maria Luisa Mandelli and Bagrat Amirbekian, department of Neurology, UCSF.

## References

1. Alexander, A.L., Lee, J.E., Lazar, M., Field, A.S.: Diffusion tensor imaging of the brain. *Neurotherapeutics* **4**(3), 316–329 (2007)
2. Berman, J.I., Chung, S., Mukherjee, P., Hess, C.P., Han, E.T., Henry, R.G.: Probabilistic streamline q-ball tractography using the residual bootstrap. *Neuroimage* **39**, 215–222 (2008)
3. Doderer, L., Vascon, S., Giancardo, L., Gozzi, A., Sonaand, D., Murino, V.: Automatic white matter fiber clustering using dominant sets. In: *International Workshop on Pattern Recognition in Neuroimaging (PRNI)*, pp. 216–219 (2013)
4. Garyfallidis, E., Brett, E., Correia, M.M., Williams, G.B., Nimmo-Smith, I.: Quickbundles, a method for tractography simplification. *Front. Neurosci.* **6**, 175 (2012)
5. Guevara, P., Poupon, C., Rivire, D., Cointepas, Y., Descoteaux, M., Thirion, B., Mangin, J.F.: Robust clustering of massive tractography datasets. *NeuroImage* **54**, 1975–1993 (2011)
6. Johnson, S.C.: Hierarchical clustering schemes. *Psychometrika* **32**(3), 241–254 (1967)
7. Moberts, B., Vilanova, A., Van Wijk, J.J.: Evaluation of fiber clustering methods for diffusion tensor imaging. In: *IEEE Visualization, VIS 05*, pp. 65–72 (2005)
8. Ros, C., Güllmar, D., Stenzel, M., Mentzel, H.-J., Reichenbach, J.R.: Atlas-guided cluster analysis of large tractography datasets. *PLoS ONE* **8**(12), e83847 (2013). doi:[10.1371/journal.pone.0083847](https://doi.org/10.1371/journal.pone.0083847)
9. Rubinov, M., Sporns, O.: Complex network measures of brain connectivity: uses and interpretations. *Neuroimage* **52**(3), 1059–1069 (2010)
10. Siless, V., Medina, S., Varoquaux, G., Thirion, B.: A comparison of metrics and algorithms for fiber clustering. In: *2013 International Workshop on Pattern Recognition in Neuroimaging (PRNI)*, pp. 190–193 (2013)
11. Zvitia, O., Mayer, A., Shadmi, R., Miron, S., Greenspan, H.: Co-registration of white matter tractographies by adaptive-mean-shift and Gaussian mixture modeling. *IEEE Trans. Med. Imaging* **29**(1), 132–145 (2010)

# A Temperature Phantom to Probe the Ensemble Average Propagator Asymmetry: An In-Silico Study

Marco Pizzolato, Demian Wassermann, Tanguy Duval,  
Jennifer S.W. Campbell, Timothé Boutelier, Julien Cohen-Adad,  
and Rachid Deriche

**Abstract** The detection and quantification of asymmetry in the Ensemble Average Propagator (EAP) obtained from the Diffusion-Weighted (DW) signal has been shown only for theoretical models. EAP asymmetry appears for instance when diffusion occurs within fibers with particular geometries. However the quantification of EAP asymmetry corresponding to such geometries in controlled experimental conditions is limited by the difficulty of designing fiber geometries on a micrometer scale. To overcome this limitation we propose to adopt an alternative paradigm to induce asymmetry in the EAP. We apply a temperature gradient to a spinal cord tract to induce a corresponding diffusivity profile that alters locally the diffusion process to be asymmetric. We simulate the EAP and the corresponding complex DW signal in such a scenario. We quantify EAP asymmetry and investigate its relationship with the applied experimental conditions and with the acquisition parameters of a Pulsed Gradient Spin-Echo sequence. Results show that EAP asymmetry is sensible to the applied temperature-induced diffusivity gradient and that its quantification is influenced by the selected acquisition parameters.

---

M. Pizzolato (✉) • D. Wassermann • R. Deriche  
Athena, Inria Sophia Antipolis - Méditerranée, Sophia Antipolis, France  
e-mail: [marco.pizzolato@inria.fr](mailto:marco.pizzolato@inria.fr)

T. Duval • J. Cohen-Adad  
Polytechnique Montreal, Montreal, QC, Canada

J.S.W. Campbell  
McGill University, Montreal, QC, Canada

T. Boutelier  
Olea Medical, La Ciotat, France

## 1 Introduction

The Ensemble Average Propagator (EAP) obtained from the Diffusion-Weighted (DW) signal in Magnetic Resonance Imaging (MRI) expresses the displacement probability of spin-bearing particles [2]. Although the displacement probability is commonly considered axially symmetric along a diffusion direction, this is generally not the case in tissue. The displacement probability, hence the EAP, may show asymmetry due to the characteristics of tissue geometry, as recently reported [7, 8]. For instance, a relationship between EAP asymmetry and axonal tortuosity variation rates—corresponding to different levels of axonal compression—is described in [8]. However the task of measuring asymmetry on real data is non-trivial, therefore here we present an in-silico study to assess the feasibility of a physical phantom to measure EAP asymmetry via DW-MRI, highlighting the relationship between the controllable experimental parameters and said asymmetry.

Technical difficulties in building a physical phantom for DW-MRI mainly consist on designing axonal geometries at micrometer scale with controllable properties and tissue-like diffusion characteristics. For instance, at the present moment building a phantom resembling compressed axons with different degrees of compression is very challenging. An alternative solution to induce diffusion asymmetry needs to be found. Other difficulties are related to the measurement of the asymmetry with the DW signal. Particularly, EAP asymmetry may only be retrieved from the complex DW signal thus implying that a problem of observability of the phenomenon also arises, specially with reference to the high sensibility of the signal's phase to noise and bulk movement. In this work, however, we mainly discuss the physical principles underlying the proposed phantom and investigate the relationships with the controllable parameters of a Pulsed Gradient Spin Echo (PGSE) sequence.

In the study we predict the DW signal acquired in a possible real experimental setup designed with the precise scope of inducing diffusion asymmetry in the sampled tissue. The adopted strategy consists in applying a temperature gradient in a spinal cord tract, along the direction of the fibers, to obtain a spatially localized diffusion coefficient. We refer to this as a temperature-induced diffusivity gradient. The diffusion coefficient will be forced to vary monotonically with the position coordinate, i.e., it will increase as the spatial location gets closer to the highest temperature position. In this way, at each point along the fiber, a water particle moving towards the highest temperature position will experience higher diffusivity values than a particle moving in the opposite direction, thus leading to asymmetry in the EAP.

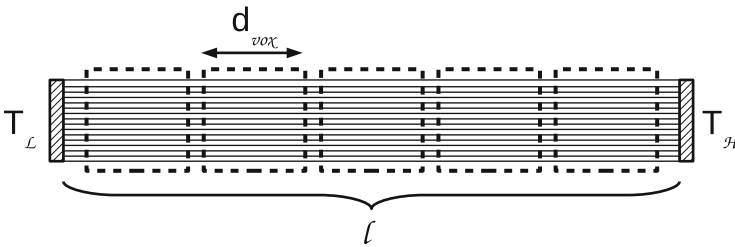
This work investigates the relationship between the temperature-induced diffusivity gradient and EAP asymmetry in order to assess the feasibility in principle of a real DW signal acquisition with a PGSE sequence. To do so we first describe the proposed phantom and the related assumptions. Then we consider an applied

temperature gradient and derive the corresponding spatial diffusivity profile induced in the phantom. With this setup we simulate a PGSE acquisition of the phantom with voxels located along its longitudinal direction, that is the direction aligned with the fibers. For each voxel we recover the complex DW signal and then compute the EAP from this to quantify the asymmetry. We then present results as the experimental conditions and acquisition parameters variate, highlighting the dependency of EAP asymmetry on the temperature-induced diffusivity gradient. Finally we discuss the feasibility of the proposed technique and its inherent limitations.

## 2 Phantom Design and Experimental Setup

The simulation considers a temperature gradient applied to a longitudinal spinal cord tract of length  $l$ , where the longitudinal direction corresponds to that parallel to the fibers. The temperature gradient is generated in the spinal cord by heating up the two extremities at two different temperatures maintained constant during time: one extremity at low temperature  $T_L$  and the other at high temperature  $T_H$ . The schematic representation of the experimental setup is illustrated in Fig. 1. The corresponding temperature profile along the spinal cord tract is consequently obtained, as discussed in Sect. 3.

The temperature difference between the extremities produces a profile  $T(z)$  of varying temperature along the longitudinal direction  $z$ . The spatially-localized temperature  $T(z)$  in the spinal cord tract is used to obtain the corresponding diffusivity value  $D(T)$ . The diffusivity values are computed along the spinal cord in order to obtain a diffusivity profile. Furthermore, values are conveniently scaled to simulate Cerebrospinal Fluid ( $D_{csf}(T)$ ), Grey Matter ( $D_{gm}(T)$ ) and White Matter ( $D_{wm}(T)$ ) diffusivities.



**Fig. 1** Schematic representation of the proposed experimental setup. A spinal cord tract of length  $l$  lies between two gears maintained at two different constant temperatures,  $T_L$  and  $T_H$ , the fibers composing the spinal cord tract being aligned along the direction connecting said gears namely the longitudinal direction. Acquisition voxels with side  $d_{vox}$  are located along the longitudinal direction so that to collect signal from tissue at different mean temperatures

The DW-MRI acquisition is simulated bi-dimensionally, similarly to [8]. The spinal cord tract is discretized in adjacent spatial units corresponding to voxels distributed along the longitudinal direction (Fig. 1). The tissue underlying each voxel is considered as being composed of straight fibers with infinitesimal thickness. Water particles diffusing within these fibers are subjected to the locally observed temperature-induced diffusivity gradient. Therefore the simulated signal takes into account the local values of the diffusion coefficient. Voxels size  $d_{vox}$  (m) and PGSE parameters such as maximum diffusion gradient strength  $G_{max}$  (T/m), pulse duration  $\delta$  (s) and separation between pulses  $\Delta$  (s) are taken into account. Finally EAP asymmetry is calculated for each voxel and studied as function of the applied temperature gradient.

The following section provides details about the assumed temperature gradient along the longitudinal direction of the spinal cord tract.

### 3 Applied Temperature Gradient

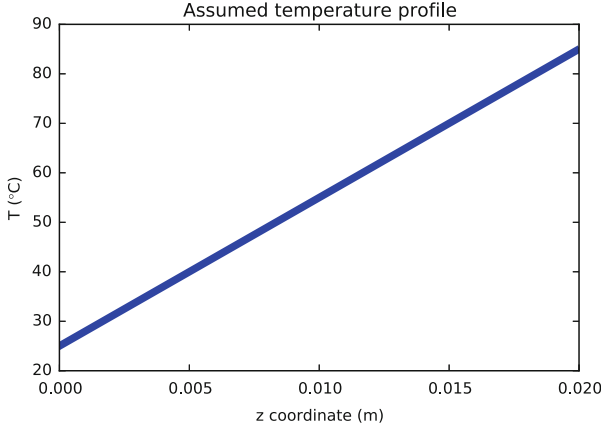
In this section we present the assumptions made for the temperature profile applied along the spinal cord tract.

The spinal cord tract is considered as a homogeneous rod extending longitudinally to the fibers' direction. Due to the long time required for the MR acquisition, stationary conditions are assumed. Therefore no transient dynamic is considered for the calculation of the resulting temperature gradient which will then be constant. Hence, the temperature gradient along the rod is obtained as the steady-state solution of the heat equation when the two extremities are maintained at two different constant temperatures, rendering a linear temperature profile

$$T(z) = z \cdot \frac{T_H - T_L}{l} + T_L \quad (1)$$

where  $T_L$  is the temperature in  $z = 0$ ,  $T_H$  is the temperature applied in  $z = l$  and  $l$  is as usual the length of the spinal cord tract (Fig. 1). Temperature will be henceforth expressed in Celsius degrees ( $^{\circ}\text{C}$ ).

The following section reports how we calculate the diffusivity profile along the spinal cord tract, for different tissue types, given the temperature profile (Fig. 2).



**Fig. 2** Temperature as function of the position as found from the steady-state solution of the heat equation. Maximum distance  $l = 0.02$  m,  $T_L = 25^\circ\text{C}$ ,  $T_H = 85^\circ\text{C}$

## 4 Induced Diffusivity Profile

In this section we calculate the diffusivity profile for different tissues as resulting from the application of a temperature gradient having the characteristics reported in Sect. 3. The diffusivity profile along the longitudinal direction of the spinal cord tract depends on the assumed temperature profile. However the diffusion coefficient depends also on the characteristics of the liquid in which particles diffuse and on the geometrical properties of the particles themselves. These dependencies are well described by the Stokes-Einstein equation:

$$D(T) = \frac{k_B(T + 273.15)}{6\pi r\eta} \quad (2)$$

where  $k_B$  is the Boltzmann constant,  $r$  the radius of the spherical particle and  $\eta$  the dynamic viscosity. Assuming free diffusion of water particles, the radius can be approximated by applying the inverse formula of Eq. (2) while knowing the reference values at  $T = 25^\circ\text{C}$  of dynamic viscosity  $\eta_{fw}^{25}$  (kg/ms) and diffusivity  $D_{fw}^{25} = 2.299 \cdot 10^{-9} \text{ m}^2/\text{s}$  [4]. However, dynamic viscosity is function of temperature and cannot simply be a constant. Therefore to calculate  $\eta_{fw}^{25}$  we employ the equation describing the relationship between free water viscosity and temperature [1], which is accurate to within 2.5 % from  $0^\circ\text{C}$  to  $370^\circ\text{C}$ :

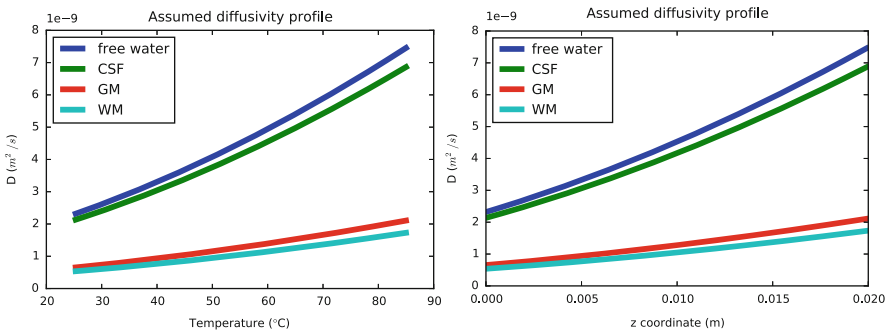
$$\eta_{fw}(T) = 2.414 \cdot 10^{-5} \cdot 10^{\frac{247.8}{T+273.15-140.0}}. \quad (3)$$

Using Eq. (3) the predicted free water viscosity at  $25^\circ\text{C}$  is  $\eta_{fw}^{25} = 0.891 \cdot 10^{-3} \text{ kg/ms}$ , then we approximate the radius inverting Eq. (2) obtaining  $r \approx 1.066 \cdot 10^{-10} \text{ m}$ .

Water diffusivity in tissues is lower than that of free water for a same temperature. Indeed dynamic viscosity increases in tissue accordingly to its microstructural properties. Assuming a constant temperature of  $37.9^\circ\text{C}$  in the living brain tissue [5], the dynamic viscosity in CSF ( $\eta_{csf}^{37.9}$ ), GM ( $\eta_{gm}^{37.9}$ ) and WM ( $\eta_{wm}^{37.9}$ ) can be calculated from Eq. (2) knowing the corresponding diffusivity values, which can be found to be [3]  $D_{csf}^{37.9} = 2.9 \cdot 10^{-9} \text{ m}^2/\text{s}$ ,  $D_{gm}^{37.9} = 0.89 \cdot 10^{-9} \text{ m}^2/\text{s}$  and  $D_{wm}^{37.9} = 0.73 \cdot 10^{-9} \text{ m}^2/\text{s}$ .

Having the viscosity values for the different tissues at  $37.9^\circ\text{C}$ , we calculate an empirical scaling factor between free water viscosity as function of temperature in Eq. (3), and tissue viscosity. Therefore viscosity values could be found as corresponding to  $\eta_{csf} \approx 1.09 \cdot \eta_{fw}$ ,  $\eta_{gm} \approx 3.54 \cdot \eta_{fw}$  and  $\eta_{wm} \approx 4.32 \cdot \eta_{fw}$ . We note that the scaling factor for gray matter is in agreement with the assumed value in [6]. These factors are adopted to scale Eq. (3) to calculate the dynamic viscosity at all the temperatures for the different tissue types. By substituting  $\eta$  in Eq. (2) with the opportunely scaled version of Eq. (3), we compute the diffusivity profiles along the spinal cord tract, as shown in Fig. 3. We point out that diffusion coefficients used to obtain the scaling factors are the apparent diffusion coefficients for the corresponding tissues. Particularly the apparent diffusion coefficient in a tissue can be seen as the product  $\lambda \cdot D^*$  where  $D^*$  is the diffusion coefficient of the media, which depends on temperature and viscosity, and  $\lambda$  is the tortuosity coefficient which solely depends on geometry. For instance in WM the tortuosity changes with the considered diffusion direction, i.e. the diffusion coefficient along the direction parallel to fibers is higher than  $D_{wm}^{37.9}$ . However we use this value aware that it renders a lower bound for the diffusivity profile along fibers. Moreover the diffusivity profile of CSF and GM may only be considered within the fibers for the sake of representing 1D diffusion in the corresponding tissues.

In the next section we calculate the Ensemble Average Propagator for adjacent voxels located along the longitudinal direction of the spinal cord tract, and obtain the corresponding complex DW signal. We then describe the quantification of the asymmetry of the EAP obtained from the signal.



**Fig. 3** Diffusion coefficient profile for different tissue types as function of the temperature (*left*) and of the position in the spinal cord tract (*right*)

## 5 EAP with Temperature-Induced Diffusivity Gradient

In this section we present the derivation of the Ensemble Average Propagator (EAP) when a temperature-induced diffusivity gradient is applied to the spinal cord tract. The obtained EAP is used to recover the complex DW signal via a Fourier relationship [9]. From the complex signal the original EAP can be recovered exploiting the inverse relationship and its asymmetry can be quantified as presented below.

The EAP is obtained similarly to [8], by considering diffusion within straight fibers with infinitesimal thickness. Fibers are considered to be aligned along the longitudinal direction of the spinal cord tract. Assuming that particles diffuse freely along the fiber, their displacement follows a normal distribution with variance  $2D(T, \eta)t_d$ , where  $t_d$  is the diffusion time and  $D(T, \eta)$  is the diffusion coefficient as function of temperature and dynamic viscosity. Then, the probability of a particle experiencing a net displacement along the z-axis  $\Delta z$  can be approximated by

$$P(\Delta z, t_d, T, \eta) = \frac{1}{\sqrt{4\pi D(T, \eta)t_d}} e^{-\frac{\Delta z^2}{4D(T, \eta)t_d}} \quad (4)$$

which depends on the temperature and, consequently, on the location of the particle within the spinal cord tract. We note that since both the temperature and the dynamic viscosity are function of the particle location  $z$ , Eq. (4) can be rewritten as

$$P(\Delta z|z, t_d) = \frac{1}{\sqrt{4\pi D(z + \Delta z)t_d}} e^{-\frac{\Delta z^2}{4D(z + \Delta z)t_d}} \quad (5)$$

where we highlight the dependency of the diffusivity on the location. The fact that the diffusion coefficient is not constant but varies monotonically with the location is the cause of the asymmetry of Eq. (5), which will be reflected in the EAP.

The EAP that will be considered for calculating the signal is that accounting for the ensemble of particles within the whole voxel. To do so we discretize the length of the spinal cord tract  $l$  in locations  $z_i$  each  $1 \mu\text{m}$ . At each location  $z_i$  we evaluate Eq. (5) over an observation frame large enough to observe the Gaussian decay, thus obtaining a local propagator. Particularly the local propagator is calculated from a maximum negative displacement  $-\Delta z_{max}$  to a maximum positive displacement  $\Delta z_{max}$  with  $\Delta z_{max} = (6D_{fw}^{37.9} t_d)^{\frac{1}{2}}$ . The final EAP for each voxel is obtained by numerical integration of the local propagators calculated for the locations  $z_i$  within the voxel's limits, considering voxels of size  $d_{vox}$  ( $= 1 \text{ mm}$  in the rest), corresponding to the numerical implementation of

$$EAP(\Delta z; t_d) = \int_{z \in \text{voxel}} \rho_0 P(\Delta z|z, t_d) dz \quad (6)$$

where  $\rho_0$  is the constant initial density of particles.



The resolution of the calculated EAP, i.e., the minimum observable displacement  $r$ , is calculated from the maximum gradient strength as  $r = 1/G_{max}$ . Sequence parameters such as  $\delta$  and  $\Delta$  are chosen in agreement with plausible real values to account for the chosen  $t_d$ . The voxel-averaged EAP is used to calculate the complex signal via Fourier transform under narrow pulse approximation [8, 9].

The final goal is to quantify the asymmetry of the EAP calculated for each voxel. To do this the EAP is re-computed from the complex signal and the EAP asymmetry is then calculated as the Hellinger distance between each EAP and its axially reflected version [8]

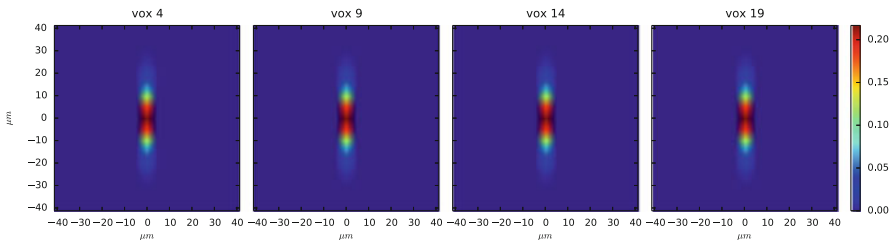
$$H^2 = \frac{1}{2} \int \left( \sqrt{EAP(\mathbf{r}|t_d)} - \sqrt{EAP(-\mathbf{r}|t_d)} \right)^2 dr \quad (7)$$

where  $\mathbf{r} = (0, \Delta z)$  and where  $0 \leq H \leq 1$ , 0 corresponding to equality, i.e., perfect symmetry, and 1 to maximum inequality, i.e., perfect asymmetry.

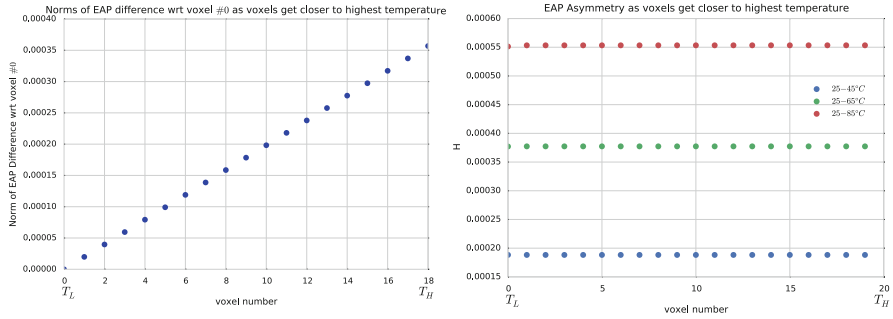
## 6 Results

Results show that the amount of EAP asymmetry increases as the temperature gradient increases. Particularly, acquisitions with increasing  $T_H$  (e.g. 45, 55, 65, 75, 85 °C) while keeping  $T_L$  fixed (i.e. 25 °C) will lead to an increasing EAP asymmetry. This relation can be predicted with the developed model such as in Fig. 6 left. In the following more detailed results and related comments are provided.

**EAP Changes Slowly Across Voxels** Under a determined temperature gradient it is hard to visually distinguish between the EAP for different voxels acquired along the spinal cord tract. For instance, Fig. 4 shows the EAP for different voxels at different locations. However values of the EAP change accordingly to the underlying mean diffusivity rates which change based on the voxel location. Indeed Fig. 5 left shows the norm of the differences between the EAP of each voxel



**Fig. 4** EAPs for voxels at different location. As the voxel number increases the location is closer to the hottest point ( $t_d = 90$  ms,  $G_{max} = 500$  mT/m). Results obtained for WM (25–45 °C)



**Fig. 5** *Left*: norm of difference between the EAP of a voxel with respect to the EAP measured for the voxel #0 corresponding to that showing the lowest temperature in the range 25–85 °C. *Right*: Hellinger distance for different voxels and temperature gradients. Results obtained for WM ( $t_d = 90$  ms,  $G_{max} = 1$  T/m)

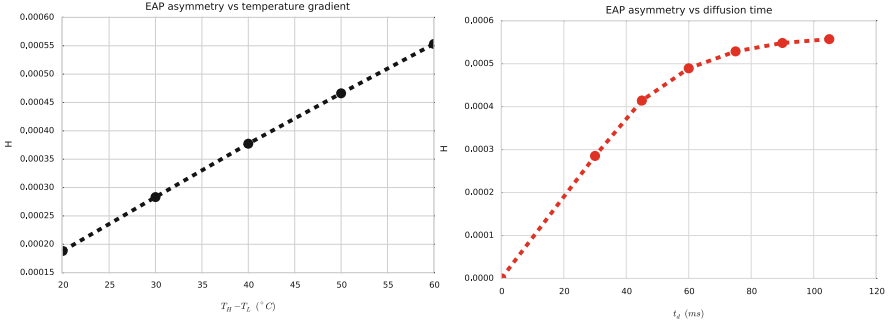
with respect to that of the coldest voxel, as the location gets closer to the highest temperature position  $z = l$ . A linear relationship can be found.

**EAP Asymmetry for Different Voxels Remains Constant** The plot in Fig. 5 right shows the EAP asymmetry for voxels at locations closer and closer to the highest temperature position  $z = l$ . Contrary to Fig. 5 left, here there are no differences between voxels. Indeed the amount of EAP asymmetry, since the diffusivity profile is quasi-linear, is constant. The only actual differences between voxels have to be ascribed to the slight non-linearity of the temperature-induced diffusivity gradient (Fig. 3).

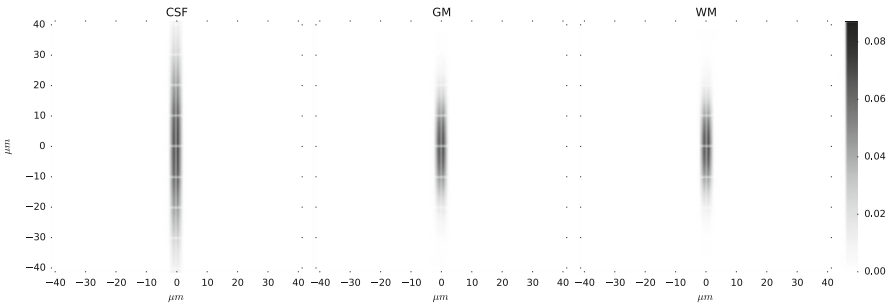
**EAP Asymmetry Increases with the Temperature-Induced Diffusivity Gradient** The most interesting result is that, despite EAP asymmetry across voxels remains substantially constant, the amount of asymmetry increases with the temperature gradient (for a given dynamic viscosity or tissue type). For instance Fig. 5 right shows EAP asymmetries for different temperature gradients, 25–45, 25–65 and 25–85 °C. The quasi-linear relationship between EAP asymmetry and temperature gradient can be better appreciated in Fig. 6 left.

**EAP Asymmetry Increases with the Diffusion Time** When particles can diffuse for a longer time they can probe a wider range of diffusivity values. Therefore the differences between the EAP values calculated for positive and negative displacements are greater. However the asymmetry dependency on the diffusion time seems to follow a saturative profile (Fig. 6 right).

**Maximum Gradient Strength Seems to Have Little Influence on EAP Asymmetry** As opposed to what stated in [8], when fibers are straight the maximum gradient strength  $G_{max}$ , i.e. the spatial resolution of the EAP, seems not to influence the asymmetry. In this experiment it was found that increasing the resolution simply leads to convergence of the asymmetry value.



**Fig. 6** EAP asymmetry averages (among the voxels) as function of: temperature gradient with  $T_L = 25^{\circ}C$  and  $t_d = 90$  ms (*left*); diffusion time with  $25-85^{\circ}C$  (*right*). Results obtained for WM ( $G_{max} = 1$  T/m)



**Fig. 7** EAP for straight fibers assuming diffusion as in Cerebrospinal Fluid, Grey Matter and White Matter ( $t_d = 90$  ms,  $G_{max} = 1$  T/m)

**The Selected Dynamic Viscosity Influences the Results** Depending on the considered type of tissue (dynamic viscosity) the results can be more or less relevant. Indeed for a given temperature gradient, considering the dynamic viscosity of free water diffusion leads to a greater diffusivity gradient than that obtained considering white matter tissue (Fig. 3 left). The considered tissue type affects the resulting EAP as illustrated in Fig. 7.

## 7 Discussion

The objective of this work is to propose a method for quantifying the asymmetry of the Ensemble Average Propagator with a real physical phantom, and assess its feasibility. Designing a physical phantom for measuring asymmetry is important in order to validate the use of EAP asymmetry as tissue biomarker as in the case of

compressed axons [8]. However it imposes several challenges. Conceptual designs accounting for specific fiber geometries inducing asymmetry face the limit of the scale required to appreciate constrained diffusion. To overcome this practical issue we propose to induce diffusion asymmetry in tissue by applying a temperature gradient to, in this case, a spinal cord tract. The temperature gradient results in a corresponding diffusivity profile which alters the local diffusion process to be asymmetric since the displacement of particles diffusing towards locations with higher diffusion coefficients is in principle greater than that towards locations with lower diffusivity.

In this work we present the study of how experimental conditions and acquisition parameters influence the generation and the quantification (via DW signal) of EAP asymmetry respectively. A first consideration is that the proposed method shows low sensitivity of EAP asymmetry to the diffusivity profile induced by the tested temperature gradients. Indeed, as opposed to the results reported for asymmetry induced by the fiber geometry in [8], here values of asymmetry are low. This might lead to issues in detecting different levels of asymmetry in the physical phantom. However results show that the amount of EAP asymmetry increases almost linearly with the temperature gradient and that asymmetry can be better quantified with a longer diffusion time  $t_d$  in the PGSE sequence. These observations suggest that an experiment investigating the relationship between EAP asymmetry and the temperature-induced diffusivity gradient is feasible. More precisely, a possible experimental strategy is to perform acquisitions of the spinal cord tract at different temperature-induced diffusivity gradients to replicate results such as those in Fig. 5 right and Fig. 6 left.

Further investigations and simulations are required. A next step is to release the infinitesimal thickness assumption that constrains particle trajectories to lie on a line. If particles were free to move along different directions their global displacement would affect differently the EAP and its asymmetry. Moreover, additive signal noise should be taken into account. Particular attention should be paid to the choice of diffusion time  $t_d$  and maximum gradient strength  $G_{max}$ . Indeed, since both influence the effective signal to noise ratio (SNR) their values should be carefully selected to obtain the best trade-off between observing asymmetry (increasing  $t_d$ ) and higher EAP resolution (increasing  $G_{max}$ ).

We have shown the theoretical EAP asymmetry sensitivity to a temperature-induced diffusivity gradient. Although we encourage further investigations on the subject, this work constitutes a fundamental step towards the design of a physical phantom for EAP asymmetry quantification through the DW signal.

**Acknowledgements** The author “Marco Pizzolato” expresses his thanks to Olea Medical and to the Provence-Alpes-Côte d’Azur Regional Council for providing grant and support.

## References

1. Al-Shemmeri, T.: *Engineering Fluid Mechanics*, pp. 17–18. Ventus Publishing ApS, Copenhagen (2012)
2. Callaghan, P.T.: *Principles of Nuclear Magnetic Resonance Microscopy*. Clarendon Press, Oxford (1991)
3. Helenius, J., Soinne, L., Perkiö, J., Salonen, O., Kangasmäki, A., Kaste, M., Carano, R.A., Aronen, H.J., Tatlisumak, T.: Diffusion-weighted MR imaging in normal human brains in various age groups. *Am. J. Neuroradiol.* **23**, 194–199 (2002)
4. Holz, M., Heil, S.R., Sacco, A.: Temperature-dependent self-diffusion coefficients of water and six selected molecular liquids for calibration in accurate 1H NMR PFG measurements. *Phys. Chem. Chem. Phys.* **2**, 4740–4742 (2000)
5. Kozak, L., Bango, M., Szabo, M., Rudas, G., Vidnyanszky, Z., Nagy, Z.: Using diffusion MRI for measuring the temperature of cerebrospinal fluid within the lateral ventricles. *Acta Paediatr.* **99**, 237–243 (2009)
6. Nicolas, R., Aubry, F., Pariente, J., Franceries, X., Chauveau, N., Saint-Aubert, L., Chollet, F., Breil, S., Celsis, P.: Water diffusion in q-space imaging as a probe of cell local viscosity and anomalous diffusion in grey and white matter. *Open-Access J. Basic Princ. Diffus. Theory Exp. Appl. Diffusion-fundamentals.org* **14**, 3, 1–4 (2010)
7. Özarslan, E., Koay, C.G., Basser, P.J.: Remarks on q-space MR propagator in partially restricted, axially-symmetric, and isotropic environments. *Magn. Reson. Imaging* **27**, 834–844 (2009)
8. Pizzolato, M., Wassermann, D., Boutelier, T., Deriche, R.: *Exploiting the Phase in Diffusion MRI for Microstructure Recovery: Towards Axonal Tortuosity via Asymmetric Diffusion Processes*. *Medical Image Computing and Computer Assisted Intervention*, Munich (2015)
9. Tanner, J.E., Stejskal, E.: Restricted self-diffusion of protons in colloidal systems by the pulsed-gradient, spin-echo method. *J. Chem. Phys.* **49**(4), 1768–1777 (1968)

# Registration Strategies for Whole-Body Diffusion-Weighted MRI Stitching

Jakub Ceranka, Mathias Polfiet, Frederic Lecouvet, Nicolas Michoux, Johan de Mey, and Jef Vandemeulebroucke

**Abstract** With the development of ultra-fast magnetic resonance imaging sequences, whole-body diffusion-weighted magnetic resonance imaging (WB-DWI) becomes a popular diagnostic tool in patient cancer screening. Modality can improve plenty of clinical investigations such as lymphoma, multiple melanoma or metastatic bone cancer diagnosis. Because of vast body coverage and MR scanner limitations, whole-body image is acquired in blocks, called stations. Precise ‘stitching’ of whole-body stations is essential to ensure correct image formation, yet there are not many commercially available registration algorithms. We developed and investigated several registration methods based on apparent diffusion coefficient (ADC) and diffusion-weighted images (DWI) to improve station-to-station registration and WB-DWI image quality. This paper reports on registration results of 52 whole-body DWI images and compares them with other already existing methods. Proposed registration techniques based on ADC images demonstrated superior performance over other registration methods.

---

J. Ceranka (✉) • M. Polfiet • J. Vandemeulebroucke  
Department of Electronics and Informatics (ETRO), Vrije Universiteit Brussel, Pleinlaan 2,  
B-1050 Brussels, Belgium

Department of Medical IT, iMinds, Gaston Crommenlaan 8 (Box 102), B-9050 Ghent, Belgium  
e-mail: [jderanka@etro.vub.ac.be](mailto:jderanka@etro.vub.ac.be)

F. Lecouvet • N. Michoux  
Department of Radiology, Cliniques Universitaires Saint-Luc, Hippocrate Avenue 10/2942,  
Brussels, Belgium

J. de Mey  
Department of Radiology, Universitair Ziekenhuis Brussel (UZ Brussel), Laarbeeklaan 101,  
B-1090 Brussels, Belgium

## 1 Introduction

Due to the recent development of parallel imaging and ultra-fast MRI sequences (i.e. echo-planar imaging), imaging of diffusion properties of tissues is no longer limited to the brain. The whole-body diffusion-weighted imaging (WB-DWI) sequence proposed by Takahara et al. [1] can cover the whole body in a scanning time of about 30 min, making the use of whole-body diffusion measurements feasible in clinical routine.

Diffusion-weighted imaging is an emerging technique in oncology, which has showed great potential in tumour detection [2, 3], evaluation of lymph nodes [4] or treatment response assessment in metastatic bone disease [5, 6]. The method can be also used as a secondary validation tool in detection of bone metastases for several imaging modalities such as positron emission tomography, computed tomography or bone scintigraphy, demonstrating higher detection accuracy [7]. Other advantages include the absence of ionizing radiation, no required contrast agents and comparatively short acquisition times, making WB-DWI a promising imaging modality for the clinic [8].

WB-DWI is acquired in separate sections, called imaging stations, which are subsequently combined into a whole-body image. However, inconsistencies between imaging stations can occur due to image distortion, scale differences in segment intensities and patient motion during acquisition. Each station is therefore acquired with an overlap of predefined length with the neighbouring segment, allowing to compensate for geometric misregistrations and intensity mismatches between the stations. In particular, the accurate *stitching* of the image stations for the whole-body image formation is crucial, as misalignment of image stations may lead to artefacts in the whole-body image. Artefacts can hinder visual assessment, influence the reproducibility of segmentation techniques and degrade the performance of subsequent inter-station intensity calibration algorithms [9, 10], used to obtain a uniform signal across the cranio-caudal direction and driven by the overlap between neighbouring image stations.

Registration of the imaging station is a challenging task in case of WB-DWI. Images have relatively low spatial resolution (e.g.  $2.3 \times 2.3 \times 6 \text{ mm}^3$ ) and signal-to-noise (SNR) ratio, and the overlapping boundary is often limited to a few slices only (i.e. five slices in case of Philips DWIBS sequence [11]). In addition, voxel intensities cannot be compared directly due to scale differences occurring between the stations. In some cases, whole-body anatomical MRI may be acquired during the same session, providing a high quality, distortion-free reference onto which the diffusion segments can be mapped. In many cases however, the corresponding anatomical images are lacking, and whole-body image formation should be performed using DWI segments only.

Commercial workstations often allow for manual compensation of intensity mismatches between stations, neglecting spatial misalignment of diffusion-weighted segments. In literature, few authors have described automated methods for WB-DWI formation. Blackledge et al. [6] proposed a station-to-station registration algorithm

based on high b-value DWI images. First, the algorithm compensates for inter-station intensity mismatches in each segment by linearly scaling station intensities such that the cumulative histograms of overlapping boundaries match. Next, phase-encoding (anterior-posterior) shifts are corrected by optimizing the mean squared differences (MSD) criterion of the overlapping region. However, the fact only uni-dimensional translations are corrected, and intensity correction is performed prior to image alignment is limiting the performance of the approach.

In this work, we studied different registration strategies for whole-body image formation of DWI. Their performance was evaluated for consistency and smoothness at the segment boundary and compared to the method proposed by Blackledge et al. [6].

## 2 Materials and Methods

### 2.1 Registration Approach

Image registration is typically defined as an optimization problem where the objective is to find the spatial transformation  $\mathcal{T}_\mu$  that aligns a target image  $g$  to a reference image  $f$

$$\hat{\mu} = \arg \min_{\mu} \mathcal{C} \left( f(\mathbf{x}), g(\mathcal{T}_\mu(\mathbf{x})) \right). \quad (1)$$

In (1),  $\mathbf{x}$  is the spatial coordinate taken from an overlapping image region  $\Omega$ ,  $\mathcal{T}_\mu$  is a spatial transformation with parameters  $\mu$  over which the optimisation is performed and  $f$  and  $g$  are the continuous intensity functions associated to the reference and target image for which we assumed an interpolation scheme.  $\mathcal{C}$  is the cost or metric function associated with the registration problem and quantifies the quality of the current solution.

The most straightforward metric comes down to computing the mean squared differences (MSD) of the overlapping intensities,

$$D_{MSD}(f, g) = \sum_{\mathbf{x} \in \Omega} \frac{(f(\mathbf{x}) - g(\mathcal{T}_\mu(\mathbf{x})))^2}{N_\Omega}, \quad (2)$$

where  $N_\Omega$  is the total number of pixels in  $\Omega$ . As MSD assumes a one-to-one correspondence between the intensities of the images under study, its use is limited to a number of mono-modal problems.

The normalised cross-correlation (NCC), which assumes a linear relationship between the intensity distributions, is typically used for images with the same



modality but under different acquisition conditions,

$$D_{NCC} = \sum_{x \in \Omega} \frac{(f(x) - \bar{f})(g(\mathcal{T}_\mu(x)) - \bar{g})}{\sigma_f \sigma_g}. \quad (3)$$

Herein is  $\bar{f}$ , respectively  $\bar{g}$ , the mean intensity of the reference and target images and  $\sigma_f$  and  $\sigma_g$  the variances thereof.

For multimodal registration problems, assuming a linear relationship is often too strong a constraint, and a more general description is needed. Mutual information (MI) assumes a statistical relationship between the intensity distributions of the two images under study and tries to maximize their joint entropy. MI is described by

$$D_{MI}(f, g) = - \sum_{a,b} p_{fg}(a, b) \frac{\log p_{fg}(a, b)}{\log p_f(a) \log p_g(b)}, \quad (4)$$

where  $p_{fg}$  is the joint probability density function (PDF) of the reference and target images and  $p_f$  and  $p_g$  the marginalised PDF's for respectively the reference and target image.

MSD can not be applied directly for registering DWI segments, due to the intensity scale differences between stations. One should either correct for the intensity mismatches in the segments, using the overlapping region given by the acquisition geometry prior to registration [6], or employ a metric suitable for this problem such as NCC or MI. Alternatively, when diffusion-weighted images with at least two different b-values are available, one can compute a map of the apparent diffusion coefficient (ADC) using

$$ADC_{xy} = \frac{1}{(b_1 - b_0)} \ln \frac{S_0}{S_1}. \quad (5)$$

In this equation,  $S_0$  and  $S_1$  are the signal intensities obtained from diffusion-sensitized T2 imaging with at least two values for the gradient factor  $b$  ( $s/mm^2$ ). ADC maps are non-susceptible to intensity scale differences between stations and their values are independent of DWI imaging sequence used. Therefore, ADC images may be beneficial for the registration process as they allow assuming a stronger relationship between the intensity distributions, e.g. through the use of the MSD metric.

Several layers of image information (e.g. diffusion-weighted images and ADC maps) can be taken into account simultaneously using a multi-channel registration approach, which can be seen as the vector-wise extension of single-channel or scalar registration.

The registration problem can be given by

$$\hat{\mu} = \arg \min_{\mu} \mathcal{C} \left( f(x), g(\mathcal{T}_\mu(x)) \right). \quad (6)$$

It is important to note that in (6), the intensity functions  $\mathbf{f}$  and  $\mathbf{g}$  have become vector-valued and the cost function  $\mathcal{C}$  should therefore handle vector-valued intensities. In this work, such multi-channel metrics were expressed as a linear combination of single-channel metrics between corresponding channels,

$$D_{MC}(\mathbf{f}, \mathbf{g}) = \sum_{i=1}^n w_i D_{SC}(f_i, g_i). \quad (7)$$

Herein is  $D_{SC}$  a single channel metric such as MSD or MI,  $f_i$  and  $g_i$  the  $i$ th channel in the multi-channel image  $\mathbf{f}$  and  $\mathbf{g}$ ,  $w_i$  the weight associated to the  $i$ th channel and  $n$  the total number of channels.

## 2.2 Experimental Design

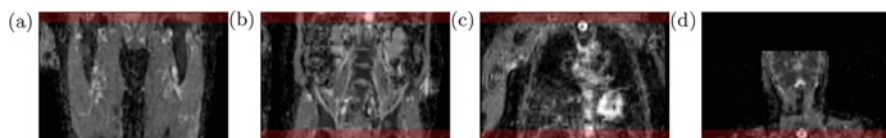
We compared eight rigid registration algorithms with 6 degrees of freedom (a rigid transformation with translations along three directions and rotations around the three axes) and one algorithm with 1 degree of freedom (anterior-posterior translation).

The first group of registration approaches consists of single-channel (i.e. one layer of image information) registration (SCR) methods based on diffusion-weighted images. We applied SCR using the NCC and MI applied on the high b-value image. The use of the high-value image was preferred over the low b-value image, due to the better observed image quality. In addition, we also evaluated the performance using MSD as a metric, after correcting for intensity mismatches using the correction algorithm described in Sect. 2.3.

The second type of SCR is based on using the computed ADC images rather than the acquired diffusion-weighted segments. As the ADC represents a quantitative voxel measure (see Fig. 1), we used MSD to optimize the alignment in this case.

The last series of experiments is based on a multi-channel (i.e. two or more layers of image information) registration (MCR) approach. The multi-channel technique based either on two diffusion-weighted channels or three channels including the ADC images. NCC or MI was used for channels of low and high b-value diffusion-weighted images (MI or NCC metric), while MSD was used for the ADC channel.

An overview of the registration approaches studied in this work is given in Table 1. All registrations were implemented in the `elastix` software package.



**Fig. 1** WB ADC images composed of four imaging stations with five slices of boundary overlay (marked *red*) for the same patient. (a) Legs image, (b) pelvis image, (c) torso image and (d) head image. ADC is not susceptible to intensity mismatches between the stations

**Table 1** Registration methods compared in the study

Images used	Metric with weights	Inter-station intensity calibration	Layers of image information (channels)
DWI	MSD b = 1000 s/mm <sup>2</sup>	Before registration	1
DWI	MSD b = 1000 s/mm <sup>2</sup> 1 degree of freedom	Before registration	1
DWI	MI b = 1000 s/mm <sup>2</sup>	After registration	1
DWI	NCC b = 1000 s/mm <sup>2</sup>	After registration	1
ADC	MSD	After registration	1
DWI	0.5 MI b = 1000 s/mm <sup>2</sup> 0.5 MI b = 0 s/mm <sup>2</sup>	After registration	2
DWI	0.5 NCC b = 1000 s/mm <sup>2</sup> 0.5 NCC b = 0 s/mm <sup>2</sup>	After registration	2
ADC DWI	0.5 MSD ADC 0.25 MI b = 1000 s/mm <sup>2</sup> 0.25 MI b = 0 s/mm <sup>2</sup>	After registration	3
ADC DWI	0.5 MSD ADC 0.25 NCC b = 1000 s/mm <sup>2</sup> 0.25 NCC b = 0 s/mm <sup>2</sup>	After registration	3

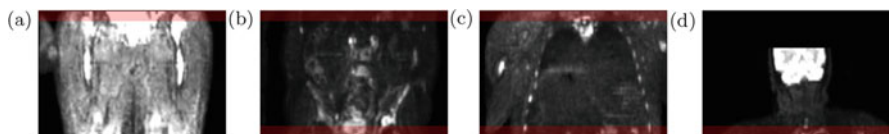
### 2.3 *Inter-Station Intensity Calibration*

The algorithm used for correction of intensity mismatches between stations was adapted from Nyúl et al. [12]. For each overlapping boundary region, the intensity histogram is calculated. The intensity histogram of the target image is then adjusted to match the intensity histogram of the reference station by optimizing an intensity scaling factor using a criterion based on the least squares error evaluated at 13 points evenly spread across the histogram.

### 2.4 *Data Description*

This study was based on retrospective materials, consisting of isotropic WB-DWI images from whole-body MRI routine examinations performed in patients with metastatic cancer in different stages. Images were acquired for evaluation of response to various anti-cancer treatments. All images were anonymized before archiving and post-processing. Fifty-two WB-DWI images were registered and evaluated. Images were acquired using Philips Medical Systems 1.5T and 3T MR imaging systems with diffusion-weighted whole-body imaging sequence with background body signal suppression (DWIBS) [11] at the Cliniques Universitaires Saint-Luc in Brussels, Belgium.

Whole-body DWI studies were achieved by sequential acquisition of four image stations, roughly covering legs, pelvis, torso and head, respectively (Fig. 2). Each station consisted of 44 or 50 slices with five overlapping slices. Axial free breathing echo-planar diffusion-weighted sequence with  $b = 0$  and  $b = 1000 \text{ s/mm}^2$  were applied. Diffusion images of three spatial directions ( $x$ ,  $y$ ,  $z$ ) were measured. Diffusion magnitude image, calculated from the three diffusion images, rendered the image weighted in global diffusion (i.e. trace image, isotropic image). The individual directional source images were not viewed separately, but combined into a single final set for diagnosis. Images were acquired using following parameters of DWIBS protocol: repetition time (TR) = 3079–6063 ms, echo time (TE) = 65–66 ms, slice thickness 4–6 mm, matrix size of  $192 \times 192$ – $352 \times 352$ , pixel spacing 1.59–2.29 mm, field of view (FOV) =  $440 \times 440$ – $530 \times 530$  mm.



**Fig. 2** WB-DWI composed of four imaging stations ( $b = 1000 \text{ s/mm}^2$ ) with five slices of boundary overlay (marked *red*) for the same patient. (a) Legs image, (b) pelvis image, (c) torso image and (d) head image. All images are displayed with the same window and level settings, yet strong intensity mismatches can be observed between stations (a) and (b)

## 2.5 Validation

Two measures were derived to evaluate the whole-body images obtained using the different registration approaches. The first consisted of computing the mean absolute differences (MAD) of the overlapping voxels. The second measure was obtained by calculating the partial derivative along the cranio-caudal direction of whole-body image using a 3D Sobel kernel. The final measure was computed as the average of the absolute intensities near the interface between two stations.

The measures were applied for both ADC and high b-value diffusion-weighted images ( $b = 1000 \text{ s/mm}^2$ ) and compared to the whole-body ADC and DWI images created from non-registered image stations. Due to application of 6 degrees of freedom, the overlay of the region changed between subjects and stations. For each of the registrations, the actual overlap was therefore recomputed and the measures were only evaluated in this region. As the measures are inherently normalized by the number of voxels, changes in size of the overlap did not influence the result. In case the registration strategy did not include intensity correction for the diffusion-weighted images, this was performed prior to computing the measures.

## 3 Results and Discussion

All of the investigated methods had 6 degrees of freedom, except of the method proposed by Blackledge et al. [6], which allows for translations only in phase-encoding direction. Our implementation of latter method failed to register 18 out of 52 whole-body DWI-MR images and results for the remaining whole-body registrations were comparable with results of non-registered stations. The results for this method were not included in the tables. We did include the results for a closely related method, involving prior intensity correction, but employing a transformation with 6 degrees of freedom. The results for eight different registration methods of the whole-body DWI images are summarized in Tables 2 and 3.

Single-channel registration on DWI using MSD method, with prior intensity correction performed, gave poor registration results. The alignment of the image stations was also visually incorrect, with frequent gaps in slice-selection direction between the stations. What is more, 7 out of 52 registrations had failed. Note that failed registrations were not taken into account for calculation of means in Tables 2 and 3. The poor registration performance of both methods based on DWI images using the MSD metric may be caused by inaccurate inter-station intensity calibration, as it is based on the overlapping region, prior to registration.

Single-channel registration on DWI using MI and NCC also returned unstable results, with 8 and 6 failures, respectively. This was most likely caused by the low SNR in some images, in particular the images acquired on 1.5T MR. In contrast, single-channel registration on ADC using MSD showed stable registration results with low MAD and gradient scores. SCR using the ADC was more stable and

**Table 2** Averaged results of the mean absolute differences (MAD) and gradient intensities (GI) for all of the registered whole-body images for eight different methods and non-registered stations validated on ADC images with number of failed registrations

Method	MAD $\pm$ SD $\times 10^{-4}$	GI $\pm$ SD $\times 10^{-3}$	Failed
Non-registered	4.46 $\pm$ 0.61	9.60 $\pm$ 0.78	0
SCR on DWI using MSD	4.68 $\pm$ 0.99	8.49 $\pm$ 0.99	7
SCR on DWI using MI	4.33 $\pm$ 0.77	8.70 $\pm$ 1.32	8
SCR on DWI using NCC	4.04 $\pm$ 0.46	8.59 $\pm$ 1.17	6
SCR on ADC using MSD	3.68 $\pm$ 0.56	8.35 $\pm$ 0.89	0
MCR on DWI using MI	4.29 $\pm$ 0.75	8.96 $\pm$ 1.51	0
MCR on DWI using NCC	3.69 $\pm$ 0.36	8.15 $\pm$ 0.88	0
MCR on ADC using MSD with DWI using MI	3.68 $\pm$ 0.56	8.13 $\pm$ 0.90	0
MCR on ADC using MSD with DWI using NCC	3.65 $\pm$ 0.35	8.10 $\pm$ 1.00	0

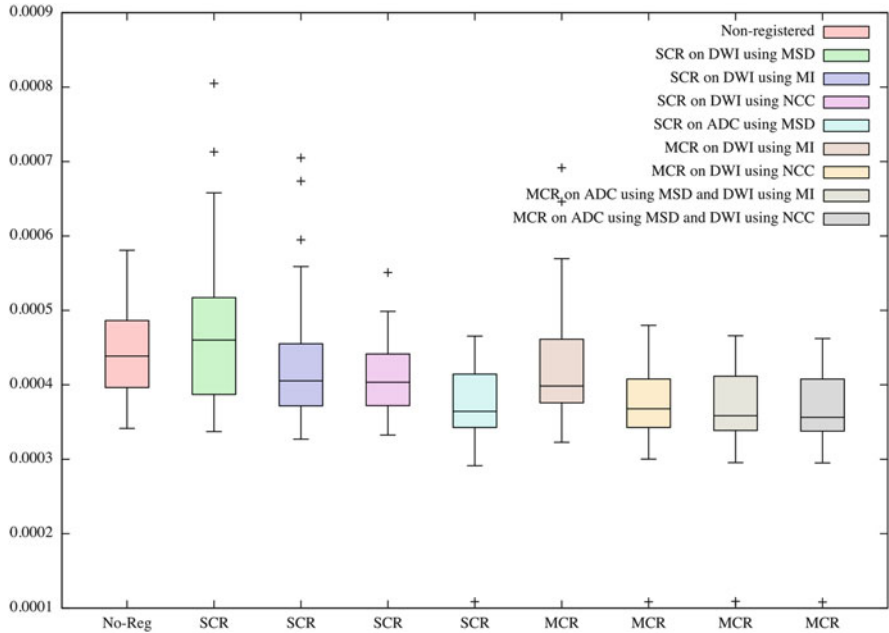
**Table 3** Averaged results of the mean absolute differences (MAD) and gradient intensities (GI) for all of the registered whole-body images for eight different methods and non-registered stations validated on DWI  $b = 1000$  s/mm<sup>2</sup> images after intensity correction with number of failed registrations

Method	MAD $\pm$ SD	GI $\pm$ SD	Failed
Non-registered	16.52 $\pm$ 4.58	358 $\pm$ 109	0
SCR on DWI using MSD	27.13 $\pm$ 13.5	396 $\pm$ 132	7
SCR on DWI using MI	15.22 $\pm$ 4.31	376 $\pm$ 151	8
SCR on DWI using NCC	14.99 $\pm$ 4.38	400 $\pm$ 163	6
SCR on ADC using MSD	14.84 $\pm$ 4.32	353 $\pm$ 113	0
MCR on DWI using MI	15.32 $\pm$ 4.31	421 $\pm$ 182	0
MCR on DWI using NCC	14.51 $\pm$ 4.10	341 $\pm$ 107	0
MCR on ADC using MSD with DWI using MI	14.65 $\pm$ 4.16	346 $\pm$ 100	0
MCR on ADC using MSD with DWI using NCC	14.55 $\pm$ 4.09	344 $\pm$ 106	0

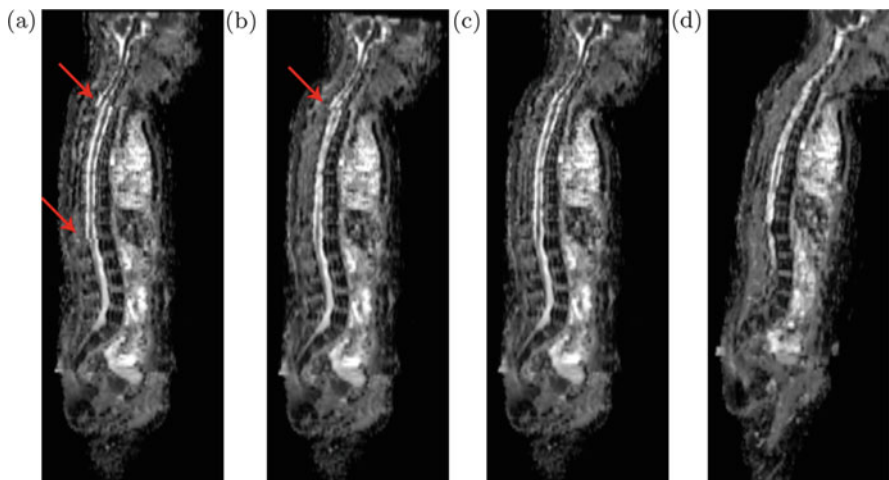
outperformed SCR registration using DWI for all measures, and the difference was significant ( $p < 0.04$ , two-tailed t-test) for all of the validation measures except for DWI image MAD validation ( $p = 0.90$ , two-tailed t-test).

Multi-channel registration of ADC maps using MSD and DWI images using NCC outperformed all of the other registration methods in mean absolute differences and gradient intensity metric based on ADC (see Fig. 3). However, multi-channel registration on DWI using NCC scored the best in DWI image validation. Multi-channel registration on ADC using MSD with DWI using NCC resulted in a slight improvement of both MAD and GI in comparison with single-channel ADC using MSD method, and the difference was significant ( $p < 0.002$ , two-tailed t-test) for all of the validation measures except for ADC image gradient validation ( $p = 0.15$ , two-tailed t-test).

An example of the obtained whole-body images using different registrations is shown in Fig. 4.



**Fig. 3** The boxplot of compared mean absolute differences evaluated for the ADC image stations for all registration algorithms. The ADC based registration techniques show the lowest MAD values



**Fig. 4** Results of different registration methods. ADC whole-body image of subject 10 ‘stitched’ from four image stations (the same slice). *Red arrows* indicate spine shift. (a) Non-registered segments. (b) SCR on DWI using MI. (c) MCR on ADC using MSD with DWI using NCC. (d) SCR on DWI using MSD. The image is unnaturally tilted to the front

## 4 Discussion and Conclusion

In this work we investigated several strategies for whole-body DW-MRI image stations registration. Eight different registration methods were compared and their performance evaluated. Overall, single-channel strategy using the computed ADC maps performed better and proved to be more stable than other single-channel registration on DWI segments. Multi-channel registration on both ADC images and DWI images using NCC metric showed marginally better consistency at the station interface, but the improvement was negligible.

## References

1. Takahara, T., Imai, Y., Yamashita, T., Yasuda, S., Nasu, S., Van Cauteren, M.: Diffusion weighted whole body imaging with background body signal suppression (DWIBS): technical improvement using free breathing, stir and high resolution 3d display. *Matrix* **160**(160), 160 (2004)
2. Gutzeit, A., Doert, A., Froehlich, J.M., Eckhardt, B.P., Meili, A., Scherr, P., Schmid, D.T., Graf, N., von Weymarn, C.A., Willems, E.M., et al.: Comparison of diffusion-weighted whole body MRI and skeletal scintigraphy for the detection of bone metastases in patients with prostate or breast carcinoma. *Skeletal Radiol.* **39**(4), 333–343 (2010)
3. Nakanishi, K., Kobayashi, M., Nakaguchi, K., Kyakuno, M., Hashimoto, N., Onishi, H., Maeda, N., Nakata, S., Kuwabara, M., Murakami, T., et al.: Whole-body MRI for detecting metastatic bone tumor: diagnostic value of diffusion-weighted images. *Magn. Reson. Med. Sci.* **6**(3), 147–155 (2007)
4. Kwee, T.C., Ludwig, I., Uiterwaal, C.S., van Ufford, H.M.Q., Vermoolen, M.A., Fijnheer, R., Bierings, M.B., Nievelstein, R.A.: ADC measurements in the evaluation of lymph nodes in patients with non-hodgkin lymphoma: feasibility study. *Magn. Reson. Mater. Phys. Biol. Med.* **24**(1), 1–8 (2011)
5. Padhani, A.R., Makris, A., Gall, P., Collins, D.J., Tunariu, N., de Bono, J.S.: Therapy monitoring of skeletal metastases with whole-body diffusion MRI. *J. Magn. Reson. Imaging* **39**(5), 1049–1078 (2014)
6. Blackledge, M.D., Collins, D.J., Tunariu, N., Orton, M.R., Padhani, A.R., Leach, M.O., Koh, D.M.: Assessment of treatment response by total tumor volume and global apparent diffusion coefficient using diffusion-weighted MRI in patients with metastatic bone disease: a feasibility study. *PLoS One* **9**(4), e91779 (2014)
7. Pasoglou, V., Michoux, N., Tombal, B., Jamar, F., Lecouvet, F.E.: wbMRI to detect bone metastases: critical review on diagnostic accuracy and comparison to other imaging modalities. *Clin. Transl. Imaging* **3**(2), 141–157 (2015)
8. Lecouvet, F., Larbi, A., Pasoglou, V., Omoumi, P., Tombal, B., Michoux, N., Malghem, J., Lhommel, R., Vande Berg, B.: MRI for response assessment in metastatic bone disease. *Eur. Radiol.* **23**(7), 1986–1997 (2013)
9. Jäger, F., Hornegger, J.: Nonrigid registration of joint histograms for intensity standardization in magnetic resonance imaging. *IEEE Trans. Med. Imaging* **28**(1), 137–150 (2009)
10. Dzyubachyk, O., van der Geest, R.J., Staring, M., Börner, P., Reijnders, M., Bloem, J.L., Lelieveldt, B.P.: Joint intensity inhomogeneity correction for whole-body MR data. In: *Medical Image Computing and Computer-Assisted Intervention—MICCAI 2013*, pp. 106–113. Springer, Heidelberg (2013)



11. Takahara: DWIBS: Diffusion-weighted whole-body imaging with background body signal suppression. *Medicamundi* **49**(3), (2005)
12. Nyúl, L.G., Udupa, J.K., Zhang, X.: New variants of a method of MRI scale standardization. *IEEE Trans. Med. Imaging* **19**(2), 143–150 (2000)

# Using Automatic HARDI Feature Selection, Registration, and Atlas Building to Characterize the Neuroanatomy of $A\beta$ Pathology

Evan Schwab, Michael A. Yassa, Michael Weiner, and René Vidal

**Abstract** The detection of white matter microstructural changes using diffusion magnetic resonance imaging (dMRI) often involves extracting a small set of scalar features, such as fractional anisotropy (FA) and mean diffusivity (MD) in diffusion tensor imaging (DTI). With the advent of more advanced dMRI techniques, such as high angular resolution diffusion imaging (HARDI), a number of mathematically inspired new scalar features have been proposed. However, it is unclear how to select the most biologically informative combinations of features for biomarker discovery. This paper proposes an automatic HARDI feature selection algorithm which is based on registering HARDI features to feature atlases for optimal clinical usability in population studies. We apply our framework to the characterization of beta-amyloid ( $A\beta$ ) pathology for the early detection of Alzheimer's disease (AD) to better understand the relationship between  $A\beta$  pathology and degenerative changes in neuroanatomy.

## 1 Introduction

Over five million Americans suffer from Alzheimer's disease (AD) today. Since the damage to the brain caused by AD is irreversible and the first symptoms appear when the disease is already sufficiently advanced, it is very important to establish indicators of AD (i.e., biomarkers) during the preclinical stage that allow for early diagnosis and intervention. Beta-amyloid ( $A\beta$ ) pathology is thought to play an important role in AD pathophysiology, but the relationship between  $A\beta$  pathology

---

E. Schwab (✉) • R. Vidal

Center for Imaging Science, Johns Hopkins University, Baltimore, MD, USA

e-mail: [eschwab3@jhu.edu](mailto:eschwab3@jhu.edu)

M.A. Yassa

Department of Neurobiology and Behavior, University of California, Irvine, CA, USA

M. Weiner

Department of Radiology, University of California, San Francisco, CA, USA

and structural changes in brain connectivity during the preclinical stage is not well understood. Currently, our understanding of changes in the white matter (WM) of the brain that occur early in the course of the disease is largely based on studies that use diffusion tensor imaging (DTI) to find changes in fractional anisotropy (FA) and mean diffusivity (MD) [6, 19, 20]. A major concern for DTI is its inability to resolve subvoxel crossing, bending, and twisting fibers due to limitations inherent in the single-direction tensor model and these limitations are observed in the ambiguity of FA and MD changes. This precludes accurate measurement of the complex subvoxel anatomical fiber interactions, which is important to understanding WM pathology implicated in AD.

High angular resolution diffusion imaging (HARDI) addresses the disadvantages of DTI by allowing one to estimate a multi-modal orientation distribution function from a large number of gradient directions. On the one hand, this permits defining new features with the hope of better characterizing WM structures and WM pathology. Indeed, in recent years there has been an influx of methods that generate rotation invariant HARDI features [4, 11, 13–15, 18, 21]. On the other hand, however, with so many different types of features to choose from, it is not clear which ones are most representative of neuroanatomical microstructure and most important for disease classification. Also, since many of these features are derived based on their mathematical properties, it is unclear which features are biologically relevant.

A common approach to feature selection is to use all features to train a classifier and let the classifier weights decide which features are most discriminative. This approach is appropriate for brain classification whenever the spatial location of the brain features is inconsequential. In practice, however, disease is localized in certain anatomical structures, such as the hippocampus for AD, and it is extremely important that these features be registered to a common coordinate system, or atlas, before the classifier is trained. However, the construction of the atlas and the registration algorithm are also based on the same features, and selecting which features are most relevant for registration is also an important problem. Indeed, errors in registration could incorrectly map the features to the atlas and result in incorrect classification.

**Paper Contributions** In this paper, rather than addressing the feature selection problem only at the very end of the classification pipeline, we propose to automatically select anatomically informative features while simultaneously registering them and constructing a feature atlas for proper comparison of different populations. Given a collection of HARDI features extracted from multiple brain images of healthy individuals, we use them to build a HARDI atlas. This atlas is built by alternating between registering all HARDI features to a current estimate of the atlas, and recomputing the atlas by “averaging” the registered HARDI features. This is done using a generalized multi-channel large deformation diffeomorphism metric mapping (mLDDMM) framework in which each HARDI feature is given a different weight that depends on the variance of the feature. This weight, which is estimated and updated as the atlas building algorithm proceeds, is used to

automatically determine the importance of the feature for registration and atlas building. In this way, our approach embeds feature selection within a HARDI registration and atlas building framework so that the selected features, which may be important for final analysis and classification, can be optimally transferred to the atlas for training a classifier. We apply our joint feature selection, registration and atlas building framework to identify neuroanatomical differences between  $A\beta$  positive (+) and  $A\beta$  negative (-) pathologies to investigate the relationship between  $A\beta$  pathology and neuroanatomical degeneration in order to discover new biomarkers for AD. Our results show that the features selected automatically by our method often agree with the features that produce the most significant differences between  $A\beta+$  and  $A\beta-$ .

**Paper Outline** The remainder of this paper is organized as follows: In Sect. 2 we review the problem of HARDI registration based on rotation invariant features. Then in Sect. 3 we present our joint feature selection, registration and atlas building algorithm. Finally in Sect. 4 we show results of our framework on a population study of  $A\beta+$  and  $A\beta-$  subjects to identify promising features for  $A\beta$  classification.

## 2 Multi-Channel Registration Using HARDI Features

The proposed framework for feature selection is driven by registration, whose goal is to align multiple datasets into a single coordinate system for proper comparison. Current medical image registration algorithms work very well for scalar-valued brain MRI volumes. However, for high-dimensional HARDI data, alignment requires not only warping the 3D volume of the baseline ( $b_0$ ) MRI, but also preserving the orientation of local diffusion information at each voxel to remain consistent within the warped neuroanatomy. To tackle this, early methods reorient the diffusion profiles after registration [1, 16]. However, this does not take into account the effect of local reorientation on the global optimization. To handle this, [7, 8, 10, 12, 24] incorporate diffusion information into the optimization. This requires computing complicated gradients and reorienting diffusivity profiles at each iteration, which can be time-consuming. Furthermore, different diffusivity profiles like the orientation distribution function (ODF), fiber orientation distribution (FOD), average ensemble propagator (EAP) or the raw signal each require a separate registration algorithm with different schemes for reorientation.

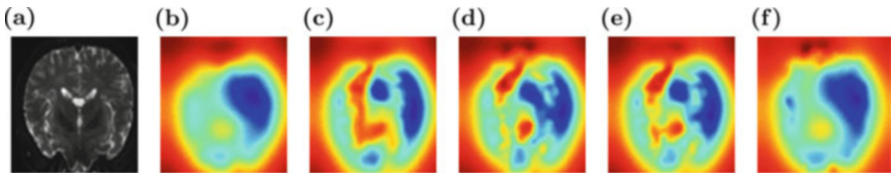
In this paper, we adopt a HARDI registration framework based on rotation invariant HARDI features. The proposed framework aligns diffusivity information accurately without having to calculate gradients or needing to reorient the data. Moreover, it can be applied to any diffusivity profile or combination thereof. More specifically, we adopt the large deformation diffeomorphic metric mapping (LDDMM) algorithm [2], which is a staple for the registration of scalar valued MRI volumes. LDDMM seeks to find an optimal diffeomorphism between two images or volumes. For registering sets of HARDI features, we use multi-channel LDDMM

(mcLDDMM), which seeks to find an optimal diffeomorphism to align information contained in multiple volumes simultaneously. In particular, suppose we have  $C$  rotation invariant HARDI features for each voxel of our 3D brain volume. Let  $\mathcal{I}_c$  denote the volume of feature  $c = 1, \dots, C$ . Then we can represent the collection of  $C$  HARDI feature volumes by  $\mathcal{I} = [\mathcal{I}_1, \mathcal{I}_2, \dots, \mathcal{I}_C]$ . Now, given two collections of feature volumes  $\mathcal{I}^0 = [\mathcal{I}_1^0, \mathcal{I}_2^0, \dots, \mathcal{I}_C^0]$  and  $\mathcal{I}^1 = [\mathcal{I}_1^1, \mathcal{I}_2^1, \dots, \mathcal{I}_C^1]$ , the goal of mcLDDMM is to find a single optimal non-linear transformation that aligns all  $C$  feature volumes jointly. That is, we wish to find a diffeomorphism  $\varphi$  such that  $\mathcal{I}_c^1 \approx \mathcal{I}_c^0 \circ \varphi^{-1}$  for all  $c = 1, \dots, C$ . Since the transformation  $\varphi$  is the same for all  $c$ , our shorthand notation will be  $\mathcal{I}^1 \approx \mathcal{I}^0 \circ \varphi^{-1}$ . The diffeomorphism is generated by the flow of a family of smooth time-dependent vector fields  $v_t \in \mathbf{V}$ , the space of vector fields, for  $t \in [0, 1]$ , defined by the ordinary differential equation  $\frac{d\phi_t^v}{dt} = v_t(\phi_t^v)$ , where  $\phi_0$  is the identity transformation and  $\phi_1^{v*} = \varphi^*$  is a diffeomorphic transformation defined as the solution to the following optimization problem:

$$\varphi^* = \arg \min_{\varphi} \left( \int_0^1 \|v_t(\varphi)\|_{\mathbf{V}}^2 dt + \sum_{c=1}^C \frac{1}{\sigma_c^2} \|\mathcal{I}_c^0 \circ \varphi^{-1} - \mathcal{I}_c^1\|_{L^2}^2 \right). \quad (1)$$

An optimal  $\varphi$  is found by gradient descent. Note that when  $C = 1$ , Eq. (1) reduces to the traditional single-channel LDDMM. Here the  $\sigma_c^2$  are fixed weighting parameters for each channel. In most formulations,  $\sigma_c^2$  is set to 1 for all  $c$ .

To illustrate the performance of mcLDDMM using various HARDI features, we generated a ground truth (GT) deformation  $g$  (Fig. 1b) by aligning a real HARDI volume  $A$  (Fig. 1a) to another real HARDI volume  $B$  (not shown) using traditional single-channel LDDMM on the b0 volumes. We then applied  $g$  to  $A$  to obtain a new transformed volume  $C = A \circ g$ . We compared various mcLDDMM methods with differing features to align  $A$  and  $C$  to measure which one was closest to the GT  $g$ . In Fig. 1 we show the qualitative results comparing: (Fig. 1c) LDDMM-b0, the baseline single-channel registration of b0 images, (Fig. 1d) mcLDDMM-GFA, the 2-channel



**Fig. 1** Qualitative results for a semi-synthetic deformation experiment. We compare out-of-plane deformations, where *blue* is deformation towards the viewer and *red* is away from the viewer. (a) b0 MRI of the dataset. (b) Ground truth (GT) deformation. (c) Deformation obtained by single channel LDDMM using b0. (d) Deformation obtained by DTI-like mcLDDMM using b0 and GFA. (e) Deformation obtained by multi-channel LDDMM using spectral norms of spherical harmonic coefficients (SHC). (f) Deformation obtained by multi-channel LDDMM using HARDI features from [21]. Note that using the features in (f) provides an estimate that is closer to the ground truth transformation

registration using b0 and GFA, which is analogous to the method of [5] that uses b0 and FA for DTI, (Fig. 1e) mcLDDMM-SHC, the 5-channel registration using b0 and three SHC norms [3], (Fig. 1f) mcLDDMM-Schwab, the multi-channel registration using b0 and a set of rotation invariant features for HARDI developed in [21]. These results demonstrate that by using the features proposed in [21] we can achieve a more accurate registration than traditional LDDMM and LDDMM based on GFA or SHC. But most importantly, we wish to understand which features out of the many available in the literature are important for driving registration and which are important for disease classification. Next we present our method for automatically selecting features based on their anatomical information.

### 3 Automatic Feature Selection Using mcLDDMM

Now that we can register HARDI features using mcLDDMM, we wish to learn which features capture the most information to drive registration and preserve the neuroanatomy. Rather than fixing each  $\sigma_c$ , we estimate the value of these parameters as a way of measuring their informativeness for registration. To that end, we employ an iterative algorithm that alternates between estimating the informativeness of a feature given a HARDI template (i.e., estimate  $\sigma_c$ ) and estimating the HARDI template given the informativeness of each feature.

Our method is derived from the Bayesian template estimation work of Ma et al. [17], which estimates a 3D shape template for computational anatomy. The work of Du et al. [9] uses the same algorithm for the single-channel HARDI registration of ODFs to build a HARDI atlas. The framework was also extended to fuse information from multiple atlases both for computational anatomy [22] and DTI [23], but the value of  $\sigma_c$  for each channel was kept constant. Our algorithm expands upon these prior works by using mcLDDMM to build a HARDI feature atlas while simultaneously learning the variance parameters  $\sigma_c$  that weight each feature channel.

More specifically, let  $\mathbf{I} = \{\mathcal{I}^1, \mathcal{I}^2, \dots, \mathcal{I}^N\}$  be a collection of HARDI volumes corresponding to  $N$  normal subjects, each volume  $\mathcal{I}^i$  having  $C$  feature channels, i.e.,  $\mathcal{I}^i = [\mathcal{I}_1^i, \mathcal{I}_2^i, \dots, \mathcal{I}_C^i]$ . Let  $J$  be a template consisting of  $C$  feature volumes  $J = [J_1, J_2, \dots, J_C]$  to be estimated from  $\mathbf{I}$ . Let  $\Theta = \{\theta_1, \theta_2, \dots, \theta_N\}$  be a collection of transformations from subject  $\mathcal{I}_n$  to  $J$ , such that  $\mathcal{I}_n \approx J \circ \theta_n^{-1}$ . Let  $J^0 = [J_1^0, J_2^0, \dots, J_C^0]$  be a set of feature volumes associated to a known HARDI brain hypertemplate, and let  $\mu$  be a transformation between the estimated template  $J$  and the hypertemplate, such that  $J = J^0 \circ \mu^{-1}$ . Under the model  $p(\mathbf{I}, \Theta, \mu; \sigma) \propto p(\mathbf{I} \mid \Theta, \mu; \sigma)p(\Theta)p(\mu)$ , the goal of atlas building is reduced to estimating a

transformation  $\mu$  given the observations  $\mathbf{I}$  and the hypertemplate  $J_0$  (assuming latent variables  $\Theta$ ) by minimizing the negative log likelihood:

$$\begin{aligned} -\log p(\mathbf{I}, \Theta, \mu; \sigma) &= \sum_{n=1}^N \sum_{c=1}^C \frac{1}{2\sigma_c^2} \|J_c^0 \circ \mu^{-1} \circ \theta_n^{-1} - \mathcal{I}_c^n\|_2^2 + \frac{1}{2} SCN \log \sigma_c^2 \\ &+ \frac{1}{2} \|v_r(\mu)\|_{\mathbb{V}_\pi}^2 + \sum_{n=1}^N \frac{1}{2} \|v_r(\theta_n)\|_{\mathbb{V}}^2 - \log(Z_\pi) - N \log(Z), \end{aligned} \quad (2)$$

where  $v_r(\mu) = \frac{d\mu_t}{dt}$  and  $v_r(\theta_n) = \frac{d\theta_n}{dt}$ , and  $Z_\pi$  and  $Z$  are normalization constants.

In theory, we could estimate  $\sigma$  and  $\mu$  using a generalized Expectation Maximization (EM) that, at iteration  $k$ , minimizes the negative expected log likelihood:

$$\sigma_c^{2(k+1)} = \frac{1}{SCN} \sum_{n=1}^N E_{\mu^{(k)}} \{ \|J_c^0 \circ \mu^{(k)-1} \circ \theta_n^{-1} - \mathcal{I}_c^n\|_2^2 \mid \mathcal{I}_c^n \}, \quad (3)$$

$$\mu^{(k+1)} = \arg \min_{\mu} \left\{ \|v_r(\mu)\|_{\mathbb{V}_\pi}^2 + \sum_{n=1}^N \sum_{c=1}^C \frac{E_{\mu^{(k)}} \{ \|J_c^0 \circ \mu^{-1} \circ \theta_n^{-1} - \mathcal{I}_c^n\|_2^2 \mid \mathcal{I}_c^n \}}{2\sigma_c^{2(k+1)}} \right\}. \quad (4)$$

However, the expectation  $E_{\mu^{(k)}} (\|J_c^0 \circ \mu^{-1} \circ \theta_n^{-1} - \mathcal{I}_c^n\|_2^2 \mid \mathcal{I}_c^n)$  w.r.t.  $\Theta$  cannot be computed analytically due to the nonlinear dependency of this quantity in  $\theta_n$ . To overcome this issue, the authors of [17] utilize the Mode Approximation Expectation Maximization (MAEM) algorithm, in which the conditional distribution of the latent variables is replaced by a Dirac measure at its mode. This leads to the MAEM Algorithm 1, where (3) and (4) are solved alternatively. To initialize MAEM, we set  $J^0$  to be a randomly selected subject in  $\mathbf{I}$  and set  $\sigma_c = 1$  for all  $c$ . Based on the findings of Ma et al. [17], the choice of the hypertemplate does not greatly effect the resulting template.

The MAEM algorithm results in estimated feature atlases  $J_c^*$  and weights  $w_c^* = 1/\sigma_c^{2*}$  for each feature channel  $c$ . By analyzing the resulting channel weights for each of our HARDI features, we are able to automatically select the most important features that drive registration. In particular, channels with large variance  $\sigma_c^2$  will receive a small weight  $w_c$  in each successive iteration. Since  $w_c = 1$  is our initialization, we may identify features with  $w_c^* < 1$  as less important for driving registration since they have a larger error  $\sigma_c^2$ . As an extreme example, a feature that contains large amounts of noise (SNR very small) will result in large  $\sigma_c^2$  and therefore  $w_c^*$  will be small. So, HARDI features with very low SNR will be weighted lower since they do not carry consistent anatomical information. On the other hand, features with  $w_c^* \geq 1$  are important for driving registration since they exhibit smaller  $\sigma_c^2$ . However, features with extremely high weights may not be informative for registration. As an extreme example, a feature which is constant for every voxel in a brain volume, and therefore anatomically uninformative, will return a  $\sigma_c^2 = 0$

---

**Algorithm 1 (Feature Selection and Template Estimation)**


---

Let  $J_c^{(k)}$  be the estimated template and  $\sigma_c^{2(k)}$  be the estimated variances for each channel  $c$  at iteration  $k$ . For iteration  $(k + 1)$ ,

1. Warp each subject  $\mathcal{I}_c^n$  to  $J_c^{(k)}$  using mCLDDMM with parameters  $\sigma_c^{2(k)}$  to obtain  $\mathcal{I}_c^n \circ \theta_n^{(k)}$  with Jacobian determinant  $|D\theta_n^{(k)}(y)|$  at each voxel  $y$  of the image volume.
2. Compute mean feature image

$$\bar{\mathcal{I}}_c^{(k+1)}(y) = \frac{\sum_{n=1}^N \mathcal{I}_c^n \circ \theta_n^{(k)}(y) |D\theta_n^{(k)}(y)|}{\sum_{n=1}^N |D\theta_n^{(k)}(y)|}. \quad (5)$$

3. Update noise variance feature weights by

$$\sigma_c^{2(k+1)} = \frac{1}{SCN} \sum_{n=1}^N \|\mathcal{I}_c^n \circ \theta_n^{(k)} - J_c^{(k)}\|_2^2, \quad (6)$$

where  $S$  is the total number of voxels in each volume and  $C$  is the number of channels.

4. Given  $\sigma_c^{2(k+1)}$ , update our template by finding the transformation that minimizes the distance between  $\bar{\mathcal{I}}_c^{(k+1)}$  and  $J_c^0$ ,

$$\mu^{(k+1)} = \arg \min_{\mu} \int_0^1 \|v_t(\mu)\|_V^2 dt + \sum_{c=1}^C \frac{1}{\sigma_c^{2(k+1)}} \|\bar{\mathcal{I}}_c^{(k+1)} \circ \mu^{-1} - J_c^0 \sqrt{A^{(k+1)}}\|_2^2, \quad (7)$$

and write the updated template as  $J_c^{(k+1)} = J_c^0 \circ \mu^{(k+1)}$ , where the weight image is given by  $A^{(k+1)} = [\alpha^{(k+1)}(y)]$  for  $\alpha^{(k+1)}(y) := \sum_{n=1}^N |D\theta_n^{(k)}(y)|$ .

5. We repeat until  $\|\sigma_c^{2(k+1)} - \sigma_c^{2(k)}\| < \epsilon$  for some small  $\epsilon > 0$  for all  $c$ .
- 

and  $w_c^* = \infty$ . Thus, our template estimation algorithm can automatically select important features that drive registration by automatically adjusting the weights. These weights can be further tuned for classification by training a classifier for a specific disease application. In Sect. 4 we analyze the relative feature weights resulting from our algorithm with respect to  $A\beta$  pathology status.

## 4 Automatic Feature Selection, Registration, and Atlas Building Applied to Characterization of $A\beta$ Pathology

In this section we will apply our automatic registration driven feature selection algorithm to characterize the WM neuroanatomy of  $A\beta$  pathology. Our goal is to identify features that are useful in the classification of  $A\beta$  pathology in order to assess novel biomarkers for the early detection of AD. To that end, we compare anatomical features selected by our algorithm with disease-specific features that present statistically significant differences in the presence of  $A\beta$  pathology. Our



automatic feature selection will provide us with a shortlist of anatomically informative features from which a subset could be chosen that may be important for classifying  $A\beta$  pathology.

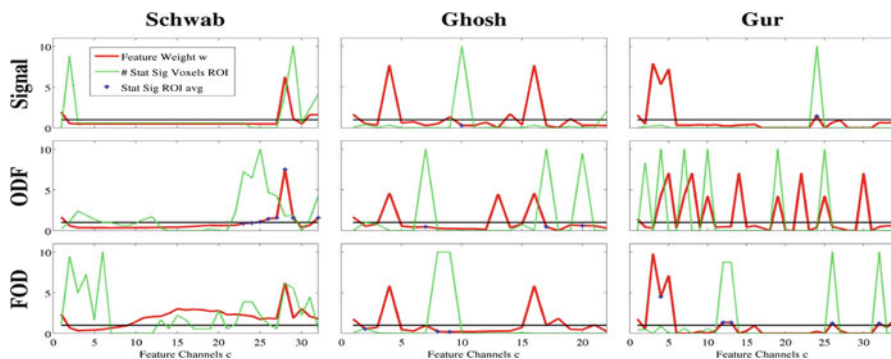
#### 4.1 *Extraction of HARDI Features*

In recent years there have been a number of innovative frameworks for extracting new rotation invariant features from HARDI data. Here, we compare these features to understand which ones have the potential to play important roles in biomarker discovery of neurological diseases. We compare three different families of features (from Schwab et al. [21], Ghosh et al. [14] and Gur et al. [15]) extracted from three different diffusivity profiles: the raw HARDI signal, the ODF, and the FOD. From [21] we extract 30 features from the 4th order SH coefficients: 25 eigenvalues, and their variance, range, median, Frobenius-norm, and 2-norm. From [13, 14] we extract 20 features from the 4th order tensor: 12 generalized invariants ( $G4$ ), which generate 4 basic ( $S4$ ) and 4 principal ( $J4$ ) invariants of homogenous polynomials. From [15] we extract 32 features of the 4th order SH coefficients: 3 coefficients contracted with coefficients ( $I$ ), 11 coefficients contracted with tensors ( $J$ ) and 18 tensors contracted with tensors ( $K$ ). For each family of features and for each spherical function, we add the baseline MRI  $b_0$  as the first channel and GFA as the second channel for comparison.

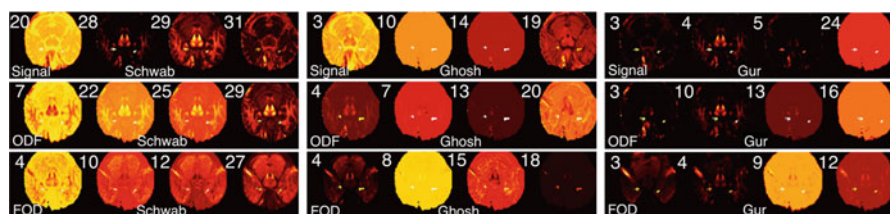
#### 4.2 *Analysis of Selected HARDI Features Compared to $A\beta$ Pathology Status*

For this study we use 15  $A\beta^-$  and 17  $A\beta^+$  subjects, identified with florbetapir (Amyvid) PET scans, from the Hippocampal Connectivity Project (HCP) at the Center for Imaging of Neurodegenerative Diseases (CIND) at the University of California San Francisco (UCSF). For each subject, 3 HARDI scans were acquired on a Siemens 4T scanner (128 gradient directions, 3  $b_0$  values, FOV: 192, number of slices: 26, resolution: 1.5 mm isotropic, b-value: 1400 s/mm<sup>2</sup>, TR/TE: 3500/86, 3n<sub>ex</sub> averaged to enhance SNR, total protocol time: 1.35 h).

For characterizing  $A\beta$  pathology, we focus on features within the parahippocampal WM, a region of interest (ROI) that has been shown to undergo fiber degradation in aging and mild cognitive impairment [25, 26]. We first choose one subject at random among the 15 healthy subjects to be our hypertemplate  $J_0$ . We then build feature atlases using each one of the features and HARDI functions described in Sect. 4.1. The resulting weights of each feature channel for each experiment after three iterations of Algorithm 1 are shown in red in Fig. 2. (Features whose weights were extremely high ( $>20$ ) were set to 0 in Fig. 2 only for visual comparison.)



**Fig. 2** Comparison of each family of features extracted from signal, ODF, and FOD after three iterations of Algorithm 1. *Red*: weights  $w_c$  for each feature channel  $c$ . *Green*: number of voxels in ROI that are statistically different between  $A\beta+$  and  $A\beta-$ . *Blue marker*: features that have statistically significant differences in means within the ROI between  $A\beta+$  and  $A\beta-$ . Notice that many features with high  $w_c$  (important for registration of WM) also contain statistically significant differences between  $A\beta+$  and  $A\beta-$



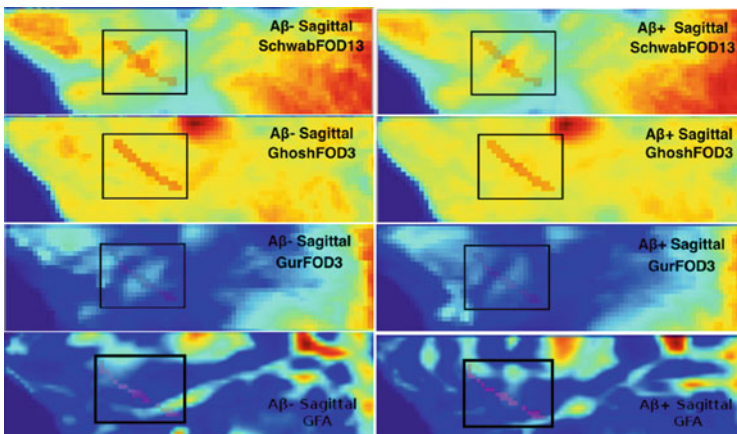
**Fig. 3** Display of a subset of the feature maps obtained by each method (Schwab, Ghosh and Gur in the *left*, *central* and *right* columns, resp.) for each function (signals, ODF and FOD in the *top*, *middle* and *bottom* rows, resp.). The numbers next to each feature map correspond to the feature channel  $c$  as ordered on the x-axes in Fig. 2

For each family, the first channel is  $b_0$  and the second channel is GFA. We also investigate feature differences between  $A\beta+$  and  $A\beta-$  groups after registering all subjects to the template. We ran a voxel-wise two sample paired t-test in the parahippocampal WM ROI. The number of voxels with statistically significant differences between groups is plotted in green for each feature. We also ran a two sample paired t-test on the means of the voxel values in each ROI (left and right brain separately) and plotted features which have statistically significant mean differences as blue markers (see legend of Fig. 2).

In Fig. 3 we display a sample of feature maps for each family and function (same  $3 \times 3$  grid as Fig. 2) to show the reader the types of feature maps associated to high and low weights in Fig. 2. Notice that a number of the selected features from Ghosh and Gur are not very informative, as they are either very sparse or close to a constant mask. In addition, it so happens that the methods of Ghosh and Gur produce duplicate features for different functions, as can be seen in the repeated peaks of

Ghosh (channels 4 and 16 for Signal, ODF, and FOD) and Gur for ODF in Fig. 2. By looking at the results, it is evident that there is a pattern between features with weights greater than one and those with statistically significant ROI differences. However, some of the homogeneous features from Gur and Ghosh can be identified by having a peak of the number of statistically significant voxels and also have statistically significant means over the entire ROI since there is little variability. In particular, the plots of Schwab for ODF and FOD show interesting correlations and variability.

In Fig. 4 we show a subset of these statistically significant features, where the left column shows  $A\beta^-$  and the right one  $A\beta^+$ , compared along the sagittal view of the ROI (long shaded region in black box). Common to each of these features, we notice a decrease in the intensity of each feature crossing perpendicular through the ROI. Unlike GFA, which is predominantly isotropic (blue) in the ROI, revealing little diffusivity information, some of the other selected features are able to reveal microstructural information directly crossing the parahippocampal ROI. Admittedly, when we say that a certain HARDI feature has decreased in value between  $A\beta^+$  and  $A\beta^-$ , physical interpretations are somewhat abstract (unlike for the well defined GFA). This is definitely the case for many of the features from Ghosh and Gur which are derived mathematically. For the features from Schwab [21], it is proven that these features follow the physical distribution of the spherical function they were extracted from. Therefore, one can characterize differences in diffusivity information or physical shapes of the signal, ODF or FOD by analyzing changes in the entire set of features together instead of individual features alone.



**Fig. 4** Comparison of average features after registered to feature atlases. We show the sagittal view of the parahippocampal WM ROI (*elongated shaded area in black box*). Red: High, Blue: low. We notice a decrease in feature values crossing over ROI in Schwab, Ghosh and Gur. GFA shows little diffusivity information in ROI

The first row of Fig. 4 shows feature 13 of the FOD as a striking example of the differences between  $A\beta + / -$ . Additionally, features 10 through 27 (not shown) vary slightly from one another and all include diverse information crossing along our ROI for  $A\beta + / -$ .

## 5 Conclusion

We have presented an algorithm for the joint selection, registration, and atlas building of HARDI features applied to the analysis of  $A\beta$  WM pathology. This method provides an automatic way to select features that may be important for disease classification based on an anatomical criteria of registration accuracy which is not specific to a particular disease study. Then given the selected features, researchers can identify a subset based on disease classifiers. We have shown that many of the features important for registration may be useful for  $A\beta + / -$  classification by showing statistically significant differences within a known ROI. We have found that the presence of  $A\beta$  pathology ( $A\beta +$ ) may be associated with feature decreases in the parahippocampal WM ROI, indicating levels of degradation in comparison to a healthy average ( $A\beta -$ ). Our future efforts will be to incorporate these significant features into a unified classification algorithm for  $A\beta$  pathology to identify potential biomarkers for the early detection of Alzheimer's Disease.

## References

1. Alexander, D., Pierpaoli, C., Basser, P., Gee, J.: Spatial transformation of diffusion tensor magnetic resonance images. *IEEE Trans. Med. Imaging* **20**, 1131–1139 (2001)
2. Beg, M.F., Miller, M.I., Trounev, A., Younes, L.: Computing large deformation metric mappings via geodesic flows of diffeomorphisms. *Int. J. Comput. Vis.* **61**(2), 139–157 (2005)
3. Bloy, L., Verma, R.: Demons registration of high angular resolution diffusion images. In: *IEEE International Symposium on Biomedical Imaging*, pp. 1013–1016 (2010)
4. Caruyer, E., Verma, R.: On facilitating the use of HARDI in population studies by creating rotation-invariant markers. *Med. Image Anal.* **20**(1), 87–96 (2014)
5. Ceritoglu, C., Oishi, K., Li, X., Chou, M.C., Younes, L., Albert, M., Lyketos, C., van Zijl, P.C.M., Miller, M.I., Mori, S.: Multi-contrast large deformation diffeomorphic metric mapping for diffusion tensor imaging. *NeuroImage* **47**(2), 618–627 (2009)
6. Chao, L., Decarli, C., Kriger, S., Truran, D., Zhang, Y., Laxamana, J., Villeneuve, S., Jagust, W., Sanossian, N., Mack, W., Chui, H., Weiner, M.: Associations between white matter hyperintensities and  $\beta$  amyloid on integrity of projection, association, and limbic fiber tracts measured with diffusion tensor MRI. *PLoS One* **8**(6), e65175 (2013)
7. Du, J., Goh, A., Qiu, A.: Large deformation diffeomorphic metric mapping of orientation distribution functions. In: *Information Processing in Medical Imaging*, pp. 448–462. Springer, Berlin (2011)
8. Du, J., Goh, A., Qiu, A.: Diffeomorphic metric mapping of high angular resolution diffusion imaging based on Riemannian structure of orientation distribution functions. *IEEE Trans. Med. Imaging* **31**(5), 1021–1033 (2012)

9. Du, J., Goh, A., Qiu, A.: Bayesian atlas estimation from high angular resolution diffusion imaging (HARDI). In: *Geometric Science of Information*, pp. 149–157. Springer, Heidelberg (2013)
10. Du, J., Hosseinbor, A.P., Chung, M.K., Bendlin, B.B.: Diffeomorphic metric mapping of hybrid diffusion imaging based on BFOR signal basis. In: *Information Processing in Medical Imaging*, pp. 1–12. Springer, Berlin (2013)
11. Fuster, A., van de Sande, J., Astola, L., Poupon, C., ter Haar Romeny, B.M.: Fourth-order tensor invariants in high angular resolution diffusion imaging. In: *Computational Diffusion MRI Workshop (CDMRI), MICCAI*, pp. 54–63 (2011)
12. Geng, X., Ross, T., Gu, H., Shin, W., Zhan, W., Chao, Y.P., Lin, C.P., Schuff, N., Yang, Y.: Diffeomorphic image registration of diffusion MRI using spherical harmonics. *IEEE Trans. Med. Imaging* **30**(3), 747–758 (2011)
13. Ghosh, A., Papadopoulo, T., Deriche, R.: Biomarkers for HARDI: 2nd & 4th order tensor invariants. In: *IEEE International Symposium on Biomedical Imaging*, pp. 26–29 (2012)
14. Ghosh, A., Papadopoulo, T., Deriche, R.: Generalized Invariants of a 4th order tensor: building blocks for new biomarkers in dMRI. In: *Computational Diffusion MRI Workshop (CDMRI), MICCAI*, pp. 165–173 (2012)
15. Gur, Y., Johnson, C.R.: Generalized HARDI invariants by method of tensor contraction. In: *IEEE International Symposium on Biomedical Imaging*, pp. 718–721 (2014)
16. Hong, X., Arlinghaus, L., Anderson, A.: Spatial normalization of the fiber orientation distribution based on high angular resolution diffusion imaging data. *Magn. Reson. Med.* **61**, 1520–1527 (2009)
17. Ma, J., Miller, M.I., Trouvé, A., Younes, L.: Bayesian template estimation in computational anatomy. *NeuroImage* **42**(1), 252–261 (2008)
18. Papadopoulo, T., Ghosh, A., Deriche, R.: Complete set of invariants of a 4th order tensor: the 12 tasks of HARDI from ternary quartics. In: *Medical Image Computing and Computer Assisted Intervention*, pp. 233–240. Springer, Berlin (2014)
19. Racine, A., Adluru, N., Alexander, A., Christian, B., Okonkwo, O., Oh, J., Cleary, C., Birdsill, A., Hillmer, A., Murali, D., Barnhart, T., Gallagher, C., Carlsson, C., Rowley, H., Dowling, N., Asthana, S., Sager, M., Bendlin, B., Johnson, S.: Associations between white matter microstructure and amyloid burden in preclinical Alzheimer’s disease: a multimodal imaging investigation. *NeuroImage Clin.* **4**, 604–614 (2014)
20. Reijmer, Y., Fotiadis, P., Martinez-Ramirez, S., Schultz, A., Reed, A., Ayres, A., Schwab, K., Rosand, J., Viswanathan, A., Johnson, K., Greenberg, S., Gurol, E.: Microstructural white matter alterations correlate with cerebral amyloid angiopathy burden and cognitive measures: a DTI/PET study. *Neurology* **82**(10), P6.313 (2014)
21. Schwab, E., Cetingül, H.E., Afsari, B., Yassa, M.A., Vidal, R.: Rotation invariant features for HARDI. In: *Information Processing in Medical Imaging*. Springer, Berlin (2013)
22. Tang, X., Oishi, K., Faria, A.V., Hillis, A.E., Albert, M.S., Mori, S., Miller, M.I.: Bayesian parameter estimation and segmentation in the multi-atlas random orbit model. *PLoS ONE* **8**(6), e65591 (2013)
23. Tang, X., Yoshida, S., Hsu, J., Huisman, T.A., Faria, A.V., Oishi, K., Kuttner, K., Poretti, A., Li, Y., Miller, M.I.: Multi-contrast multi-atlas parcellation of diffusion tensor imaging of the human brain. *PLoS one* **9**(5), e96985 (2014)
24. Yap, P.T., Chen, Y., An, H., Yang, Y., Gilmore, J., Lin, W., Shen, D.: SPHERE: spherical harmonic elastic registration of HARDI data. *NeuroImage* **55**(2), 545–556 (2011)
25. Yassa, M.A., Muftuler, L.T., Stark, C.E.: Ultrahigh-resolution microstructural diffusion tensor imaging (msdti) elucidates perforant path degradation in aged humans in vivo. *Proc. Natl. Acad. Sci.* **107**(28), 12687–12691 (2010)
26. Yassa, M.A., Mattfeld, A.T., Stark, S.M., Stark, C.E.L.: Age-related memory deficits linked to circuit-specific disruptions in the hippocampus. *Proc. Natl. Acad. Sci.* **108**(21), 8873–8878 (2011)

# Reliability of Structural Connectivity Examined with Four Different Diffusion Reconstruction Methods at Two Different Spatial and Angular Resolutions

J.E. Villalon-Reina, T.M. Nir, L. Zhan, K.L. McMahon, G.I. de Zubicaray, M.J. Wright, N. Jahanshad, and P.M. Thompson

**Abstract** Diffusion magnetic resonance imaging (dMRI) has had a great impact on the study of the human brain connectome. Tractography methods allow for the reconstruction of white matter fiber tracts and bundles across the brain, by tracing the estimated direction of water diffusion across neighboring voxels. The tracts can then be used in conjunction with cortical parcellations to create structural connectivity matrices, to map the pattern and distribution of connections between cortical regions. However, the reliability of connectivity matrices is unclear. Tractography results depend on image resolution, and some reconstruction methods used to resolve the voxel-wise microstructure may be more robust to changes in resolution than others, leading to more stable connectivity estimates. We examined the reliability of structural connectivity matrices in 20 healthy young adults imaged with both high and low-resolution dMRI at two time points. We found that the Constrained Spherical Deconvolution (CSD) model produces the most reliable connections for both lower resolution and high resolution scans.

---

J.E. Villalon-Reina (✉) • T.M. Nir • L. Zhan • N. Jahanshad • P.M. Thompson  
Imaging Genetics Center, USC Stevens Neuroimaging and Informatics Institute, University of Southern California, Marina del Rey, CA, USA  
e-mail: [julio.villalon@ini.usc.edu](mailto:julio.villalon@ini.usc.edu)

K.L. McMahon  
Center for Advanced Imaging, University of Queensland, Brisbane, QLD, Australia

G.I. de Zubicaray  
School of Psychology, University of Queensland, Brisbane, QLD, Australia

M.J. Wright  
QIMR Berghofer Medical Research Institute, Brisbane, QLD, Australia

## 1 Introduction

The study of the human connectome continues to show great promise for identifying cortical connections disrupted in disease. A common approach to study human structural networks is to generate connectivity matrices via a multimodal approach, namely segmenting cortical and subcortical regions of interest (ROI) on high-resolution T1-weighted anatomical images and tracing the white matter (WM) connections between these regions using diffusion magnetic resonance imaging (dMRI) [1]. Anatomical connections are inferred by computing the intersection between each pair of ROIs and the extracted streamlines, which connect them. In this way, the existence of an anatomical connection between a pair of brain regions can be established. This information is represented in a graphical matrix form, with nodes representing each of the segmented ROIs and edges corresponding to the weights of the WM connections.

A major criticism of dMRI and tractography methods is validation, as we do not typically have an independent source of biological ground truth when scanning the living human brain. Even more so, a myriad of acquisition protocols are used, and numerous reconstruction methods have been proposed to model the anisotropic diffusion of water at the voxel level. These models include parametric models such as diffusion tensor imaging (DTI) [2] and mixture models [3] as well as high angular resolution imaging (HARDI) [4] and diffusion spectrum imaging (DSI) [5].

With the expansion of global multi-site neuroimaging initiatives such as ENIGMA ([enigma.ini.usc.edu](http://enigma.ini.usc.edu)) and CHARGE ([chargeconsortium.com](http://chargeconsortium.com)), as well as data sharing initiatives such as ADNI ([adni.loni.usc.edu](http://adni.loni.usc.edu)), analyses are often run on data from different sites as part of the same study. Results may be meta-analyzed and data from different acquisition protocols may be pooled together and analyzed; as such, it becomes increasingly necessary to standardize processing protocols across sites to limit the effects of inter-site acquisition and processing differences. With diffusion imaging in particular, acquisition parameters such as voxel size and angular resolution can have a large impact on the results of a population study [6]. Protocols often standardize tractography by requesting that a single method be used, but it is just as important to find a reconstruction technique for dMRI that remains stable across many different acquisition parameters when using a particular tract-tracing algorithm. Due to the multimodal aspect of connectivity matrices, sources of variance may come from many sources. The most reliable estimates of connectivity matrices are essential for further comparison across sites.

Here we aimed to determine the test-retest reliability of the full structural connectomes of healthy adults, derived from four different diffusion reconstruction methods and one deterministic tracking method. First, we focused on the commonly employed diffusion tensor model (DTI) and other three reconstruction methods optimized for single-shell HARDI-type acquisitions, i.e., Constrained Spherical Deconvolution (CSD) [7], Constant Solid Angle  $q$ -Ball Imaging (CSA) [4], and

the “Ball and Stick” (B&S) model [8]. These four models are a good sample of the most commonly used diffusion models for single-shell data, and belong to the four main types of white matter microstructure reconstruction algorithms: DTI is a parametric model that assumes one main fiber direction; the B&S model is a mixture model of multiple fiber compartments with an isotropic component for unrestricted water molecule movement; CSA is a non-parametric  $q$ -ball reconstruction technique that represents the angular structure of the diffusion propagator, and CSD uses the convolution theorem to model the fiber orientation density.

The aim of this study is to make a general comparison of the structural networks derived from different common models, not necessarily to directly compare the reconstruction accuracy at the voxel level, for which simulation studies are better suited [9]. We also do not test the accuracy of the resulting tractography as for that case, a phantom or ex vivo data would be more suitable [10]. Instead, we aimed to determine how the overall connectivity is affected by differences in angular and spatial resolution. We aim to determine whether there is a particular reconstruction algorithm that yields reliable connections for both high and low resolutions, or whether one would be better suited for low resolution images and another for high resolution scans. It is critical to know what protocols can be used, and which connections are reliable, for consortium work where many potential protocols are combined to estimate pooled statistical effects.

## 2 Methods

### 2.1 Scanning Protocols

We scanned 20 young healthy adults (mean age: 23.6 years, SD 1.47) on a Bruker Medspec 4 Tesla MRI scanner at two time points three months apart using two different dMRI acquisitions at each time point and a single T1-weighted acquisition. The specifics of both acquisition protocols are presented in Table 1. We will refer to the acquisition schemes as the lower angular and higher angular resolution protocols, or dMRI-27 and dMRI-94, respectively. It is important to note here that these protocols not only differ in terms of their angular resolution but also their spatial resolution. Thus, we investigated the joint effect of the number of diffusion gradient directions as well as the size of the voxel. T1-weighted images were also acquired with a gradient-echo sequence (TI/TR/TE: 700/1500/3.35 ms; flip angle: 8°; slice thickness: 0.9 mm; 256 × 256 acquisition matrix).



**Table 1** Shows the parameter differences between both diffusion MRI acquisition protocols

Parameters	Low angular resolution	High angular resolution
No. of slices	21	55
Slice gap	0.5 mm	n/a
Orientation	Transverse	Transverse
FOV	230 mm	230 mm
Slice thickness	5 mm	2 mm
TR	290 ms	150 ms
TE	91.7 ms	92.3 ms
Base resolution	128	128
Multi-slice mode	Single-shot	Single-shot
Voxel size	$1.8 \times 1.8 \times 5.0$	$1.8 \times 1.8 \times 2.0$
B value max	$1146 \text{ s/mm}^2$	$1159 \text{ s/mm}^2$
Diffusion sensitized volumes	27	94
Number of B0 volumes	3	11

## 2.2 Image Preprocessing and Tractography

After removing extracerebral tissue from dMRI and T1 images, both were aligned to a standard space (MNI-Colin27 brain) with a voxel matrix of  $220 \times 220 \times 220$  and voxel size of  $1 \times 1 \times 1 \text{ mm}^3$ . The dMRI was denoised using non-local means [11]. We automatically extracted a whole white matter mask from each subject's T1-weighted image, which was then warped to the non-diffusion sensitized image of the dMRI ( $b0$ ). We then fitted tensors within the boundaries of the mask for each voxel, as well as orientation distribution functions (ODFs) from the CSA model, fiber orientation distributions (FODs) from the CSD model, and peak orientations from the B&S model. We computed the peaks from the CSA ODFs and the CSD FODs. The principal eigenvectors from the tensors, as well as the peak orientations from CSA, CSD and B&S reconstructions were fed into the EuDX deterministic streamline tractography algorithm from the DIPY package ([nipy.org/dipy](http://nipy.org/dipy)). For each subject, four sets of seeds were calculated, one for each time point and scan resolution. Seeds were selected within the white matter mask selecting them randomly with a spatial probability distribution proportional to the fractional anisotropy derived from the diffusion tensor. We used the same step size and angle threshold for all the tractographies to ensure consistency for the comparisons (angle threshold =  $60^\circ$ , step size = 0.5 voxel)

### 2.3 *Connectivity Matrix Calculation*

We segmented the cortex into 34 ROIs per hemisphere according to the Desikan-Killiany atlas using FreeSurfer ([freesurfer.net](http://freesurfer.net)). The segmented ROIs were dilated with a disk-type structuring element of size 1 voxel to ensure that the reconstructed fiber tracts reached the cortical labels. The number of fiber tracts intersecting each pair of regions was calculated and normalized with respect to the total fiber count and the volume of the ROIs to create fiber-density weighted connectivity matrices, also known as adjacency matrices. This process resulted in 16 connectivity matrices per subject, four for each reconstruction method: two for the lower resolution (dMRI-27) and two for the higher resolution (dMRI-94), one per time point.

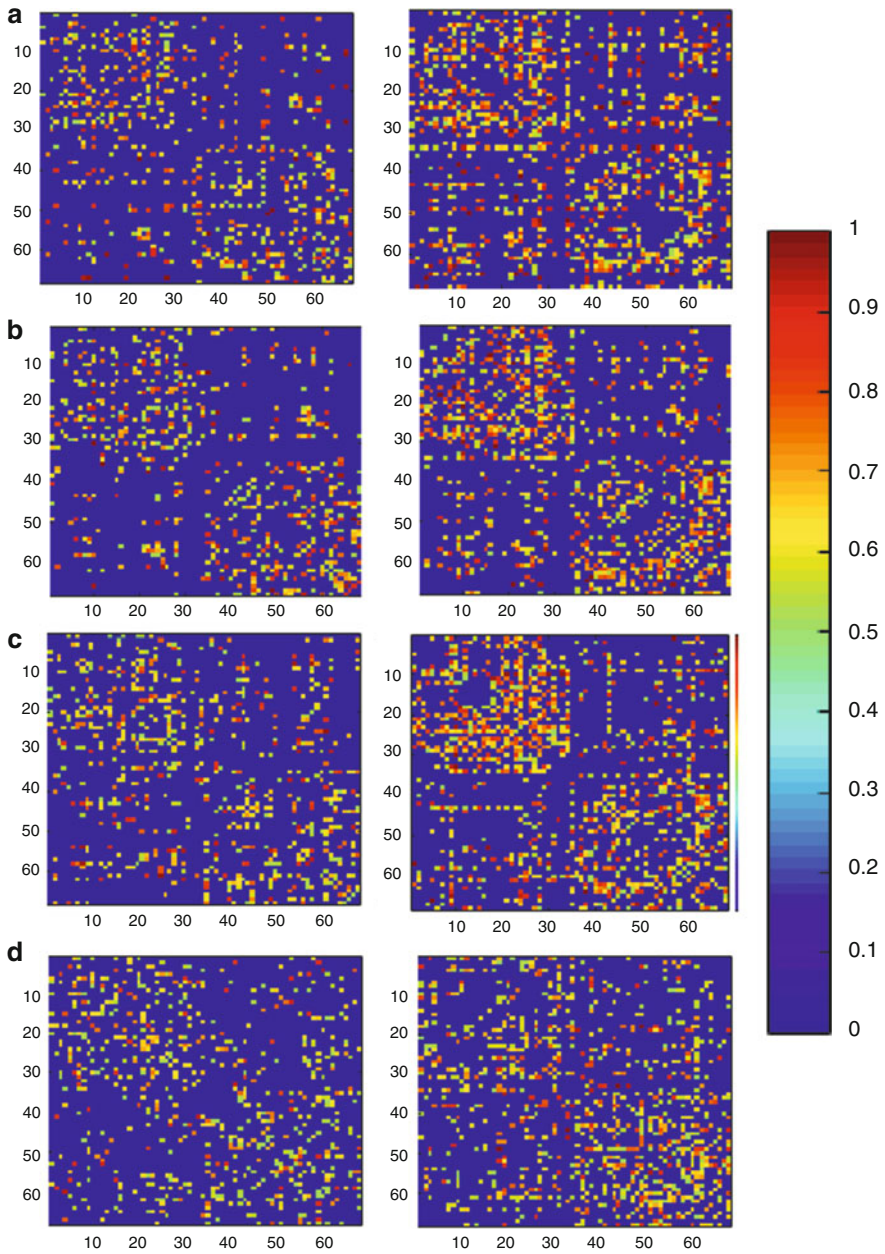
### 2.4 *Matrix Reliability Analysis*

To assess reliability between the two time points we used intra-class correlation (ICC). We used the R package PSYCH ([personality-project.org/r/html/ICC.html](http://personality-project.org/r/html/ICC.html)) to calculate one-way measures of ICC. The correlation was computed across all subjects, between the two time points and for each edge of the connectivity matrix. We thresholded the resulting ICC coefficients at 0.5. Figure 1 shows the eight matrices of  $ICC > 0.5$ , two per reconstruction model. We then masked the 16 connectivity matrices for each subject to only use connections that had an ICC value greater than 0.5.

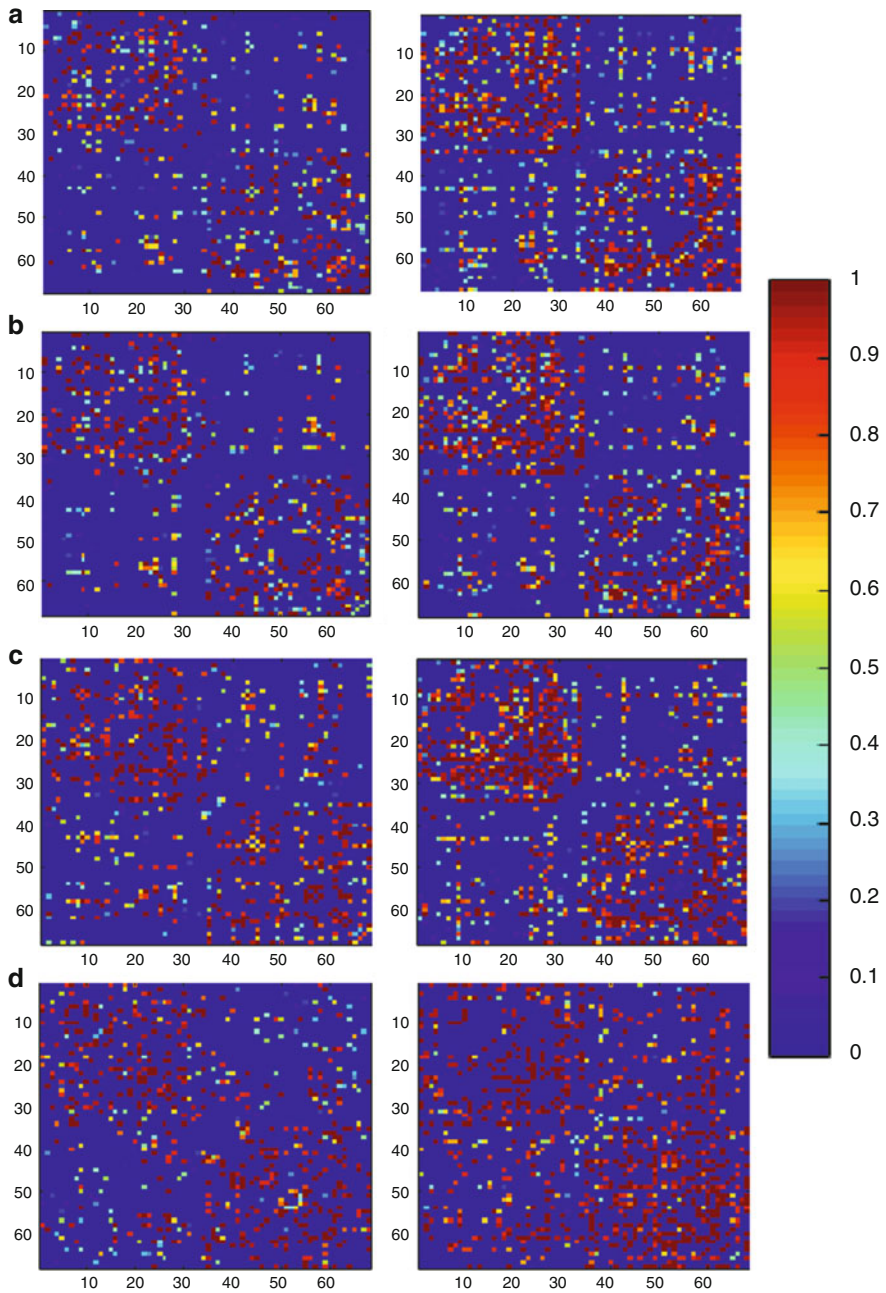
To obtain a probability map of the existing connections across the 20 subjects we added the matrices from time point one of all the subjects for each reconstruction model and for each acquisition protocol. We divided the resulting matrices by the number of subjects. The resulting probability matrices can be seen in Fig. 2.

We subsequently ran a paired t-test to compare the matrices from each protocol at a single time point. Finally, we corrected each p-map for multiple comparisons by using the false discovery rate method (FDR) [9].

To examine test-retest variability introduced by the automatic cortical segmentation, we computed the Dice coefficient between time points one and two for all the dilated cortical ROIs. Table 2 shows the mean and standard deviation across subjects of the Dice coefficient for each ROI. The average Dice coefficient value was above 0.7 for all but one ROI—the right entorhinal cortex—which is an anatomical location known to be prone to tissue induced inhomogeneities in gradient-echo T1-weighted images.



**Fig. 1** Reliable connections with ICC coefficient higher than 0.5. The *left column* shows the ICC thresholded matrices for the lower resolution dMRI protocol and the *right column* shows the ones for the higher resolution dMRI protocol. (a) Results for DTI, (b) CSA, (c) CSD and (d) B&S. The number of connections that are reliable is lower for the lower resolution dMRI than for the higher resolution



**Fig. 2** Probability matrices for each reconstruction method. The *left column* shows the probability maps of the lower resolution dMRI and the *right column* for the higher resolution dMRI, based on the following models: **(a)** DTI, **(b)** CSA, **(c)** CSD, and **(d)** B&S. The color bar represents the probability of existence of the connection across subjects. More connections are constantly found with the higher resolution imaging regardless of reconstruction model

**Table 2** This table shows the means and standard deviations of the Dice coefficients calculated by comparing the cortical ROIs from time point one and two

Cortical region of interest	Left hemisphere		Right hemisphere	
	Mean	Standard deviation	Mean	Standard deviation
Banks of the superior temporal sulcus	0.83	0.06	0.76	0.09
Caudal anterior cingulate	0.83	0.04	0.85	0.04
Caudal middle frontal	0.89	0.03	0.88	0.03
Cuneus	0.76	0.10	0.79	0.07
Entorhinal	0.74	0.07	0.68	0.09
Fusiform	0.80	0.04	0.79	0.05
Inferior parietal	0.90	0.04	0.91	0.03
Inferior temporal	0.84	0.05	0.84	0.04
Isthmus cingulate	0.84	0.07	0.84	0.04
Lateral occipital	0.91	0.03	0.91	0.03
Lateral orbitofrontal	0.84	0.03	0.82	0.04
Lingual	0.88	0.04	0.89	0.04
Medial orbitofrontal	0.75	0.08	0.78	0.08
Middle temporal	0.87	0.03	0.88	0.03
Parahippocampal	0.89	0.03	0.88	0.03
Paracentral	0.82	0.07	0.83	0.05
Pars opercularis	0.87	0.02	0.82	0.05
Pars orbitalis	0.87	0.03	0.87	0.04
Pars triangularis	0.91	0.02	0.91	0.02
Pericalcarine	0.85	0.08	0.87	0.05
Postcentral	0.86	0.06	0.83	0.07
Posterior cingulate	0.90	0.03	0.90	0.02
Precentral	0.93	0.02	0.93	0.03
Precuneus	0.91	0.04	0.91	0.03
Rostral anterior cingulate	0.86	0.03	0.82	0.04
Rostral middle frontal	0.93	0.01	0.92	0.02
Superior/frontal	0.94	0.01	0.94	0.01
Superior parietal	0.93	0.03	0.93	0.03
Superior temporal	0.89	0.03	0.87	0.03
Supramarginal	0.93	0.02	0.93	0.03
Frontal pole	0.79	0.07	0.80	0.08
Temporal pole	0.77	0.10	0.71	0.12
Transverse temporal	0.86	0.05	0.86	0.03
Insula	0.89	0.03	0.88	0.04

### 3 Results

We calculated the total number of edges that had an ICC coefficient above 0.5. Out of a total of 2312 connections the higher resolution DTI model had 22.8 % (528) reliable connections, while CSA had 20.7 % (479), CSD had 23 % (534), and BS had 19.2 % (444). For the lower resolution protocol, DTI had 13.1 % (304) reliable connections, CSA had 13.5 % (313), CSD had 14.7 % (340) and BS had 13.7 % (318). For both scanning protocols CSD had the highest number of reliable connections. As can be seen in Fig. 1, the thresholded ICC connectivity matrices of the lower resolution protocol appear to be sparser than the higher resolution ones. The mean percentage of reliable connections for the lower resolution protocol across the four reconstruction methods is 13.7 % (637.5), whereas for the higher resolution protocol it is 42.9 % (992.5). We also ran a two-sample *t*-test on the subjects' weighted thresholded matrices (time point one) to compare the lower and higher scanning protocols. We did not find any statistical differences after multiple comparisons correction between both scanning protocols and all reconstruction methods. The probability matrices in Fig. 2 show that the most reliable connections in our sample of subjects are largely within a hemisphere, and less between hemispheres.

We also studied the overlap of reliable connections across resolutions and across reconstruction models. The results can be seen in Table 3. The highest overlap within a single reconstruction method and across resolutions was shown for the CSD method, with 8.5 % overlap, followed by DTI with 8.1 % overlap. Interestingly, the overlap between CSA and CSD was above 8 %, within the same resolution and also between resolutions (lower vs. higher). A final test looked for the reliable connections present in all the ICC thresholded matrices, for all reconstruction methods and across resolutions. There were 14 reliable connections out of 2312 (0.6 %) present in all the matrices. The connections that were not present (i.e., empty edges) in all the matrices added up to 1156 of 2312 (50 %).

Most of the connections that were common to all matrices were those between regions of the frontal cortex (lateral and medial orbitofrontal, *pars opercularis* and *pars orbitalis*) and regions of the occipital (lingual, calcarine, lateral occipital regions and cingulate) and temporal regions (temporal poles, superior temporal gyrus and parahippocampal gyrus) (Table 4).

**Table 3** This table shows the proportion of fibers shared between the different reconstruction models and acquisition protocols

	DTI_27	CSA_27	CSD_27	BS_27	DTI_94	CSA_94	CSD_94	BS_94
DTI_27	*	7.2 % (167)	6.9 % (160)	3.2 % (188)	8.1 % (188)	7.7 % (179)	7.5 % (175)	4.5 % (106)
CSA_27	*	*	8.1 % (189)	3.1 % (73)	7.8 % (181)	7.7 % (188)	5.9 % (137)	4.5 % (111)
CSD_27	*	*	*	3.9 % (91)	8 % (187)	7.9 % (184)	8.5 % (198)	4.5 % (111)
BS_27	*	*	*	*	4.88 % (113)	5.1 % (119)	5.2 % (122)	5.3 % (121)
DTI_94	*	*	*	*	*	13.7 % (317)	13.3 % (309)	6.7 % (155)
CSA_94	*	*	*	*	*	*	14.8 % (343)	7 % (162)
CSD_94	*	*	*	*	*	*	*	7.3 % (169)
BS_94	*	*	*	*	*	*	*	*

It also shows the absolute numbers of shared connections out of the 2312 possible connections. The headers of the rows and the columns indicate the name of the reconstruction model (DTI, CSA, CSD or BS) and the scan resolution (27 for the lower resolution and 94 for the higher resolution, which indicate the number of diffusion weighted directions)



**Table 4** Each row shows a pair of cortical ROIs that are connected by streamlines. These connections were reliable across diffusion reconstruction methods and acquisition resolutions

Left bank of superior temporal gyrus	↔	Right medial orbitofrontal
Right fusiform	↔	Right lateral occipital
Right isthmus cingulated	↔	Left pars opercularis
Right lateral orbitofrontal	↔	Right pars opercularis
Left middle temporal	↔	Left lingual
Right lingual	↔	Right isthmus cingulated
Left lingual	↔	Left lateral orbitofrontal
Right medial orbitofrontal	↔	Right supramarginal
Right parahippocampal	↔	Right inferior temporal
Right pars orbitails	↔	Left temporal pole
Right pars orbitails	↔	Right supramarginal
Left pericalcarine	↔	Right rostral anterior cingulate
Right posterior cingulated	↔	Left superior frontal

## 4 Discussion

In this study we evaluated the test-retest reliability of four different dMRI reconstruction methods by tracing streamlines with one deterministic tractography algorithm and a standard processing pipeline to generate whole brain cortical connectivity matrices. We found that higher angular and spatial resolutions together yield more reliable connections in structural connectivity matrices computed with a deterministic streamline algorithm. Additionally, the CSD model yielded the greatest number of reliable connections for both scanning protocols. This was followed by the DTI model for the higher resolution and by the CSA model for the lower resolution scans. The higher reliability seen in CSD derived matrices may be related to the fact that previous publications have found more accurate tractographies when they are based on sharper ODF glyphs [10]. When looking for the most reliable connections across all matrices, we found a high overlap in fronto-occipital and fronto-temporal connections, as well as connections between ROIs of the frontal lobes.

Many studies have been published comparing reconstruction models for dMRI [9]. Most are based on simulated data and focus on the accuracy of the reconstruction in terms of the number of the recovered fiber compartments and the angular accuracy. Other studies focused on comparing fiber-tracking methods, testing the algorithms on phantoms to determine the proportion of correct connections traced [10]. In this study, we explored the problem from a different perspective, comparing the resulting structural connectome across methods, with two different imaging protocols in the same subjects. This study design can help reveal reliable and replicable network components, for situations where data from various sites are analyzed together to gain statistical power.



Two similar studies analyzing human dMRI scans have been previously published [13, 14]. Baumgartner et al. designed an optimization framework to estimate parameters from any reconstruction model and perform tractography in a standardized way. Within this framework, they compared seven models and reconstructed two major fiber bundles in ten subjects. By using two measures, called traceability and coverage they assessed the quality of the tractographies. The mixture models with more than one tensor and free water components scored higher for both measures, but DTI scored very high for traceability only. The authors did not extend the analysis to the whole range of connections across the entire brain. Yo et al. compared four different reconstruction models (DTI, CSD, B&S and Persistent Angular Structure) on one subject and reconstructed connectivity matrices from whole brain probabilistic and deterministic tractographies and 14 language-related cortical regions. They found that the connectivity matrices were significantly correlated across all four reconstruction methods and tracking algorithms. The deterministic tractography yielded less sparse connectomes with stronger connections between the regions of interest.

Even though the results from these previous studies differ, they are similar to our findings here, in that relatively large *cortical* ROIs were used for the comparisons. One general conclusion is that models that reconstruct multiple fibers, such as multi-tensor models and CSD are better suited to trace reliable connections between cortical regions. While DTI appears to be very reliable, as Baumgartner and colleagues found, it is an optimal strategy to trace the connections between a pair of regions but has less coverage. This means that the fiber bundles do not diverge to reach neighboring regions; this can be problematic when reconstructing long-range fibers. This may explain our results in Table 3, where only 7–13 % (lower—higher resolution) of connections overlap between DTI and CSA/CSD, but slightly more connections overlap between CSA and CSD (8 % for the lower resolution, 14 % for the higher resolution).

Future work will focus on replicating these findings across more datasets for test-retest reliability studies, and finding more refined ways to determine the brain connections that prevail regardless of the acquisition parameters or the type of reconstructions model used.

## References

1. Hagmann, P., Cammoun, L., Gigandet, X., Meuli, R., Honey, C.J., et al.: Mapping the structural core of human cerebral cortex. *PLoS Biol.* **6**(7), e159 (2008)
2. Basser, P., et al.: MR diffusion tensor spectroscopy and imaging. *Biophys. J.* **66**(1), 259–267 (1994)
3. Kreher, B., Schneider, J., Mader, I., Martin, E., Hennig, J., Il'yasov, K.: Multitensor approach for analysis and tracking of complex fiber configurations. *Magn. Reson. Med.* **54**, 1216–1225 (2005)
4. Aganj, I., et al.: Reconstruction of the orientation distribution function in single- and multiple-shell q-ball imaging within constant solid angle. *Magn. Reson. Med.* **64**, 554–556 (2010)

5. Wedeen, V.J., et al.: Mapping complex tissue architecture with diffusion spectrum magnetic resonance imaging. *Magn. Reson. Med.* **54**(6), 1377–1386 (2005)
6. Jahanshad, N., et al., Diffusion imaging protocol effects on genetic associations. *Proc. IEEE Int. Symp. Biomed. Imaging* 944–947 (2012)
7. Tournier, J.D., Calamante, F., Connelly, A.: Robust determination of the fibre orientation distribution in diffusion MRI: non-negativity constrained super-resolved spherical deconvolution. *Neuroimage* **35**(4), 1459–1472 (2007)
8. Behrens, T.E.J., Johansen-Berg, H., Jbabdi, S., Rushworth, M.F.S., Woolrich, M.W.: Probabilistic diffusion tractography with multiple fibre orientations. What can we gain? *Neuroimage* **34**(1), 144–155 (2007)
9. Daducci, A., Canales-Rodríguez, E.J., et al.: Quantitative comparison of reconstruction methods for intra-voxel fiber recovery from diffusion MRI. *IEEE Trans. Med. Imaging* **33**(2), 384–399 (2014)
10. Côté, M.A., Girard, G., et al.: Tractometer: towards validation of tractography pipelines. *Med. Image Anal.* **17**, 844–857 (2013)
11. Manjon, J.V., et al.: Adaptive non-local means denoising of MR images with spatially varying noise levels. *J. Magn. Reson. Imaging* **31**(1), 192–203 (2010)
12. Benjamini, Y., Hochberg, Y.: Controlling the false discovery rate—a practical and powerful approach to multiple testing. *J. R. Stat. Soc. B Met* **57**, 289–300 (1995)
13. Baumgartner, C., et al.: A unified tractography framework for comparing diffusion models on clinical scans. In: *Proceedings of CDMRI 2012. 15th International Conference on Medical Image Computing and Computer Assisted Interventions, Nice* (2012)
14. Yo, T.S., Anwender, A., et al.: Quantifying brain connectivity: A comparative tractography study. In: *Medical Image Computing and Computer-Assisted Intervention – MICCAI 2009. Lecture Notes in Computer Science*, vol. 5761, pp. 886–893 (2009)

# Index

- Adaptive enhancement, 137
  - coefficient bound, 137
- Alzheimer's disease, 41–52
- Alzheimer's Disease Neuroimaging Initiative (ADNI), 42, 43, 46
- Asymmetry, 194
  
- Biophysical models, 55, 56
  
  
- Classification, 41–52
- Cylindrical pore, 68
  
  
- Diffusion MRI (dMRI), 42, 43, 46, 48, 50, 51, 65, 87, 194, 219–230
  - fiber orientation, neighborhood information, 87
  - HARDI, model comparison, HCP, AIC, BIC, cross validation, 159
  - holistic reconstruction, super resolution, 28
  - micro-structure imaging, variable separation, 56
  - phantom, EAP, asymmetry, temperature, viscosity, 183
  - q-space sampling, HARDI, 75
  - tractogram alignment, registration, linear assignment problem, 109
- Diffusion-weighted MRI, microstructure, EAP, SHORE, 65
- dMRI. *See* Diffusion MRI (dMRI)
- 3D-SHORE, 66
- DWI, HARDI, fiber clustering, redundancy reduction, metrics comparison, 171
- EAP. *See* Ensemble average propagator (EAP)
- Enhancement, 131
  - apparent diffusion coefficient, 134
  - coefficient bound, 133
  - diffusion tensor imaging, 133
  - generalized diffusion tensor imaging, 136
- Enhancement, sharpening, deconvolution, diffusion MRI, 131
- Ensemble average propagator (EAP), 132, 194
  
  
- Fiber orientation, 87
  
  
- Global tractography, diffusion MRI, Markov chain Monte Carlo, parallelization, 122
  
  
- High angular resolution diffusion imaging (HARDI)
  - feature selection, atlas, Alzheimer disease, 46, 207
  
  
- Implicit method, arbitrary geometry, microstructure, 3
- Intra-voxel fibre structure estimation, 75
  
  
- Likely FOs, 90
- Low-rank approximations, 15–24
  
  
- MAPMRI, 66
- Model fitting, 56, 60

- MT-MAPMRI, [67](#)
- Multi-compartment models, [55](#), [56](#), [63](#)
- Multi-tensor, [66](#)
- Multimodal brain atlas, probabilistic white matter parcellation map, HIV, DTI-T1 brain template, [99](#)
  
- Parameter estimation, [55](#), [56](#)
- Phantom, [194](#)
- Power sharpening, [138](#)
  
- Resolution enhancement, [146](#)
- Return to the axis probability (RTAP), [68](#)
  
- Single  $q$ -shell sampling schemes, [77](#)
- Spatial coherence, [88](#)
- Spherical harmonic transform, [75](#)
  
- Spherical harmonics, [76](#)
- Structural connectivity, [219–230](#)
- Super resolution, [15–24](#), [146](#)
  
- Temperature, [194](#)
- Test-retest reliability, [220](#), [229](#), [230](#)
- Total variation, [15–24](#)
- Tractography, [220–222](#), [229](#), [230](#)
  
- Variable projection method, [55](#)
- Viscosity, [194](#)
  
- White matter (WM), [220–222](#)
- White matter (WM) microstructure, [50](#)
- Whole-body diffusion-weighted MRI, multi-station acquisition, registration, apparent diffusion coefficient, [195](#)